NOTE TO USERS

Dissertation

The Response of Precipitation and Surface Hydrology to Tropical Macro-climate Forcing in Colombia

Submitted by

Saul Marín

Department of Civil Engineering

In partial fulfillment of the requirements
For the Degree of Doctor of Philosophy
Colorado State University
Fort Collins, Colorado
Spring 2004

COLORADO STATE UNIVERSITY

December 15, 2003

We hereby recommend that the dissertation prepared under our supervision by Saul Marín titled "The response of precipitation and surface hydrology to tropical macro-climate forcing in Colombia" be accepted as fulfilling in part requirements for the degree of Doctor of Philosophy.

Committee on Graduate Work

Roger A. Pielke Sr.
Dr. Roger A. Pielke, Sr.

José D. Salas
Dr. José D. Salas

Freeman M. Smith
Dr. Freeman Smith

Ellen Wohl
Dr. Ellen Wohl

Jorge A. Ramírez
Advisor: Dr. Jorge A. Ramírez

Sandra Woods
Department Head

ABSTRACT

THE RESPONSE OF PRECIPITATION AND SURFACE HYDROLOGY TO TROPICAL MACRO-CLIMATE FORCING IN COLOMBIA

Regional and local weather and climate behaviors are strongly affected by macroclimate phenomena that perturb the general atmospheric circulation. In tropical regions, and specifically tropical South America, weather and climate are affected by such factors as the meridional oscillation of the Inter-tropical Convergence Zone, the Pacific and Atlantic oceans, the Amazon basin, and the Andes Mountains, among others. Interactions between atmosphere and oceans in this region produce the so-called El Niño/Southern Oscillation (ENSO) phenomenon, which is recognized as the dominant mode of the inter-annual climate variability in the Tropical Pacific. Colombia is among the South American countries that experience large climate anomalies because of ENSO. In fact, ENSO variability explains about 50% of the observed variance of Colombian hydrology beyond the annual cycle when a linear relationship is assumed. However, the hydrologic response in Colombia to a particular ENSO event is highly complex and non-linear.

In order to describe this complex, non-linear hydro-climatic response to large scale atmospheric forcing in Colombia, a coupled atmospheric-land surface hydrology modeling approach was implemented whose main components are Colorado State University's Regional Atmospheric Modeling System (RAMS) and the Swedish Hydrologiska Byråns Vattenbalansavdelning Hydrologic Modeling System (HBV-HMS). RAMS is used in a two-nested grid domain for seasonal simulations and a four-nested grid domain for daily simulations. Seasonal simulations emphasize the annual cycle at regional scales, focusing on the spatial and temporal distribution of the hydro-climatic response to ENSO forcing at monthly time scales. Daily simulations focus on describing the diurnal cycle for specific watersheds. The HBV-HMS is implemented for a set of specific watersheds and used to examine watershed response at daily time scales.

Results showed that the spatial distribution of precipitation in Colombia is highly dependent on the local circulation processes generated by complex interactions between large scale atmospheric forcing and the complex surface features present in the region.

Results of the seasonal simulations showed that temperature, pressure, water mixing ratio, relative humidity and wind velocity distributions are very well represented. On the other hand, pronounced differences are observed in the precipitation field, especially in centers of higher precipitation, and an imbalance between mountains and valleys is produced. However, the general pattern of precipitation is good enough as a criterion to qualify areas of deficit or surplus rainfall. Remarkably, results show that the warm phase of ENSO leads to a generalized decrease of precipitation along the Andes ranges and that the low lands of Colombia get more precipitation than during a cold ENSO phase.

Similarly, daily simulated fields show a very good agreement with observed values. However, the simulated diurnal cycle of precipitation exhibits a temporal phase lag of several hours. Furthermore, daily simulations tend to underestimate both the total amount of precipitation and the duration of precipitation events. Despite these discrepancies, the results of the coupled modeling effort clearly demonstrated the ability of this approach to capture the non-linear and complex interactions of large-scale atmospheric forcing and local characteristics as indicated by the satisfactory simulation of streamflow responses for a set of small watersheds.

Results show the great potential of using this tool for regional climate forecasting for at least one season ahead in Colombia, which is fundamental in water resources planning. The ability to describe appropriately the effects of macroclimatic phenomena and general climatic circulation on the regional and local hydro-climate system of Colombia is important, especially because of the complexity of the processes occurring in this mountainous region, with its local atmospheric circulations and the complex thermally driven circulations. Finally, the feasibility to link the output of the atmospheric modeling system with a hydrologic modeling system shows a great potential for developing operational short-term forecasting essential for an optimal operation of water resources systems.

Saul Marín
Department of Civil Engineering
Colorado State University
Fort Collins, CO 80523
Spring 2004

ACKNOWLEDGEMENTS

An undertaking such as a dissertation is a challenge in life and it is possible to complete only because of the support of many people. Dr. Jorge A. Ramirez was not only my academic support but also my friend during my graduate studies. He gave me the necessary encouragement during the difficult moments and provided me the foresight to proceed in my purpose; for him my first debt of gratitude. My special gratitude to Professor Roger A. Pielke Sr., who not only provided access to the CSU-RAMS model but most important, extensive support and assistance throughout this challenging task.

Special thanks to my others committee members, Dr. José D. Salas, Dr. Freeman Smith, and Dr. Ellen Wohl for their guidance and helpful suggestions. Thanks to Dr. Robert Walko, Christopher Castro and Dr. Bill Cotton of the Department of Atmospheric Science at Colorado State University, and Brian Mapes from NOAA-CIRES Climate Diagnostics Center. They took time from they busy schedules to provide me with suggestions and assistance.

Supercomputing time and access to datasets were provided by the National Center for Atmospheric Research. Interconexion Electrica (ISA) of Colombia provided financial support. Empresas Publicas de Medellin (EPM) of Colombia provided computing time and access to the HBV hydrologic modeling system. ISA together with EPM and the Universidad Nacional de Colombia provided observed precipitation data of Colombia.

I want to acknowledge my wife Mirian, and our children Samir and Adrian. They patiently gave me love, support and encouragement for dealing with all the challenges I have faced. They are my best.

Without the help of all these people and many others that I have not mentioned this dissertation would not have been possible.

LIST OF FIGURES

LIST OF TABLES

TABLE OF CONTENTS

THE RESPONSE OF PRECIPITATION AND SURFACE HYDROLOGY TO TROPICAL MACRO CLIMATE FORCING IN COLOMBIA

1 INTRODUCTION

1.1 Generalities

The annual cycle is generally accepted as the most familiar variation of climate. In addition, the average annual cycle is considered the most predictable climatic variation. For example, in middle latitudes the annual cycle presents four seasons characterized mainly by variation in temperature according to the sun's position. On the other hand, in tropical zones, where intra-annual variations in temperature are not large, the annual cycle is characterized by wet and dry periods as a function of the intra-annual distribution of precipitation. However, because of the presence of aperiodic macroclimate phenomena that perturb the mean state of the general atmospheric circulation, the inter-annual variance of the annual cycle is large. For this reason, increasing the ability to simulate and explain the annual cycle will be helpful in understanding not only the inter-annual but also the intra-annual climate variability in any region (GOALS, 1994). Deviations of the actual values with respect to the average climatic values are known as anomalies and the skill in climate prediction depends on knowing how these anomalies will behave in the future.

Even though the global average annual cycle could be described as a function of the global patterns of climate behavior and of their associated patterns of atmospheric general circulation, its character varies from region to region according to the particular processes that affect each region. Year-to-year fluctuations of precipitation within a region could be large; therefore, predictions of these variations, with lead times of at least a season, would help mitigate their negative impacts and enhance their positive impacts. This requires identification of the mechanisms and the interactions between the land

surface and the atmosphere that produce and influence this variability. In tropical regions, specifically continental tropical South America, weather and climate are largely affected by factors such as the meridional oscillation of the Inter-tropical Convergence Zone (ITCZ), the influence of the Pacific and Atlantic oceans, the Amazon jungle, and the Andes Mountain range, among others. In addition, the interaction between atmosphere and oceans, which plays an important role in large scale climate variability, in this region produces the so-called El Niño/Southern Oscillation (ENSO) phenomenon, which is recognized as the dominant mode of the inter-annual climate variability in and over the tropical Pacific. The ENSO is a quasi-periodic phenomenon that occurs every four to eleven years. It is characterized by a warm current that appears in the tropical Pacific (El Niño, oceanic component) accompanied by a negative atmospheric pressure difference between Tahiti, French Polynesia (18°S, 150°W), and Darwin, Australia (12°S, 131°E), called the Southern Oscillation (atmospheric component). See for example Rasmusson and Wallace (1983), Rasmusson and Carpenter (1982), or Horel and Wallace (1981).

Because of its great influence on weather and climate, in recent years there have been a great number of studies focusing on the behavior and effects of ENSO on tropical South America. Among them are those by Waylen et al. (1996), Waylen and Poveda (2002), Poveda and Mesa (1995, 1996, 1997), Pulwarty et al. (1992), Gessler (1995), Kousky and Kayano (1994), Marengo and Hastenrath (1993), Halpert and Ropelewski (1992), Richey et al. (1989), Kiladis and Diaz (1989), Aceituno (1988, 1989), Rogers (1988), Hastenrath (1976, 1990). Additionally, the scientific community has made great efforts to improve ENSO predictions by using coupled ocean-atmospheric modeling systems. However, these predictions do not give much information about regional ENSO effects. On the other hand, until now, researchers have used mainly regression analyses and other statistical techniques to describe the regional effects of ENSO (e.g., testing statistics between ENSO and non-ENSO years, or using ENSO variables as a perturbation function on stochastic models (e.g., Woolhiser et al. 1993)). However, these studies recognize that the climate anomalies have large variability under the same ENSO phase and their relation with hydrology is highly nonlinear. For instance, Moss et al. (1994) think that, due to the heteroscedasticity present, linear regression between ENSO and stream flows is very questionable for use in New Zealand. This means that

statistically based models cannot be effective enough in capturing ENSO effects in specific regional areas. Therefore the applicability of physically based models should be extended to these regions and scales.

Colombia is among the tropical South American countries that experience climate anomalies because of ENSO. Colombia has shown critical changes in its precipitation regimes during ENSO episodes. The effects of ENSO on Colombian weather and climate have been analyzed by Carvajal et al. (1998), Poveda and Mesa (1993, 1995, 1996, 1997), Mesa et al. (1994a,b), Poveda (1994), Poveda and Penland (1994), Salazar et al. (1994b), among others. Current understanding about how this phenomenon affects Colombian hydro-climatology has been obtained through several empirical analysis and statistical techniques such as correlation analysis, empirical orthogonal functions, principal components, and spectral analyses, among others. These studies have made particular emphasis on trying to understand ENSO effects on Colombian precipitation and stream flows regimes. As a result of these studies two conclusions seem to be clear: first, ENSO variability could explain about 50% of the observed variance of Colombian hydrology beyond the annual cycle when a linear relationship is assumed; and second, there is a complex variation in the response of the Colombian hydrologic system to a particular ENSO event. A good example of this is the difference between the Colombian hydrologic system responses to both the 1982-83 and 1991-92 ENSO episodes. These two ENSO events had similar long temporal durations, but the 1991-92 episode produced larger effects on Colombian hydrologic system response, even though the 1982-83 event is considered stronger. In conclusion, no matter how detailed our knowledge about ENSO is, and how our ability to predict its occurrence and dynamics improves, further knowledge in developing physically based techniques is required in order to translate the general ENSO knowledge into information that can be used for regional and local economic planning.

This dissertation focuses on the use of a coupled land surface-atmospheric modeling system to study the role that factors interacting during ENSO and non-ENSO phases play in the Colombian hydrologic system response. Northern South America will be used as a geographic central region for a coupled atmospheric-hydrologic modeling effort, including part of Central America, a portion of the Caribbean Sea and the tropical

Pacific Ocean. Additionally, this modeling effort uses several resolutions; the highest resolution analysis will be centered over Colombia since this is the particular area of study. Special attention will be given to the surface physics model taking into account the great effect that the Andes mountain range plays in the spatial distribution of the Colombian hydrologic system response.

A difficult task in developing these modeling systems is the coupling of the atmospheric and the hydrologic models. This is because the spatial and temporal scales of important phenomena are different for atmospheric processes when compared to the dominant surface hydrologic processes. Therefore, as implied above, several resolutions will be necessary considering aggregation/disaggregation (upscaling/downscaling) to link the processes in both domains. One option is to consider statistical downscaling of the average spatial rainfall from a General Circulation model that will be used as the input to the hydrologic model. An alternative option is to use the large-scale atmospheric data set to drive a regional atmospheric modeling system in a nested grid domain, such that the finest resolution is appropriate to obtain precipitation input for a hydrologic model. A few researchers have addressed the difficult upscaling/downscaling task, see for example Kang and Ramírez, (2002), Yu et al. (1999), Cox et al. (1998), Kidson and Thompson (1998), Kite (1997), Wilby and Wigley (1997), Over (1995), Wood (1995), Over and Gupta (1994), Epstein and Ramírez (1994), and Avissar (1993), among others. In this study, we take the second alternative option, that is, we use a regional atmospheric model to develop hydrologic input fields of the appropriate resolution. Because of the extremely mountainous nature of the area of interest, an important aspect for choosing the models of this coupling is the hill-slope scale soil moisture re-distribution model.

One of the major challenges to achieve the goals of this study is the availability of information or lack thereof. In this study, we use data and information collected by the National Oceanic and Atmospheric Administration (NOAA) and the National Center for Atmospheric Research (NCAR) of the United States of America; the Hydrology, Meteorology and Environmental Studies Institute (IDEAM) (Instituto de Hidrologia, Meteorologia y Estudios Ambientales), the Electric Interconnection Utility (ISA) (Interconexion Electrica), the Public Utility Company of Medellin (Empresas Publicas de

Medellin) and the National University (UN) (Universidad Nacional) of Colombia, among others.

In summary, this study attempts to implement a regional atmospheric modeling system for addressing two objectives. The *first objective* is to simulate precipitation fields at local scales over central Colombia. The *second objective* is to use those fields to determine the local hydrologic response to large-scale atmospheric phenomena. The *overarching* objective is to improve current knowledge of how macroclimate phenomena, in particular ENSO, affect the regional and local hydrologic system response in Colombia beyond those variances that can be explained by using statistically based methods.

1.2 Atmospheric and orographic factors affecting the weather and climate of Colombia

Colombia is a country of about 1140000 km^2 of surface land area and extends from the Caribbean (12° 31' N) to the Amazon basin (04° 14' S), and from the Orinoco-Negro river (66° 51' W) to the Pacific Ocean (79° 03' W). Because of its geographic location, the major observed circulation features of the tropical atmosphere affect its climate. See Figure 1-1

According to Mesa et al. (1997), tropical South American climate is mainly affected by the following macro-climate phenomena: ENSO, the North Atlantic Oscillation (NAO), the easterly waves, the mesoscale convective complexes (MCC), the Quasi-biennial Oscillation (QBO), and the Amazon jungle circulation. In addition, these macro-climate phenomena are themselves affected by other lower frequency phenomena such as the North Pacific Oscillation (NPO), which has a quasi-decadal variability. For example, according to Gershunov and Barnett (1998), climate patterns associated with ENSO in North America are more consistent and stronger only during the high phase of the NPO. Current knowledge of the interactions among these phenomena and their effects on the regional hydrologic system must be improved, improvement that constitutes one of the main objectives of this study. Associated with these large-scale phenomena are the characteristics of the region such as its complex orography and its coastline. As a final result of the interaction among these factors, tropical South America presents a large

variety of climate. In particular, Snow (1976) described Colombia as a country of climate extremes, and some researchers have concentrated in trying to explain the mechanisms that produce this large spatial variability in such a small land surface area. For example, Lopez and Howell (1967) described the mechanisms that convert the Colombian Pacific coast into the rainiest place of the American continent; and, in the same direction, Velasco and Fritsch (1987) analyzed how MCCs are favored to form over some particular Colombian locations.

In general, the coupling between atmosphere and land surface is established by precipitation (an excitation to land surface from the atmosphere) and by evaporation and transpiration (a feedback from the land surface to the atmosphere - referred to hereafter as evapotranspiration). The amount of evapotranspiration depends on the land water availability, that is, on the soil moisture state variable that controls the land surface fluxes. Additionally some studies seem to show that topography is the major control of the distribution of soil moisture (e.g., Stieglitz et al., 1997), implying that a modeling system that reflects the impact of the topography on soil moisture will be necessary. Therefore, particular attention will be given to the hill-slope modeling system because of the complex orographic features of the region. In summary, the modeling system must be able to deal with spatial aggregation/disaggregation precipitation schemes, spatial distribution and temporal evolution of the soil moisture, and evapotranspiration process.

It is clear that the accurate simulation of the atmospheric processes of this particular region is dependent on how well the above influencing factors are modeled and how many of them are taken into account. In the particular case of Colombia, a good modeling system must be able to describe (Mesa et al., 1997): the Hadley cells, the tropical dynamics where the MCCs are very important, the dynamics of the Inter-tropical Convergence Zone (ITCZ) (considered responsible for the temporal distribution of precipitation over tropical South America as a result of its meridional displacement year round), the Equatorial waves or well known easterly waves, a good representation of the topography, and of the vertical structure of the atmosphere.

1.3 Objectives

The main goal of this research is to perform representative simulations of the regional weather and climate of Colombia using a regional climatic model, and to couple it to a regional model of surface hydrology for purposes of hydrologic impact studies. This coupled modeling system should be able to describe the major mechanisms or factors forcing the actual weather and climate and the associated hydrologic response. Among these mechanisms special attention will be given to macroclimate phenomena such as the ENSO and to locally important tropical general circulation features such as the periodic movement of the Inter-tropical Convergence Zone (ITCZ). The expectation is that such modeling effort will improve our knowledge of how ENSO forces the response of the hydrologic system in Colombia beyond those variances that can be explained by using empirical correlation assuming a linear relationship between both processes. Therefore, special attention will be given to the precipitation and stream flow obtained by simulations during ENSO periods.

Three specific objectives summarize the main goal:

The first objective is to describe and model the main features of precipitation in Colombia at a seasonal time scale by using a regional climate model, which will be the main link between the macroclimatic atmospheric circulation and precipitation over Colombia.

The second objective is to describe, model and reproduce the main features of individual storm events over a specific region of Colombia and make these data suitable as an input to a hydrologic model.

The third and last objective is to implement a hydrologic modeling system that will be driven by output from the atmospheric model in order to simulate stream discharges for a specific watershed in Colombian.

1.4 General Methodology

The basic principle is the linkage of a set of models to translate general circulation information into precipitation and stream flow responses over Colombian territory.

Climate general circulation information is obtained from the global tropospheric analysis data set of the National Meteorological Center (NMC) that has a 2.5° latitude-longitude resolution combined with surface and upper air measurements. This information is used as an input to a regional atmospheric modeling system to produce precipitation. In turn, this precipitation is used as an input to a hydrologic modeling system to produce stream flow. See Figure 1-2

In order to achieve the goals of this research, three main steps are necessary. First, definition and collection of the data required to characterize the surrounding atmosphere, oceans, and land surface to support simulation and weather/climate prediction over Colombia. Second, implementation and calibration of the atmospheric-hydrologic modeling system required to simulate observed hydrologic response in Colombia. By simulating a historical ENSO event, the hydrologic responses in Colombia will be compared with historical data. In this process, several simulations are done to adjust the model parameters until the results are as close as possible to historical data. Third, performing sensitivity analyses essential to study the hydrologic response to the same atmospheric forcing when the land surface characteristics (topography, soils, land-use, etc) are changed. Finally, these physically based analyses are complemented with standard statistical analyses to elicit behavior.

1.4.1 Model Implementation

Choosing the platform and the options necessary to have a good representation of the dynamics of the tropical atmosphere is one of the most important tasks in this project. Unlike extra-tropical circulation systems, which are analyzed by using quasi-geostrophic theory, there is no theoretical framework to provide an overall understanding of large-scale tropical motion. However, what seems to be clear is that this understanding, at least, requires consideration of equatorial wave dynamics, interaction of cumulus convection and mesoscale circulation with large-scale motions and air sea interactions (Holton, 1992). In summary, a methodology able to simulate phenomena on a wide range of scales and allow the feedback among them is necessary. To achieve this purpose, versions 4.2 and 4.3 of the Regional Atmospheric Modeling System (RAMS) developed at Colorado State University (CSU) (CSU-RAMS) are used as a component of the modeling system

to simulate the mesoscale atmospheric circulation. A thorough description of this modeling system can be found in McQueen et al. (1997), Walko et al. (1995), and Pielke et al. (1992). CSU-RAMS will be set up on two different nested-grid configurations; for both of them, the coarsest grid spans northern South America including part of Central America, the Caribbean Sea and the tropical Pacific, while the finest resolution focuses on Colombia. Seasonal simulations will use a two-nested grid configuration. Storm event simulations will use a four-nested grid configuration.

The last component of this implementation involved the use of a surface hydrologic model to simulate surface runoff. The linkage between the CSU-RAMS and the hydrologic modeling system was implemented only for results obtained with the four-nested grid domain because of the differences in spatial scales between the atmospheric and hydrologic models.

1.4.2 Simulations

In order to understand and describe how ENSO affects hydrologic response in Colombia, it is necessary to consider both of its phases, the warm and the cold phase. Accordingly, the 1991-92 warm period and the 1989 cold period are analyzed. Since these episodes are recent, the existing associated observed precipitation data for their analyses are more reliable. The 1991-92 and 1997-98 warm periods were different, not only in their duration but also, and most important, in their effects on Colombian weather and climate, e.g., while the 1991-92 phenomenon was longer in duration, its hydrologic effects were less profound, which is why the 1991-92 is chosen. The 1989 cold period is chosen as an opposite condition to the warm periods and because it is helpful to this analysis due to the large amount of precipitation over Colombia during this year. Simulations through a whole season (six months) are done.

Three dimensionally variable initial model fields of velocity, temperature, pressure and moisture are used as initial conditions. Boundary conditions are provided to the model every six or twelve hours for each one of the variables mentioned above. Comparisons between generated (by the model) and historical data of streamflow and precipitation are made. Furthermore, prognostics for daily periods in some watersheds are

calculated, and particular emphasis is made on those Colombian watersheds where the electrical power generation is concentrated.

Summarizing, a regional surface hydrology-atmospheric modeling system is used. This modeling system is capable of representing multiple scale interaction using a telescopic sequence of nested grid domains. In particular, the solution implemented a range of grid sizes from 160-km to 2.5-km in order to consider the main regional and local processes responsible for producing precipitation in Colombia. It is expected that this modeling system combined with the grid configuration, captures precipitation patterns moderately well. Figure 1-2 shows a schematic representation of the study approach.

1.5 Contributions of this research

This research focuses on the implementation and application in Colombia of a new coupled modeling system consisting of an existing regional climatic model and an existing hydrologic model. This methodology of implementation attempts to take explicit account of the non-linear relationship between macroscale atmospheric processes, large-scale climatic phenomena and the regional weather/climate of Colombia. To the best knowledge of the author, this is the first time that this methodology is implemented for Colombia. Additionally, it is expected that, using this methodology, further knowledge of macroclimate phenomena will be translated to improvements in understanding of local weather and climate, e.g., better information will be available for regional and local planning in Colombia.

Figure 1-1: Geographic location of Colombia

Figure 1-2: Schematic of the general solution approach

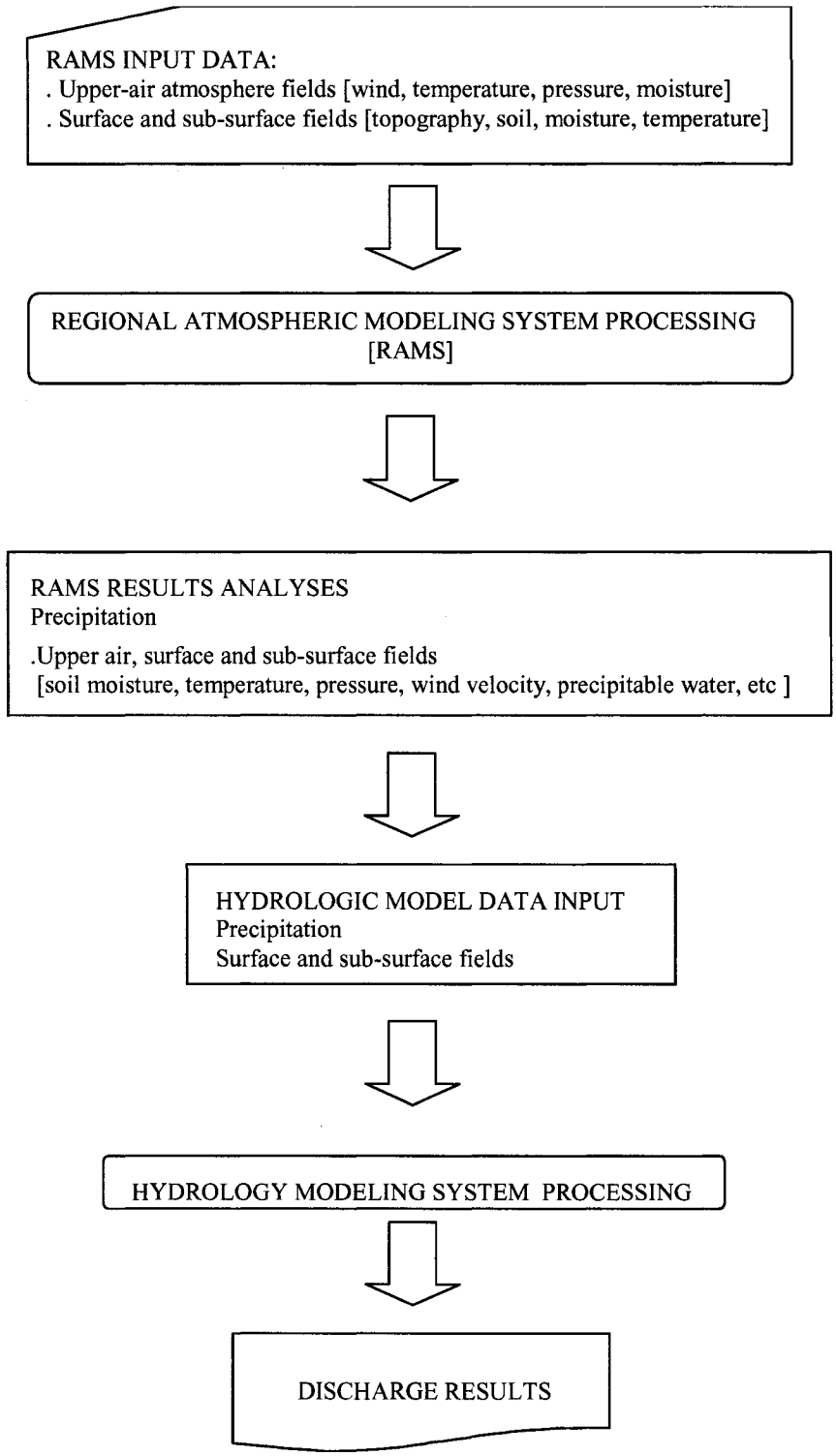

2 TROPICAL PATTERNS AND COLOMBIAN CLIMATE

Because of its geographic location, as stated in section 1.2, the climate of Colombia is affected by the major circulation features of the tropical atmosphere. Before describing the regional climate of Colombia and to provide a context for a better understanding of climate variability in Colombia, a brief review of tropical general circulation patterns and climate of tropical South America will be presented first.

2.1 Trade Winds (Alisios)

The average meridional distribution of absorbed energy is quite non-uniform. While the low latitudes absorb considerably more solar radiation (short wave radiation) than the higher latitudes (as a result of the characteristics of Earth's orbit around the sun, the characteristics of Earth's rotation about its axis, and the relative angle between the axis of rotation and the plane of the ecliptic), the average latitudinal variation of terrestrial energy emission (long wave radiation) is relatively less pronounced. This leads to a net latitudinal energy imbalance that produces a temperature gradient between the equator and the poles. On account of this temperature gradient between the equator and the poles, there is thermal convection with its associated circulation that produces the so-called trade winds or "alisios winds" at the tropics. These are near-surface winds that flow equatorward turning westward. Therefore, the trade winds blow from the northeast in the Northern Hemisphere, and from southeast in the Southern Hemisphere, carrying a large amount of moisture and converging around the equator. The associated circulation is known as the Hadley cell in honor of George Hadley (Englishman, XVIII century) who gave the first satisfactory physical interpretation of it. His model considered a thermally driven circulation resulting in lifting of warm air in the tropics, poleward motion and cooling aloft, sinking of denser colder air at mid-latitudes, and equatorward motion in the lower troposphere. Because of Coriolis effects, in the Northern Hemisphere, the high troposphere poleward winds tilt eastward and the low troposphere equatorward winds (alisios wind) tilt westward. Even though physically this circulation could be extended

from the equator to the poles, it is restricted to the tropical zone probably due to the baroclinic instability that would be present in middle latitudes because of this circulation (Holton, 1992).

2.2 Mesoscale Convective Complexes (MCC)

The study of this kind of Mesoscale Convective System (MCS) started with Maddox (1980, 1981) based on his observations of satellite imaginary for midlatitudes. He classified MCC's based mainly on three physical factors, size and shape, temperature, and duration. An MCS was classified as an MCC when the area covered by the –32°C isotherm was more than 100000 km² or when the area covered by the –52°C isotherm (low IR temperature) was more than 50000 km² for at least six hours. According to Cotton et al. (1989), an MCC is a stable MCS characterized by being almost in geostrophic balance and having a horizontal scale around or greater than the Rossby radius of deformation. Tremback (1990) presents a complete review and mathematical formulation of MCCs.

Even though most MCC studies have focused on those systems formed in midlatitudes, it is known that tropical cloud clusters behave as MCCs and some studies have emphasized MCCs in the tropics. For example, according to Velasco and Fritsch (1987), the west coast of Colombia is the most active area for the development of MCCs in the Americas and at low latitudes. In this area, a combination of warm water, orographic lifting and large-scale low-level convergence enhances deep convection. Here, over north-western South America, macroscale atmospheric convergence is generated when the trade winds from the southern hemisphere cross the equator, and then turn eastward penetrating into Colombian territory from the Pacific Ocean and leading to the formation of macroscale convergence with the warmer alisios winds coming from the northern hemisphere.

MCCs are deep barotropic systems. Barotropic systems are characterized by isothermal isobaric surfaces (Velasco and Fritsch, 1987). Their development is driven and governed by latent heat release, however, they transport little energy meridionally. Therefore, knowing that in the tropics the main energy source for synoptic perturbations

seems to be associated with latent heat release, as opposed to middle latitudes where the main energy source for synoptic perturbations is the potential energy associated with latitudinal temperature gradients, the major precipitation sources in the tropics may be these MCCs and particular attention must be given to their modeling. For this reason, in this study we take into account the recommendations of previous investigators in modeling these kinds of systems, as those in Tremback (1990).

2.3 The Intertropical Convergence Zone (ITCZ)

This zone is formed where the *alisios* or trade winds converge. It corresponds to a latitudinal (zonal) belt of low pressure where large scale convection is concentrated. The ITCZ is rarely on the equator and generally is characterized by clusters of clouds surrounded by clear skies. This zone migrates meridionally following the apparent sun's position and, over northern South America, its translation has a small east-west component, being over the Panama Gulf during the Northern Hemisphere summer and over the South Central Amazon during the Southern Hemisphere summer. This translation has a large effect on the annual temporal distribution of precipitation over Colombia. According to Holton (1992), records have shown that the amount of precipitation occurring in the ITCZ is greater than the amount of moisture gotten by local evaporation, which means that the difference in moisture is advected by the alisios winds. Additionally, the outgoing long wave radiation (OLR) from this zone exhibits one of the smaller average values and a large variance, a fact that is indicative of transitory and deep convective processes there.

From the above, it is clear that major convection over tropical South America is associated with the position of the ITCZ. Pulwarty (1994), taking as a criterion that the center of deep convection is associated with OLR fluxes less than or equal to 220 Wm^{-2}, draws a path of migration of the deepest convection that has the following features. During the southern hemisphere summer, the ITCZ is centered at about 12° S and has activity in a broad area from about 5° S to 20° S. The ITZC center moves north-northwestward crossing the equator during the northern hemisphere spring (austral autumn), reaching about 10° N and centering its activity over the eastern Pacific next to Panama during the northern hemisphere summer.

2.4 *Equatorial Wave Disturbances (EWD)*

The source of these westward-moving weak wave perturbations seems to be barotropic instability or conditional instability due to organized convection. Equatorial wave disturbances are driven by the latent heat released in the associated precipitation regions. These waves are also known as easterly waves and they are responsible for the cloud variance associated with the ITCZ. Colombia is affected by easterly waves formed in western Africa. These waves move westward crossing Colombia from the Caribbean coast to the Pacific coast. These waves are a source of climate and precipitation variability in Colombia; in particular, they affect the climate in northern and eastern Colombia, and in the Magdalena River valley (Martinez, 1993).

2.5 *Regional Climate*

According to Snow (1976), the climate of northern South America can be classified into five different types of tropical climate: two maritime (dry and wet), two continental (dry and wet), and one mountain type. Colombia has all of these five types of climate, which are characterized based on the annual rainfall and mean temperature. One of the main characteristics of these climatic regions is that their diurnal range of temperature, which generally is less than 10 °C, is greater than its annual range measured as the temperature difference between the hottest and the coolest months, which in general is less than 5 °C. The main factors affecting the climate of northern South America, besides the sun's apparent position and the general atmospheric circulation of the tropics, are the Atlantic and Pacific oceans, the Andes Mountains and the Amazon jungle. All these factors are specifically present in the Colombian climate: Colombia borders the Caribbean Sea in the north, the Pacific Ocean in the west, the Amazon basin and the Ecuadorian Andes in the south and, additionally, the Andes mountain range crosses its territory in a north-south direction along the Pacific coast.

In a general sense, two seasons, one dry occurring from December through April, and the other wet from May through November, characterize the climate of Colombia. In addition, the annual (temporal) distribution of rainfall over Colombia, which is directly dependent on the position of the Intertropical Convergence Zone (ITCZ), may be

unimodal or bimodal depending on the region. These rainfall maxima are associated with the time when the ITCZ passes over the specific region in its seasonal north-south seesaw motion. Regions with unimodal distribution are the central and central-eastern regions of Colombia. Furthermore, the spatial distribution of Colombian precipitation is mainly forced by the Andes Mountains together with the Pacific and Atlantic oceans, the Amazon basin, and the vegetation and soil moisture contrasts. The Andes Mountains, which are the major orographic feature and exhibit all the varieties of mountain climate, extend in a north-south direction across the entire country and are located in western Colombia. However, mountain climate in Colombia differs from that occurring at higher latitudes because in Colombia, even in the glaciered peaks, the relationship between diurnal and annual temperatures mentioned above prevails. Colombia is a country of climate extremes (Snow, 1976); in its territory one can find the rainiest and the driest areas, the warmest lowlands and the coldest mountain peaks, the windiest tropical coast and one of the calmest interiors. Velez et al. (2000) present a good detailed review of the factors affecting spatial and temporal precipitation distributions in Colombia.

The Andes mountain range traverses Colombia from the Ecuadorian border in the south, following a north-northeastward direction. It is considered the most important regional factor affecting Colombian climate characteristics (Mesa et al., 1997). When the Andes mountain range enters Colombia, it splits into three branches: eastern, central and western ranges. Consequently, these three branches and the associated longitudinal valleys separating them act both as barriers and as channels for the atmospheric flows, respectively, generating their own local atmospheric circulations. These circulations are significant, especially in the equatorial atmosphere context where, due to the large scale circulation, the wind speeds are generally small. The Central range has an average width of about 90 km. It is the highest of the three branches with average elevations of 3500 m above sea level, but with some glaciered peaks that reach more than 5000 m above sea level. The western range is the lowest with average elevations of about 2000 m above sea level, and an average width of about 40 km. The eastern range has average elevation of about 2500 m above sea level and an average width of about 150 km. Between these ranges there are two valleys, each one with a major river. The Cauca Valley, between the Western and Central ranges, is high and narrow. The Magdalena Valley, between the

Central and eastern ranges, is low and broad. The Central range ends at the confluence of both Magdalena and Cauca rivers, the Western range extends north into Panama and the Eastern range extends northeastwardly into Venezuela.

The Andes Mountains allow partitioning Colombia into five, well defined geographic zones, namely the Caribbean, the Andes, the Llanos, the Amazon and the Pacific Coast zones. Figure 2-1 shows the geographic location of the zones. The main characteristics of each zone follow.

The Caribbean zone is in the northern section of the country beyond the end of the Central range. In general, lowlands with an average annual precipitation of about 1500 mm/year conform this region. However, the coastal Sierra Nevada of Santa Marta, which has a peak with summit elevation of around 5800 m above sea level, is the rainiest area of the region with about 4000 mm/year on its west face (lee slope). In contrast, the northeastern part of the Caribbean zone, the Guajira Peninsula, presents the minimum rainfall of the region with 300 mm/year.

The Andes Mountains zone, which is formed by the three ranges, has an average annual precipitation of 1500 mm/year. The northwestern section is the rainiest area of this region with annual precipitation reaching up to 6000 mm/year. In addition, when windward and leeward slopes may be identified, the former has around double the precipitation when compared with the latter (Snow, 1976).

The Pacific Coast zone, between the shoreline of the Pacific Ocean and the Western range, has an average annual precipitation of about 5500 mm/year. The rainiest region of the American Continent is located in this zone, with a maximum annual rainfall above 13300 mm/year and with a river that has one of the largest water productions per unit area in the world, the Atrato River (Poveda and Mesa, 1997). Its range of annual precipitation is wide; for instance, the northern and western extremes have around 3000 mm/year, whereas the area close to the Atrato River reaches more than 10000 mm/year.

The Llanos zone is in the eastern section of the country and its average precipitation is about 2800 mm/year. Lowlands (100-250 m above the sea level) form this region, with a high-drainage density river network draining into the Orinoco River. However, its precipitation is more concentrated in the southwestern section; excluding

this portion, the annual average precipitation is around 2300 mm/year which is more associated with the specific Llanos (grasslands).

The Amazon zone is located in the southern section of the country next to the border that Colombia has with Brazil, demarcated by the Amazon River, and with Peru. This region is composed, in general, of rainforest draining into the Amazon River system. Its annual average precipitation is about 3500 mm/year, but the maximum is about 4000 mm/year, occurring in a portion of the western range, and the minimum is approximately 2500 mm/year next to the Amazon River.

2.6 Statistical relationship between hydrologic and macroclimatic variables in Colombia

Monthly series of macroclimate indices defined with climate data such as sea surface temperatures (SST) from the tropical Pacific and tropical Atlantic, surface atmospheric pressures, wind velocities, and outgoing long wave radiation, among others, have been related to precipitation and stream flow discharges in Colombia (e.g., Mesa et al., 1997). These indices are used to characterize a pattern or a behavior in a specific region. Among these indices and variables, the Southern Oscillation Index (SOI), the SST of the tropical Pacific, the total Outgoing Long Wave Radiation (OLR), and the zonal low wind velocity in the tropical Pacific are frequently used to identify the ENSO phenomenon. In particular, SSTs are measured in specific regions known as Niño 1-2 (SST N-1-2), Niño 3 (SST N-3), Niño 4 (SST N-4), and Niño 3-4 (SST N-3-4). These data are available from the Comprehensive Ocean-Atmospheric Data Set (COADS). This data set consists of global marine data dating from 1854 and has been compiled by the following United States government agencies: The Cooperative Institute for Research in Environmental Sciences (CIRES), the National Oceanic and Atmospheric Administration (NOAA), the National Center for Atmospheric Research (NCAR), and the National Climatic Data Center (NCDC). Table 2.1 describes these data series and gives the geographic location points for each one.

Table 2-1: Series of macroclimate data

SERIES NAME	LOCATION
Southern Oscillation Index (SOI)	Tahiti (18S, 150W) Darwin (12S, 131E)
Sea Surface Temperature (SST) N-1-2	(0-10S) (90W-80W)
Sea Surface Temperature (SST) N-3	(5N-5S) (150W-90W)
Sea Surface Temperature (SST) N-4	(5N-5S) (160E-150W)
Sea Surface Temperature (SST) N-3-4	(5N-5S) (170-120W)
Outgoing Long Wave Radiation (OLR)	Equator (160E-160W)
850 MB Trade Wind Index (wpac850)	(135E-180W) 5N-5S West Pacific
850 MB Trade Wind Index (cpac850)	(175W-140W)5N-5S Cent Pacific
850 MB Trade Wind Index (epac850)	(135W-120W) 5N-5S East Pacific

Mesa et al. (1997) and Poveda and Mesa (1993, 1995, 1997) reported results of several statistical analyses examining the linear dependence between Colombian hydrology and macroclimate variables. These results have shown that the extreme phases of ENSO are significantly related to the climate anomalies of Colombia, and that the cold phase of ENSO is associated with wet periods whereas the warm phase is associated with dry periods in Colombia. As an example, Figure 2-2 shows the observed relationship between the standardized annual discharges at Salvajina on the Cauca River and the series of SOI and (SST) N-1-2 for the period 1950-1995. From this figure it is clear that the discharge increases at Salvajina when SST N-1-2 decreases and vice versa, while the patterns of SOI and discharge are almost the same. Using the classification of cold (La Niña) and warm (El Niño) years proposed by Kiladis and Diaz (1989), Figure 2-3, taken from Poveda and Mesa (1997), shows the effect of ENSO on monthly discharges at Puerto Berrio on the Magdalena River in Colombia.

From these studies it also has been found that ENSO, quantified in terms of the SOI index, has its major influence on western Colombia and in the Andes regions. Results have shown that the SOI index leads Colombian stream flow discharges with cross-correlation coefficients around 0.6 at lag periods of three months. According to these correlation coefficient values, the northern section of Colombia next to the Caribbean coast is the region least affected by ENSO. Additionally, ENSO has a lesser effect in eastern Colombia, where its effects appear later than in western Colombia (see Figure 2-4, taken from Poveda and Mesa, 1997). Hydrology anomalies occur one month,

two-four months, and as much as six months, after SOI anomalies have occurred, in western, central, and eastern Colombia, respectively (Poveda and Mesa, 1997). It is important to notice that the observed correlation coefficients show the Southern Oscillation (SO) as a precedent phenomenon except for the Caribbean coast region, where some stream flow anomalies actually precede the SO.

Correlation analyses between Colombian stream flows and sea surface temperatures (SST) of the tropical Pacific have shown similar results to those found using the SO index. The larger correlations have been found with SST indices from regions distant from the Pacific coast. Correlation analyses using variables such as wind velocity and outgoing long wave radiation (OLR) support the above results.

In addition to those variables directly related with ENSO, correlation analyses with other variables associated with tropical climate, for example, the North Atlantic Oscillation (NAO) index, have also been carried out. These correlation analyses have shown that NAO anomalies occur later than Colombian stream flow discharge anomalies, except for streamflows in the Caribbean coast region.

In general, the best relationships were found with macroclimate indices measured on the Pacific Ocean. Among these indices are SOI, SST and the Pascua Island atmospheric pressure. These relationships show that, at least for those regions where they were evaluated (in general the Andes region), the warm phase of ENSO forcing is associated with low precipitation and low stream flow discharges, while the cold phase forcing is associated with high precipitation and high stream flow discharges in Colombia, which is consistent with the observation of the physical phenomenon. Furthermore, correlations were larger during those years in which a strong warm or cold event was present.

Taking advantage of these observed relationships, many researchers have tried to implement statistical linear and non-linear methodologies for predicting stream flow in Colombia; see for example Poveda et al. (2001), Carvajal et al. (1998), Mesa et. al (1994b), Poveda and Penland (1994), Salazar et al. (1994b), and Poveda and Mesa (1993).

In summary, from cross-correlation analyses between ENSO variables and Colombian stream flow discharges, it has been found that the effects of ENSO appear earlier in the Pacific coast of Colombia (western Colombia) and later in the eastern part of the country with lags that go from two to six months, respectively. How far the effects are propagated inland depends on the hydrological processes, and on the interaction of precipitation, soil moisture and evapotranspiration. In addition, by simple observation, it is clear that the warm phase of ENSO is associated with a reduced influx of moisture from the west, reduced MCC activity, and a reduction in the easterly waves, all of which lead to a reduction of precipitation over Colombia, whereas during the cold phase of ENSO the overall effect is totally the opposite.

Figure 2-1: Geographic location of the five climatic zones in Colombia: Caribbean, Andes, Llanos, Amazon and Pacific.

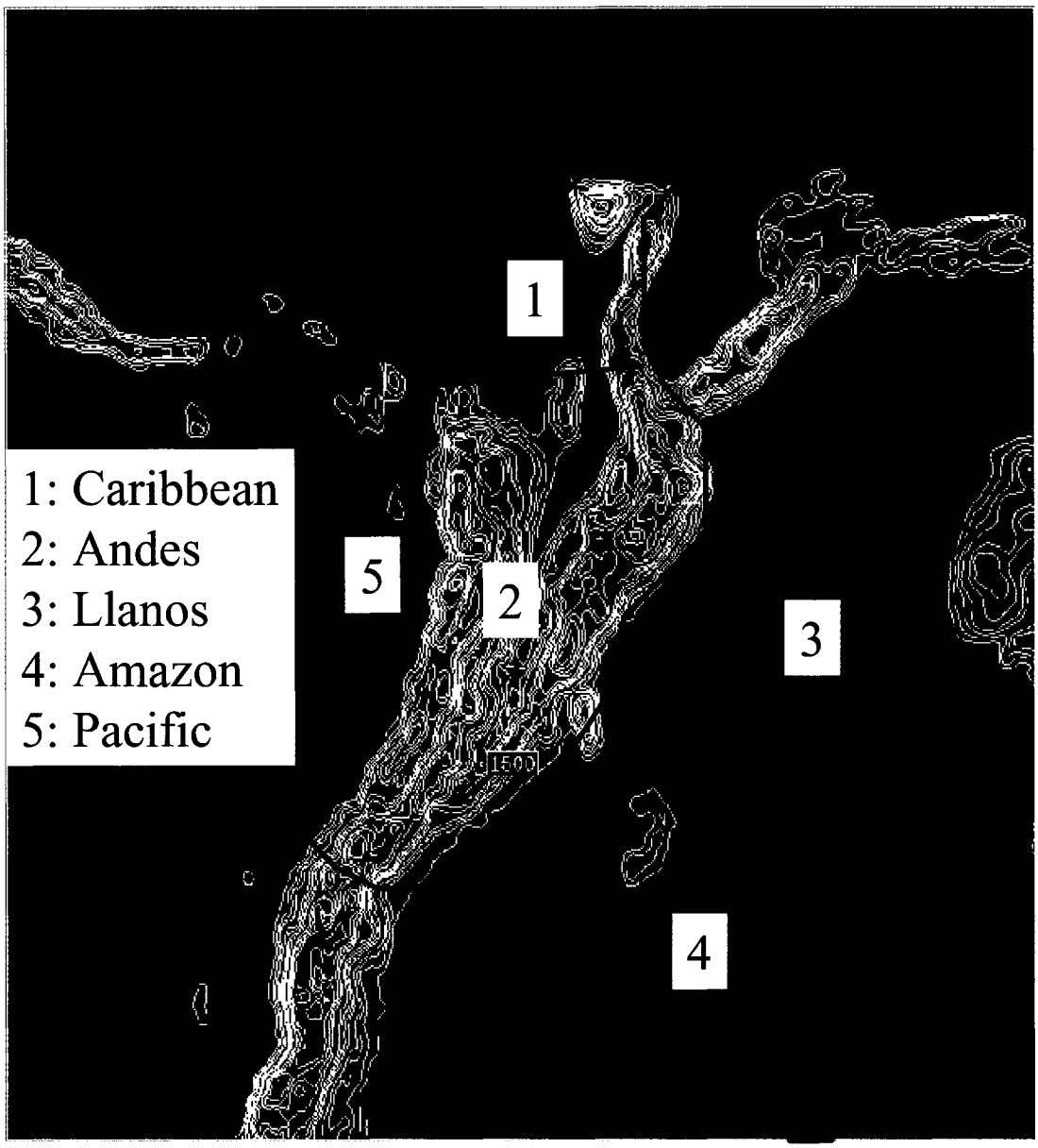

Figure 2-2: Relationship between the standardized annual discharges at Salvajina point on the Cauca River, Colombia, and the series of (SST) N-1-2 and SOI, throughout the period 1950-1995.

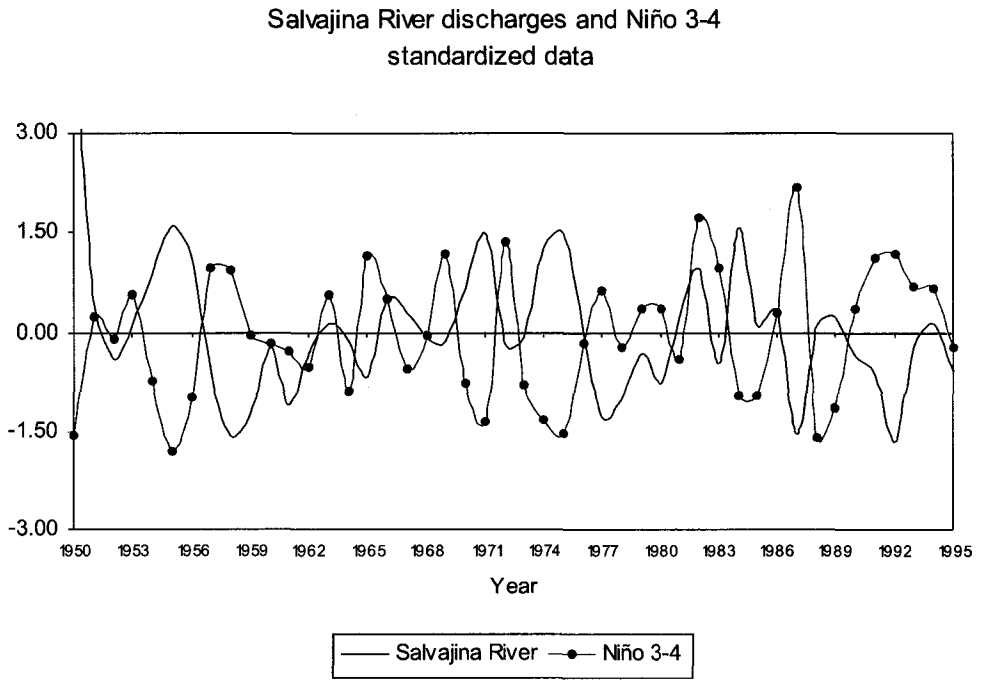

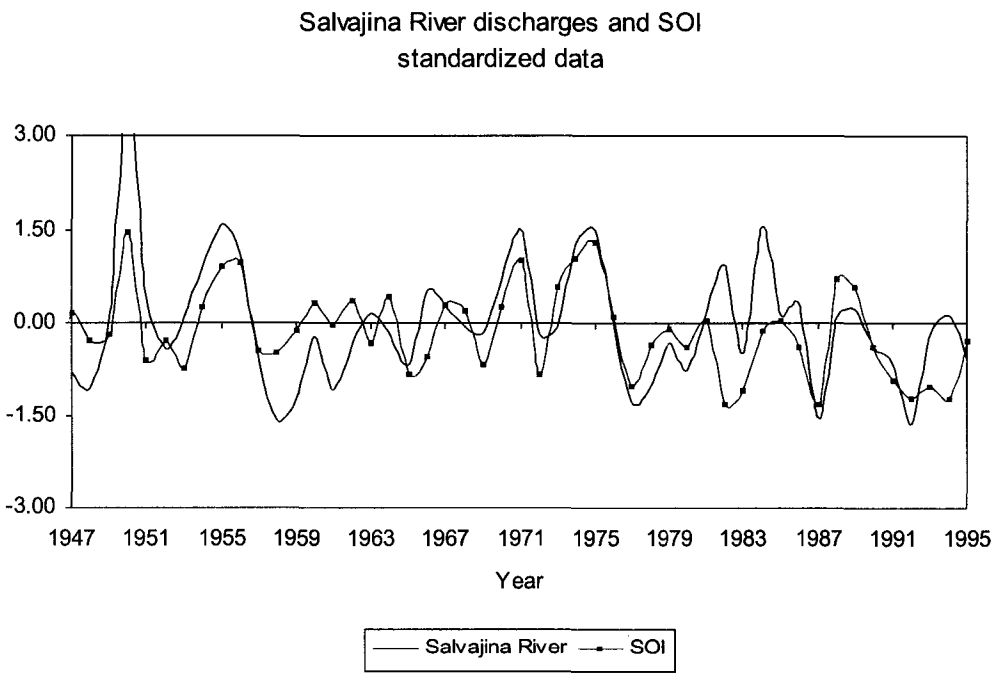

Figure 2-3: Monthly anomalies of the Magdalena River at Puerto Berrío, Colombia, with respect to the multi-annual mean for El Niño (triangles) and La Niña (squares) years (top). Ratio of the average monthly discharges for El Niño (triangles) and La Niña (squares) to the multi-annual averages (bottom). Taken from Poveda and Mesa (1997)

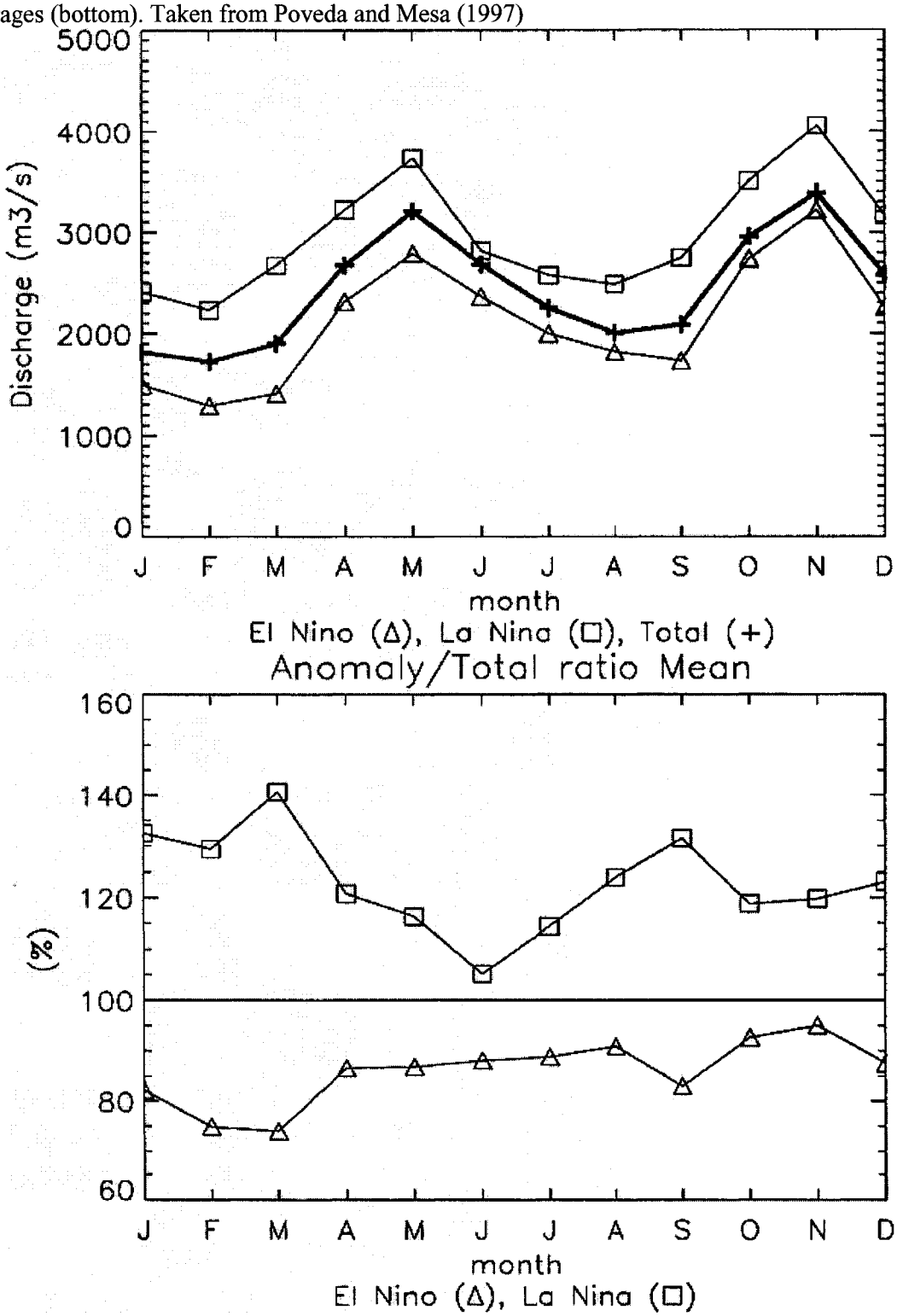

Figure 2-4: Behavior of the cross correlation between the SOI and the streamflows of four rivers in Colombia. From west to east: La Vieja (Cartago, Valle del Cauca, 4°46N, 75°54W), Luisa (Pavo Real, Tolima, 4°13N, 75°12W), Sumapaz (El Profundo, Cundinamarca4°00N, 74°30W), and Chivor (Ubalá, Boyacá, 4°47N, 73°09W). Negative lags correspond to the SOI leading the hydrology. Notice that the peaks of the cross correlation occur later as the stations are farther east. The correlations are statistically significant at the 99.9% level. Vertical and horizontal axes correspond to Latitude and Longitude, respectively. Taken from Poveda and Mesa (1997).

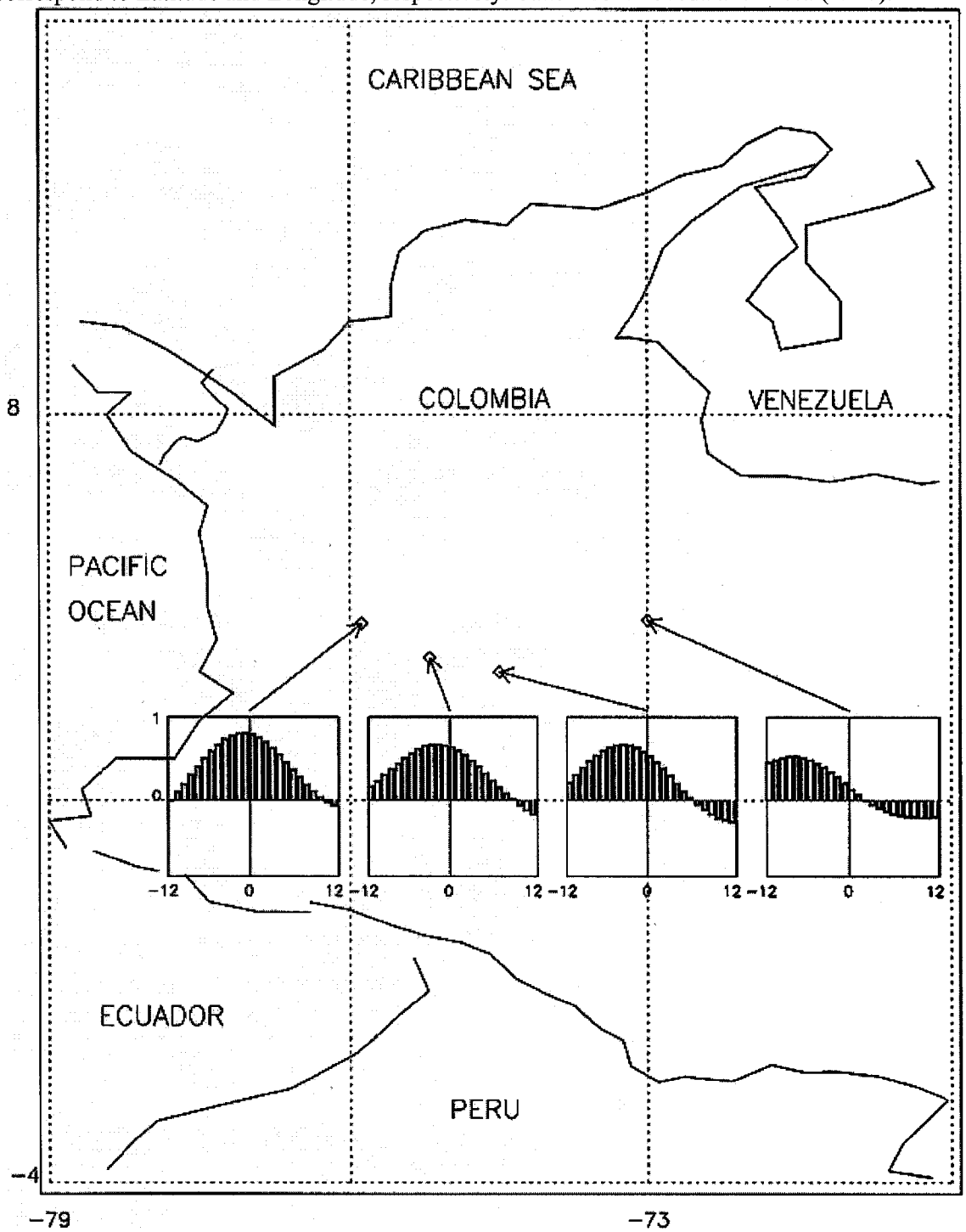

3 METHODOLOGY

As presented in Chapter 1, the primary objective of this dissertation is the development of a modeling approach based on coupling a set of models to translate climate general circulation information into precipitation and stream flow responses in Colombia. Climate general circulation information obtained from the global tropospheric analysis data set of the National Meteorological Center (NMC) at a 2.5° latitude-longitude resolution combined with surface and upper air data measurements drive a regional atmospheric modeling system to produce precipitation at a local scale. In turn, precipitation fields from the regional atmospheric model are used as input data to a hydrologic modeling system to produce stream flow.

To reach the goals of this research a regional surface-atmospheric modeling system with the ability to represent scale interactions is used. This ability allows the model to translate information from general circulation scales to local circulation scales by using a telescopic sequence of nested grid domains. Output from this model is coupled with a regional hydrologic modeling system to obtain stream flow discharges at specifics points in selected watersheds of Colombia. A wide range of spatial scales of solution, ranging from 160 km to 2.5 km, are used in this work in order to consider the main regional and local processes responsible for producing precipitation in Colombia. The size of the finest grid used is chosen such that the physical accuracy of the simulation is maximized while at the same time minimizing the ever increasing computational demands. Comparisons between model results and observations are based on basic statistical tools.

The following sections present the methodologies used in each ones of the main modeling efforts of this work, namely, those associated with the atmospheric model and with the hydrologic model. Special attention and emphasis are given to the atmospheric modeling system description because of its importance to the successful completion and reaching of the goals of this research, in particular that of understanding and describing

the effects of large scale macroclimatic phenomena on the regional and local hydro-climatic response in Colombia.

3.1 Colorado State University Regional Atmospheric Modeling System (CSU-RAMS)

The atmospheric modeling component of this thesis uses the Colorado State University Regional Atmospheric Modeling System, versions 4.2 and 4.3 (CSU-RAMS), which is a comprehensive atmospheric modeling system that has been run on a wide variety of platforms. CSU-RAMS is set up on two different nested-grid configurations. For both of them, the coarsest grid spans northern South America including part of Central America, the Caribbean Sea, and the tropical Pacific; the finest grid focuses on Colombia. One configuration is a two-nested grid domain that is used for seasonal simulations and the other is a four-nested grid domain that is used for storm event simulations and whose finest grid focuses on a specific watershed.

A brief description of the CSU-RAMS modeling system is given here. Four main sources are utilized for this description: RAMS Technical Manual, which provide a technical description of RAMS; McQueen et al. (1997), who summarize the major features of the Air Resource Laboratory (ARL) version of RAMS (Version 3a) and the enhancements made in its implementation; Walko et al. (1995), who present a user's guide for version 3b with a description of the software and name-list of parameters that control model configuration; and Pielke et al. (1992), who present a range of RAMS applications such as Large Eddy Simulation (LES) and simulations of thunderstorms, cumulus fields, mesoscale convective systems (MCS), mid latitude cirrus clouds, winter storms, mechanically and thermally forced mesoscale systems, and mesoscale atmospheric dispersion.

The RAMS model development at CSU started in 1986 with two atmospheric models, a mesoscale model and a cloud model. Since then it has undergone innumerable enhancements, including a dynamic enhancement to simulate mesoscale and microscale atmospheric circulation. At the present, this modeling system merges the capabilities of several separate models with the ability to represent a large-scale area and then to nest

progressively to smaller scales. CSU-RAMS has both non-hydrostatic and hydrostatic formulations, which permit representing all meteorologically-relevant spatial scales. For example, RAMS has methods for modeling microscale dynamic systems, microphysics processes, mesoscale systems, and the influence of land surface characteristics on the atmosphere, among others.

3.1.1 Basic equations

The basic equations of CSU-RAMS are the standard hydrostatic or non-hydrostatic Reynolds-average primitive equations. Tripoli and Cotton (1982) describe the cloud prognostic equations of motions in detail (non-hydrostatic, time-split compressible). Tremback et al. (1985) describe the hydrostatic incompressible or compressible system. Tremback (1990) describes the equations used for simulating MCCs. McQueen et al. (1997) describe the basic equations for the RAMS version used at the NOAA Air Resources Laboratory. General description equations are presented in Appendix 1, taken from the technical description of RAMS, (RAMS Technical Manual)

3.1.2 Grid structure

To represent the grid, RAMS has incorporated two coordinate systems. One is the simple Cartesian coordinates system and the other is an oblique stereographic horizontal grid, which utilizes an Arakawa-C staggered grid for the thermodynamics and momentum variables to reduce finite differencing error (Mesinger and Arakawa, 1976). Thus, thermodynamic, pressure and moisture variables are defined at the same point and the velocity components, u, v, and w, are staggered 0.5 Δx, 0.5 Δy and 0.5 Δz, respectively. The oblique stereographic projection horizontal grid coincides with the polar stereographic coordinates when the pole is in the center of the RAMS model. In other cases, the projection is done considering a pole near the center of the simulation domain, minimizing the projection distortion in the main area of interest.

Additionally, RAMS has a nested grid scheme option that permits higher spatial resolution in selected areas as well as simulation of scale interactions. This option allows using a finer mesh grid to solve local scale circulation over an area of interest and a coarser mesh outside of this area for larger scale circulation. Between the coarsest and the

finest mesh multiple mesh layers may be used. The nested grid does not replace the coarse grid, but both grids must coincide. That is, an integer number of nested cells must match into one coarse cell grid. On the other hand, a coarse grid may have more than one nested grid and the number of vertical levels in the nested grid could be less or equal to that of the coarse grid. Another special characteristic is that the nested grid may move with respect to the coarse grid, which is very important because this permits simulation of small scale phenomena that are changing their spatial position at every time, like tornadoes.

The vertical grid structures are based on a terrain-following height coordinate system Z^*, such that, (Gal-Chen and Somerville, 1975).

$$Z^* = Z_{top}\left(\frac{z - Z_g}{Z_{top} - Z_g}\right)$$

Where Z_g is the local topographic elevation as a function of the horizontal coordinates, Z_{top} is the elevation of the model top, and $(z - Z_g)$ is the elevation above the ground of the model surface.

The above implies that the model top is a geopotential surface exactly flat. Inner levels are a given fraction of the distance between the surface and the top geopotential, and the surface level follows the terrain. On the other hand, variables are alternated on the vertical, such that horizontal wind speed components (u and v), potential temperature (θ), mixing ratio (r), and pressure (P) indicated by the Exner function $\pi = C_p(P/P_o)$, are defined at one set of levels and the vertical motion (w) is defined at intermediate levels. The first half level is defined below the ground, so the first realistic half level is defined at level two. A nested grid may or may not extend from ground to the top of the coarsest grid, and a nest may be done in the vertical and variable with height. Linking and data exchange between coarser and finer nested grids is accomplished by nested algorithms conserving mass, momentum and internal thermodynamic energy.

3.1.3 Main Parameterizations

Because of the impossibility to resolve all the physical processes explicitly due to a diversity of problems such as lack of knowledge of the real physical process, scale incompatibility, lack of information to follow the real process, use of excessive computational resources, etc., RAMS has implemented the following parameterizations (a brief description of these parameterizations can be found in RAMS Technical Manual):

3.1.3.1 Turbulent Mixing Parameterization

Horizontal and vertical grid spacings determine the spatial scales of prognostic field variables that can be explicitly resolved. Those scales that cannot be explicitly resolved must be parameterized. Under this category there are two main schemes implemented: Deformation-based parameterization and turbulent kinetic energy parameterization.

3.1.3.2 Surface Layer Parameterization

Surface layer fluxes of heat, momentum and water vapor into the atmosphere are computed with the scheme of Louis (1979). This scheme is used for water surfaces, bare soil and vegetated surfaces. The computed fluxes are imposed as the lower boundary condition for the sub-grid diffusion scheme for the atmosphere.

3.1.3.3 Soil and Vegetation parameterization

These parameterizations provide the surface characteristics, including temperature and moisture, needed for the surface layer parameterization.

3.1.3.4 Convective Parameterization

The parameterization of convection is considered the most complex problem in mesoscale, synoptic and global modeling. RAMS has implemented modifications of the two most popular schemes in mesoscale modeling, the Kuo (1974)-type scheme and the Fritsch and Chappell (1980a) scheme.

3.1.3.5 The bulk microphysics parameterization

This parameterization includes the precipitation process. The scheme takes into account several kinds of water including cloud water, rain, pristine, crystals, snow, graupel and aggregates. A full description of this microphysics scheme can be found in Piotr et al. (1989).

3.1.3.6 Radiation Parameterization

RAMS has implemented two options for long wave and two options for short wave radiation, hereafter referred to as the Mahrer and Pielke parameterization (Mahrer and Pielke, 1977) and the Chen and Cotton parameterization (Chen and Cotton, 1983).

3.1.4 Surface variables

The lower boundary of the CSU-RAMS modeling system can be either ocean or land. The following surface variables are taken into account in the CSU-RAMS modeling system: sea surface temperature (SST), soil and vegetation type, ground surface temperature, soil moisture, canopy temperature, soil water content and surface roughness, among others. RAMS has two options to deal with ground surface variables, constant or spatially varying surface variables.

The surface layer and soil parameterizations described in detail by Tremback and Kessler (1985) are used for the lower boundary condition of the atmospheric model. The soil model consists of a grid representing finite volumes in the uppermost meter or two of the ground. Soil temperature and moisture are estimated on this grid based on equations governing their internal transport and external exchange with the atmosphere. The horizontal dimensions and resolution of the soil model are identical to those of the atmospheric model grid above. Therefore, this scheme formulates prognostic equations for the soil surface temperature and water content by assuming a finite depth soil/atmosphere interface layer. The surface layer fluxes of heat, momentum, and water vapor are computed using the Louis (1979) scheme. More details about the surface model and turbulence model incorporated in RAMS are given in Appendix 1.

3.1.5 Synoptic Analysis

CSU-RAMS uses isentropic coordinates because they have advantages in large-scale data analysis. However, when the atmospheric stability decreases the vertical resolution decreases, causing the isentropes to intersect the ground. Although the current version of the CSU-RAMS supports the most commonly used and most useful standard data sets, the modeling system also has a flexible structure that easily allows using non-standard data sets. Among the standard data sets are the mandatory level 2.5° global analysis of the National Meteorological Center (NMC) (the NMC operational analysis fields), the 2.5° global analysis of the European Center for Medium-range Weather Forecasting (ECMWF), and the NMC rawinsonde and surface observations. These standard data sets are archived at the National Center for Atmospheric Research (NCAR) as standard data sources.

Table 3-1: RAMS capabilities - summarizes most of the characteristics and options of the present version. (adapted from Pielke et al., 1992).

CATEGORY	AVAILABLE OPTIONS AND REFERENCES
Basic equations	Non-hydrostatic; incompressible (Tripoli and Cotton, 1982) Hydrostatic; anelastic or incompressible (Tremback et al., 1985)
Dimensionality	1D, 2D and 3D
Vertical coordinates	Cartesian Terrain following σ_z (Clark, 1977)
Horizontal coordinates	Cartesian Stereographic tangent plane
Grid Stagger and structure	Arakawa C grid, single grid (fixed) Arakawa C grid, multiple nested grid (fixed) Arakawa C grid, multiple nested grid (movable)
Time differencing	Leapfrog; time split; 2^{nd} 0r 4^{th} order spatial accuracy (Tripoli and Cotton, 1982) Forward; 2^{nd} 0r 6^{th} order spatial accuracy (Tremback et al., 1985)
Turbulence closure	Smagorinsky deformation K (Smagorinsky , 1963) O'Brien K / Blackadar K (McNider and Pielke, 1981) Deardorff level 2.5 K (Deardoff, 1980)
Stable precipitation	No condensation Condensation

Cumulus parameterization	None Modified Kuo (Tremback, 1990) Fritsch and Chappell (1980a)
Explicit microphysics	None Warm microphysics (Tripoli and Cotton, 1982) Ice microphysics – specified nucleation (Cotton et al., 1982) Ice microphysics – predicted nucleation (Cotton et al., 1986) Cloud microphysics (Piotr et al., 1989)
Radiation	None Short-wave I (Chen and Cotton, 1983 and 1987) Short-wave II (Mahrer and Pielke, 1977) Longwave I (Chen and Cotton, 1983 and 1987) Longwave II (Mahrer and Pielke, 1977)
Surface layer	Louis (1979)
Lower boundary	Specified air-surface temperature and moisture differences Diagnosed surface temperature and moisture fluxes based on a prognostic soil model (Tremback and Kessler, 1985; McCumber and Pielke, 1981) Vegetation parameterization: RAMS uses the Big Leaf approach (Avissar and Mahrer, 1988; Lee, 1992)
Upper boundary	
Lateral boundaries	Radiative boundary condition I (Orlanski, 1976) Radiative boundary condition II (Klemp and Wilhelmson, 1978a,b) Radiative boundary condition III (Klemp and Lilly, 1978) Radiative boundary condition and MCR (Tripoli and Cotton, 1982) Large scale sponge boundary conditions (Perkey and Kreitzberg, 1976) Large scale nudging boundary condition (Davies, 1983)
Initialization	Horizontal homogeneous (HHI) HHI plus variation to force cloud initiation Variable initialization I Variable initialization II (Tremback, 1990)
Transport and diffusion	Lagrangian particle dispersion module (McNider, 1981; McNider et al., 1988; Uliasz, 1993)

3.1.6 Data Initialization and Boundary conditions

The objective is to provide the initial values and boundary values for a simulation for all state variables at every grid point. In this process, both vertical and horizontal interpolation of the variables are used. Interpolation is required because, in general, points where observations are available do not match the grid configuration. The vertical

interpolation is linear in $P^{k/Cp}$ and the horizontal interpolation uses the overlapping polynomial technique of Bleck and Haagenson (1968). In general, there are two main groups of fields of variables to consider, the atmospheric fields and the surface fields.

Two methods may be used for initialization of atmospheric fields. These methods are known as the horizontal homogeneous initialization and the *variable* initialization. In the first method a single vertical sounding is given, which is used to interpolate the data horizontally homogeneously onto the model grids. Considering the large scale, this method is not very common, but it is useful in doing special studies and modeling tests. The second method, *variable* initialization, consists in blending data from multiple locations to produce three-dimensionally variable initial model fields of velocity, temperature, pressure and moisture. The process of *variable* initialization is summarized below.

Using observational data, three main tasks are involved in a simulation: 1) data analysis for initial conditions, 2) large-scale lateral boundary tendencies: dynamic boundary conditions, e.g., it is necessary to provide boundary conditions for the period of simulation, and 3) the four-dimensional data assimilation scheme (FDDA).

To setup the data analysis for initial conditions, first a polar stereographic/pressure coordinate dataset over the area of interest is created by accessing and interpolating over the RAMS grid the global National Meteorological Center (NMC) dataset, the rawinsondes dataset and the surface observations dataset. These data are interpolated vertically to both the isentropic and the terrain-following (σ_z) vertical coordinates. In processing rawinsondes and surface observations, the Barnes (1973) objective analysis scheme is applied to the wind, pressure and relative humidity on the isentropes, and to the wind, temperature and relative humidity on the σ_z levels. Second, as a result of the above analysis, three RAMS grid data sets are available, the isentropic upper-air, the σ_z upper-air and the surface datasets, which are blended to find the final initial conditions. In a lower layer, no more than three km from the surface, the σ_z data set is used; above this layer the data are defined from the isentropic dataset. Then, the surface data are blended to the upper-air data taking into account that it is difficult to

know how deep the effect of the surface data should extend and how representative of the surface area is the surface observation.

To set up the initial surface characteristic data is a complex problem since no good datasets are available. The initialization of the soil temperature and moisture cannot be done accurately due to the lack of routine measurements. The following assumptions are used: (a) surface analysis of atmospheric relative humidity at 12:00 UTC describes the relative humidity of the air in the top layer of soil, (b) temperature in the top layer of soil is assumed to be 4 K lower than the surface analysis temperature. Using these values, the soil moisture content in the top layer of soil is evaluated from the parameterized equations from the soil model that is used as a lower boundary condition for the atmospheric model. Then the soil temperature profile is assumed with a linear increase of 7 K in the first 20 cm, and then constant. The moisture profile is assumed to increase a hundred percent in a linear way from the surface to the soil bottom. Global terrain height data and global vegetation type data files are obtained from The Earth Resources Observation Systems (EROS) Data Center (EDC) of the U. S. Geological Survey (USGS). In particular, for the digital elevation model of South America, see Bliss and Olsen (1996).

Topographic data for the grid model are interpolated from the topographic dataset GTOPO 30, which has a global 30 arc-second latitude-longitude grid size. The accuracy of the model topographic data depends on the grid size used, since when interpolated on a model grid some smoothing is necessary to avoid numerical error due to high topographic slopes. Additionally, if nested grids are used, it is necessary that terrain heights be compatible between different grids.

The international Geosphere-Biosphere Programme (IGBP) land cover classification is used to define the model grid vegetation distribution. The model grid Sea Surface Temperature (SST) is defined from the Global Sea Surface Temperature (SST) obtained from the optimum interpolation (OI) SST analysis that is produced weekly on a one-degree grid by the Climate Diagnostics Center (CDC) of the National Oceanic Atmospheric Administration (NOAA) (see Reynolds, 1988; Reynolds and Marsico, 1993; and Reynolds and Smith, 1994).

During the period of simulation, Four Dimensional Data Assimilation (FDDA) and nudging of boundary conditions are used, e.g., the model data is smoothly forced to the observational data. This means that the model fields are nudged toward observational data as a simulation progresses. Nudging boundary conditions works as an absorbing layer to minimize wave reflections due to the border assumptions by limitations of the domain. The FDDA scheme is a nudging-type scheme where an additional term is added to the model prognostic equations. The general expression for this term is

$$\frac{\partial \phi}{\partial t} = \frac{\phi_{obs} - \phi_m}{\tau}$$

Where ϕ represents the prognostic variable, τ is time-scale which controls the nudging, and the subscripts *obs* and *m* represent the observational and model data, respectively. This nudging methodology is used to provide the lateral boundary conditions and the top boundary conditions, and the FDDA inside the domain.

For the lateral boundary conditions, the nudging is done for a number of grid points from the border using the scheme of Davies (1976). The assimilation to the data analysis is done more strongly in the border grid and it tends to zero in the most interior grid point by using a parabolic function for the time-scale controlling the nudging. This function is:

$$\tau_{lat} = \tau_B \frac{(x - x_i)^2}{(x_B - x_i)^2}$$

Where τ_{lat} is the lateral boundary nudging time-scale, τ_B is the actual lateral boundary nudging time-scale, x_B is the x coordinate of the lateral boundary point, and x_i is the x coordinate of the interior point.

For the top boundary conditions a similar procedure is followed, but in this case the nudging time-scale is defined as a simple linear function of height. This function is:

$$\tau_{top} = \tau_T \frac{z - z_i}{z_T - z_i}$$

Where τ_{top} is the top boundary nudging time-scale, τ_T is the actual top boundary nudging time-scale, z_T is the z coordinate of the top boundary point, and z_i is the z coordinate of the interior point.

Since the data to be used as boundary conditions are available at time intervals of six hours or longer, variables are linearly interpolated in time to each model time step.

Additionally, RAMS has the option to do nudging in the interior of the domain (FDDA). The technique used is called analysis nudging where the model field is nudged to the grid analysis. A weighting function is used to give stronger nudging to the points where the observational data are located.

3.1.7 RAMS applications - Brief summary.

3.1.7.1 Mesoscale Convective Systems (MCS)

These systems are characterized by having horizontal scales of several hundred kilometers and being composed of clusters of thunderstorm cells. This means that MCSs are difficult to model since they have large horizontal scale and long lifetimes and are strongly dependent on smaller scale motions associated with cumulonimbus. As a result of experience gained in using RAMS to model MCSs it became clear that: (a) the thunderstorms embedded in those systems should be modeled by using three dimensions; (b) MCSs can be simulated with the coarsest horizontal resolution but the cumulus parameterization scheme should be implemented to simulate the smaller scale cloud processes; (c) the convective parameterization should be used even in models with grid point separation as small as five kilometers (Pielke et al., 1992).

3.1.7.2 Physiographically-Forced Mesoscale Systems (PFMS)

Because of the interaction between the Earth's surface and the atmosphere, mechanically and thermally forced circulations are constantly generated. Mechanically forced circulations are generated as a result of the topographic obstacles and thermally forced circulations as a result of spatial variations in landscapes and consequent differential surface heating. These kinds of circulations have been modeled successfully with RAMS and some interesting analogies have been found. For example, landscape

variability leads to regional circulations analogous to those produced by sea-breeze convergence, and both processes can generate deep cumulonimbus convection (Pielke et al., 1992)

3.1.7.3 Winter Storms Simulations and Thunderstorms

By using the non-hydrostatic version of the model and its capability to combine several grids, RAMS has been used to investigate the effects of topography on winter storms (Wesley, 1991; Meyers and Cotton, 1992). Additionally, RAMS has simulated specific thunderstorms such as the tornadic thunderstorm of Del City of 20 May 1977 (Grasso, 1992.)

3.1.7.4 Cumulus Convection

These kinds of systems are very common over the Florida peninsula, where RAMS has been used to simulate them. It is important to mention that these vertical motion systems required three-dimensional simulations and in some cases a model mesh size no larger than 1 km in order to describe the microphysics with fidelity.

3.2 Surface Hydrologic Modeling System

In order to simulate basin hydrologic response to the hydroclimatic forcing from RAMS and, specifically, to produce streamflow discharges on a specific watershed, we used the Swedish Hydrologiska Byråns Vattenbalansavdelning (HBV) model. This model is a hydrologic model developed mainly for rainfall-runoff simulation and hydrological forecasting and classified as conceptual, partially distributed. The first version of the HBV dated from early 1970s (Bergström and Forsman, 1973). Since then the model has been updated focusing on more reliable routines for automatic model calibration and a user-friendly interface (see for example Bergström, 1995 and Lindström, 1997). Initially, the HBV model started as a very simple lumped hydrological model and it has gradually been developed into a semi-distributed model. Today, there are a variety of model versions, with origins from different institutions, and applications have been made in more than 40 countries. Here, the version obtained by Empresas Publicas de Medellin - Colombia (EPM) is used. This model is selected taking into

account that EPM has implemented it for its watersheds for operational forecasts and these watersheds are a focus of this research. The version owned by this company is one of the last versions, HBV-96 (Lindström et al., 1997), and it has as a basic principle full distribution into sub basins and statistical distribution of some properties within these. This version uses sub basin division with a typical resolution of 40 km^2, but any resolution can be used.

The HBV-Model uses precipitation, air temperature, and potential evaporation data to compute snow accumulation, snow melt, actual evapotranspiration, soil moisture storage, groundwater and runoff from the catchment. The catchment is divided into elevation bands and temperature and precipitation is corrected to each band. Main catchment characteristics and parameters required by the model are those related with orographic precipitation gradient, temperature lapse rate, and threshold temperatures for snow precipitation and melt. These values should be obtained from studies, from the literature or through calibration. For this particular application the model is already calibrated since it has been used for at least six years in the area of study.

The general water balance used in the HBV model to describe the hydrological processes at the catchment follows (Bergström, 1976, 1992):

$$P - E - Q = \frac{d}{dt}(SP + SM + UZ + LZ + lakes)$$

where:

P:	Precipitation
E:	Evapotranspiration
Q:	runoff
SP:	Snow Pack
SM:	Soil Moisture
UZ:	Upper Groundwater Zone
LZ:	Lower Groundwater Zone
Lakes:	lake volume

This model may be used as a semi-distributed model by dividing the catchment into subbasins. Consequently, each subbasin is then divided into zones according to altitude and vegetation.

Most commonly the model is used with daily values of rainfall and air temperature, and daily or monthly estimates of potential evaporation, where air

temperature data are used for calculations of snow accumulation and melt, therefore temperature normally is omitted in snow free areas.

Figure 3-1, taken from The Swedish Meteorological and Hydrological Institute's (SMHI) electronic homepage, shows the schematic structure of one sub basin in the HBV-96 version model (Lindström et al., 1997). Basic routines of the model are for meteorological interpolation, snow accumulation and melt, evapotranspiration estimation, a soil moisture accounting procedure, runoff generation and a simple routing procedure between subbasins and in lakes. The HBV-96 version incorporates a geostatistical method based on optimal interpolation for computation of areal precipitation and air temperature. For determining the dynamics of the generated runoff, the division into sub basins, defined by the outlets of major lakes, is of great importance. The routing between subbasins can be described by the Muskingum method (Shaw, 1988).

It is important to mention that among its applications, the HBV model has been used in studies of the impacts of climate variability and change (see for example Vehvilainen and Lohvansuu, 1991 or Saelthun et al., 1998). Model developers are still improving the model to deal with a good harmonization of soil parameterizations, as well as the energy and the water budgets that will have to be solved simultaneously in climate and hydrologic models. Looking to bridge the scale gap between hydrological models and climate models, the HBV model has been applied to the land area of the entire catchments of the Baltic Sea (Graham, 1999) which showed needs for model improvements.

Figure 3-1: The schematic structure of one sub basin in the HBV-96 version model. Top: snow routines. Middle: soil routines. Bottom: response routines. Taken from The Swedish Meteorological and Hydrological Institute (SMHI), electronic homepage.

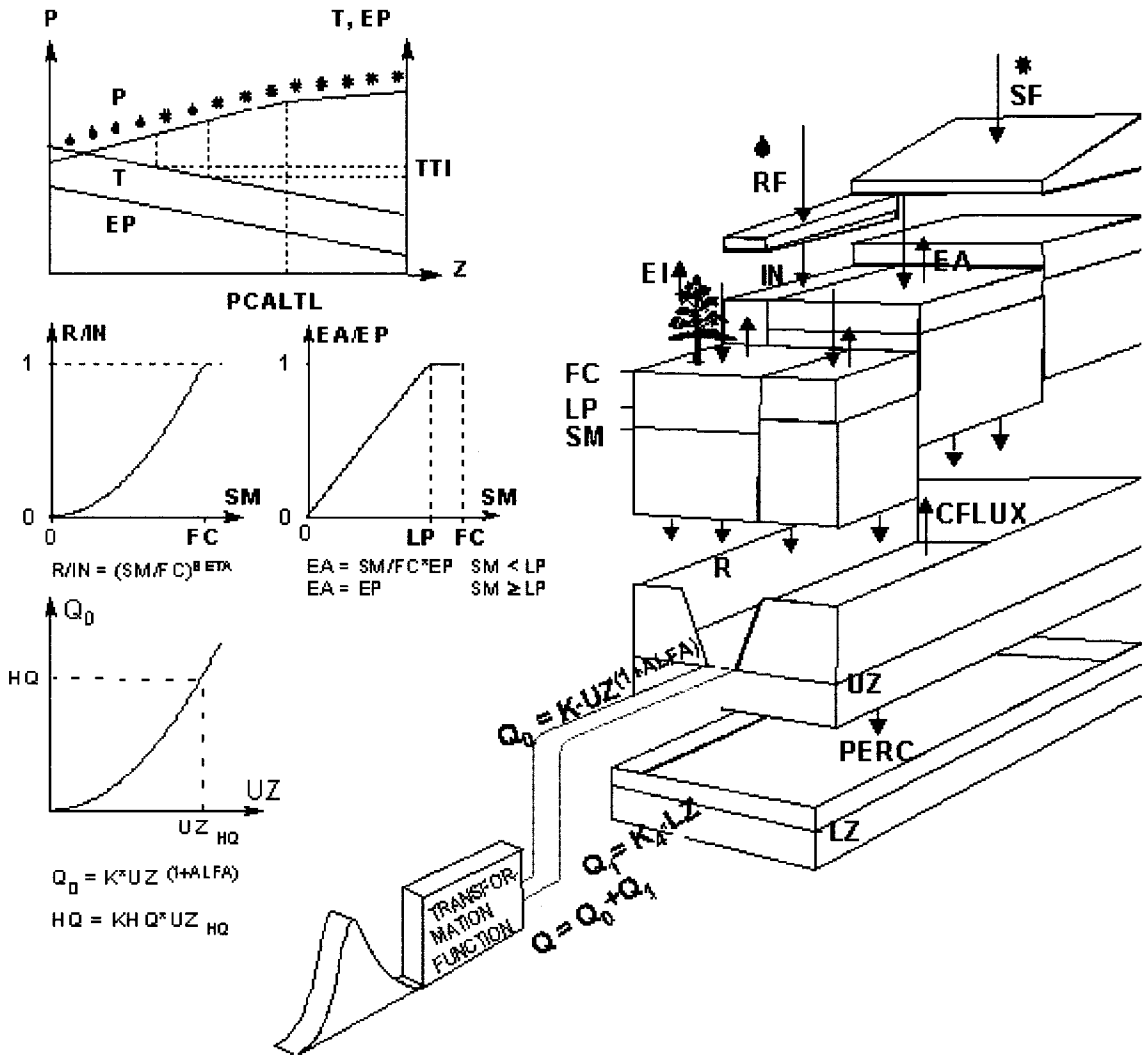

P = Precipitation
T = Temperature
SF = Snow
RF = Rain
Z = Elevation
PCALTL = Threshold for altitude correction
TTI = Threshold temperature interval
IN = Infiltration
EP = Potential evapotranspiration
EA = Actual evapotranspiration
EI = Evaporation from interception
SM = Soil moisture storage
FC = Maximum soil moisture storage
LP = Limit for potential evapotranspiration
BETA = Soil parameter
R = Recharge
CFLUX = Capillary transport
UZ = Storage in upper response box
LZ = Storage in lower response box
PERC = Percolation
K, K_1 = Recession parameters
ALFA = Recession parameter
Q_0, Q_1 = Runoff components
HQ = High flow parameter
KHQ = Recession at HQ
HQ_{UZ} = UZ level at HQ

4 DATA

In order to carry out the research reported here, it is necessary to have access to good global upper air meteorologic and land surface data. Basically, three kinds of data are required, upper-air atmospheric data, surface hydrologic data, and data on soil characteristics. Specifically, upper-air atmospheric fields of wind velocity, temperature, pressure and moisture; surface hydrologic fields of precipitation and stream flow and global terrain height data from digital elevation models; surface/subsurface distributions of moisture and temperature; and soil type and land-use data are necessary. Components of these data are required as a model input and others are required for comparison to and verification of the model results.

4.1 Data sets of Atmospheric variables and surface variables

Climate general circulation information obtained from the global tropospheric analysis and stored in a global dataset is required as input data to RAMS. The available atmospheric datasets range from four-dimensional climatologies to a 40-year GCM data analysis to compilations of over 10,000 weather stations (Kalnay et al, 1996). The main sources of these data sets are: OORT, a global dataset of atmospheric circulation statistics from Oort (1983) including an atmospheric surface climatology; NCEP-NCAR, a reanalysis project gridded global analyses from National Meteorological Center (NMC) (see Kistler et al., 1999); ECMWF, gridded global analyses from the European Center for Medium-Range Weather Forecasting (see Trenberth, 1992); and NOAA weather station data summaries that are available monthly and gridded, monthly by station, and daily by station.

In particular, here, the standard datasets available at NCAR are used. Specifically, for atmospheric variables, the global NMC-NCEP-NCAR reanalysis pressure level data, which is defined on a global 2.5° latitude-longitude grid on seventeen mandatory pressure levels; the global rawinsodes; and the global surface data are used.

The NCEP/NCAR Reanalysis Pressure Level Data include the following mandatory pressure levels (hPa), 1000, 925, 850, 700, 600, 500, 400, 300, 250, 200, 150, 100, 70, 50, 30, 20, and 10. For all these pressure levels, fields of Zonal Wind Component (m/s), Meridional Wind Component (m/s), Geopotential Height (m), and Temperature (K) are included. Additionally, Vertical Pressure Velocity (Pa/s) for the lower twelve levels, Relative Humidity (%) and Specific Humidity (kg/kg) for the lower eight levels, Surface Pressure (Pa), Sea Level Pressure (Pa), Surface Geopotential (m^2/s^2), and Precipitable Water (kg/m^2) are included. These data are available four times daily, at 00:00, 06:00, 12:00, and 18:00 hours in Universal Time Coordinates (UTC or GMT).

To get the surface characteristics, global terrain height data, global sea surface temperature data and global vegetation type data files obtained from The Earth Resources Observation Systems (EROS) Data Center (EDC) of the U. S. Geological Survey (USGS), and from NOAA are used. These data files have been organized as RAMS input files at CSU's Atmospheric Science Department. The topographic data set is called GTOPO30 which is a global digital elevation model (DEM) obtained from the U.S. Geological Survey's EROS Data Center in Sioux Falls, South Dakota. In particular, for the digital elevation model of South America, see Bliss and Olsen (1996). Elevations in GTOPO30 are regularly spaced at 30-arc seconds longitude latitude (approximately 1 kilometer) with a global coverage. The elevation values range from -407 to 8,752 meters above mean sea level. Ocean areas are masked as "no data" and lowland coastal areas have an elevation of at least 1-meter. Due to the nature of the raster structure of the DEM, small islands in the ocean less than approximately 1 square kilometer are not represented. Figure 4-1 is a shaded relief image, focusing on the topographic characteristics of Central America and northern South America, produced by the USGS using an 8 km grid data, and represents a reduced resolution version of the GTOPO30 for this region. The vegetation data set, stored at USGS-EROS, is derived from 1 km Advanced Very High-Resolution Radiometer (AVHRR) data spanning a 12-month period (April 1992-March 1993) and is based on a flexible data base structure and seasonal land cover regions concepts. The Global Sea Surface Temperature (SST) dataset is obtained from the optimum interpolation (OI) SST analysis that is produced weekly on a one-degree grid by the Climate Diagnostics Center (CDC) of the National Oceanic and

Atmospheric Administration (NOAA) (see Reynolds, 1988; Reynolds and Marsico, 1993; Reynolds and Smith, 1994).

4.2 Colombian Hydro-meteorological Data

Information collected from Colombian institutions is used for verification of and comparison with model results. Among the different climatologic and hydrologic variables required, precipitation and stream flows are the two most reliably recorded in Colombia. However, the precipitation gauge network is not only very sparse but its gauge density is extremely heterogeneous (see Figure 4-2). The development and implementation of the precipitation observation network are generally driven by development needs associated with water supply for growing population centers, warning of floods, hydroelectric power developments, or the agricultural industry. Consequently, as shown in Figure 4-2, most of the measurements are made in those regions where large hydroelectric or agriculture projects exist, zones with a high flood risk, or in the most populated and industrialized zones. Figure 4-2 shows the spatial distribution of the rainfall gauge network used in this study; the black symbols represent positions of gauges with daily data available (about 200 gauges) and the blue symbols represent positions of gauges with hourly data available (about 130 gauges). Observations of other important climatologic and hydrologic variables required such as temperature, dew point temperature, vapor pressure, atmospheric pressure, relative humidity, soil moisture and evaporation are available only at very low spatial and temporal density. For most of these variables, only monthly and in some cases annual averages were available.

Unfortunately, as shown in Figure 4-2, there are large areas of Colombia without climatologic and hydrologic measurements. A detailed description of the hydro-meteorological data collected for and used in this work is given in Appendix 2. The gauge locations and altitudes above sea level, record length and period of record, and system of units are included. Mesa et al. (1997), in addition to presenting results of a homogeneity analysis on the hydro-meteorological data available from IDEAM, summarized the hydrological data available in Colombia. However, one of the main sources of information for this thesis was the work of Velez et al. (2000). In their study, Velez et al. not only did an outstanding effort to collect all data available, but they also

did data homogenization and produced high quality maps of the spatial distribution of the observations, which were very useful in this study for comparison with RAMS results.

4.3 Macroclimatic Data Consideration

As mentioned in Chapter 2, climate anomalies in Colombia have a "predictable behavior" during the extreme phases of ENSO, ENSO cold phases being associated with wet anomalies and ENSO warm phases with dry anomalies. In consequence, special attention will be given to these variables. Also as indicated in the previous section, reanalysis data are provided every six hours UTC time. However, SSTs are provided at least weekly.

Figure 4-1: Shaded relief image, produced by the USGS using 8-km gridded data, a reduced resolution version of the GTOPO30.

Figure 4-2: Rainfall gauges. Black symbols represent positions of gauges with daily data (about 200 gauges). Blue symbols represent positions of gauges with hourly data. (About 130 gauges).

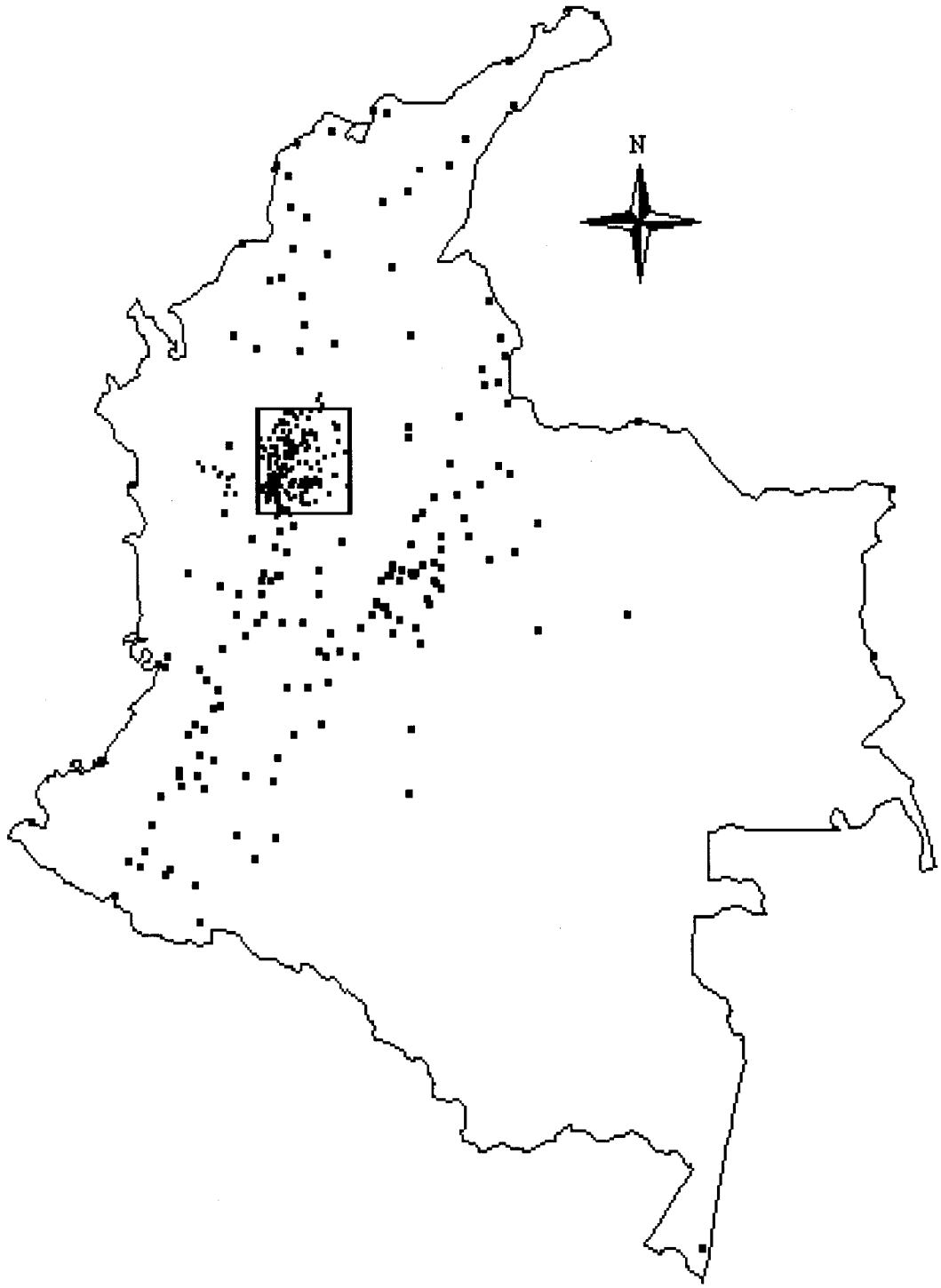

5 SIMULATIONS: DESIGN AND RESULTS

In reaching the goals of this research, several simulations are performed taking into account that the climatic cycle may be characterized according to the temporal and/or spatial scales of interest. For example, the annual cycle, at least on average, can be defined in a global sense as a function of latitude, and then its particularities vary from region to region according to the atmospheric general circulation processes that affect each region. On the other hand, the daily cycle, even though associated with the atmospheric general circulation, is highly dependent on the regional/local land surface and topographic characteristics present in the region. Both seasonal and daily precipitation responses are of special interest in this research. Seasonal, because of the strong relationship between the temporal distribution of precipitation in Colombia and the position and north-south migration of the Intertropical Convergence Zone (ITCZ) (Snow, 1976); and daily, because of the strong relationship between the spatial distribution of precipitation in Colombia and the Andes mountains. In both seasonal and daily responses, it is important not only to characterize the temporal and spatial distribution but also to quantify the amount of precipitation, essential for planning and management of water resources in Colombia. Looking to meet both objectives, two main simulation modes are used in this research. The *seasonal* simulation mode focuses on describing the general characteristics of the spatial distribution of precipitation in a large region of the Colombian Andes Mountains, whereas the *daily* simulation mode focuses on a detailed (i.e., high spatial and temporal resolutions) description of the spatial distribution of precipitation in a smaller region of the Andes Mountains in Colombia. Three seasonal simulations are carried out corresponding to 1) the entire 1999 calendar year, 2) 6 months of the 1989 calendar year, and 3) 6 months of 1992. Two daily simulations are carried out simulating two different periods, one in 1998 and the other in 1999.

5.1 Seasonal simulations

These simulations focus on describing the annual cycle in a regional response sense, trying to reproduce not only monthly temporal variations but also spatial distribution of precipitation. For the *seasonal* mode, two main simulations are performed. First, a full 1999-year simulation focused on the sensitivity of the general characteristics of the spatial and temporal distributions of precipitation in Colombia. The main purpose of this simulation is to test the ability of RAMS to preserve and reproduce the most important climate features in Colombia. That is, the objective is to determine whether CSU-RAMS is able to reproduce in a general sense the monthly cycles and patterns of spatial distributions of surface temperature, vapor pressure, atmospheric pressure, and precipitation among other variables. Second, two 6-month simulations, one for the period January-June of 1989 and the other for the period January-June of 1992, are performed, focusing on the response of the climate of Colombia to ENSO and non-ENSO phases. The main objectives of these 6-month simulations for these two periods are: first, to bring into focus the RAMS capabilities to reproduce spatial and monthly climate patterns driven by corresponding cold and warm ENSO phases; and second, to determine whether RAMS is capable of differentiating between a dry and a wet year in Colombia as a result of ENSO forcing. The period January-June of 1989 corresponds to a cold ENSO phase and the period January-June of 1992 corresponds to a warm ENSO phase. A major challenge and objective of these seasonal simulations is the description of the non-linearity of the precipitation process response, especially the significant impact of general circulation interacting with regional relief in capturing the monthly climate cycle, and in defining the magnitude and the spatial patterns of precipitation. The expectation is that the initial and boundary conditions used to drive these simulations with RAMS contain the main information interacting in the Colombian hydrologic system response during the warm and cold ENSO phases. In order to ensure that this requirement is met, northern South America is used as a geographic central point for the modeling effort, including part of Central America, a portion of the Caribbean Sea, a portion of the Amazon jungle and the tropical Pacific Ocean.

5.2 *Daily temporal scale mode simulations*

These simulations focus on describing the diurnal cycle for a specific watershed and try to reproduce not only the amount of precipitation but also the spatial location of a storm. For daily scale simulations, two periods focusing on a detailed temporal distribution of precipitation on a specific watershed in the Andes are performed. First, a watershed was selected considering the information availability; then, two periods are selected based on the amount of precipitation, one wet and one dry. As for the seasonal simulations, a major challenge and objective of the daily simulations is the description of the non-linear behavior exhibited by the precipitation process, in order to explicitly capture especially the significant impact of local relief, and the great importance of the diurnal cycle in defining the magnitude and the spatial and temporal patterns of precipitation. On this order of ideas, September 25-30 of 1998 is selected as a wet period and February 01-08 of 1999 as a dry period. Analogously to the seasonal simulations, the expectation is that the initial and boundary conditions used to drive these simulations in RAMS contain the main information interacting in the Colombian hydrologic system response to produce the observed precipitation.

5.3 *Results analysis*

Results are analyzed carefully considering that it is not trivial to determine whether the result of a simulation is a good representation of the historical observation. Model results are strongly dependent on the great number of model assumptions. In addition, when comparing model results to observations, the former need to be considered as area or volume averages, whereas the actual upper air or surface data are point observations. A standard practice has been to compare model results with the data analysis performed by operational centers such as the National Meteorological Center (NMC), which are used to produce the initial and boundary conditions for the simulations. However, this practice could be considered inappropriate when the results being compared come from a grid much smaller than the one used in the reanalysis and the corresponding region is topographically complex. In this study, reanalysis data are used for checking model results from the coarse grid only. Emphasis is given to the wind

components, the air temperature and the relative humidity fields. In addition, we concentrated our analyses of model results on the atmospheric model precipitation output, and the base of reference is the hydrologic surface data available from Colombian gauges. In order to compare observed and simulated precipitation data, the inverse distance weighted (IDW) interpolation method is used to produce a grid map from both simulated data and observed data, and then a comparison is made between these two maps. The IDW determines cell values using a linearly-weighted combination of a set of sample points. The weight is a function of inverse distance between the points. The input can be limited by the number of sample points to be used (specified as a variable radius object), or by a radius (specified as a fixed radius object), within which all points are to be used in the calculation of the interpolated locations. The output value from a cell using IDW is limited to the range of values used to interpolate. Because the IDW is a weighted average, the average cannot be greater than the largest or smaller than the smallest input. Therefore, it cannot create ridges or valleys if these extremes have not already been sampled (Watson and Philip, 1985). The influence of an input point on an interpolated value is isotropic. Since the influence of an input point on an interpolated value is distance related, IDW is not "ridge preserving" (Philip and Watson, 1982). The best results from IDW are obtained when sampling is sufficiently dense with regard to the local variation that it is attempting to simulate. If the sampling of input points is sparse or very uneven, the results may not sufficiently represent the desired surface (Watson and Philip, 1985). Unfortunately, these conditions are met here only for the simulated data but not for the observed data, forcing a careful analysis of fields of observations.

Finally, agreement between observed and simulated data will be evaluated and assessed using the following qualifiers: very good, very well, quite well, good, well, satisfactory, reasonable, moderately, acceptable and accurately. Clearly, the use of these qualifiers encodes a large degree of subjectivity. However, they will be used because the complexity of the comparisons being made, including characteristics of pattern in space and time at different scales, precludes the development of a general index to quantify the agreement between observed and simulated data. The assessment of agreement, on which the use of the above qualifiers depends, will focus first on the spatial distribution patterns, and second on the temporal distribution, independently of whether or not there is

agreement in the magnitudes of the variables being compared. Quantitative agreement is considered last in the assessment. Nevertheless, in some cases, comparisons will also include analyses of histogram characteristics. Finally, in some other cases, comparisons between maximum values, minimum values, or average values are used.

Results from these different simulations and their analyses are presented in the following chapters.

6 SEASONAL SIMULATION – FULL 1999-year

This simulation is designed to examine the ability of the RAMS model to reproduce spatial and monthly climate patterns in Colombia as driven by the interaction between the general atmospheric circulation and regional surface features, especially the topographic features.

CSU-RAMS is implemented in a two-grid domain configuration. Both grids are centered over Colombia at 5° N of Latitude and 75° W of Longitude. The coarsest grid is composed of 28 x 28 grid-points with a cell size of 160 km; the finest grid is composed of 34 x 34 grid-points with a cell size of 40 km. Both the coarse and the fine grids use eight vertical soil levels; in addition, the coarse grid uses twenty-two vertical atmospheric levels whereas the fine grid uses twenty-nine vertical atmospheric levels. The vertical grid spacing of the lowest atmospheric level on the domain is 250-m for the coarsest grid. Above this level the vertical grid spacing is increased at a rate of 20% until reaching a spacing of 2000-m, which is set as the maximum vertical grid spacing permitted; after this maximum is reached, the vertical grid spacing is kept constant. Vertical nesting is used in the five lower levels of the coarsest grid to get a smaller height of the lower vertical levels in the finest grid. Each of the first two lower levels of the coarsest grid are split into three levels and the following three levels into two levels each. As a result of this nesting, the vertical grid spacing of the lowest atmospheric level is around 80-m for the finest grid. Time steps of 120 seconds related with the coarsest grid are used. For the finest grid the time step is reduced using a 1:3 ratio. The domain configuration, its location, grid sizes, and other grid characteristics are presented in Table 6-1 and illustrated in Figure 6-1.

6.1 Boundary and initial Data

Atmospheric variable data for initialization and lateral boundary conditions are prepared for the twenty-two levels of the coarse grid set-up of the RAMS model from reanalysis pressure, rawinsondes and surface observations of 1999. These data include

horizontal wind components, relative humidity and air temperature available every six hours referenced to Universal Time Coordinates (UTC or GMT). Specifically, initial data correspond to 01-01-99 00:00 UTC, and boundary data correspond to 00:00, 06:00, 12:00, and 18:00 UTC hours times daily for the full 1999-year. The variables are linearly interpolated in time to each model time step to get boundary data for each time step. Both lateral and top nudging are used. Lateral nudging to the analyzed data on the first seven grid points from the lateral boundary of the coarsest grid is implemented using an 1800-second nudging time scale, and top nudging above 16-km with a 1000-second nudging time scale.

An initial soil moisture condition of 60% saturation in the deepest soil layer, 50 % in the upper soil layer and a linear variation between these two extreme values is used

Model topography is prepared from the digital elevation model (DEM) GTOPO30 that has elevations regularly spaced at 30-arc seconds longitude latitude (approximately 1 km) with a global coverage. Figure 6-2 illustrates the topography of the region, dominated by the Andes Mountain range, parallel to the west coast of South America, as the main topographic feature. The upper plot of Figure 6-2 is a shaded relief image, produced by the USGS using an 8 km grid data, representing a reduced resolution version of the GTOPO30 for that specific region; the lower plot shows the coarse domain topography used by RAMS after the process of transferring the data from the 1 km grid to the 160 km grid. It is clear that the smoothing process required when the data are transferred to a larger grid size leads to a crude approximation of the topographic relief and that the roughness fidelity depends strongly on the grid resolution.

The vegetation data used are derived from 1 km Advanced Very High-Resolution Radiometer (AVHRR) data spanning a 12-month period (April 1992-March 1993) and are based on a flexible database structure and seasonal land cover regions concepts.

The Sea Surface Temperature (SST) data for initial and boundary conditions are obtained from a dataset produced weekly on a one-degree grid by the Climate Diagnostics Center (CDC) of the National Oceanic Atmospheric Administration (NOAA). Specifically, initial data correspond to the first week of 1999, and boundary data are updated every week of the 1999-year.

As an example of reanalysis data transferred to the RAMS Domain, Figure 6-3 shows the horizontal surface wind velocity (arrows) and surface pressure contours once the data are transferred to the 160 km grid (upper plot); the surface temperature field in degrees Celsius on the 160 km grid is shown in the lower plot. These examples correspond to grid analysis on June 30 1989 at 00:00 UTC.

6.2 Main parameterization used in this simulation

For radiation, the Chen and Cotton short wave and long wave radiation parameterizations, which include the cloud effects (Chen and Cotton, 1988), are chosen. The radiation tendency is updated every 1000 seconds and longitudinal variation of short wave is considered. The soil vegetation model parameterization, LEAF2, is activated. For horizontal diffusion, coefficients are computed as the product of the horizontal deformation rate (horizontal gradients of horizontal velocity) and a length scale squared, based on the original Smagorinsky formulation. The length scale is evaluated as twenty-five percent of the horizontal grid spacing. Vertical diffusion is computed from a 1-dimensional analog of the Smagorinsky scheme in which vertical deformation is evaluated from vertical gradients of horizontal wind, and vertical length scale is twenty five percent of the local vertical grid spacing. Modifications of the vertical diffusion coefficient due to static stability or instability are used, based on formulations of Hill (1974) and Lilly (1962).

For precipitation, the convective parameterization of Kuo (Kuo, 1974; Molinari, 1985) is used, with updates every 1800 seconds and the bulk microphysics parameterization including only cloud water and rain (Piotr et al., 1989) are activated. For cloud water, the total cloud droplet number concentration (number of droplets per kg of air) is specified directly and the mean droplet diameter is automatically diagnosed from this concentration and the estimated mixing ratio. For rain, a prognostic equation for droplet number concentration is used, and a special array for this quantity is added, and the average rain droplet diameter is diagnosed from the prognosed mixing ratio and number concentration. Both cloud water and rain are assumed to follow a gamma droplet size distribution where the shape parameter guarantees that the size distribution peaks at a positive diameter.

6.3 *Results*

It is not possible to compare all feasible model arrangements, first because there is no available dataset of observations including all possible information obtained in a simulation and, second, because many of the variables come from secondary calculations, as parameterizations, involving the basic variables contained in the set of equations used to describe the physical process. Accordingly, in this analysis of results, we concentrate on two sets of variables: first, we concentrate on basic variables including temperature, pressure, moisture content of the air as measured by water mixing ratio or relative humidity, and wind velocity; second, we concentrate on precipitation, which is the main variable of interest in this thesis, and which is evaluated with a parameterization scheme involving the basic variables. It is important to make this distinction since a parameterization scheme may be changed or adjusted by tuning its parameters in order to obtain more comparable results, but not the set of basic equations without making a major change in the modeling system.

In this chapter, results from RAMS simulations for the full year 1999 are analyzed. One of the main goals is to examine how accurately the RAMS modeling system simulates intra-annual (seasonal) and inter-annual variability of precipitation. In order to do so, model output is compared first with NCEP/NCAR reanalysis temperature, pressure, moisture transport and general circulation. Then, modeled precipitation is compared to observed precipitation data directly measured at existing rain gauge stations and from the GOES Precipitation Index for 1999. These comparisons focus directly on the Colombian territory specifically using results from the finest grid.

6.3.1 Temperature field

Figure 6-4 presents the surface temperature field plotted for the last day of January, June and November of 1999 at 24:00 UTC hours. Figure 6-4 shows plots using both reanalysis data and simulated data; in addition, it shows observed average data from specific points throughout the 1999-year. Figure 6-5 shows observed annual average surface temperature in Colombia and values along arbitrary transects as shown on the

map profiles. Profiles along arbitrary transects are included as a guide of map scale. Observed temperature information was taken from Velez et al. (2000).

The graphs show that the simulated surface temperature field compares reasonably well with the reanalysis and observed data. The simulation reproduces well the average behavior of the reanalysis field both with respect to its spatial and its temporal distributions. Both simulation and reanalysis data show high variability of temperature in the Andes Mountains region and the simulated variability compares well with that of the reanalysis data. However, as expected, there are small discrepancies in some regions, for example in the southeast plains and the Amazon region (i.e., Los Llanos and Amazonas) simulated temperature tends to be a little warmer than reanalysis data. These discrepancies could be associated with a better representation of the orography features in RAMS domain than in the reanalysis data, and with the grid-size.

Even though the only available observed temperature data correspond to a monthly average, they still provide a good base against which to compare simulation results because both the diurnal and the intra-annual temperature variation or range are small in the tropics. Taking a look at the specific points shown on the map, Figure 6-4 (lower plot) shows a close agreement between RAMS simulated surface temperature and observations. For example, observed average monthly temperature at point #3 exhibits values around 6 °C (degrees Celsius) year long, which is consistent with RAMS simulated data for this location showing values in the range 3-7 °C (white color). The same generally good agreement between RAMS simulated temperature and observations is seen at all of the other sample points; points #1, #5 and #6 have average monthly temperature values that exceed 25 °C, whereas point #2 has values around 12 °C and point #4 around 17 °C, all of which compare very well with reanalysis and RAMS simulated values. However, we must keep in mind that the sample point values are monthly average temperatures whereas shown simulated values are for a specific time. Because the diurnal temperature range in these tropical regions is around 10 °C, differences of about 5 °C are expected and acceptable.

Taking into account that in low latitudes the annual temperature range for a specific location is very narrow, an annual average temperature plot produces a good

approximation of the spatial distribution of temperature. Figure 6-5 shows a plot of the observed annual average temperature and profiles along a few arbitrary transects as shown on the maps. These profiles are included as a guide of scale for the spatially distributed temperature maps. Variations of temperature along these profiles range from around 5 to 28 °C, being consistent with values shown for simulations.

A major characteristic observed in these plots is the large dependence of the spatial distribution of temperature on Colombian orography. Clearly, the Andes ranges play an important role in modulating and determining the spatial distribution of temperature in Colombia. On the other hand, the intra-annual temporal distributions of temperature at a monthly scale remain almost constant, implying a very narrow range of variations. These descriptions of simulated temperature are satisfactory based on the fact that observed data are expected to be more uniform because of the small number of stations used to get the information.

6.3.2 Pressure field

Figure 6-6 presents plots of the surface pressure field for the last day of January, June and November of 1999 at 24:00 UTC hours. Figure 6-6 shows plots using simulated and reanalysis data; in addition, it shows the annual distribution of observed monthly average pressure from three specific points. Figure 6-7 shows observed annual average surface pressure in Colombia and values in millibars along arbitrary transects as shown on the maps. Profiles along arbitrary transects are included as a guide to map scale. Observed information was taken from Velez et al. (2000).

As was the case for surface temperature, RAMS simulated surface pressure fields match well the observations. There are no major discrepancies between simulated pressure fields and those from reanalysis data. As with the temperature field, the spatial distribution of surface pressure depends highly on Colombian orography. The Andes ranges mainly modulate the spatial distribution of this variable, whereas the temporal distribution at a monthly scale is almost constant, as shown for the observed specific points plotted. Temporal variations at a monthly scale are almost negligible. Three points from observed data are selected to show the range of variation of the pressure field and the agreement between RAMS simulated and observed data. The graphs clearly show that

RAMS simulated pressure matches very well those observed values at points #1, #2 and #3.

Finally, the spatial distribution of the pressure field is almost constant throughout the year in Colombia. This can be observed in Figure 6-7, which shows the field of observed annual average pressure and profiles along arbitrary transects as shown on the plots. As before, these profiles are included in lieu of a scale for the observed spatially distributed pressure maps. Variations of pressure along these profiles range from around 700 mb to 1000 mb, being consistent with values shown for simulations.

6.3.3 Water Mixing Ratio field

Figure 6-8 shows plots of the surface Water Mixing Ratio (WMR) field for the last day of January, March, June, August, October and November of 1999 at 24:00 UTC hours. Figure 6-8 shows plots using simulated and reanalysis data. In addition, Figure 6-9 shows plots from observed average data for January, June and November, and profiles arbitrary transects as shown on the maps for each one of these three months. The observed information was taken from Velez et al. (2000).

The WMR from the reanalysis data, as shown in Figure 6-8, presents smaller values of around 5 g/Kg (0.005) at high altitudes in the Andes ranges, and then a general increase as we descend to the foothills of the Andes and in the valleys. Higher values of WMR, around 20 g/Kg (0.020), exist in some areas of the Amazon and Llanos regions as well as in the Pacific and the Caribbean coastal regions. In a general sense, RAMS simulated WMR fields exhibit a spatial distribution as expected and as exhibited by the reanalysis data. However, some aspects are not simulated well. A major discrepancy seems to be associated with the range of variation where simulated spatial distribution of WMR is more uniform than that from reanalysis data. Consequently, reanalysis data present smaller and larger values than simulated values.

Figure 6-9 shows a plot with observed monthly average WMR and profiles along arbitrary transects, as shown on the plots. As before, these profiles are included in lieu of a scale for the spatially distributed WMR maps. Unfortunately, because of lack of data, these maps show large areas with zero WMR, which actually means no data were

available; however, these profiles of observed WMR are consistent with simulated and reanalysis data. Major differences occur in the magnitudes (observed data do not show values higher than 0.006 (6g/Kg)), but the spatial distribution seems to be sufficient.

6.3.4 Relative Humidity field

Figure 6-10 shows the surface Relative Humidity (RH) field for the last day of January, March, June, August, October and November of 1999 at 24:00 UTC hours. Plots shown in Figure 6-10 were produced using simulated and reanalysis data. In addition, Figure 6-11 shows plots using observed annual averages and profiles along arbitrary transects, as shown on the maps. The observed information was taken from Velez et al. (2000).

The RH from reanalysis data, as shown in Figure 6-10, tends to have smaller values in the eastern part of the study area with values around 50%; higher values occur in the mountains and in the Pacific coastal area. In general, RH from reanalysis data shows some areas with values greater than 100%, meaning the presence of supersaturation conditions. Simulated RH fields do not reach supersaturation values for the times shown; however, the simulated values compare well in spatial distribution and magnitude with those from reanalysis data. Although simulated values exhibit the same general patterns as the reanalysis, they represent drier conditions in the Llanos and Amazon regions.

Figure 6-11 shows observed annual average RH and profiles along arbitrary transects as shown on the plots. Here again, these profiles are included in lieu of a scale for the spatially distributed maps. Simulated data are very consistent with these average values. The spatial distribution is also satisfactorily simulated. Even though observed values do not show supersaturation as reanalysis does, they range from 70% to 100%, with higher values in the eastern part of the study area than those from the simulated data. Observed and simulated data are very consistent in the Andes region, implying that the RAMS model captures the main features of the RH field. Although the simulation does not match exactly the relative humidity from reanalysis data, as expected, results from the simulation are in general agreement with topographic features and the observed data available.

6.3.5 Wind Velocity

Figure 6-12 shows the surface wind velocity field for the last day of January, June and November of 1999 at 24:00 UTC hours. Plots shown in Figure 6-12 are produced using simulated and reanalysis data. RAMS model results of surface wind velocity are in good agreement with plots from reanalysis data. Maps show small discrepancies, especially in June when the reanalysis northward component of the wind is weaker, presenting a major difference in the northwest area of the map. However, observe that the ability of the model to reproduce the patterns of the surface wind field improves for later times, as shown for the month of November.

Comparison between reanalysis and simulated maps shows better agreement in the oceanic regions. There are more focalized differences on land that may be explained by the data grid used to plot these maps; whereas reanalysis data come from a data set with a grid size of around 300-km, simulated data are obtained from a grid size of 160-km. Therefore, we conclude that RAMS simulations are able to capture the main patterns of wind flows, an ability that is a priority for the achievement of our objective because it ensures the proper humidity flow in the area of interest.

6.3.6 Precipitation

Plots of observed and simulated precipitation fields are shown and compared for every month from the beginning of the simulation. In addition, plots of the 1999 GOES Precipitation Index are shown and used to qualify RAMS results. It should be noted and emphasized that western Colombia is one of the rainiest regions of the American continent, exhibiting annual precipitation amounts of up to 13300 mm/year (Snow, 1976). As a reminder, simulation results come from two parameterization schemes, the convective parameterization and the bulk microphysics scheme.

Figure 6-13 shows RAMS precipitation results for each month of the 1999 year. Figure 6-14 shows maps of observed monthly cumulative precipitation for 1999. Figure 6-15, middle plot, is included in lieu of a scale for the observed distributed maps; it shows the actual monthly values for specific locations as indicated in the observed maps. In addition, the lower plot of this figure shows a map of the observed annual precipitation

field for 1999 and a profile showing the spatial variation along an arbitrary transect as shown on the map.

Observed precipitation maps clearly indicate that there exists a common spatial distribution pattern of both monthly and annual precipitation. This pattern can be described as follows: the area between the Western and Eastern Ranges of the Andes is relatively dry with spots of high precipitation; the foothills of the west slope of the Western range and the foothills of the east slope of the Eastern range are relatively wet; the area between the Pacific coast and the west slope of the West range is very wet; the area along the Caribbean coast is relatively dry; and the plains areas of the Llanos and the Amazon basin are wetter but with large variations year round. On the other hand, the maps also clearly show the strong dependence between precipitation and the annual movement of the ITCZ that controls the annual distribution of rainfall. Consequently, northern areas are drier during the first semester and southern areas during the second semester, and this behavior is more clearly observed in the regions with more data availability.

Despite the existence of this common pattern, precipitation is extremely variable in space and in time; in space because of the orographic factors and in time because of the dynamics of the ITCZ. The largest temporal variability occurs in the mountain region (see Figure 6-15, middle plot), whereas the Southeastern region (Amazon and Llanos) have less variability year round (points #3 and #4 in the middle left plot, Figure 6-15).

In general, results show that simulated precipitation compares reasonably well with observations; the simulated precipitation reproduces fairly well the spatial and temporal distribution of precipitation, as shown in Figure 6-13. It can also be observed that the simulated precipitation is consistent with the annual movement of the ITCZ, with northern areas drier during the first semester and southern areas drier during the second semester.

The simulated precipitation exhibits two main areas of high precipitation, the first one starting in the Pacific Region and reaching the foothills area of the west slope of the Western range; and the second in the foothills area of the east slope of the Eastern range. These two zones themselves exhibit two other zones of relatively high precipitation, one

in the north and the other in the south. This pattern seems to suggest that the amount of the spatial distribution is related to zonal bands in Colombia. Thus, looking at the middle plot of Figure 6-15 as a reference, it must be said that, for two imaginary bands defined by points #1 and #2 and by points #3 and #4, Colombia has places with the highest concentration of precipitation. The same pattern is present in observed precipitation plots as show by the profile plotted in Figure 6-15.

However, RAMS seems to produce more precipitation than observed in wet regions, for example in some locations in the Pacific region; and less precipitation than observed in non-mountainous areas at the Amazon, Llanos and the Caribbean regions. As shown in Figure 6-13, simulated RAMS precipitation amounts in wet areas exceed the observations by more than 200% of the observed values. For example, Figure 6-15 shows that at point #1, which is close to a region of high precipitation, observed precipitation values are generally below 1000 mm per month and the maximum value of about 1000 mm occurs in August. Something similar occurs with precipitation at point #2. However, simulated precipitation, as shown in Figure 6-13, seems to indicate that whereas simulated precipitation associated with point #2 is in agreement with observed values, the simulated precipitation associated with point #1 exhibits values as high as 5000 mm in November, which is five times the observed value. Even though the RAMS simulation produces this anomalous behavior, it only occurs in three small areas: 1) a small area located in western Colombia next to the coast of the Pacific Ocean, 2) another small area located in southern Colombia, east of the Andes and 3) another located in north central Colombia, next to Venezuela. It must also be emphasized that these three areas are also zones of high precipitation in the observations. Other than for these three small regions, values of simulated precipitation in the Pacific and Andes regions tend to match fairly well the observed values. However, it is clear that RAMS simulations are excessively dry in the Llanos and Amazon regions; simulated values for these two regions do not show more than 100 mm per month for large areas, whereas observed values are around 250mm.

Figure 6-16 shows GOES Precipitation Index (GPI) for each month of 1999. The GPI, developed by Arkin and Meisner (1987), is an algorithm to estimate tropical rainfall using cloud-top temperature as the sole predictor. The estimation procedure follows:

Precipitation (mm) = FRAC x RATE x TIME

Where:

FRAC is the fractional coverage of IR (infrared) pixels less than 235°K over a reasonably large domain (50 km x 50 km and larger). RATE is 3 mm/hour. TIME is the number of hours over which "FRAC" is compiled.

GPI has shown useful results in the tropics and for warm-season extratropics. Its major advantage is to be based on IR data that are available over most areas of the globe from geostationary and polar orbiting satellites. Its major weakness is that estimation of precipitation from cloud-top temperature is relatively far removed from the physics of the precipitation generation process.

In a general sense, as shown in Figure 6-16, GPI plots are consistent with observed and simulated plots. They show both periods, wet and dry, year-round very well. The dry period ranges from November to March, whereas the wet period ranges from April to October.

6.4 Discussion

As indicated in previous chapters, macroscale atmospheric convergence is generated over north-western South America when winds from the southern hemisphere cross the equator, turn eastward and penetrating into Colombian territory from the Pacific Ocean and converge with the warmer winds coming from the northern hemisphere. In the Americas and in low latitudes, the area of the Pacific Ocean right off the western coast of Colombia and the northwestern coastal region of Colombia constitute one of the most active areas for the development of mesoscale convective complexes due to the combination of warm water, orographic lifting, and large-scale low level convergence that enhances deep convection. Consequently, centers of high precipitation are generated in Colombia along the Pacific coast with localized points with extremely high precipitation well exceeding the observed average values. According to Velasco and Fritsch (1987), observed data have shown a maximum of precipitation exceeding 13300 mm/year.

Observed data clearly demonstrate the large effect of the Andes Mountains in determining the spatial distribution of precipitation in Colombia. Surface moist winds coming from the Amazon and Llanos regions (i.e., the trade winds) find a barrier in the Eastern range of the Andes, which causes forced ascent triggering the precipitation process and producing large amounts of rainfall along the eastern foothills of this range. The same process is applicable to the winds coming from the Pacific Ocean. For that reason, the spatial distribution map shows two north-south bands with high values of precipitation to the west and to the east of the Andes and parallel to the West and East ranges, respectively. In the Andes region, that is, the region between the West and East ranges of the Andes, the spatial distribution of precipitation is extremely variable and more dependent on the local processes generated as a consequence of the interactions between orographic features, local heterogeneities in the characteristics of the land surface, and the trade winds. Valleys between the ranges present a high gradient in precipitation but the amount of rain is much less than in the east and west slope of East and West ranges, respectively. This could be explained as the result of the precipitation shadow effect for both ranges; however, the central range, which reaches the highest elevations of the three ranges, is one of the main factors triggering precipitation in the valleys between the ranges, precipitating moisture from wind-driven air masses passing west and east ranges or from katabatic winds generated in these ranges.

On the other hand, it is clear that Colombia is very humid, with large amounts of precipitation year-round. However, the northern and southern regions appear to be complementary, one being dry during periods when the other is wet. This is explainable as the result of the longitudinal cyclic migration of the Intertropical Convergence Zone (ITCZ). As introduced earlier in this thesis, the ITCZ is one of the main mechanisms of moisture convergence to produce precipitation in Colombia and its periodic migration ensures that it is located over some point in Colombia at all times. Its movement is harmonic and directly dependent on the apparent position of the sun, ensuring that it is located over the same area at approximately the same period of time every year. However, the actual position of the ITCZ exhibits anomalies (i.e., displacement from the expected position) due to the presence of forcing by low frequency macroclimate phenomena in the tropical Pacific, such as the ENSO phenomenon. For that reason, the

actual annual temporal distribution of precipitation in Colombia is affected, resulting in the observed inter-annual variability.

Consequently, given the complexity of the atmospheric processes occurring in and around the Colombian mountains, it is highly desirable to have a high density of surface and rawinsonde observations to obtain an adequate analysis of mesoscale features. Furthermore, to capture detailed orographic features, such as the mountains and coastline, and to resolve mesoscale and local scale systems contributing to convection, high resolution grids are required. However, the existing convective cumulus parameterizations available in the RAMS model were designed and tested for specific ranges of horizontal resolutions, which forced the use of different parameterization schemes for each one of the nested grids (coarse and fine grids), producing unrealistic model solutions at the interface of the grids. For this reason the contribution of the bulk microphysics parameterization, designed for a cell size less than or equal to 2 km, is questionable in this simulation where the smallest cell size was 40 km. In this case, the horizontal model resolution is too coarse to explicitly resolve convection well.

Considering all of the above comments and accepting that they explain the deviation between simulated and observed data, it is appropriate to say that the RAMS model, as implemented here, replicated reasonably well observed data over Colombian territory. For this specific case, simulated values come from a grid cell size of 40-km, with an acceptable representation of orographic characteristics; on the other hand, reanalysis data and observed data are very sparse, which may produce maps with high uncertainty. In conclusion, the CSU-RAMS system's ability to simulate observed climate in Colombia is satisfactory for the purposes of this thesis.

Table 6-1: Location and dimensions of the two-grid domain configuration used in the full 1999-year simulation

DESCRIPTION	GRID ONE	GRID TWO
Northwest Point	23.406 °N, 95.46 °W	10.891 °N, 81.027 °W
Northeast Point	23.406 °N, 54.54 °W	10.891 °N, 68.973 °W
Center Point	5.0 °N, 75.0 °W	5.0 °N, 75.0 °W
Southwest Point	13.999 °S, 94.306 °W	0.945 °S, 80.919 °W
Southeast Point	13.999 °S, 55.694 °W	0.945 °S, 69.081 °W
West Coordinate (Km)	-2160	-660
East Coordinate (Km)	2160	660
South Coordinate (Km)	-2160	-660
North Coordinate (Km)	2160	660
Bottom Coordinate (m)	0.0	0.0
Top Coordinate (m)	25895.1	25895.1
Delta-X (m)	160000	40000
Delta-Y (m)	160000	40000
Bottom Delta-Z (m)	250	78.3
Number of vertical levels	22	29
Delta-t (s)	120	40

Figure 6-1: Domain of simulation. Grid-1 spans from (14°S, 94.31°W) to (23.41°N, 54.54°W), pole (5.0°N, 75.0°W), $\Delta x = \Delta y$=160 km. Grid-2 spans from (0.94°S, 80.92°W) to (10.89°N, 68.97°W), pole (5.0°N, 75.0°W), $\Delta x = \Delta y$ =40 km.

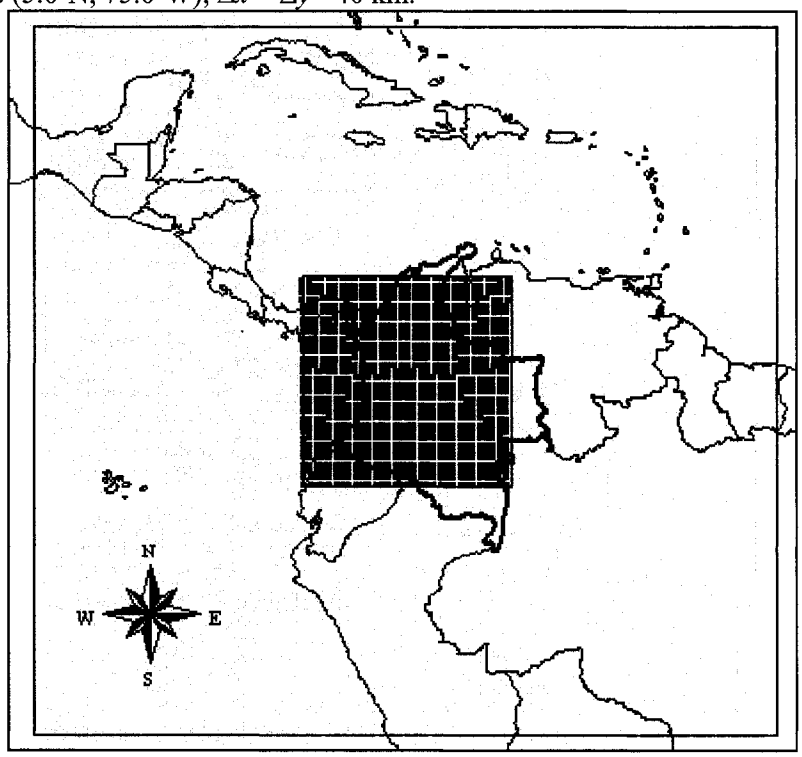

Figure 6-2: The upper plot is a shaded relief image prepared by the USGS. The lower plot shows the coarse domain topography used by RAMS; contour lines, starting at 400 m above sea level, are shown every 200 m of height

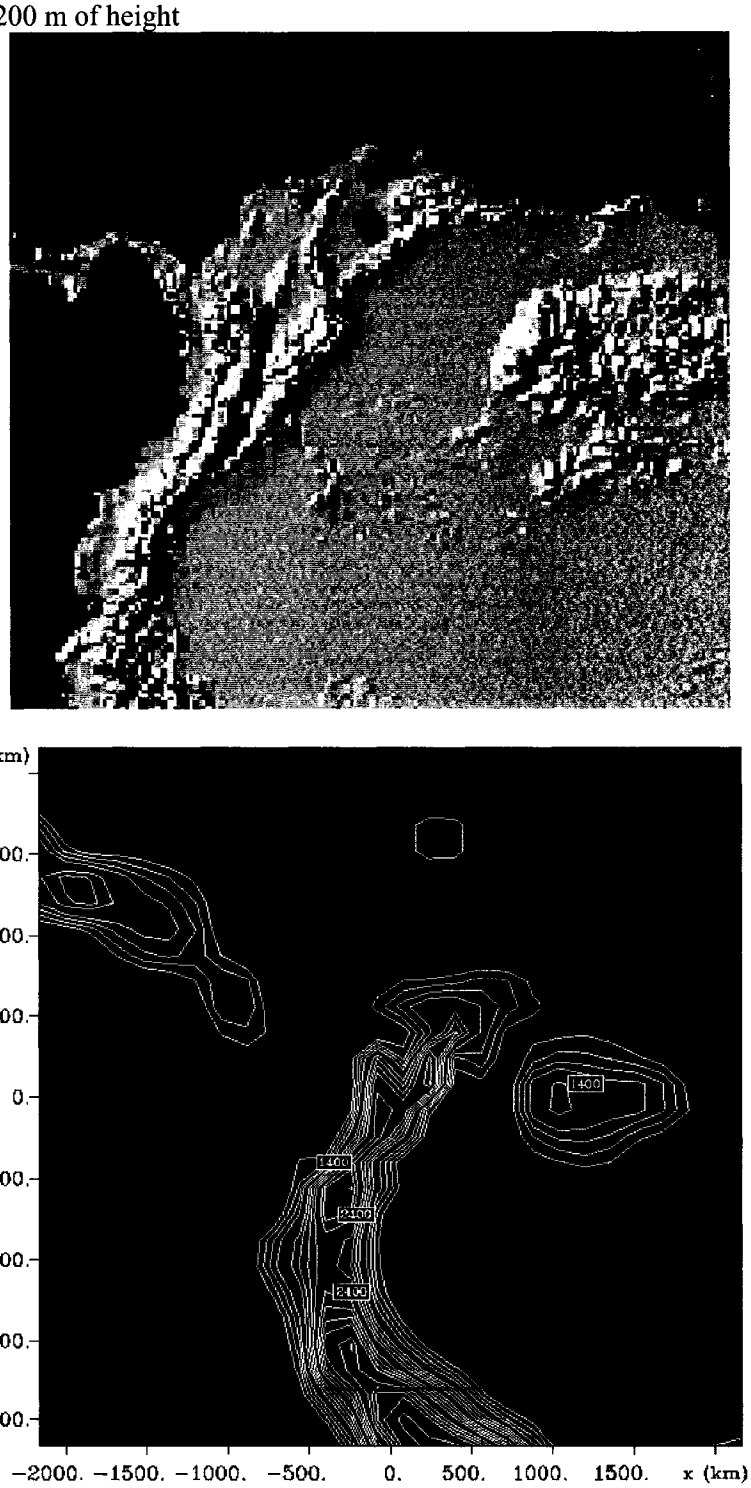

Figure 6-3: Upper plot shows surface pressure field (mb) and surface winds velocity field. Lower plot shows surface temperature field (°C). These plots correspond to reanalysis data at 06-30-89 00:00 UTC

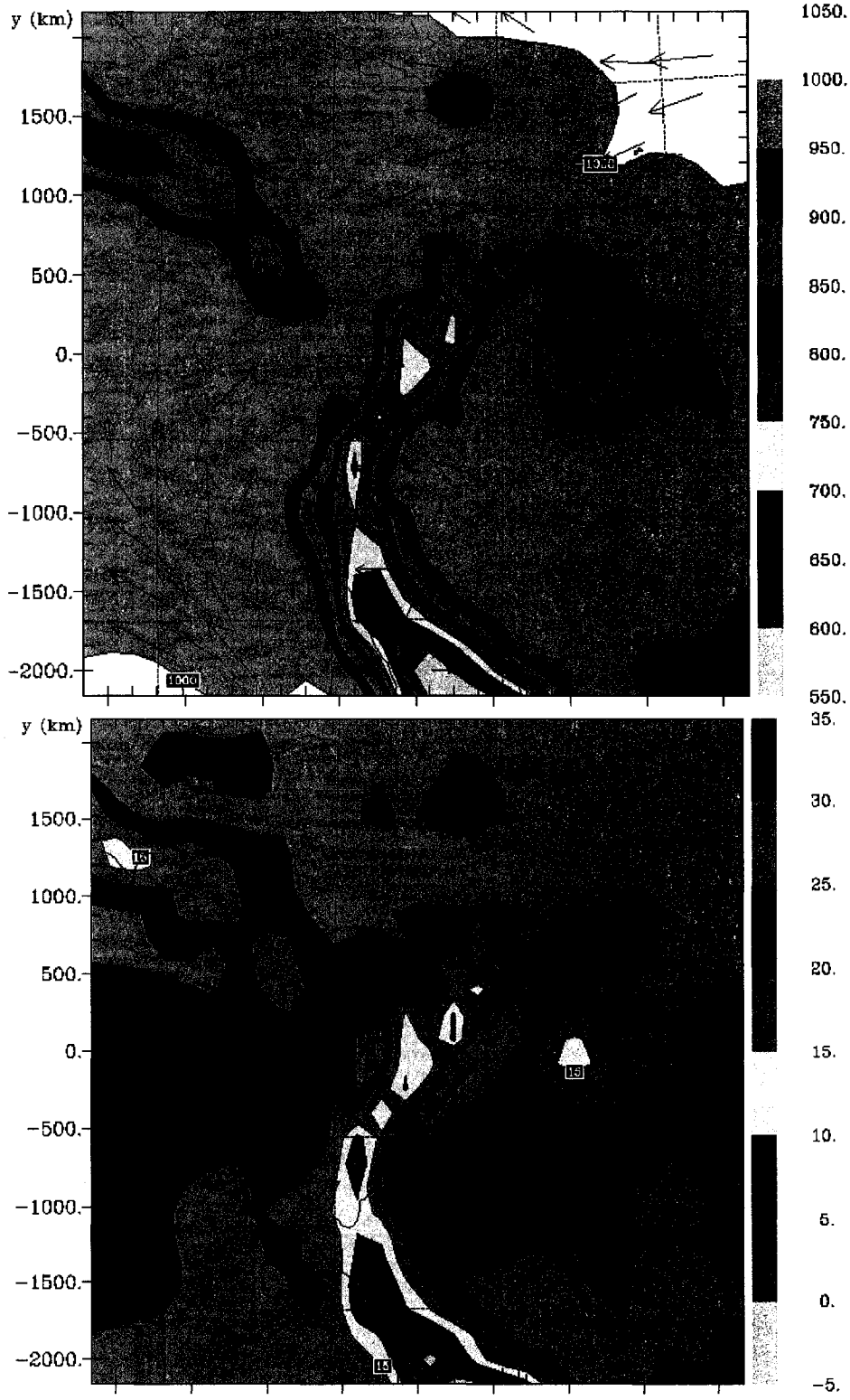

Figure 6-4: Upper plots show simulated values of surface temperature field (°C). Lower plots show values of surface temperature field (°C) from reanalysis data. Plots correspond to the last day of the month shown at 24:00 UTC hours. Lower curves show monthly average observed temperature values at the location points specified on the map.

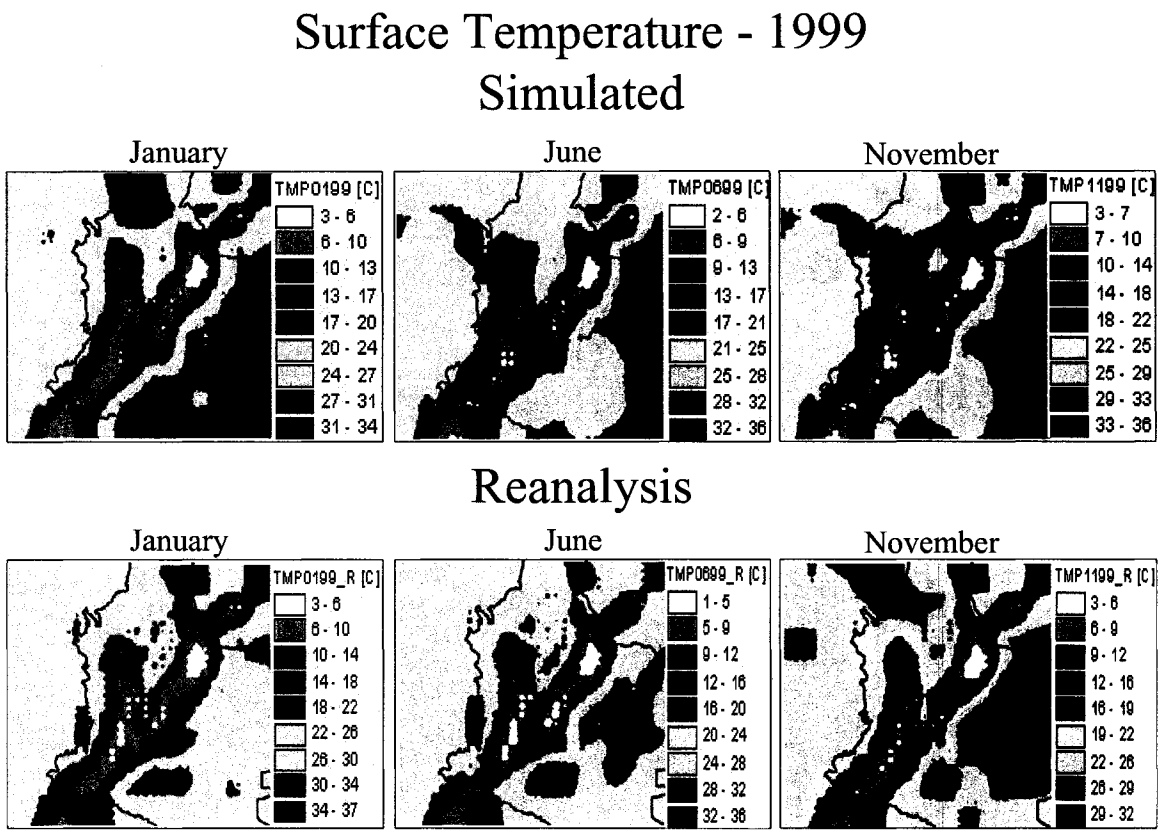

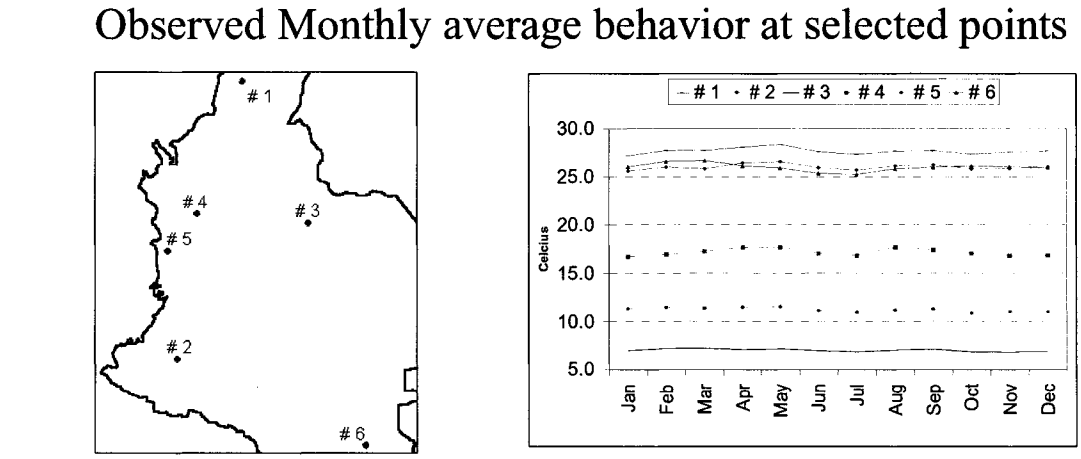

Figure 6-5: Plots show annual average surface temperature in Colombia and values along arbitrary transects as shown on the maps.

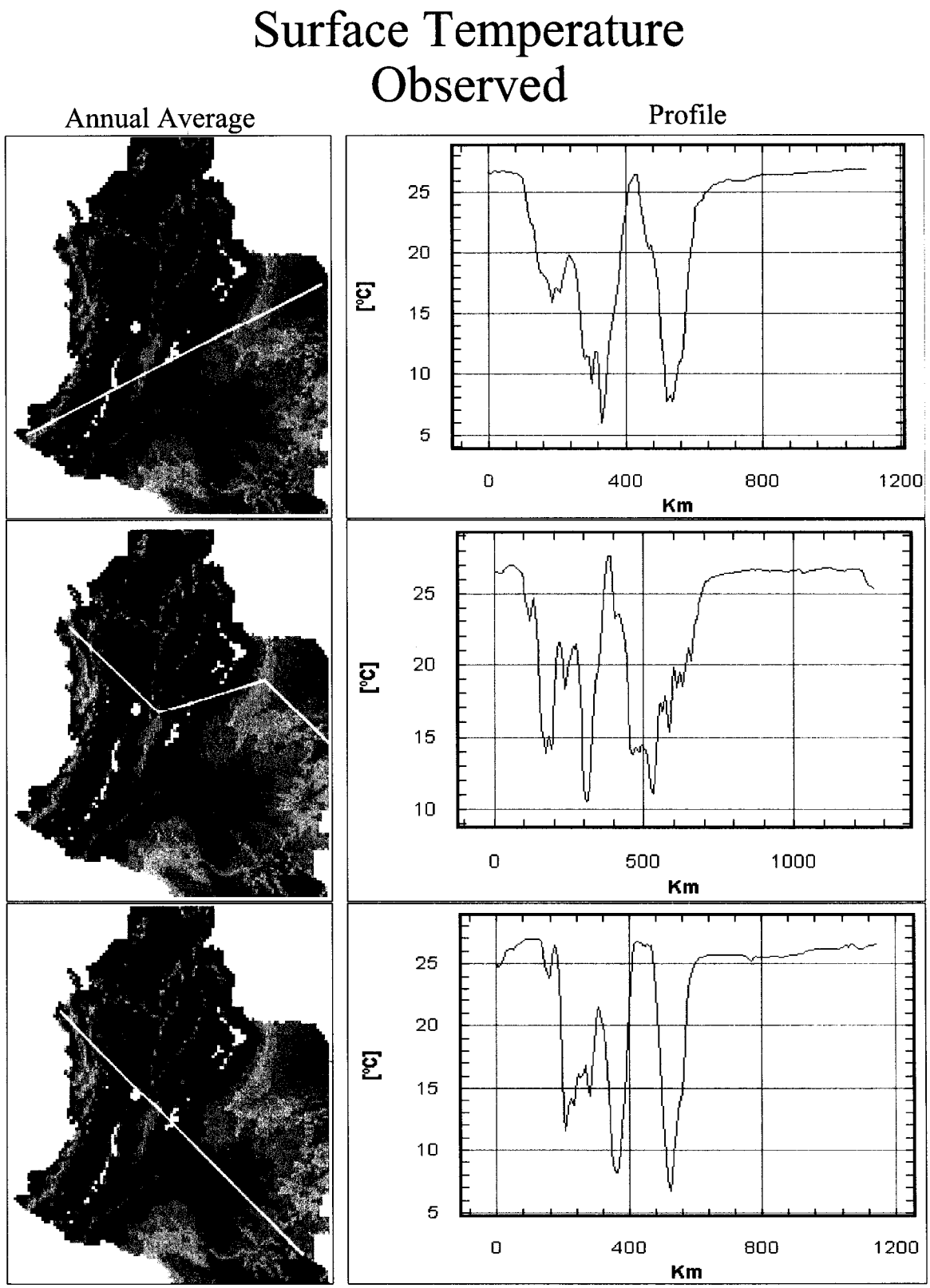

Figure 6-6: Upper plots show simulated values of surface pressure field (mb). Lower plots show observed average values of surface pressure field (mb). Plots correspond to the last day of the shown month at 24:00 UTC hours. Lower curves show monthly average observed pressure values at the location points specified on the map.

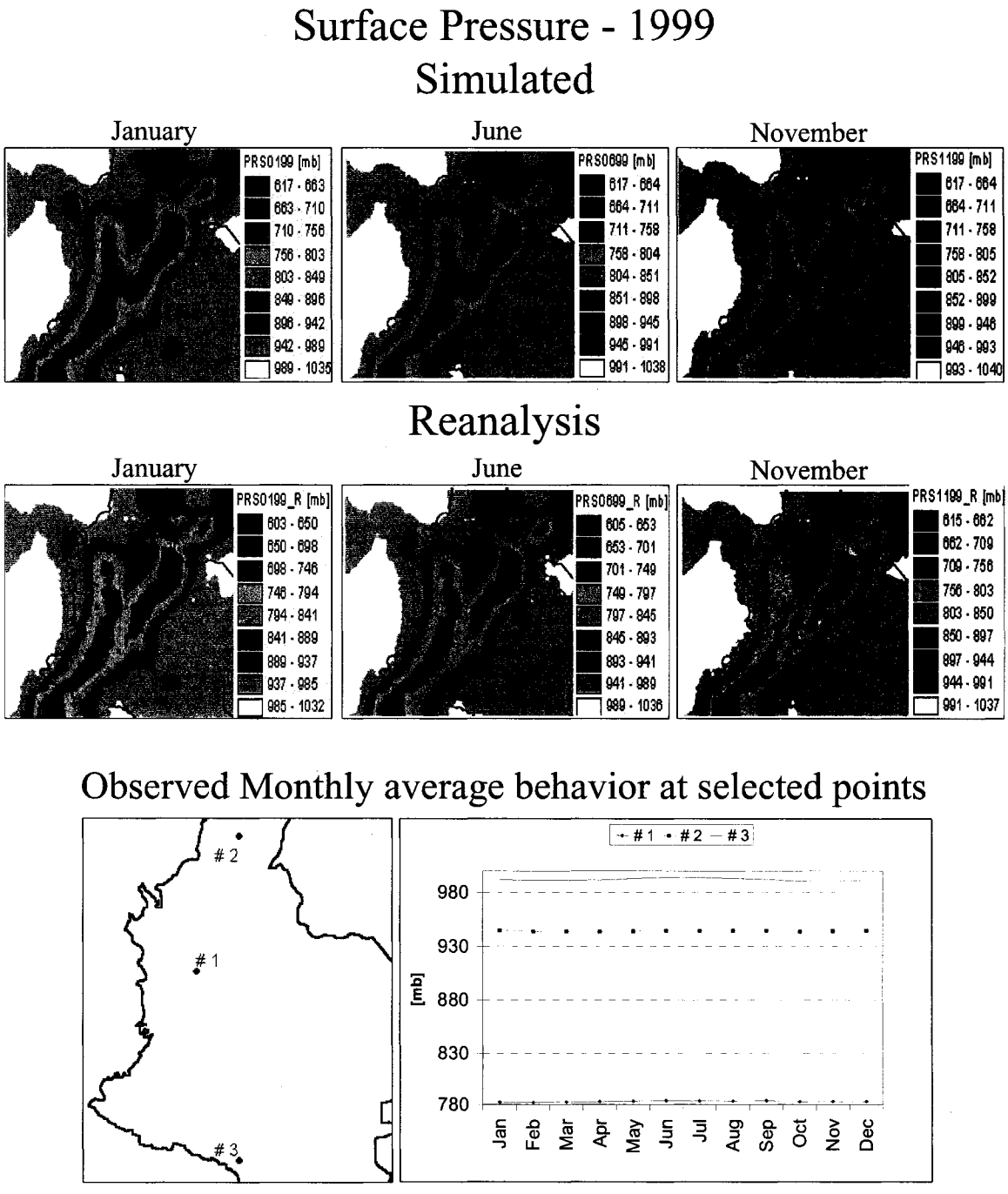

Figure 6-7: Plots show annual average surface pressure in Colombia and values (mb) along arbitrary transects as shown on the maps.

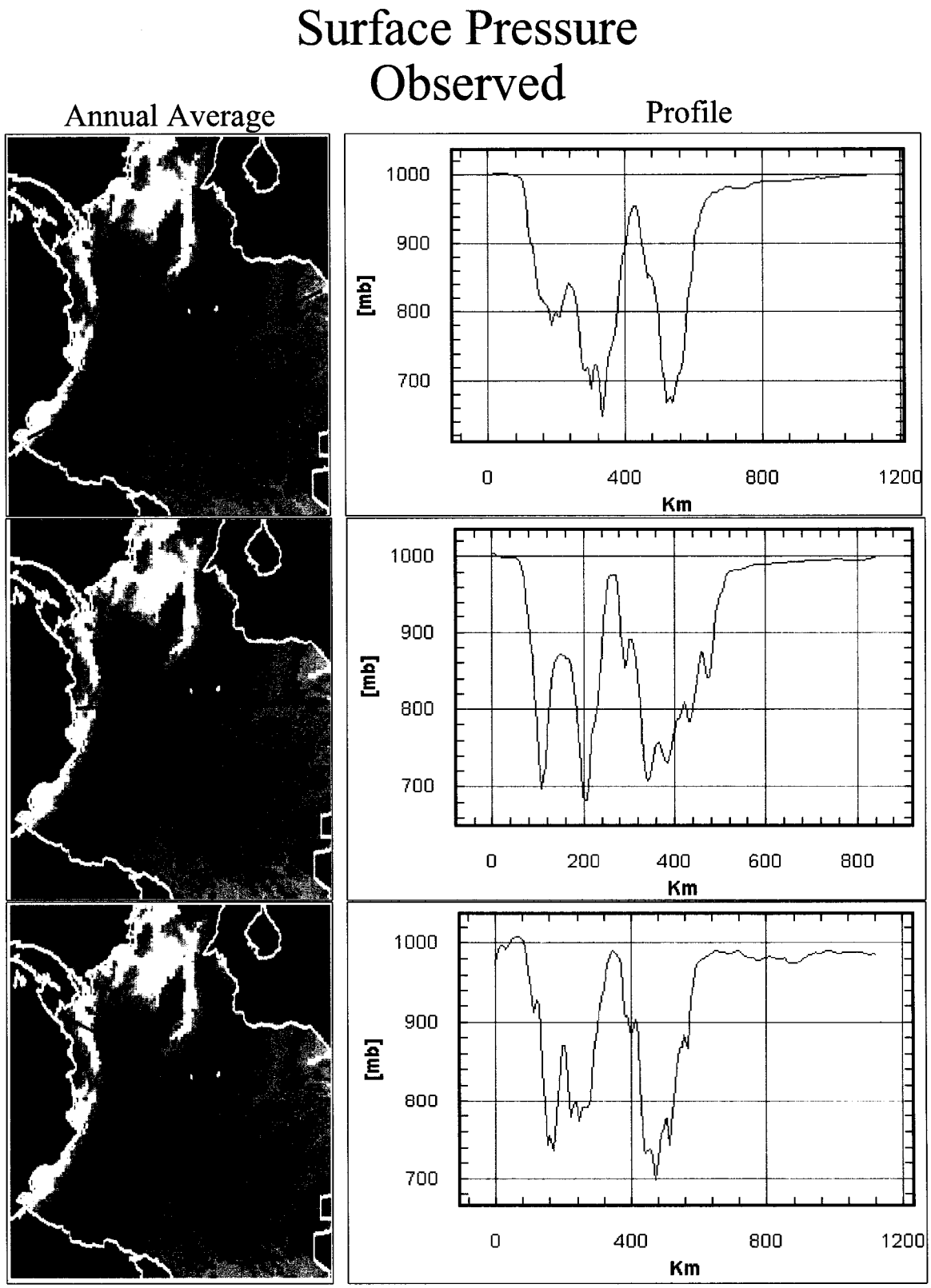

Figure 6-8: Upper plots show simulated values of surface water mixing ratio (WMR) (g/Kg). Lower plots show values of surface WMR from the reanalysis data

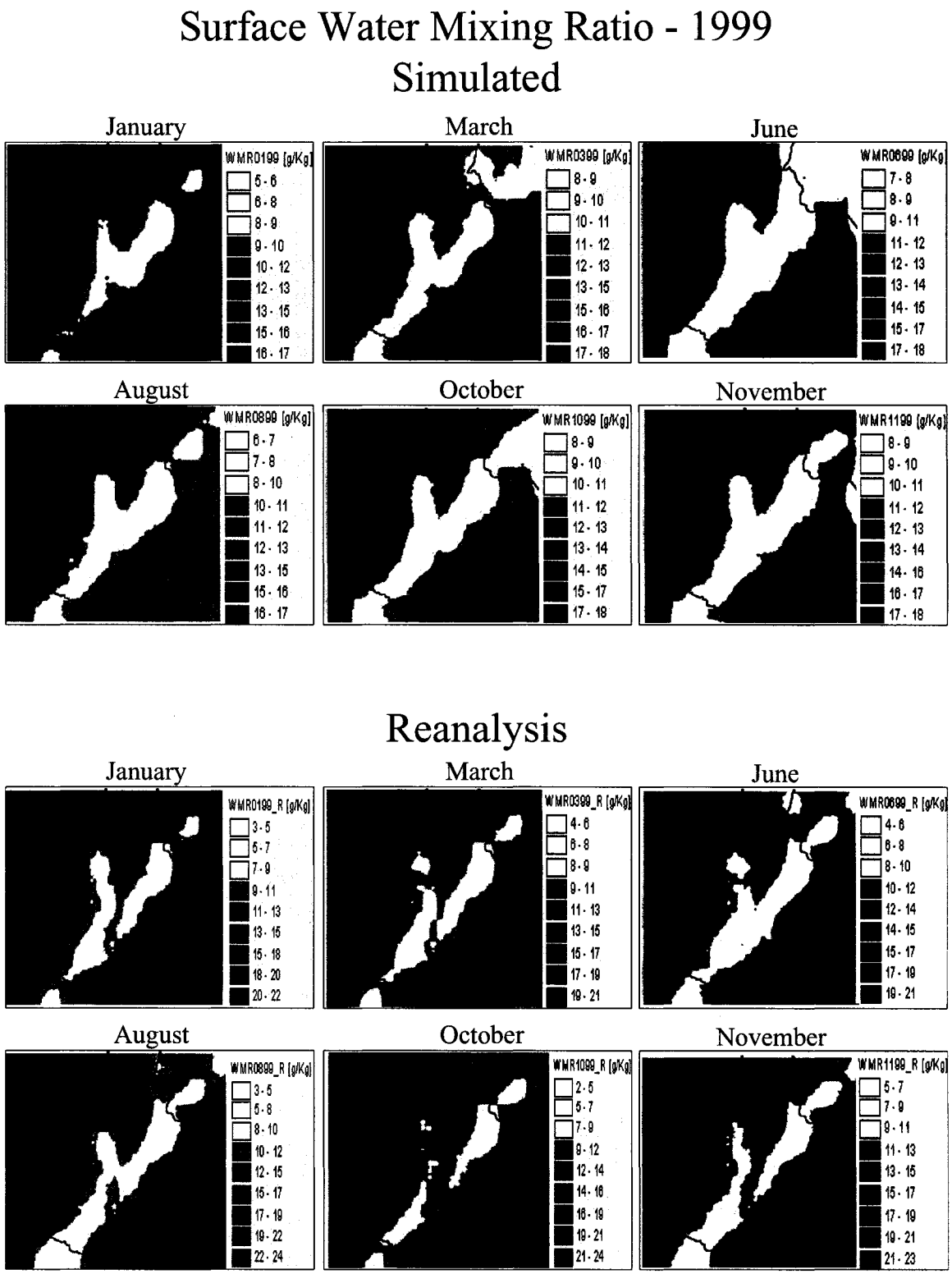

Figure 6-9: Plots show observed WMR for January, June and November and the profile along the transects shown on the maps. Values in the profiles are dimensionless.

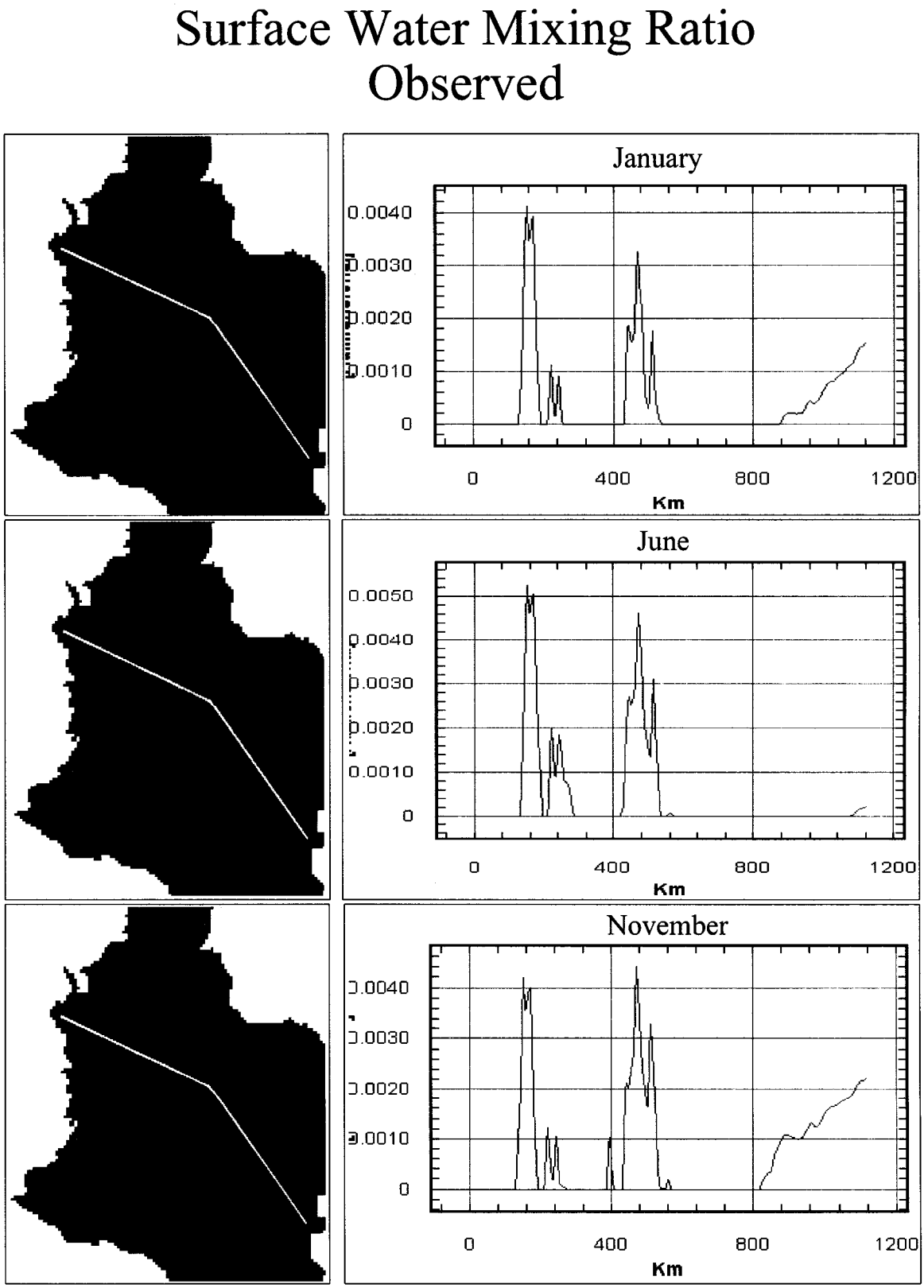

Figure 6-10: Upper plots show simulated values of surface relative humidity (RH) (%). Lower plots show values of surface RH (%) from reanalysis data.

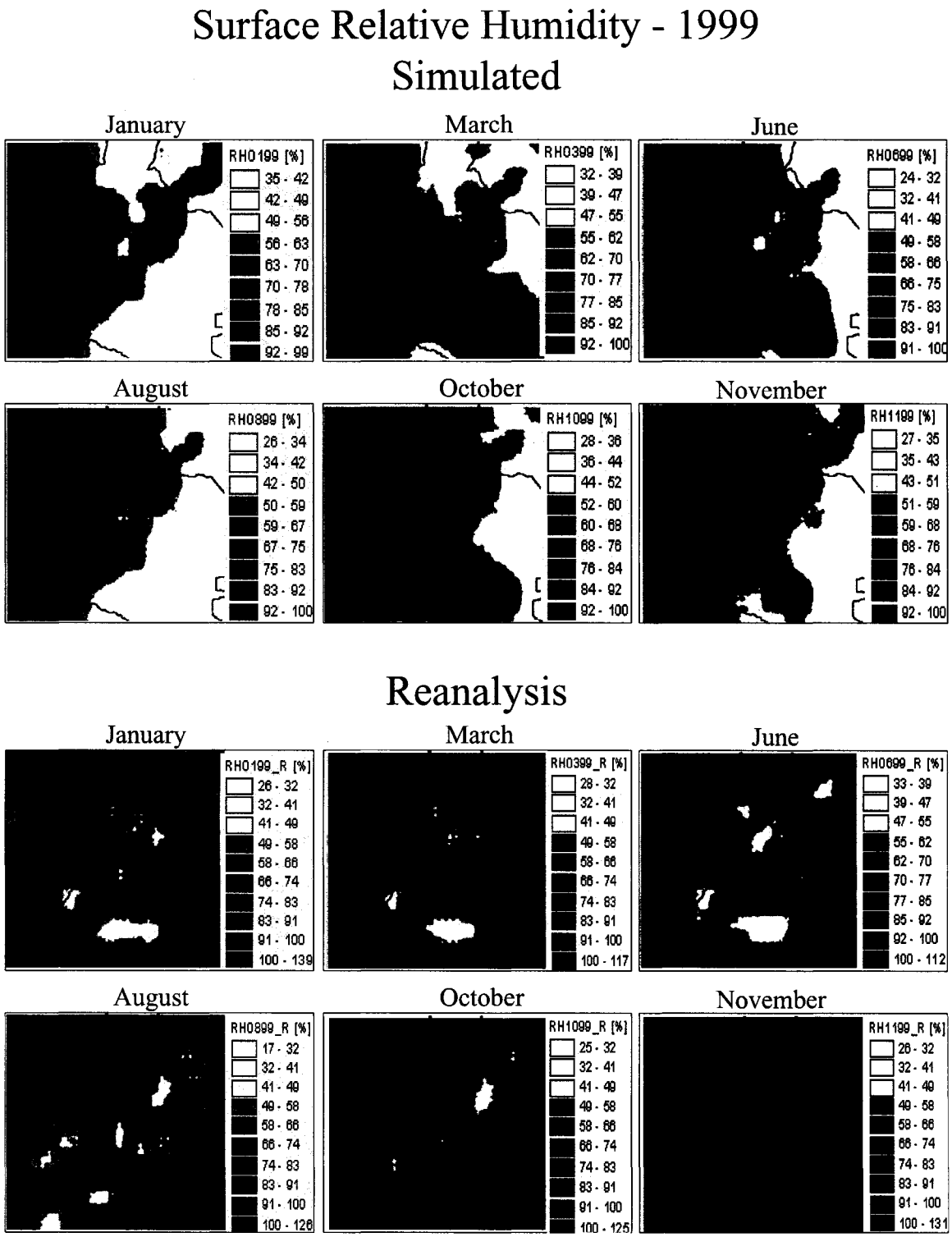

Figure 6-11: Plots show observed annual average RH (%) and the corresponding profiles along the transects shown on the maps.

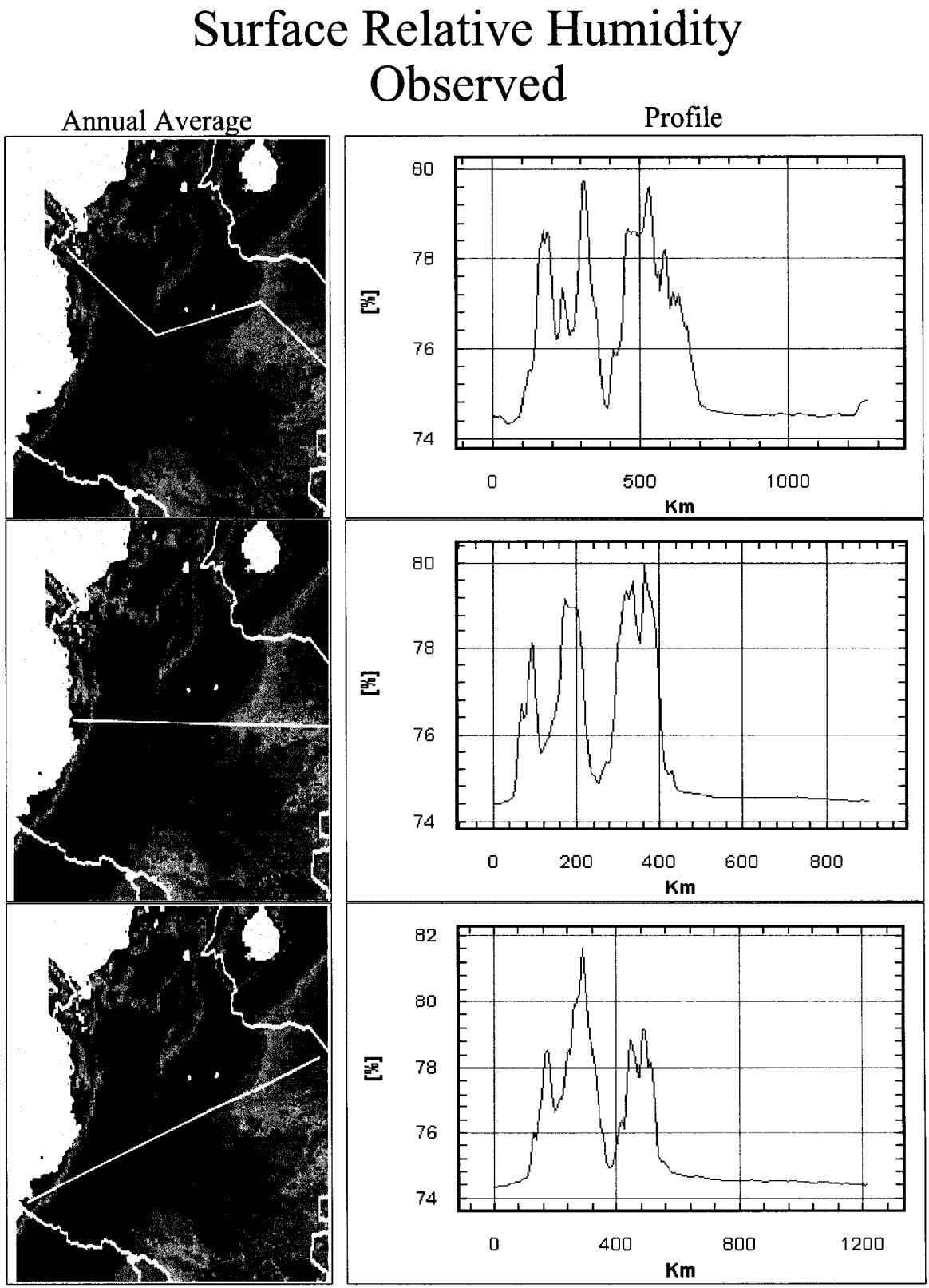

Figure 6-12: Surface wind velocity from reanalysis and simulated data (m/s).

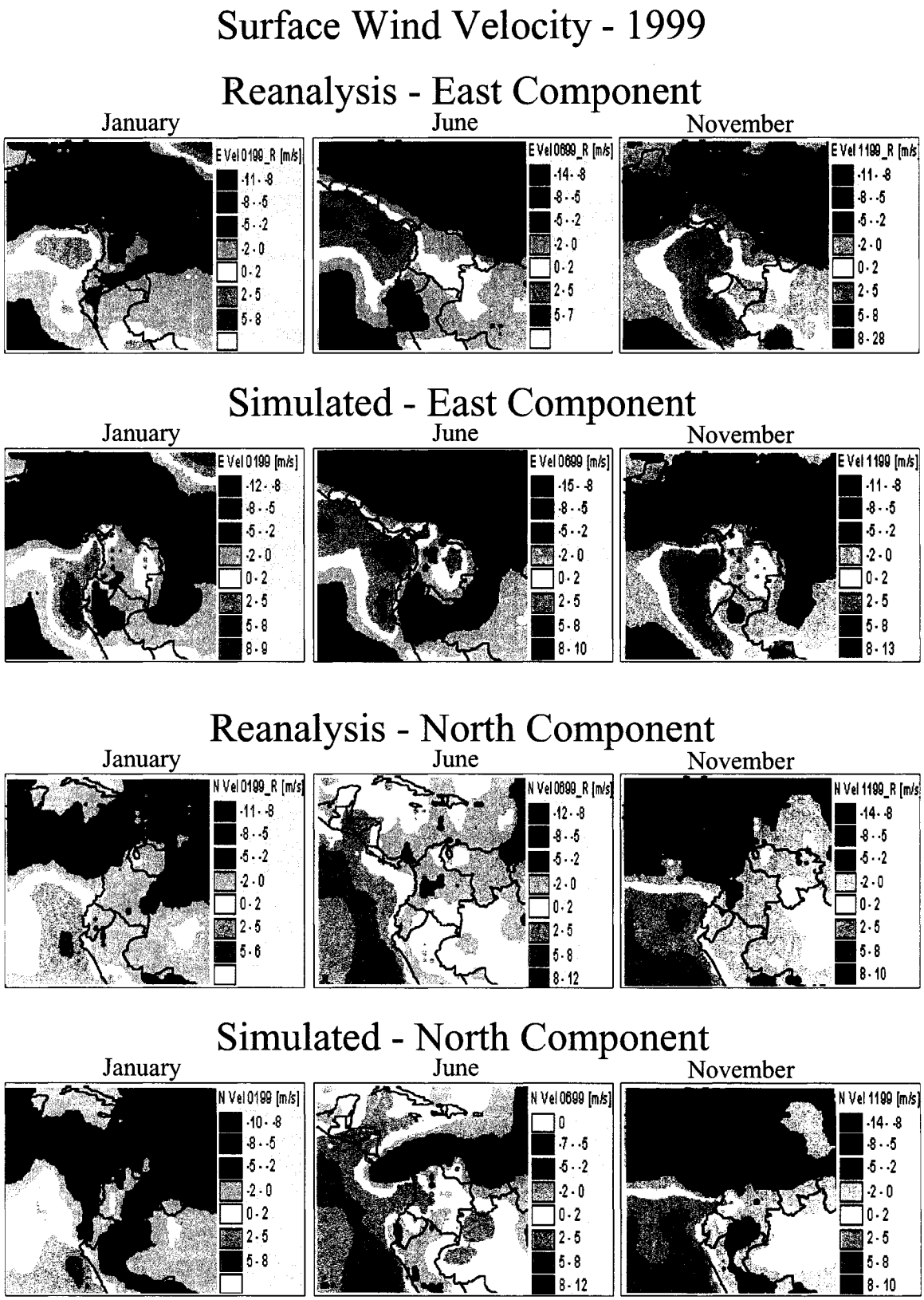

Figure 6-13: Monthly cumulative simulated values of precipitation (mm). Plots illustrate values from January through November.

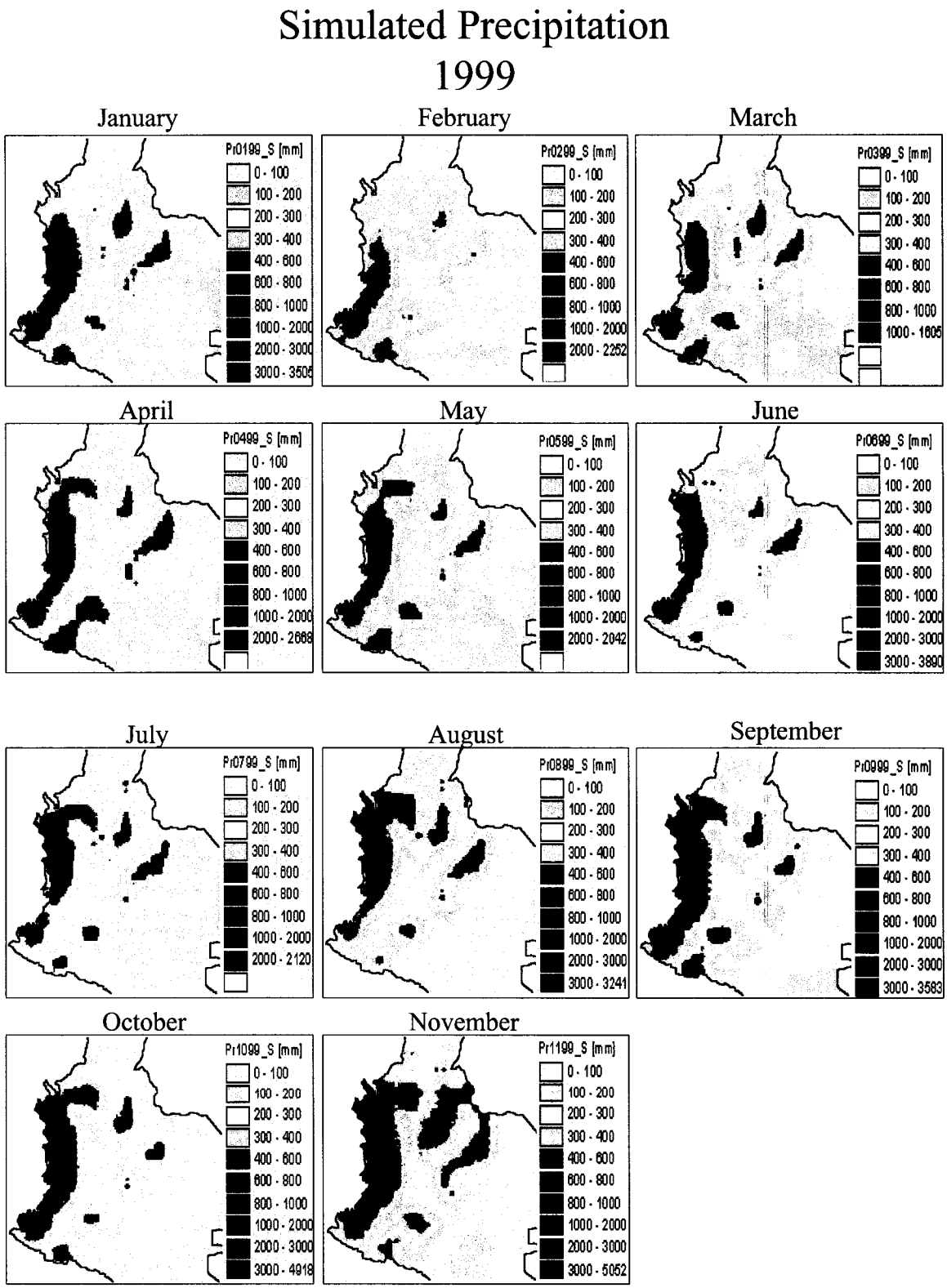

Figure 6-14: Monthly cumulative observed precipitation (mm). Going from the wettest to the driest regions the color scale goes from dark blue (wettest), to dark red (driest), passing through lighter shades of blue, dark green to light green, shades of browns and finally red.

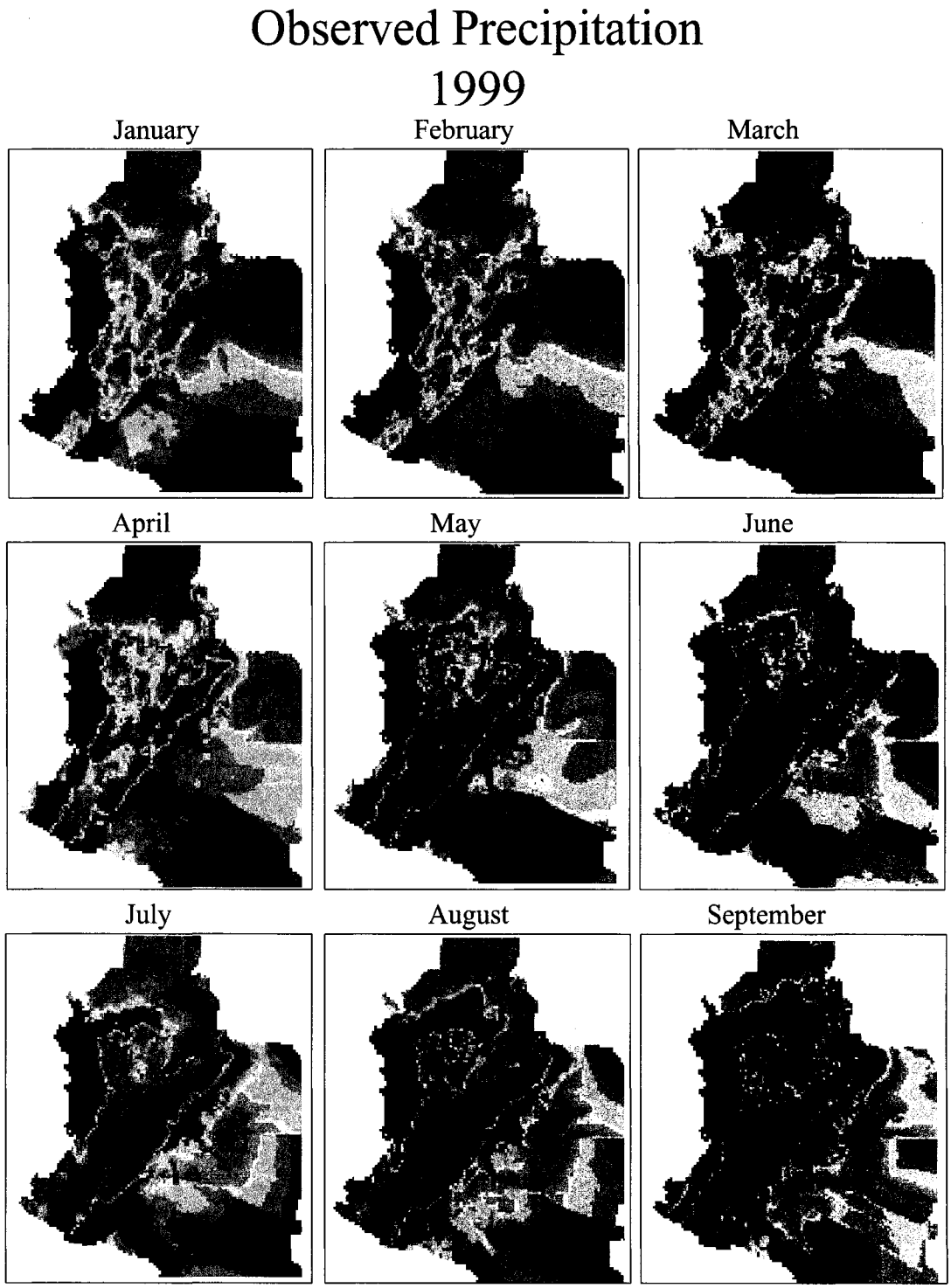

Figure 6-15: Monthly cumulative observed precipitation (mm). Lower plots illustrate monthly values at the location points specified on the map and values in the profile shown on the map.

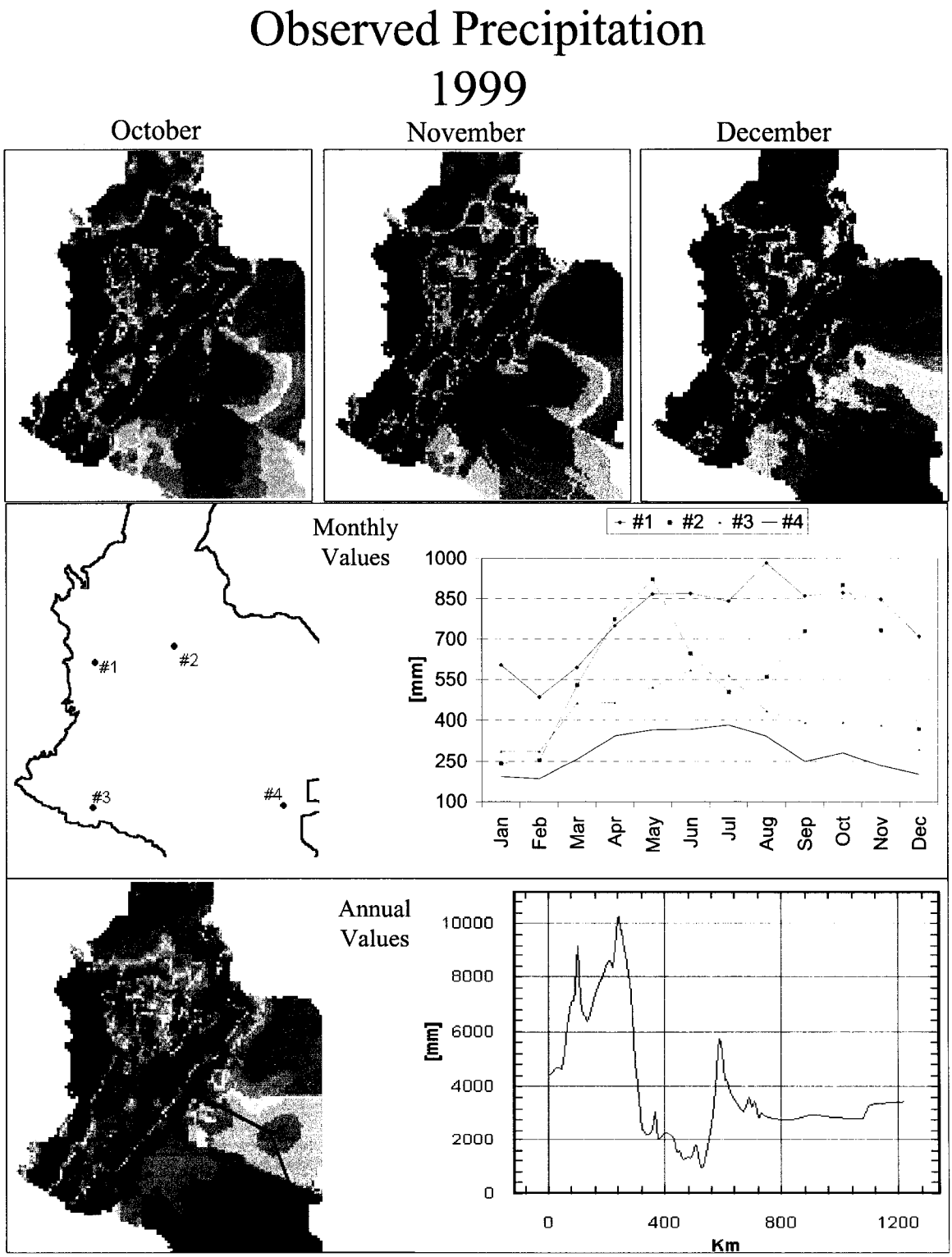

Figure 6-16: GOES Precipitation Index (GPI). Plots illustrate values from January through December of 1999 in mm.

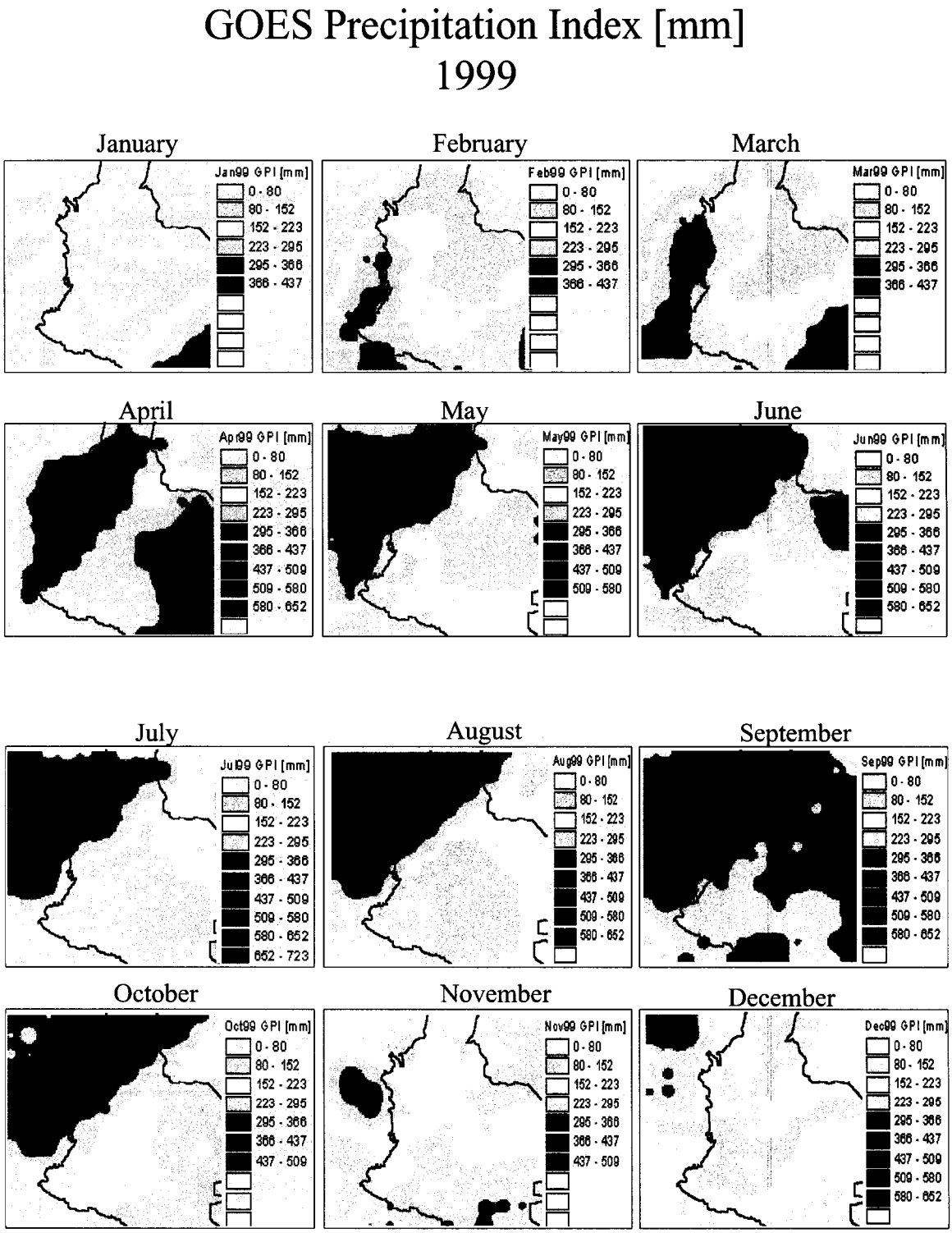

7 SEASONAL SIMULATION – January-June of 1989 and 1992

Colombian climate is basically characterized by two main seasons; in general, there is a dry period between December and April, commonly referred to as summer, and a wet period between May and November, commonly referred to as winter. Major differences between these two seasons are wind velocities and amount of rain, both of them directly dependent on the presence and activity of the Intertropical Convergence Zone (ITCZ) in the region. However, as expected, there are important regional variations that require a more detailed description; for example, throughout the Andes mountains, the annual rainfall presents a bimodal distribution with two wet seasons, from mid March to May and from October to mid December, and two dry seasons, from mid December to mid March and from June to September. Even though this intra-seasonal variability is very important, year-to-year fluctuations of rainfall in Colombia are even more dramatic during ENSO episodes. Accurate predictions of these variations, with lead times of at least six months, would help alleviate their negative impacts. Even a simple categorical forecast indicating whether upcoming seasons will be anomalously wet or anomalously dry would help in taking measures to mitigate potential economic and societal impacts, especially related to the agricultural and hydro-electric power sectors of the economy.

As is well known, ENSO phases are normally characterized by two related phenomena: 1) the development of sea surface temperature anomalies in the tropical Pacific ocean called El Niño/La Niña (EN) and 2) changes in atmospheric circulation driven by anomalies in the pressure gradient between Tahiti and Darwin, called the Southern Oscillation (SO); the warm/cold phase is associated with positive/negative temperature (i.e., EN) anomalies and negative/positive pressure gradient (i.e., SO) anomalies. Accordingly, there are strong macro scale anomalies that could be captured by a limited-area or a regional climate model resolving mesoscale features as RAMS may do. Thus, one of the main objectives of these simulations is to examine the capabilities of the CSU-RAMS to simulate observed spatial and temporal (i.e., monthly) climate patterns in Colombia as driven by cold and warm ENSO phases, and then to determine its

ability to differentiate between a dry and a wet year in Colombia when the model is forced by macroclimate variables. The analyses in this chapter focus on precipitation taking into account that, as shown in Chapter 6, the variation in climatologic and hydrologic variables other than rainfall is minimal.

The years 1989 and 1992 were chosen because they are generally recognized in the scientific literature as years with cold and warm ENSO episodes, respectively. Specifically, the 1992 warm ENSO episode is considered as one of the strongest such phenomena in the last century.

In order to carry out these simulations, the CSU-RAMS modeling system was implemented in a two-grid domain configuration. The model was set up in the same manner as for the annual simulations presented in Chapter 6. That is, initial conditions, boundary conditions, and optional model parameterizations were identical to those used for the full 1999-year simulation. The only difference comes from the specific data used, in this case using data from January to June of 1989 and from January to June of 1992. See chapter 6 for a detailed description of the grid domain configuration and other options of the simulation.

7.1 Precipitation Simulation Results

Cumulative precipitation results for one moth (January), three months (January-March) and six months (January-June) are analyzed. Plots are prepared from both simulations, 1989 and 1992, and from observed data. In addition to graphical comparisons between simulated and observed precipitation, comparisons are also made based on actual differences between both simulations and between simulated precipitation and the observations.

7.1.1 One-month precipitation

Figure 7-1 shows simulated precipitation for January of 1989 and 1992. Both simulations produced the same spatial pattern of precipitation but cumulative amounts are quite different for some regions. In general, both simulations have two well differentiated regions; large amounts of precipitation occur in western Colombia, whereas the central

and eastern sections of the country do not show significant amounts. In addition, the western section of Colombia exhibits great spatial variability, which seems to be associated with interactions with the western branch of the Andes ranges; specifically, in this region there are two zones of high precipitation: one located in the center and the other in the south of the Pacific coastal region of Colombia. Both zones of large amounts of precipitation are located in or close to the west flank of the western range of the Andes. Furthermore, in central Colombia, going from southwest to northeast, there are a few other local areas with significant precipitation accumulations; these areas are located in or close to the east flank of the Andes. Focusing on the maximum amounts, although some areas in the southwest show precipitation amounts reaching 1250 mm in the January 1989 simulation, the simulation of January of 1992 has one much smaller area located in the same region but reaching no more than 992 mm of precipitation.

With respect to precipitation amounts, the simulation for January of 1992 produces a drier month in the Andes region than the January 1989 simulation. Major differences are concentrated in the western territory. Specifically, these differences are more evident in zones with high precipitation amounts, e.g., while the central west zone of high precipitation shows a large area with precipitation amounts reaching around 985 mm for January of 1989 (see Figure 7-1 upper plot), the same zone just shows a small area reaching around 600 mm for January 1992 (see Figure 7-1 lower plot). Something similar happens in the southwest zone; both simulations produced the largest precipitation amounts in this zone. However, it is clear that the simulation for January of 1992 not only produced less precipitation but also that the areas of maximum precipitation amounts are much smaller than their counterpart in the simulation for January of 1989. Finally, with respect to the rest of the country, there are no major differences between the simulations.

7.1.2 Three-month precipitation

Figure 7-2, upper and lower plots, shows simulated cumulative precipitation for the periods January-March of 1989 and January-March of 1992, respectively. As for the month of January, both simulations produced the same spatial pattern of precipitation, but the cumulative amounts are quite different. In general, there is great spatial variability in

the entire Andes region. Those zones with the highest amounts of precipitation in the one-month simulation continue to be zones of maxima after two more months of simulation but the difference between amounts of precipitation for 1989 and 1992 is more pronounced. That is, the Andes region continues to become less wet in 1992 results. After three months, simulation differences in the eastern sections of Colombia seem to be more appreciable; while results for 1992 show a large region in the southeast reaching values around 300 mm, results for 1989 show values around 200 mm for the same region. This means that the 1992 simulation produces wetter conditions over the east and southeast regions of the country and much drier over the rest of the country. With respect to maximum values, while the January-March simulation of 1989 produces one area located in the southwest reaching around 4630 mm and a large zone in the central-west section reaching around 4265 mm, the same zones in the January-March 1992 simulation reached no more that 2325 mm and 1500 mm, respectively.

Focusing on precipitation amounts, the simulation for January-March 1992 produces a drier Andes region than the January-March 1989 simulation. Again, major differences are concentrated in the western region, and as before, these differences are more pronounced in zones with high precipitation, e.g., while the central-west zone of high precipitation shows a large area ranging from 2500 mm to 4265 mm of cumulative precipitation for January-March 1989 (see Figure 7-2 upper plot), the same zone only shows a small area reaching around 1300 mm for January-March 1992 (see Figure 7-2 lower plot). Similarly, in the southwest, both simulations reached the highest precipitation values in this zone. However, it is clear that the 1992 simulation not only produced less precipitation but also that the area with high values is much smaller than its counterpart in the simulation for 1989. In northern Colombia near where the Central range ends, there is also an area showing appreciable differences, however, no appreciable differences are produced over the rest of the country.

Quantifying the spatial distribution of these differences, Figure 7-4 upper plot shows magnitude differences (in mm) between the simulated cumulative precipitation amounts at the end of three months for 1989 and 1992. Positive differences indicate greater precipitation amounts for 1989. Positive and negative differences divided the country in two regions separated by the eastern branch of the Andes mountains; positive

differences (i.e., wetter 1989) are distributed over the north and west regions of Colombia, whereas the negative differences (i.e., drier 1989) are distributed over the south and east regions of the country. The largest positive differences are concentrated in the Andes Mountains and northern Colombia; most of the negative differences are concentrated in the low land regions (Llanos and Amazon regions) and over an isolated zone located in the north of the Pacific coastal region.

7.1.3 Six-month precipitation

Figure 7-3, upper and lower plots, shows simulated cumulative precipitation for the periods January-June 1989 and January-June 1992, respectively. As for the one-month and three-month simulations, the six-month simulations produced the same spatial pattern of precipitation for both years. Cumulative amounts are quite different and even more pronounced than in the three-month simulations. Characteristics highlighted for the one-month and three-month simulations are still valid for the six-month simulations. With respect to maximum precipitation amounts, although the January-June simulation of 1989 presents a few areas located in the western section of the country reaching precipitation amounts around 8500 mm, the same zones in the January-June 1992 simulation reached no more that 5500 mm.

Focusing on precipitation amounts, while there is a considerable difference in those zones where the largest precipitation amounts occur, the rest of the country shows values of precipitation within similar ranges. For example, Figure 7-3 shows that the areas with precipitation amounts less than 500 mm are very similar in both simulations. However, there is a major difference in the southeast region where the 1992 simulation shows a large area ranging between 500 and 800 mm that does not exist in the 1989 simulation. Areas with precipitation amounts ranging between 800 and 1400 mm are relatively similar in both simulations; the largest amounts of precipitation also occur over the same areas in both simulations, although amounts for 1989 are much higher. In order to quantify the spatial distribution of these differences, Figure 7-4 lower plot shows the magnitude of the differences (in mm) between six-month cumulative precipitation for 1989 and 1992. Positive differences indicate greater precipitation amounts for 1989. As in the three-month simulations, positive differences are concentrated in the Andes

Mountains, and most of the negative differences are concentrated in the low land regions (Llanos region). However, at this stage of the simulation, a large zone with negative differences appears in northern Colombia that is not present in the three-month differences, and areas close to the foothills of the east flank of the Andes increase their negative differences.

7.2 Observed versus simulated precipitation for 1989 and 1992

Table 7-1 shows the maximum values of observed and simulated precipitation obtained for both periods. Identifying the magnitude of the maximum values of precipitation obtained by simulation (e.g., peak values) and making associations between corresponding macroclimatic indices for both phases of the observed ENSO phenomenon could lead to a potentially useful indicator to classify a given year as wet or dry. Additionally, it is very important to make a comparison between observed and simulated maximum values in order to determine how accurate simulated values may be, especially for further purposes as planning and operation of water resource systems in a specific region.

Table 7-1: Difference between maximum amounts for simulated and observed data.

Observed data			**Simulated data**		
1989 (1)	**1992 (2)**	**[(1)–(2)]/(1) %**	**1989 (3)**	**1992 (4)**	**[(3)–(4)]/(3) %**
January			**January**		
1815	985	46	1250	992	21
January - March			**January – March**		
4265	2160	49	4630	2325	50
January - June			**January – June**		
9382	5510	41	8500	5517	35

Simulated values in Table 7-1 are of the same order of magnitude as the observed values for each one of the three periods shown. For example, while the maximum observed cumulative precipitation for January-June is around 9400 mm in 1989, simulated amounts reached a maximum of 8500 mm for the same year in the same period. Similarly for 1992, both observed and simulated amounts are around 5500 mm.

Analyzing 1989 versus 1992, the largest differences for both observed and simulated data show that simulated data reproduced quite well the observed differences.

In order to make comparisons between differences in the spatial distributions of precipitation, an index of normalized differences (ID) was computed not only for observed but also for simulated cumulative values in two periods, January-March and January-June of 1989 and 1992, as follows.

$$ID = \frac{(1989\_value - 1992\_value)}{1989\_value}$$

This index is evaluated for every pixel with positive amounts of precipitation. Positive values of the index correspond to 1989 precipitation amounts greater than for 1992.

Figure 7-5 shows the spatial distribution of the index for the period January-March. The upper plot of this figure shows ID results for observed values, and the lower plot shows ID results for simulated values. The white squares in the upper plot indicate the locations of the gauges. Because of the relatively small number of gauges used to generate the observed plot, any inferences made from the observed spatial distribution of the index should be evaluated carefully and the analysis must concentrate on those regions where number and density of gauges are relatively high, as in some areas of the Andes region. The spatial distribution of the index based on simulation results (lower plot) shows two well-differentiated regions such that positive differences are concentrated in the northwestern section of the country and negative differences in the southeastern section (notice that black color shows a positive index). Although observed differences also exhibit two well-differentiated regions, these are regions not completely similar to those produced by the simulations. Concentrating only on the Andes regions where the number and density of gauges are larger, it is clear that simulated precipitation matches considerably well observed precipitation. Simulation results for the Andes region reproduce quite well the observations corresponding to cold and warm ENSO episodes. This means that, at the end of a three-month simulation period, the model precipitation results reproduce well the spatial distribution of observed precipitation differences between a dry and a wet Colombian year.

Figure 7-6 shows the spatial distribution for the period January-June. The upper plot shows ID results for observed values, and the lower plot shows ID results for simulated values. Simulation differences show that positive values are concentrated in the Andes region, while this is not totally clear for observed values. Although most of the positive differences for observed values are in the Andes region, there is a large area in the western and central ranges with negative values.

Nothing can be said for the Amazon and the Llanos regions because of the almost complete absence of gauge stations available there. As the plot of observations shows (i.e., upper plot in Figures 7-5 and 7-6), there are only around a dozen stations along and near the east flank of the Eastern range of the Andes and only one or two in southeastern Colombia. However, making an inference even from this small number of stations, it seems that the southern portion of the Llanos region and the Amazon region had more rainfall in 1992, therefore exhibiting a different relationship with the ENSO phenomenon than that exhibited by the Andes region. From these simulations it is totally clear that these regions had more precipitation during the 1992 episode. Accepting these results as valid, they imply that the warm phase of ENSO leads to increases in precipitation amounts in the Llanos and Amazon regions. In addition, Figure 7-6 seems to indicate that the Andes region is the region more affected by rainfall deficits during the warm phase of ENSO. The Pacific region shows a large area with large precipitation increases during this phase.

7.3 Discussion

Simulation results exhibit very well what is expected in the Colombian Pacific region. Along this region there are centers of higher precipitation with localized points presenting large precipitation values, and this is the pattern for both simulated years. Both simulations display fairly similar spatial and temporal distributions of precipitation for the period simulated. More pronounced differences between both years are concentrated in these centers of higher precipitation. For instance, for 1989, at the end of the first, third, and sixth month of simulation, the model precipitation results reproduce larger maximum values than for 1992 simulation.

The comparison between simulated results for 1989 and 1992 clearly highlighted the main difference between both ENSO phases. This comparison shows that the warm phase of ENSO, which corresponds to the year 1992, leads to a generalized decrease of precipitation along the Andes ranges. In addition, these simulated results in conjunction with the scarce observed data show that, during a warm ENSO phase, the low lands of Colombia get more precipitation than during a cold ENSO phase. In this order of ideas, there is a large area in the Pacific region and some local spots in the Caribbean region also showing more precipitation during 1992.

The above behavior explains why the Colombian hydroelectric power system was deeply affected by the 1991-1992 event. Taking into account that the main hydroelectric power projects of Colombia are in the Andes region, the results of these simulations are in perfect agreement with observed ENSO effects. On the other hand, observed precipitation data seem to verify what simulated data are showing; even though the number and density of gauge stations are not sufficient to describe well the observed spatial distribution of precipitation, the available observations show that during the warm event, Colombia does not have a generalized deficit of precipitation and that in the low lands there seem to be increases in precipitation.

In one way or another, it cannot be forgotten that the major industrialized zones in Colombia are located in and around the triangle formed by the cities of Bogotá, Medellin and Cali, and that a large fraction of the area of this triangle is located in the Andes region. It is for this reason that, in societal and economic terms, Colombia has a generalized deficit of precipitation during the ENSO warm phase. In a global sense, this is true because what affects the main industrialized areas affects Colombia as a whole.

In summary, these results show the great potential of using this modeling tool for regional climate forecasting for at least one season ahead in Colombia. As expected, the spatial distribution of precipitation in Colombia is highly dependent on the local circulation processes generated by the conjunction of macroclimate circulation with the complex surface features present in the region. Using this methodology has the advantage of determining the effects of macroclimatic phenomena and general climatic circulation on the regional and local hydro-climate system of Colombia. These

simulations show correspondence between a warm ENSO year and decreased precipitation in the Andes region. This result is very important, especially because of the complexity of the processes occurring in this region, including the fact that the region itself generates important local atmospheric circulation of its own, acts as a barrier that interferes with the trade winds, and produces complex thermally driven circulations resulting from differential heating due to the variability in the absorption and emission of the short and long-wave radiation.

As a final comment, it is important to say that simulation results for the mountains and valleys seem unbalanced when compared with observed data. There seems to be explosive production of rain leading to excess precipitation at some points in or close to the mountains, whereas the valleys regions show deficit when compared to observations. However, the general pattern of precipitation is reproduced reasonably well to serve as a criterion to qualify deficit or surplus rainfall in an area.

Figure 7-1: Upper plot shows simulated cumulative precipitation for January 1989 (mm). Lower plot shows simulated cumulative precipitation for January 1992 (mm).

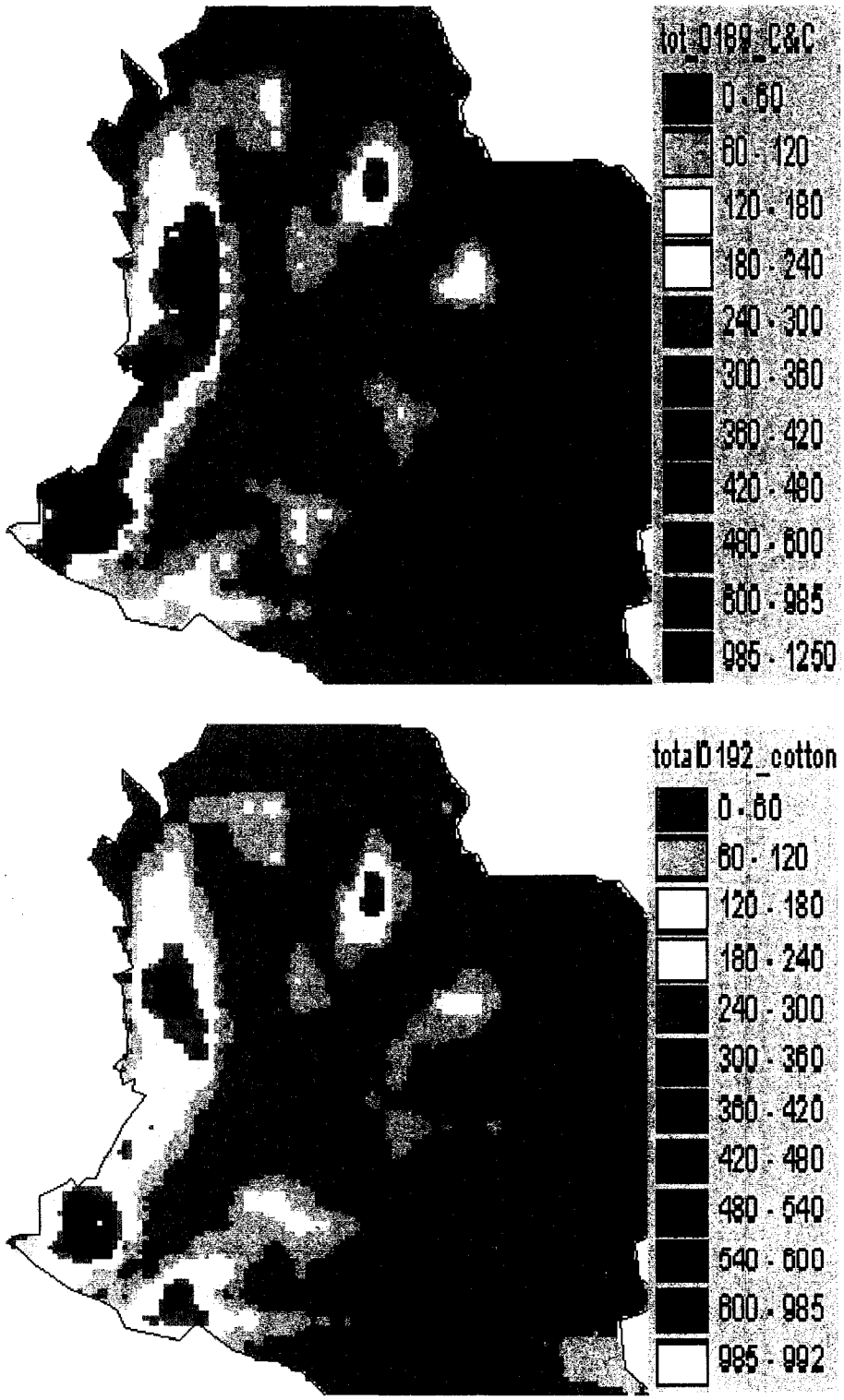

Figure 7-2: Upper plot shows simulated cumulative precipitation for January-March 1989 (mm). Lower plot shows simulated cumulative precipitation for January-March 1992 (mm).

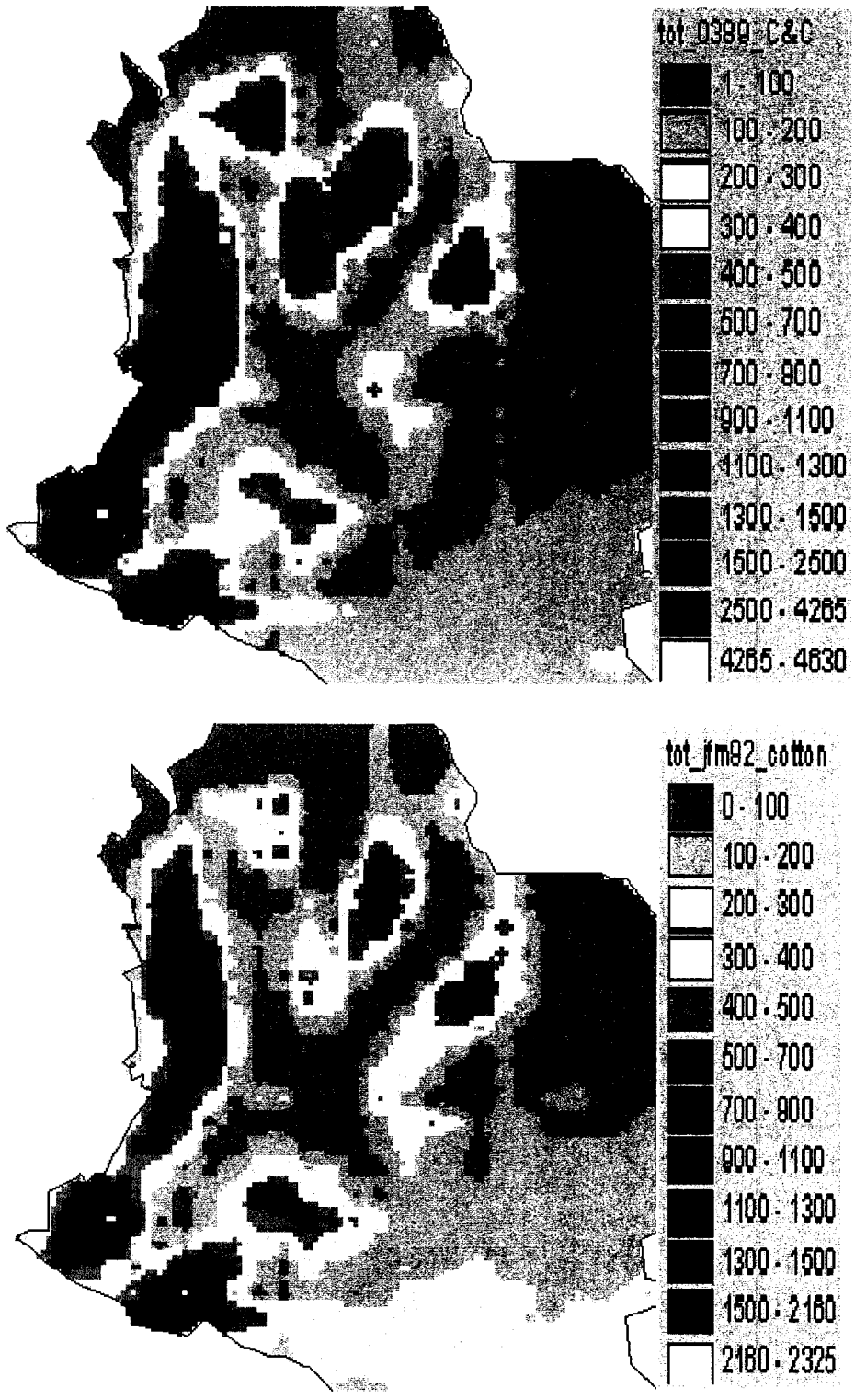

Figure 7-3: Upper plot shows simulated cumulative precipitation for January-June 1989 (mm). Lower plot shows simulated cumulative precipitation for January-June 1992 (mm).

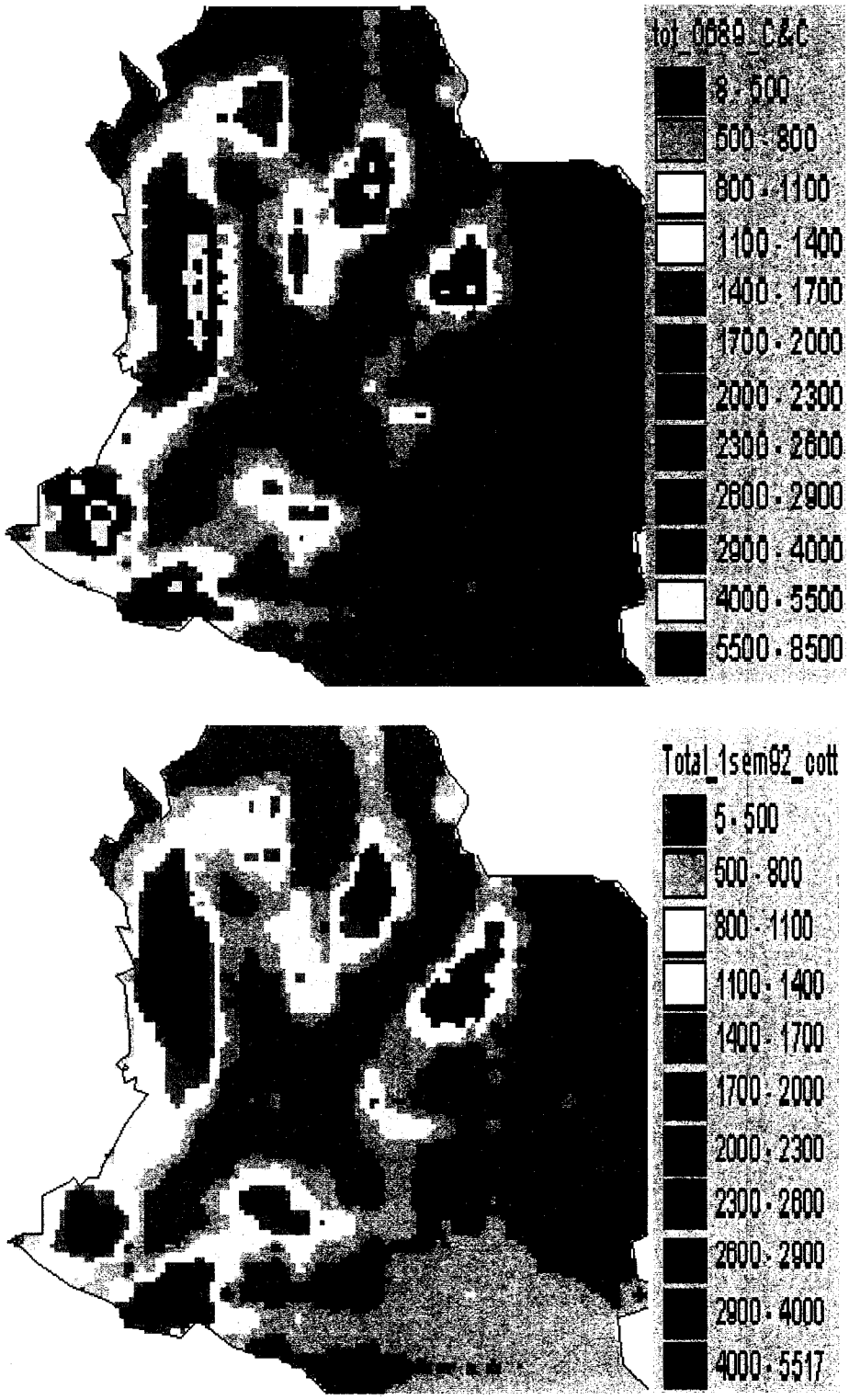

Figure 7-4: Differences in simulated cumulative precipitation between results for 1989 and 1992. Upper plot corresponds to January-March period, and lower plot corresponds to January-June period. Values in (mm).

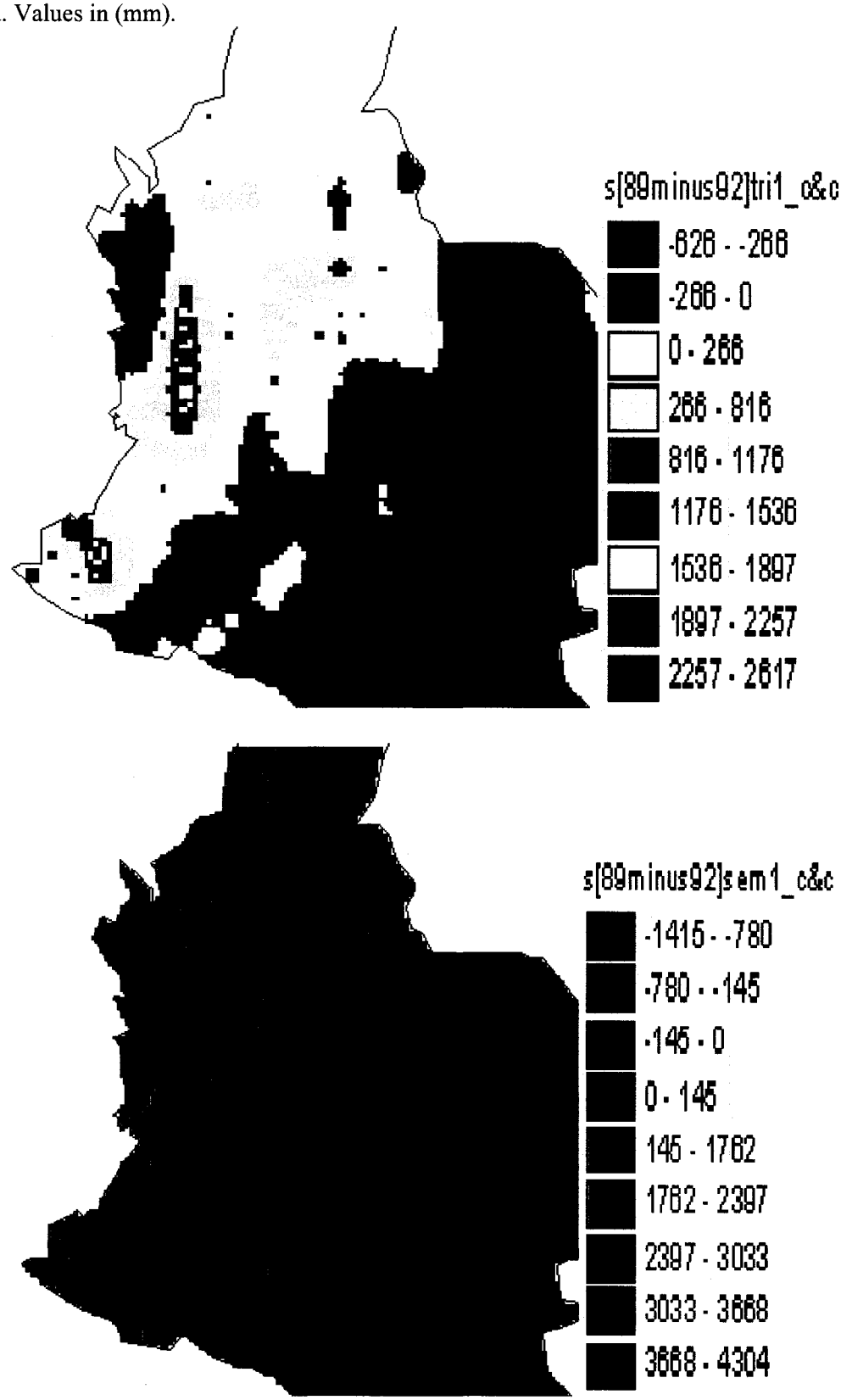

Figure 7-5: Normalized precipitation differences evaluated as $Id = \frac{(1989\_value - 1992\_value)}{1989\_value}$. Upper plot corresponds to the cumulative observed January-March and lower plot to the cumulative simulated January-March period.

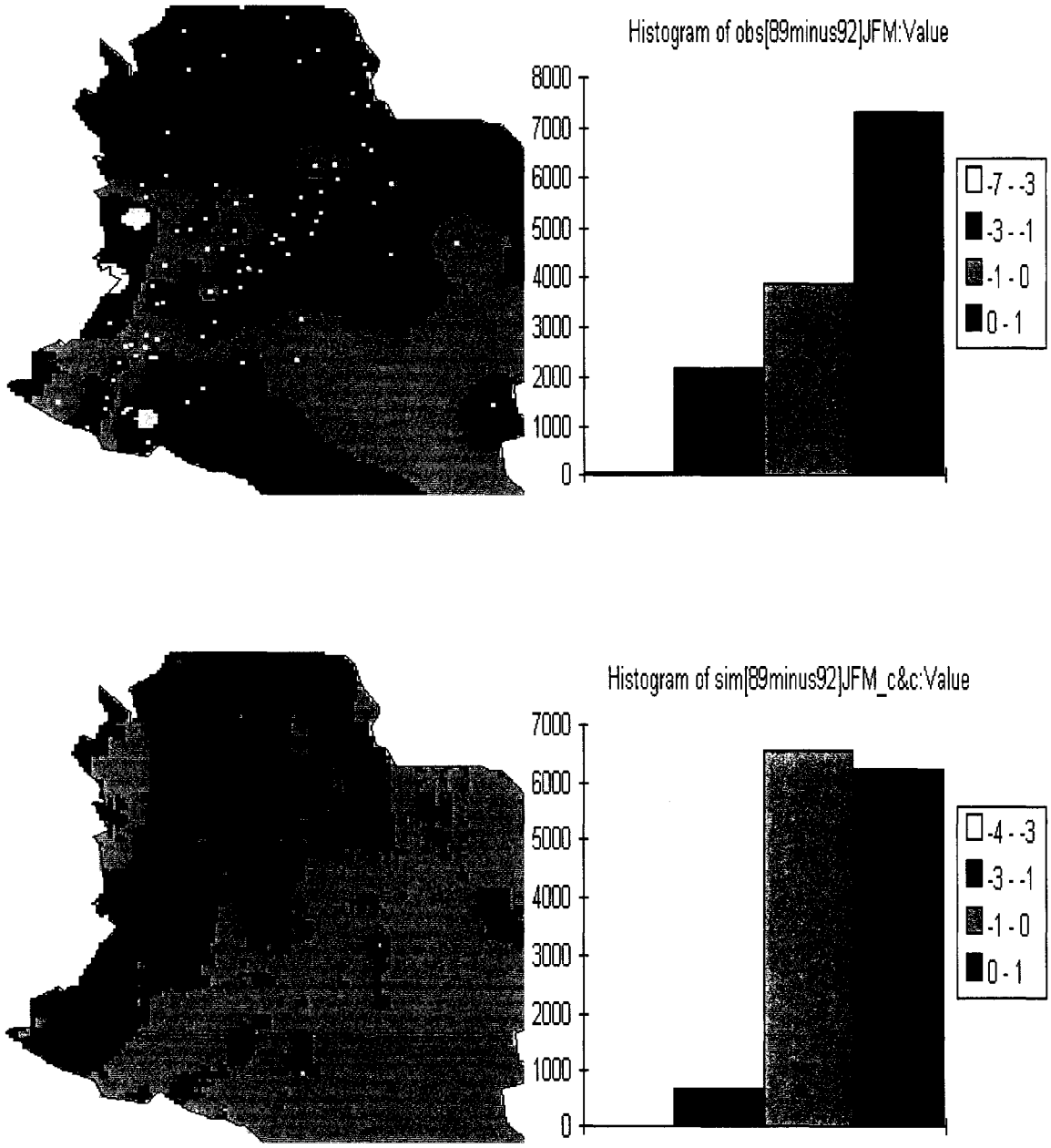

Figure 7-6: Normalized precipitation differences evaluated as $Id = \frac{(1989\_value - 1992\_value)}{1989\_value}$. Upper plot corresponds to the cumulative observed January-June and lower plot to the cumulative simulated January-June period.

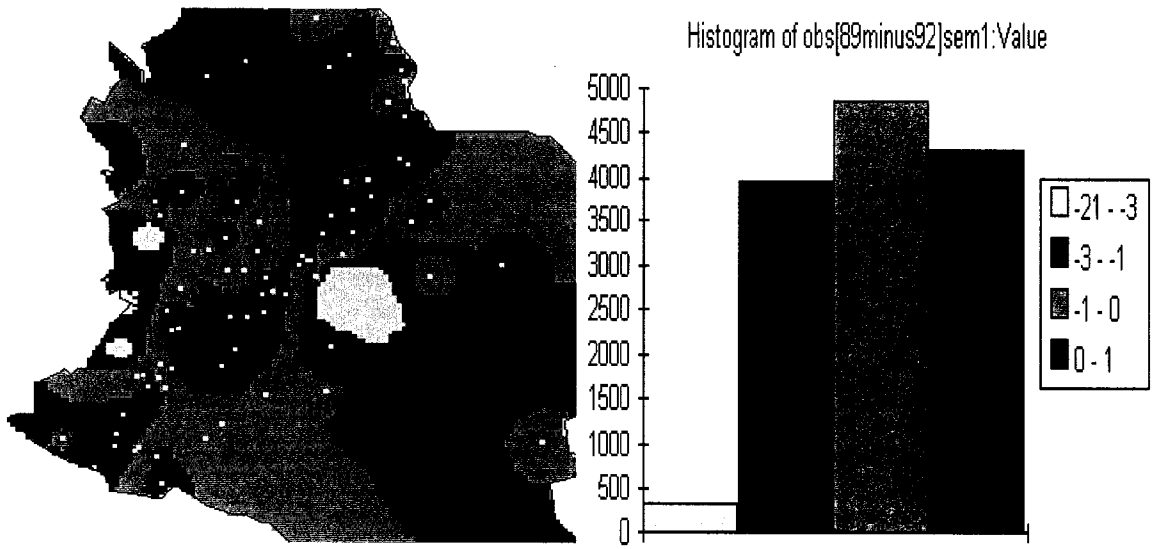

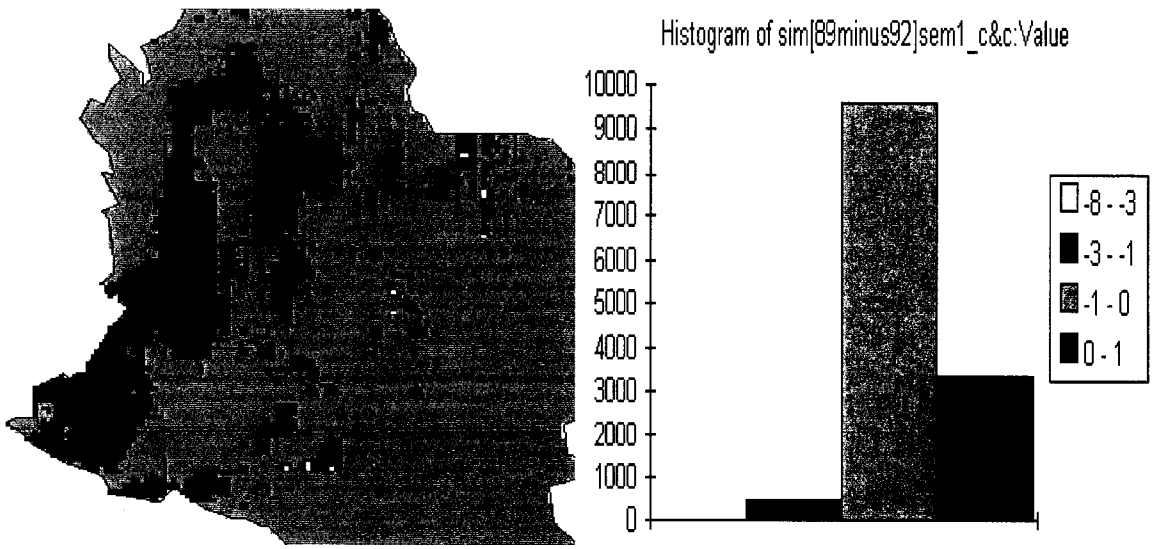

8 DAILY SIMULATIONS

While daily oceanic tropical rainfall and cloudiness are well defined by the dynamics of the ITCZ, in continental areas land-atmosphere interactions play a major role in weather variability and its associated temporal cycle. The dominant physical processes of the region should define the diurnal variation of rainfall over land. These in turn depend on the physical geography of the region (e.g., high plateau, low lands, coast, mountains, etc), and the characteristics of the general circulation delineated by its geographical position. Complex topography may locally change the tendency of the general circulation serving as a barrier and as a channel to generate local circulations that create a particular regional pattern. This is the case of Colombia where the Andes mountain range splits into three longitudinal branches that act as a barrier to the surface trade winds and forming two large avenues, the Magdalena and Cauca river valleys, that trap moist air and eventually produce rainfall along the slopes and in the valleys themselves.

Mapes et al. (2002a,b) and Warner et al. (2002) studied the physical processes responsible for the diurnal cycle of rainfall in northern South America with emphasis on the Panama Bight and the Pacific Littoral of Colombia. Their review helps explain some commonly observed patterns in this region as the afternoon maximum of rainfall over lands driven by small convective systems and the nocturnal maximum of rainfall observed in the large valleys of the Andes. On the other hand, Snow (1976) makes a few generalizations about the diurnal rainfall pattern in the Colombian Andes. These patterns may be summarized as follows: (a) maximum rainfall occurs at intermediate elevations with nocturnal maximum in the low lands, (b) afternoon maximum near or above 1000 m, (c) valley rainfall normally at night and (d) slope or altiplano rainfall (as in the Bogota city region) during the day time.

Studies have shown that models, especially global models, have difficulties in capturing the phase of the observed diurnal cycle of convection. Model results are strongly dependent on the particular parameterizations of cloud and cumulus convection

processes. Therefore, radiation and convective parameterization schemes should be appropriately determined considering major synoptic forcing that may initiate rainfall development. Common observed disagreements are that simulated deep convection may appear several hours earlier than observed deep convection, and often the amplitude of the simulated cycle is too weak. See for example Randall et al. (1991), Timothy et al. (1999), Lin et al. (2000), and Yang and Slingo (2001). Because the energy and water budgets are strongly influenced by the diurnal cycle of deep convection, it is of paramount importance to properly simulate the observed diurnal cycle of convection. Therefore, of particular interest is the role that diurnal forcing plays in determining the variability and mean climate of the region.

The main objective of this chapter is to examine whether or not the CSU-RAMS modeling system is able to capture the diurnal cycle in a specific region of Colombia. The region of analysis is located in the Andes with most of the area of interest placed in the Central cordillera and characterized by an extremely complex relief (See Figures 8-1 and 8-2, finest grid). Consequently, the CSU-RAMS modeling system is implemented in a four-grid nested configuration as explained below, ensuring that the interactions between large-scale general circulation patterns and local surface features, in particular the complex relief, are adequately captured. Additionally, the resolution of the finest grid to be used for the RAMS model should be small enough to guarantee a representation of the topography with sufficient detail to incorporate the significant impact of local relief.

Four successively nested grids over a specified limited area are used in order to scale down consistently NMC-NCEP-NCAR reanalysis to the size scales of interest that will capture the local circulation. The two coarsest grids are centered over Colombia at 5°N of Latitude and 75°W of Longitude. The coarsest grid is composed of 28 x 28 grid-points with a 160 km cell size; the second grid is composed of 34 x 34 grid-points with a 40 km cell size; the third grid is centered over Colombia at 5.18°N of Latitude and 75.361°W of Longitude, and composed of 50 x 70 grid-points with a 10 km cell size; and the finest grid is centered over Colombia at 6.575°N of Latitude and 75.136°W of Longitude, and composed of 54 x 62 grid-points with a 2.5 km cell size. In the vertical direction, this implementation considers 8 soil levels, 22 atmospheric levels for the coarsest grid and 29 levels for the other three grids. The vertical grid spacing of the

lowest atmospheric level on the domain is 250 m for the coarsest grid. Above this level the vertical grid spacing is increased at a rate of 20% until reaching a spacing of 2000 m, which is set as the maximum vertical grid spacing permitted. Once this maximum is reached, the vertical grid spacing is kept constant. Vertical nesting is used in the five lower levels of the coarsest grid to get a smaller height of the lower vertical levels in the other grids. Therefore, the first two lower levels of the coarsest grid are split into three levels each and the following three levels into two levels each. As a result of this nesting, the vertical grid spacing of the lowest atmospheric level is around 80 m for the last three smaller grids. A time step of 120 seconds is used with the coarsest grid. For the other grids, the time step is reduced using a ratio 1:3, successively. Table 8-1 summarizes the main characteristics of the four nested grids, including geographic location and dimensions. Figure 8-1 shows the finer grid embedded in the coarser grid successively.

Two simulations are performed. One simulation focuses on the period September 25 to 30 of 1998. For this simulation, the two coarser nested grids are integrated from January 1 at 0:00 hours to September 25 at 0:00 hours UTC time, at which time the two finer nested grids are activated and the four-nested grid configuration is integrated for five additional days, from September 25 at 0:00 hours to September 30 at 6:00 hours UTC time. The other simulation focuses on the period February 1 to 8 of 1999. For this simulation also, the two coarser nested grids are integrated from January 1 at 0:00 hours to February 1 at 0:00 hours UTC time, at which time the two finer nested grids are activated and the four nested grid configuration is integrated for 8 additional days, e.g., from February 1 at 0:00 hours to February 9 at 6:00 hours UTC time. Each nested grid takes its boundary condition from the adjacent larger domain and the largest domain with the coarsest grid-size of 160 km is forced with 6-hourly NMC-NCEP-NCAR data. Results focus on a specific area in the mountains extending south-north where the diurnal cycle will be modulated by orography, surface heating patterns, and mountain wind flow behavior.

8.1 Boundary data, initial data and main parameterization

Initial conditions, boundary conditions, and physical parameterizations are as implemented in the full 1999-year simulation of Chapter 6, but using the data

corresponding to the two specific periods of interest here. For precipitation, the convective parameterization is deactivated for the two finer grids while the bulk microphysics parameterization, including cloud water, rain water, pristine water, snow, graupel and hail (Piotr et al., 1989), is activated. For cloud water, the total cloud droplet number concentration (number per kg of air) is specified directly and the mean diameter is automatically diagnosed from this concentration and the estimated mixing ratio. For rain water, pristine water, snow, graupel and hail, a prognostic equation for droplet number concentration is used, and a special array for this quantity is added, and the average droplet diameter is diagnosed from the prognosed mixing ratio and number concentration. The concentrations of cloud water, rain water, pristine water, snow, graupel and hail are assumed to follow a gamma distribution where the shape parameter guarantees that the size distribution peaks at a positive diameter.

Figure 8-2 shows the topographic features as represented on the two finer grids. These plots represent an approximation of the actual topography as it is used by CSU-RAMS; the upper plot corresponds to the approximation on the third grid and the lower plot corresponds to the approximation on the finest grid. See chapter 6 for a detailed description of the grid domain and other options of the simulation.

In order to give a better idea of the characteristics of the area represented in the finest grid, a brief description follows. Even though the area enclosed in this grid is relatively small (a little more than 20000 km^2), it has a complex relief and large spatial and temporal climate variability.

The finest grid is located in central eastern region of the Antioquia Department (see Figure 8-3, upper plot), with all of the area in the Central Range of the Andes. The geography of Antioquia includes every clime and landscape characteristic of Colombia and the specific area in the finest grid includes plains, savannas, lakes (natural and artificial reservoirs), jungles, rivers, mountains, and canyons. Elevations ranging from 100 m to 3100 m above sea level are found because of the complex topography in this area. The climate in the Central range is characterized by a dry west slope with about 1000 mm of precipitation per year and an average temperature of 27 °C, wet altiplanos with 1700 mm per year, and a wet east slope with 2700 mm/year and an average

temperature of 23 °C. Vegetation is classified as Andino and Sub-Andino Forest. Soils are deep to moderately deep, limited by the phreatic boundary, gravels, stones, and some zones with rocky blooming. Soils are generally well drained, originating from igneous rocks, volcanic ash, and river alluvium. Main activities of the region are mining, agriculture and cattle business (IGAC, 1990). In addition, in this region, there exist large hydroelectric power developments .

In the southwest section of the area is the Aburra Valley, a long and narrow valley with general orientation in a southwest-northeast direction (Figure 8-2, lower plot). The source of the Medellin-Porce River is located in this valley and an important hydroelectric power development (the Riogrande - Porce hydroelectric development) is located in it. The city of Medellin, capital of the Antioquia Department, known as the city of flowers or the city of eternal spring, is located in this valley. Medellin is at an average elevation of 1500 m above sea level, and has a temperature ranging from 20 to 28 °C, and receives 1500-2000 mm of average precipitation per year. The Rionegro Altiplano, source of the Nare river, is located 40 km east from the Aburra Valley. One of the largest hydroelectric power developments in Colombia is located in the Nare river basin (see figure 8-3, lower plot.)

The Nare–Guatape hydroelectric power development consists of four hydroelectric projects: Guatapé with an installed capacity of 560 MW, Jaguas with an installed capacity of 170 MW, Playas with an installed capacity of 200 MW and San Carlos with an installed capacity of 1240 MW. The Nare river has an annual average discharge of around 50 m^3/s, the Guatape river has an annual average discharge of around 32 m^3/s. Precipitation on the watershed has a large spatial variability ranging from 1500 to 4000 mm per year. The last destination of the discharge of this system is the Magdalena River.

The Riogrande-Porce hydroelectric power development consists of two hydroelectric projects: Riogrande with an installed capacity of 300 MW and Porce II with an installed capacity of 400 MW. The Riogrande river has an annual average discharge of 34 m^3/s, and the Porce river has an annual average discharge of 75 m^3/s. Precipitation on

the watershed ranges from 1500 to 3000 mm per year. The last destination of the discharge of this system is the Cauca River.

The temporal distribution of precipitation in the region of the smallest grid is bimodal, with two wet periods intercalated with two dry periods. The first wet period occurs between March and May and the second one occurs from September to November. Periods with less rain occur at the beginning and in the middle of the year. The spatial distribution of precipitation is very variable with some places receiving less than 1500 mm/year in the western part of the region, and areas receiving more than 4000 mm/year in the central south and central north of the region close to the Guatape project.

8.2 Results

Based on the fact that the seasonal simulations by RAMS showed an acceptable spatial representation of Colombian climate as inferred from analysis of results of the finer grid (40 km cell size, see chapters 6 and 7) of that simulation, analysis of results of these additional simulations will focus only on the two new grids added to the domain. The main emphasis of these analyses is to determine whether the improved representation of the relief resulting from the reduction of the grid size used to model the precipitation process (a grid size approaching the size recommended for use with the bulk microphysics parameterization), together with the implementation of 4 grids (as opposed to only 2 grids), leads to improvements in the simulation of the local circulation driving the diurnal cycle in this region.

This chapter summarizes results for temperature, pressure, surface winds and precipitation obtained for the finest grid during the period September 25-30 of 1998. For the period February 1-8 of 1999, only precipitation results are presented. Analysis focuses on the diurnal cycle using observations and simulated results over three-hour periods.

8.2.1 Temperature Field

Figure 8-4 shows the behavior of surface temperature for one, two, and three days of simulation, September 25 to 27 of 1998. The left plots correspond to the observed

values and the right plots to the simulated values. Even though observed data were available just from 14 gauges, it is clear that the model replicates well the main characteristics of temperature. As expected, simulated and observed values keep a strong relationship with topographic characteristics and the simulated temperature variation is in good agreement with the observed range. Given the strong correlation between temperature and elevation, it should be expected that the more accurately topography is represented in RAMS, the more accurately RAMS will be able to reproduce the observed behavior of temperature.

Figure 8-5 shows the diurnal cycle of surface temperature during three days of simulation, from September 25 to 27 of 1998. Plots show temperature fields every twelve hours highlighting the diurnal pattern of this variable. Plots at midday (left side of the figure) display increasing temperatures, whereas plots at midnight (right side of the figure) display decreasing temperatures. Focusing on the Aburra Valley, the narrow area with direction southwest-northeast, and on the Southwest area of the region, it is clear that simulated temperature patterns are in agreement with the observed behavior of temperature in the region, and that the diurnal temperature range is less than 10°C, as expected.

As can be inferred from the lower plot in Figure 8-2, the range of variation of elevation in this area is around 3000 m. Figure 8-5, on the other hand, shows a simulated range of variation of temperature between high and low elevations in this area of around 21°C. Consequently, the implied average rate of decrease of temperature with terrain elevation is around 7°C/km.

In conclusion, the diurnal cycle of temperature simulated by the CSU-RAMS system compares favorably with the observed diurnal cycle.

8.2.2 Pressure Field

Figure 8-6 shows the behavior of surface pressure during three days of simulation, from September 25 to 27. Plots show pressure fields every twelve hours highlighting the diurnal pattern. Simulated surface pressure behaves as expected according to the topographic characteristics. The diurnal cycle is almost negligible, with minor variation

in some areas. The range of spatial variation in the area is around 300 mb and it is directly related with the relief, while temporal variation is nearly negligible. Examining Figure 8-2, lower plot, and Figure 8-6, pressure plots closely mimic relief plots, with high pressure in low lands and low pressure in high lands.

8.2.3 Wind fields

Figures 8-5 and 8-6 present results for surface wind fields (vectors) from September 25 to 27. Plots in Figure 8-5 show surface wind fields every twelve hours corresponding to midnight and midday, while Figure 8-6 shows surface wind fields every twelve hours corresponding to 6:00 and 18:00 local hours (for Colombia, local time equals UTC time minus 5 hours), respectively. This implies that these two figures present a sequence of surface wind field every six hours for three days.

The expectation is that the interaction between trade winds and topography actively influences air motions producing local circulations. From these figures it is inferred that, in general, surface wind has a predominant southward component in the eastern section of the area where topography is principally longitudinal. Relief is more complex in the western section of the area, causing a more intricate pattern of the wind field where it is possible to identify areas with dominant wind in all directions. In Figures 8-5 and 8-6, it is observed that surface wind behavior is very uniform during all three days of simulation and winds may be characterized as light with the most active periods occurring predominantly during daylight hours. The most active period seems to be in the afternoon hours, as shown in plots of Figure 8-6 for 18:00 local hour. Additionally, for these active hours, wind has a strong southward component.

As a final comment, vigorous air motion is responsible for the transport of moisture required to produce precipitation in a specific area. Therefore, the better RAMS replicates the wind field, the more accurately the simulated diurnal distribution of rainfall will approximate the observed one.

8.2.4 Precipitation field

Focusing on the diurnal cycle, we consider the volume of precipitation for every three hours during the period of simulation. The emphasis is on the temporal distribution

as opposed to the spatial distribution on the finest grid. This is because the spatial distribution is strongly dependent on the nested grid configuration. It is expected that the average distribution on the finest grid has a strong relationship with the average value on the coarsest grid, which may produce displacement of centers of high concentration of precipitation. Taking into account the fact that the finest grid covers an area slightly smaller than a single cell of the coarsest grid, we will ignore any discrepancies in the spatial location of precipitation within the finest grid.

8.2.4.1 September 25 to 30 of 1998

Figures 8-7 to 8-11 show successively observed and simulated precipitation every three hours for a five-day period starting on September 25 of 1998 at 0:00 local hour. According to the observed precipitation plots, during this period rainfall occurs mainly during the night, between the 18:00 and 6:00 local hours. RAMS results indicate that the model produces precipitation somewhere in the inner domain every time precipitation actually occurred; however, the actual spatial location is not well reproduced. Major discrepancies can be seen on September 29 where simulated data show much more precipitation than observed data. As shown by the observations, simulated RAMS precipitation tends to occur at night but, as expected, the spatial distribution is out of phase. In any case, although simulated precipitation seems to replicate the storms observed during this period, there are some discrepancies in their duration and intensity.

September 25, Figure 8-7: Observed data show temporal concentration of rainfall during the night hours. Largest 3-hourly precipitation volume occurred during the period 18:00 to 21:00 hours, reaching around 93 mm during the three hours. Observed precipitation does not occur in a spatially generalized manner over the entire region, being more concentrated in the southern section during the first hours of the day and in the northern section during the late hours of the day. On the other hand, simulated precipitation shows two periods of maximum 3-hourly rainfall volumes; one between 3:00 and 6:00 and the other between 21:00 and 24:00 hours. The largest 3-hourly volume is around 20 mm and occurs in the last three hours of the day.

September 26, Figure 8-8: Observations show that precipitation occurred at some point in the finer domain almost continuously during this 24-hour period. Early afternoon

is the only period of time with almost no precipitation. The largest 3-hourly precipitation volume occurred the first three-hour period of the day reaching a value of around 35 mm. Otherwise, RAMS simulated precipitation replicates the observations quite well, not only in terms of the temporal distribution but also the spatial distribution. However, the simulated rainfall intensity after midday is much smaller than the observations but, as in the observations, the maximum simulated volume occurs at the beginning of the day with a value of around 33 mm.

September 27, Figure 8-9: Observed data show concentration of rainfall between 0:00 to 6:00, 15:00 to 18:00 and 21:00 to 24:00 hours, whereas simulated data show important amounts of rainfall between 0:00 to 6:00, and 21:00 to 24:00 hours.

September 28, Figure 8-10: Observed data show rainfall during the first 6 hours and then a small area of relatively less intense precipitation of around 10-mm in early afternoon. On the other hand, RAMS simulations produced rain during the first 9 hours of the day, with widely scattered and weak (values no larger than 3-mm) precipitation activity for the duration of the day. For this day, observed and simulated diurnal cycles are in good agreement.

September 29, Figure 8-11: observed data show a dry day characterized by only a few small areas of light precipitation, with 3-hourly accumulations of no more than 10 mm throughout the day. However, and in stark contrast, the RAMS simulation produced precipitation throughout the day with low intensity but more generalized in the region of study.

Considering the complete period as shown in Figure 8-12, we can infer from the observations that a storm that started September 25 in the late afternoon lasted until noon of September 26. The simulated storm started late in the night of September 25 and ended after 9:00 hour on September 26. Therefore, RAMS simulation reproduces this storm well, but the simulated intensity and duration are less than observed. Although the duration of the simulated storm is around twelve hours, the duration of the observed precipitation is approximately twenty-one hours and the observed storm appears six hours earlier in time. Continuing with the analysis of the entire period, observed data show a storm starting September 26 around 18:00 and ending September 27 approximately at

9:00 hours. Once again, the RAMS simulation reproduced this storm but, as for September 25, the simulated storm started a little later than its observed counterpart. The simulated storm evolution started on September 26 around 18:00 hours with light rain, then at about 18:00 hours the intensity increases, and then decreases abruptly at 6:00 hour on September 27, after which precipitation turns to drizzle until 21:00 hours when the intensity increases once again. Once again as for late September 25 and early September 26, RAMS is able to model a storm between late September 26 and early September 27 but with lower duration and intensity. In this case, both simulated and observed data present the maximum intensity between 0:00 and 3:00 hours on September 27.

From the above analysis, the following points may be highlighted in both observed and simulated data: (a) Major precipitation amounts occurred during the night time, e.g., between 18:00 to 6:00 of consecutive days. (b) The period under consideration may be considered as a rainy period with three major storms from September 25 to 28, each one starting during the late hours of the day and ending during the early hours of the following day. Even though the three observed storms are more or less well reproduced by the RAMS simulations, the intensity and duration are lower in the simulations. (c) Major disagreement between observations and simulations occurs for September 29 where the observations indicate a dry day with no precipitation and the model simulates a fairly wet day with precipitation occurring throughout the day. For September 28, while observations show that dry conditions start on September 28 at 15:00 local time and last through September 29, simulated data show a drizzly day.

Figure 8-13 shows a comparison between high intensity values in the area of study. The horizontal axis shows the diurnal cycle from noon to noon every three hours and the vertical axis shows three hours cumulative values for every day of the analyzed period. The observed diurnal cycle, upper plot, verifies that at least for these five days, there is a strong tendency for the maximum in precipitation to occur between 15:00 and 21:00 local hour, and that the rainfall gradually decays in intensity, reaching its minimum value before midday. Definitely, the period 6:00 to 12:00 seems to have the least amount of precipitation with its minimum between 6:00 and 9:00. Figure 8-13, lower plot, shows simulated results. RAMS reproduces the maximum in precipitation between 0:00 and 6:00 local hours, showing a delay of around four to six hours with respect to the observed

data. The lowest high values of rainfall are reproduced around midday, whereas observed data show a gradual increase in intensity after noon. RAMS tends to maintain low high values until 18:00 to 21:00 local hours. Maximum values are not directly comparable, however while observed data correspond to point measurements, RAMS data are more representative of an average over a cell of 2.5 km of size. It is clear that RAMS precipitation exhibits a deficit in precipitation when compared with observed data.

Similar to high intensity values, Figure 8-14 shows a comparison between average intensity values in the area of study. For evaluating these average values, only those stations with observed values and those cells with simulated precipitation amounts greater than zero for the three-hour period are considered. Comments made with respect to Figure 8-13 are applicable to Figure 8-14. Average observed and simulated values over the area of study show less variation than maximum intensity throughout the day. Observed values show that precipitation tends to occur much more during night time hours, before the end of the day (15:00 to 21:00 hours) and at the beginning of the day (0:00 to 06:00), presenting a bimodal distribution in time. As with the observed precipitation, simulated precipitation tends to show more precipitation during night time hours, with much more precipitation between 21:00 and 6:00 but, as opposed to the observations, the simulated precipitation exhibits only a single peak.

Figure 8-15 upper plot shows maximum daily values in the area of study, and the lower plot shows average cumulative daily values. From these figures we can infer that the daily behavior of the model results is in reasonably good agreement with that of the *in situ* observations. From Figure 8-15, upper plot, it is clear that the maximum cell precipitation amounts produced by RAMS do not have a general tendency to be less than the maximum observed values during the whole period. Maximum simulated amounts are lower on some days and higher on others. The average in Figure 8-15, lower plot, is evaluated taking into account only those points (observed values) and cells (simulated values) where precipitation is greater than zero during the three hours period. The simulated average values evaluated in this way compare reasonably well with the observed values, except for September 25 and 29.

In conclusion, RAMS replicates in a reasonable manner the diurnal cycle observed during September 25 to 30 of 1998. The most important points to keep in mind are: (a) Simulated values show deficit of precipitation of around 40%. (b) RAMS seems to show a delay (phase shift) in reproducing precipitation of around four to six hours. (c) Definitely, the general characteristics of the diurnal cycle are well replicated by RAMS with a strong tendency to have a concentration of precipitation during night hours and minimum values around midday.

8.2.4.2 February 1 to 8 of 1999

Figures 8-16 to 8-17 show successively observed and simulated precipitation every three hours for the eight-day period starting on February 1st of 1999 at 0:00 local hour. Based on observed precipitation plots, this 8-day period may be classified as dry with only brief episodes of precipitation of low intensity during the local afternoon and night hours.

A plot of the observations, Figure 8-16 (upper plot) shows a short storm starting during the night time on February 1 and ending February 2. The hours between 9:00 and 18:00 hours on February 1 are dry followed by a short storm starting at around 18:00 and ending February 2. The figure also shows that there are several areas with drizzle occurring after midday on February 2, 3 and 4. Simulation results (lower plot) do not reproduce the storm starting before midnight on February 1 and show that the period February 1 to 4 is relatively dry. However, the simulation replicates the storm starting at around 18:00 on February 1 and ending February 2 early morning. In addition, the simulation also reproduces some of the drizzle events during February 3 and 4 but the intensity and duration of these drizzles are much smaller than the observed. Finally, they occur out-of-phase in time with respect to the observed ones. After February 5, the observations (Figure 8-17, upper plot) show a change in the weather with more rainfall than during the first four days. There are two storms, one starting February 6 and ending February 7 early in the morning, and the other starting in the afternoon of February 7 and ending in the morning of February 8. The RAMS simulations also produce relatively more precipitation after February 5. As expected, and similar to the period September 25

to 30, there is a clear tendency of precipitation to occur during night time hours, with hours around midday having almost no precipitation at all.

Figure 8-18 shows a comparison between high intensity values in the area of study for each three-hour period. The horizontal axis shows the diurnal cycle from noon to noon every three hours and the vertical axis shows three hours cumulative values for every day of the analyzed period. The observed diurnal cycle, upper plot, shows a strong tendency for the maximum in precipitation to occur at night, in this case in the period 18:00 to 21:00 local hour. This period of maximum precipitation is followed by a gradual decay in precipitation intensity, which reaches its minimum around midday. Simulated values, lower plot, exhibit a phase shift of three hours with respect to the observed precipitation maxima. Both observed and simulated data reach a minimum around midday, even though simulated data seem to show this minimum a little later than the observed data. The same behavior is observed in Figure 8-19, which shows the average among values with precipitation greater than zero. From these two figures we can infer that observed data seem to have a tendency to have two periods of maximum precipitation in the night time separated by a period of relatively less precipitation, with high precipitation before midnight, decreasing rainfall around midnight and then again increasing precipitation in the predawn hours. Simulated values do not exhibit the local minimum observed around midnight.

Figures 8-20, 8-21 and 8-22 show a comparison between average intensity values for areas with elevation above sea level less than 1000 m, in the range 1000-2000 m and greater than 2000 m, in the area of study, respectively, and for each three-hour period. The horizontal axis shows the diurnal cycle from midnight to midnight every three hours and the vertical axis shows three hours cumulative values for every day of the analyzed period. The most important differences seem to be associated with the areas with elevations less than 1000 m (see Figure 8-20); observed data show a large variability for this elevation band, with values around 30 mm during the hours 3:00 to 6:00 and 18:00 to 21:00 that are not reproduced in the simulations. Simulated values reproduce higher average intensity for these slopes, but they show only one maximum during the period 21:00 to 3:00 hours. For elevations between 1000-2000 m the agreement is acceptable except for the period 18:00 to 21:00 hours (see Figure 8-21). For elevations greater than

2000 m, Figure 8-22, simulated data present excess of rainfall between 3:00 to 12:00 and deficit during the other periods.

Figures 8-23 and 8-24 show daily cumulative values during the eight days. From these figures we can infer that the daily behavior of the model results is in reasonable agreement with that of the *in situ* observations. From Figure 8-24, upper plot, it is clear that the maximum simulated values are lower than the maximum observed values during the entire period. Figure 8-24, lower plot, shows the average daily intensity in the area of study for February 1 to 8 of 1999 for both observed and simulated precipitation. The average is evaluated taking into account only those points (observed values) and cells (simulated values) where precipitation is greater than zero during each three-hour period. Similar to the period September 25 to 30 of 1998, the average values evaluated in this way compare very well with the observed values.

In conclusion, CSU-RAMS replicates reasonably well the diurnal cycle observed during February 01 to 08 of 1999. As for the period September 25 to 30 of 1998, observed and simulated data show a strong tendency to have concentration of precipitation during the night time hours and minimum values around midday.

8.3 Basin hydrologic response to the hydro-climatic forcing from RAMS

As stated earlier in this chapter, the observed difficulty in reproducing the spatial distribution of precipitation in the area of study is expected. This is because no specific sounding for the area of study is used in the simulation of the storms, so that the basic signal for simulated precipitation comes from large scale reanalysis information. As a result, the spatial distribution of simulated precipitation is strongly dependent on the grid configuration and, therefore, highly dependent on the location of the coarse grid. Therefore, a representative daily amount of precipitation on each watershed is calculated as the average of precipitation from those stations, with values greater than zero in the finest grid. This amount of precipitation is evaluated for both observed and simulated precipitation for the periods September 25-30 of 1998 and February 1-8 of 1999. These values are then used as an input to the hydrologic model to obtain stream flow. Therefore, for this particular application, the hydrologic modeling system (HMS) uses a daily time

step to correspond to the average daily precipitation data calculated from simulation results.

Comprehensive calibration of the Swedish Hydrologiska Byråns Vattenbalansavdelning Hydrologic Modeling System (HBV-HMS) is not conducted in this study because the model already has been calibrated and implemented for forecasting purposes in the area of study by EPM. Calibration by EPM was based on average precipitation from those stations where registers are processed every twenty-four hours. Consequently, it is assumed that the model is already calibrated and that the parameters used are those which best represent the areas of interest.

Among the watersheds included in the finest grid only the basins of the Guadalupe, Guatape and Nare rivers are analyzed. Each one of these three watersheds, Guadalupe, Guatape and Nare, contains a man-made reservoir associated with a hydroelectric power system. Streamflow affluences to each reservoir are measured using the daily operation of the hydroelectric system by applying a simple mass balance equation. These derived (measured) streamflows are then compared with the simulated streamflow at each reservoir obtained as a result of applying the hydrologic model. Although a quantitative comparison is performed, it should be emphasized that the daily derived (measured) streamflow is highly uncertain. The input data for the hydrologic model are obtained as follows: (a) the latitude/longitude range covered by physical stations available on each watershed is selected; (b) all simulated results at grid points on the selected latitude longitude range are extracted; (c) averages for all variables are computed for every three-hour period based on those points with precipitation amounts greater than zero; (d) accumulated values for every day are obtained from the average values; and (e) these accumulated values are used as input to the hydrologic model.

Figures 8-25 to 8-30 show the comparisons of the streamflows in the three watersheds. According to these figures, average precipitation amounts as obtained above are acceptable as a representative sample to model daily streamflows. In general, there is no discernible pattern in the differences between simulated and observed values. Simulated stream flow compares reasonably well with the observed stream flow at the basin outlet (the reservoir); however, it should not be expected that the simulated results

compare well with the observed data at a sub basin scale because the spatial distribution of precipitation is out of phase. In addition, there is much uncertainty in the soil moisture because no soil moisture observations are available within the basin. Furthermore, because the model is only a semi-distributed model using the sub-basin scale as the smallest resolvable scale, the model is not able to account for the spatial variability in the hydraulic parameters.

A brief summary of the results for each one of the basins is given below. Figures 8-25 to 8-30, upper plots, show the daily average amount of precipitation used to drive the hydrologic model. Figures 8-25 to 8-30, lower plots, show model-simulated streamflows compared with the measured streamflows.

8.3.1 Guadalupe Watershed

According to Figure 8-25 for the period September 25-30 of 1998, observed streamflow shows a decreasing tendency characteristic of recession curves, possibly associated with precipitation occurring prior to the period of simulation. However, simulated and observed precipitation show a similar intensity of rainfall during the whole period. For this period, the model underestimates observed streamflow during the first day. It generally overestimates observed streamflow for the rest of the period, although it tracks the observations quite closely during the second and third days.

There is a better agreement between observed streamflow and results of the hydrologic model for the period February 1-8 of 1999, Figure 8-26 lower plot. Both simulated and measured streamflows have the same tendency, but there is a major discrepancy on February 7 where measured streamflow has a maximum that is not present in model results.

8.3.2 Guatape Watershed

For the period September 25-30 of 1998 daily precipitation, Figure 8-27 upper plot, shows a 24-hour delay between the maximum of observed precipitation and that of simulated precipitation. This fact is translated to model streamflow results, producing a large discrepancy in the middle of the period. Although measured streamflow implies a dry September 27, observed and simulated precipitation indicate the opposite; this could

be associated with errors in the measured streamflow. On the other hand, there is a good agreement at the beginning and at the end of the period.

As in the case of the Guadalupe watershed, there is a better agreement between observed streamflow and results of the hydrologic model for the period February 1-8 of 1999, Figure 8-28 lower plot. Both simulated and measured streamflows have the same tendency; there is a major discrepancy on February 6 where simulated precipitation is underestimated and so is the streamflow.

8.3.3 Nare Watershed

For this watershed there is a good agreement between daily observed and simulated precipitation, therefore a good agreement with respect to basin response would be expected. However, in both periods, Figures 8-29 and 8-30 show that the hydrologic model overestimates the streamflow. The tendency of the streamflow values is similar, indicating the need to recalibrate the hydrologic model for this watershed.

8.4 Discussion

According to these analyses based on simulated results for two specific periods, one dry and the other wet, the CSU-RAMS replicates the diurnal cycle in the area of study reasonably well. Plots for variables other than precipitation show a very good agreement between observed and simulated values. However, with respect to precipitation, three important discrepancies are apparent. First, the CSU-RAMS has difficulty capturing exactly the observed phase of the diurnal cycle, presenting a delay in the time with the maximum concentration of rainfall. Second, simulated precipitation tends to underestimate observed precipitation. Third, simulated storms appear to be of shorter duration. This could be explicated by fundamental difficulties in the specific parameterizations implemented in this analysis, suggesting testing the model with other options in order to match more exactly the diurnal cycle. An additional source of these differences is the fact that the boundary data are provided to the model every six hours, and that between each update of the boundary condition data, the model interpolates linearly. This implies that there could be important transport of moisture not captured in

the reanalysis data and, consequently, we should not expect to replicate exactly the observed rainfall for short periods of time such as three hours.

The area selected for this analysis has an extremely complex relief and a wide range of elevation differences. Clearly then, we should expect to have a set of correspondingly complex interactions between precipitation-producing mechanisms, including mainly orographic lifting and density driven (i.e., thermal or moisture) circulations. Additionally, we should expect that the diurnal cycle is characterized by dominant local processes. However, the scale of the finest grid used in this analysis (i.e., 2.5-km cell size), is a little larger than recommended for the bulk-microphysics parameterization and smaller than recommended for the convection parameterization. For this particular case, the convective parameterization was not activated for the third and fourth grids, so the results are just from the bulk microphysics parameterization. This can explain in part the RAMS simulated precipitation deficit, because there is no contribution from convective precipitation. Otherwise, the characteristics of the simulated diurnal cycle agree well with some universal characteristics of the diurnal cycle for tropical landmasses, such as continental convection that generally peaks in the evening. Additionally, variations from universal characteristics indicate the effects of complex mountain–valley breezes, as well as the life cycle of mesoscale convective systems.

In conclusion, the CSU-RAMS simulation results indicate that the model is capable of replicating the observed diurnal cycle in the study area reasonably well. RAMS simulations capture reasonably well the temporal storm patterns over the study area during the two periods studied; however, spatial discrepancies exist between observed and simulated precipitation fields. In order to deal with the misrepresentation of the spatial distribution of precipitation, average observed and average simulated precipitation data for the periods Sep 25-30 of 1998 and February 1-8 of 1999 are used to drive the Hydrologic Model System (HMS). The output from HBV-HMS is compared to the measured streamflow hydrograph at the Guadalupe, Guatape and Nare reservoirs. The simulated streamflow with the RAMS-simulated precipitation is closer to the simulated streamflow with observed precipitation. However, both present larger and lower values than the measured streamflow. In synthesis, the linked model system captured the storm patterns accurately and simulated the basin outflows moderately well.

With reference to the Hydrologic Model System (HMS), it is clear that its results depend on how well RAMS reproduces the climatic variables. In this particular study this aspect is considered secondary because the focus of the research is not to select the best HMS, but to show the feasibility to deal with this kind of link and the great importance that it could have in water resources planning and management.

Table 8-1: Location and dimensions of the four-grid domain configuration used in the full 1999-year simulation

DESCRIPTION	GRID ONE	GRID TWO
Northwest Point	23.406 °N, 95.46 °W	10.891 °N, 81.027 °W
Northeast Point	23.406 °N, 54.54 °W	10.891 °N, 68.973 °W
Center Point	5.0 °N, 75.0 °W	5.0 °N, 75.0 °W
Southwest Point	13.999 °S, 94.306 °W	0.945 °S, 80.919 °W
Southeast Point	13.999 °S, 55.694 °W	0.945 °S, 69.081 °W
West Coordinate (Km)	-2160	-660
East Coordinate (Km)	2160	660
South Coordinate (Km)	-2160	-660
North Coordinate (Km)	2160	660
Bottom Coordinate (m)	0.0	0.0
Top Coordinate (m)	25895.1	25895.1
Δx (m)	160000	40000
Δy (m)	160000	40000
Bottom Δz (m)	250	78.3
Number of vertical levels	22	29
Δt (s)	120	40

DESCRIPTION	GRID THREE	GRID FOUR
Northwest Point	8.277 °N, 77.589 °W	7.260 °N, 75.737 °W
Northeast Point	8.280 °N, 73.137 °W	7.260 °N, 74.535 °W
Center Point	5.18 °N, 75.361 °W	6.575 °N, 75.136 °W
Southwest Point	2.072 °N, 77.564 °W	5.888 °N, 75.735 °W
Southeast Point	2.074 °N, 73.155 °W	5.888 °N, 74.536 °W
West Coordinate (Km)	-285	-81.25
East Coordinate (Km)	205	51.25
South Coordinate (Km)	-325	98.75
North Coordinate (Km)	365	251.25
Bottom Coordinate (m)	0.0	0.0
Top Coordinate (m)	25895.1	25895.1
Δx (m)	10000	2500
Δy (m)	10000	2500
Bottom Δz (m)	78.3	78.3
Number of vertical levels	29	29
Δt (s)	12.33	4.44

Figure 8-1: Domain of simulation. Grid-1 span from (14°S, 94.31°W) to (23.41°N, 54.54 °W), pole (5.0°N, 75.0°W), $\Delta x = \Delta y$ =160-Km. Grid-2 span from (0.94°S, 80.92°W) to (10.89°N, 68.97°W), pole (5.0°N, 75.0°W), $\Delta x = \Delta y$ =40-Km. Grid-3 span from (2.07°N, 77.56°W) to (8.28°N, 73.13°W), pole (5.18°N, 75.36°W), $\Delta x = \Delta y$ =10-Km. Grid-4 span from (5.88°N, 75.73°W) to (7.26°N, 74.53°W), pole (6.57°N, 75.13°W), $\Delta x = \Delta y$ =2.5-Km.

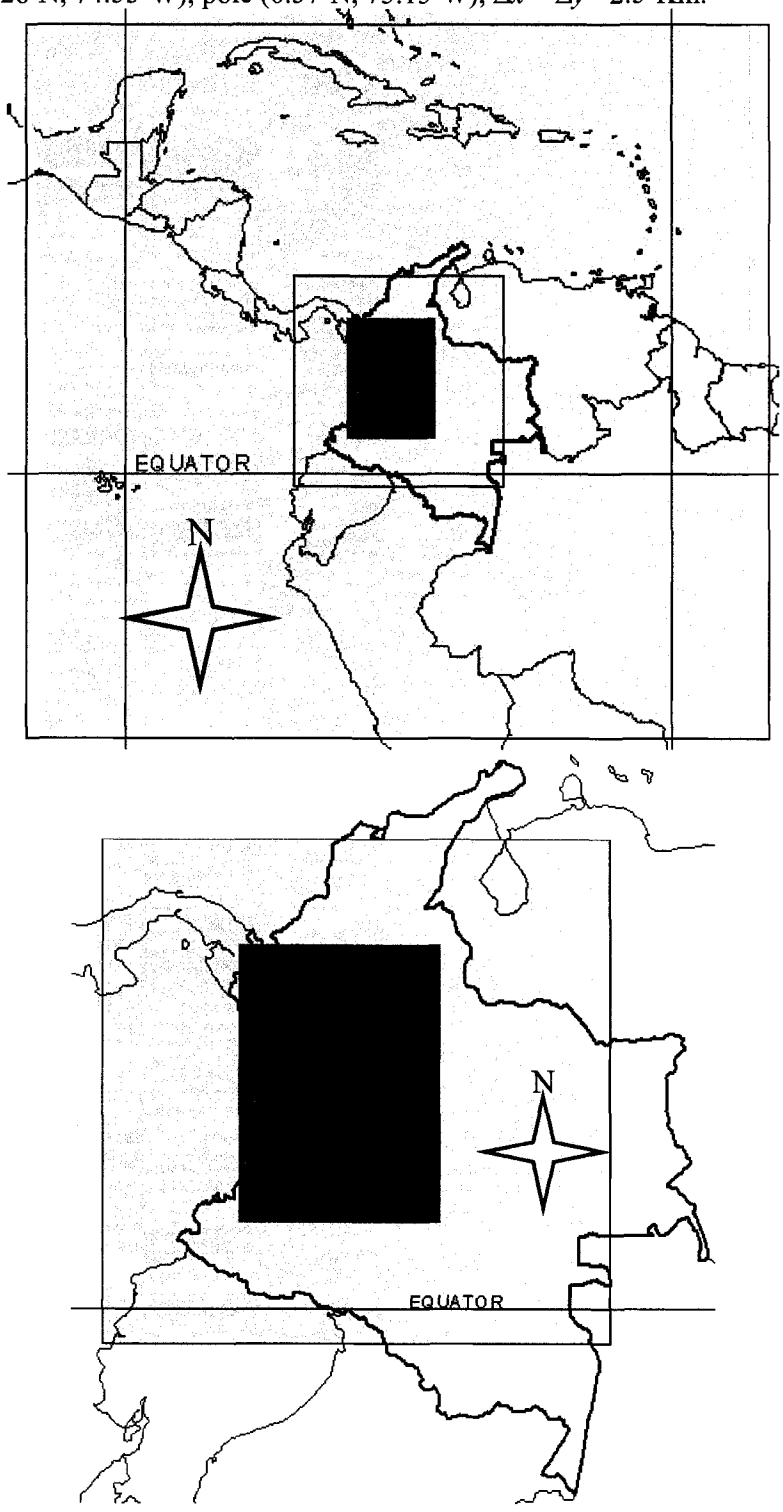

Figure 8-2: Upper plot shows CSU-RAMS topography approximation in the 10-km cell size grid. Lower plot shows CSU-RAMS topography approximation in the 2.5-km cell size grid.

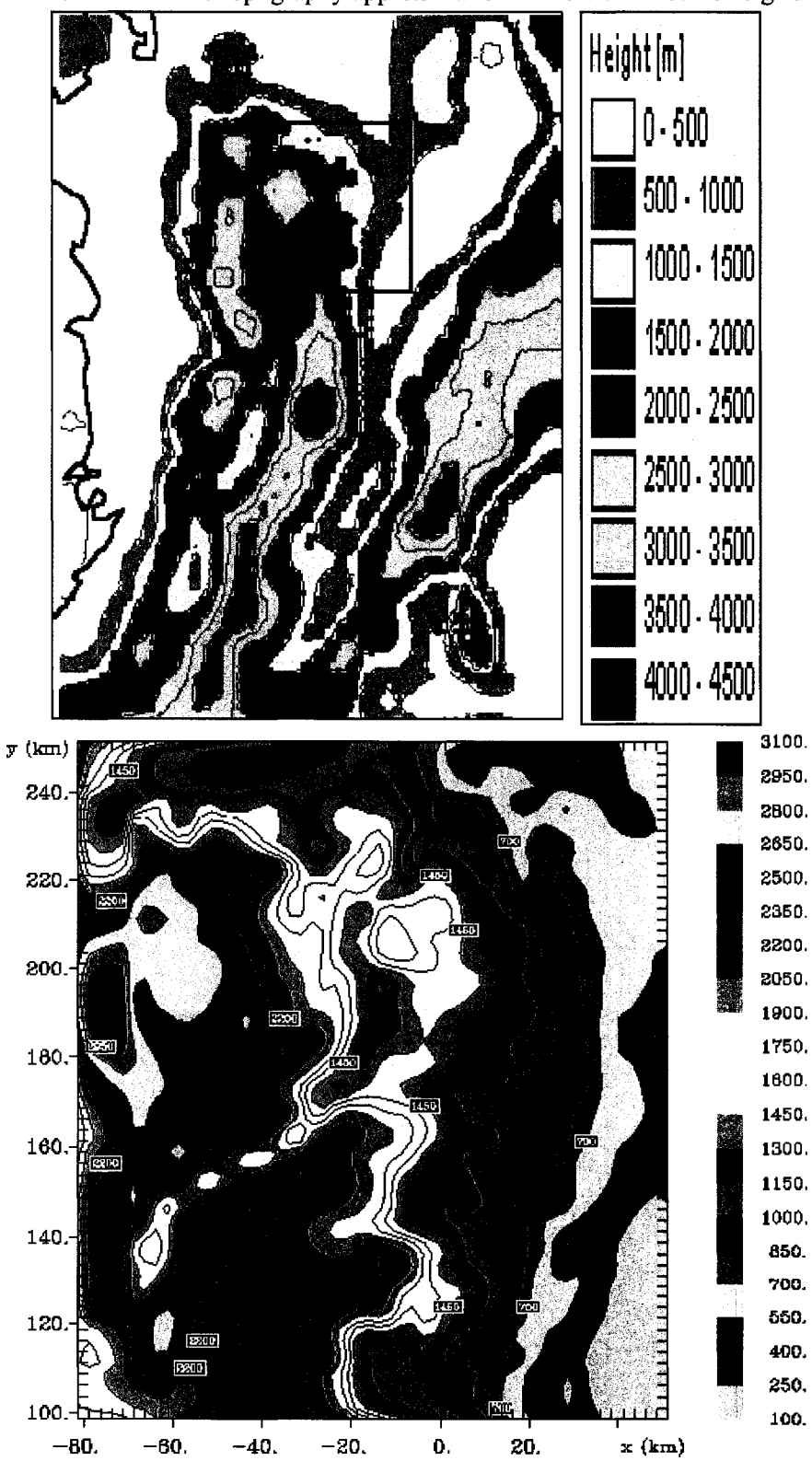

Figure 8-3: Hydroelectric developments located on the finest grid of the simulation.

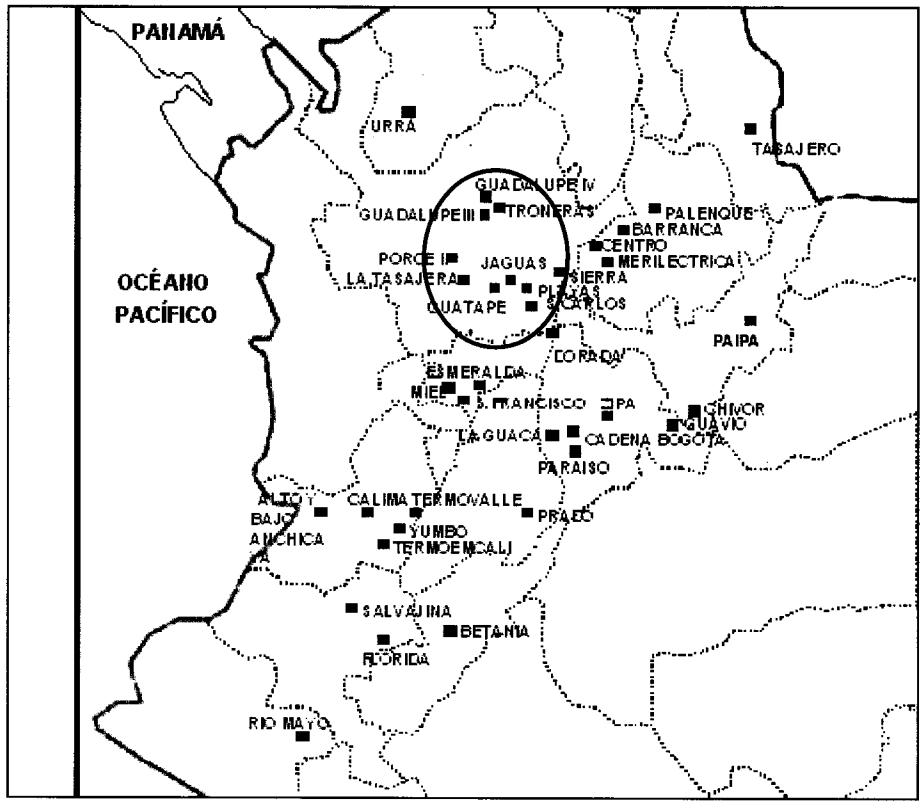

RIOGRANDE - PORCE DEVELOPMENT

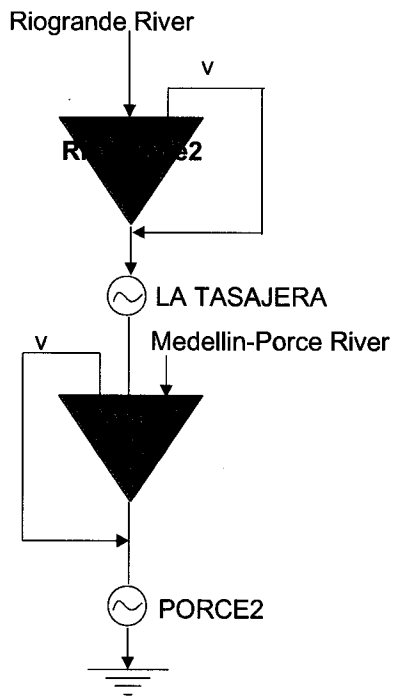

NARE - GUATAPE DEVELOPMENT

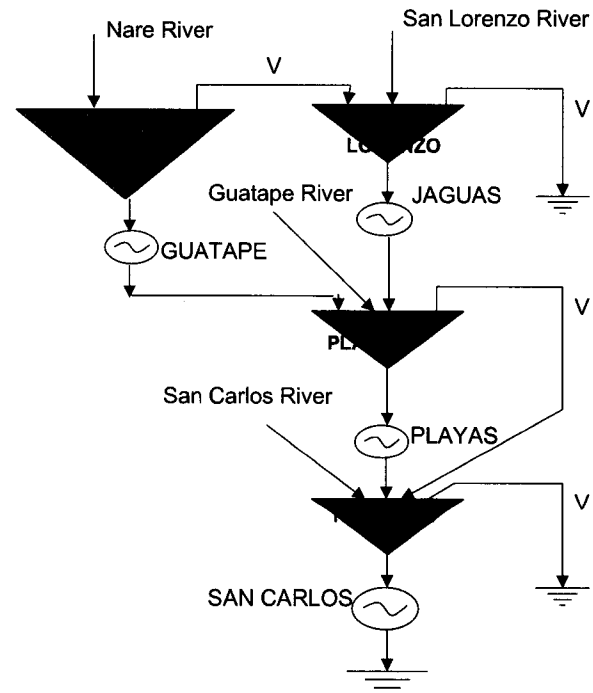

Figure 8-4: Temperature field. The left image shows observed values and the right image shows the corresponding simulated values obtained after one, two, and three days of simulation.

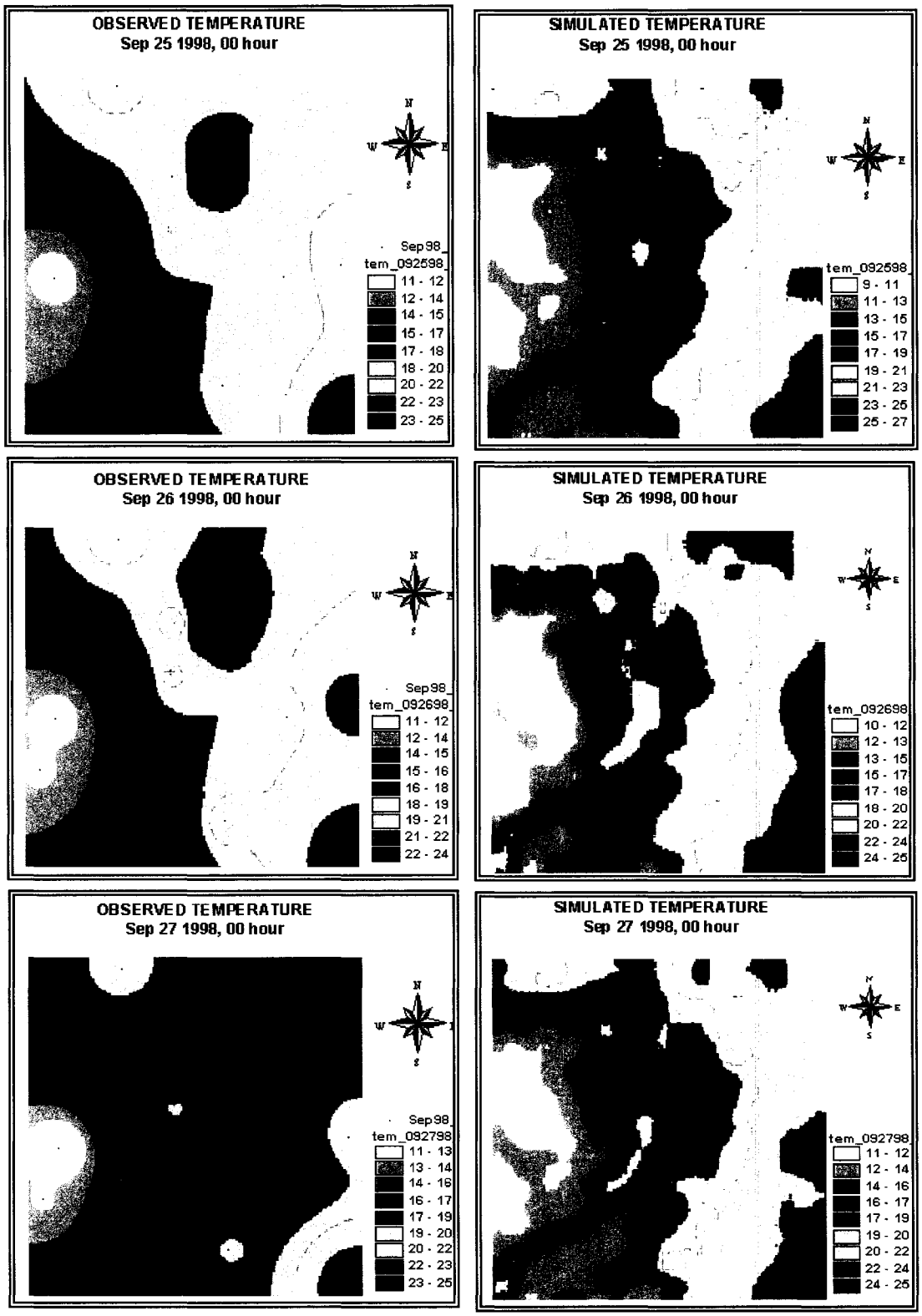

Figure 8-5: Temperature field results every twelve hours during the three days of simulation. Time from left to right and top to bottom is respectively: 09-25-98 at 12:00h, 09-25-98 at 24:00h, 09-26-98 at 12:00h, 09-26-98 at 24:00h, 09-27-98 at 12:00h and 09-27-98 at 24:00h.

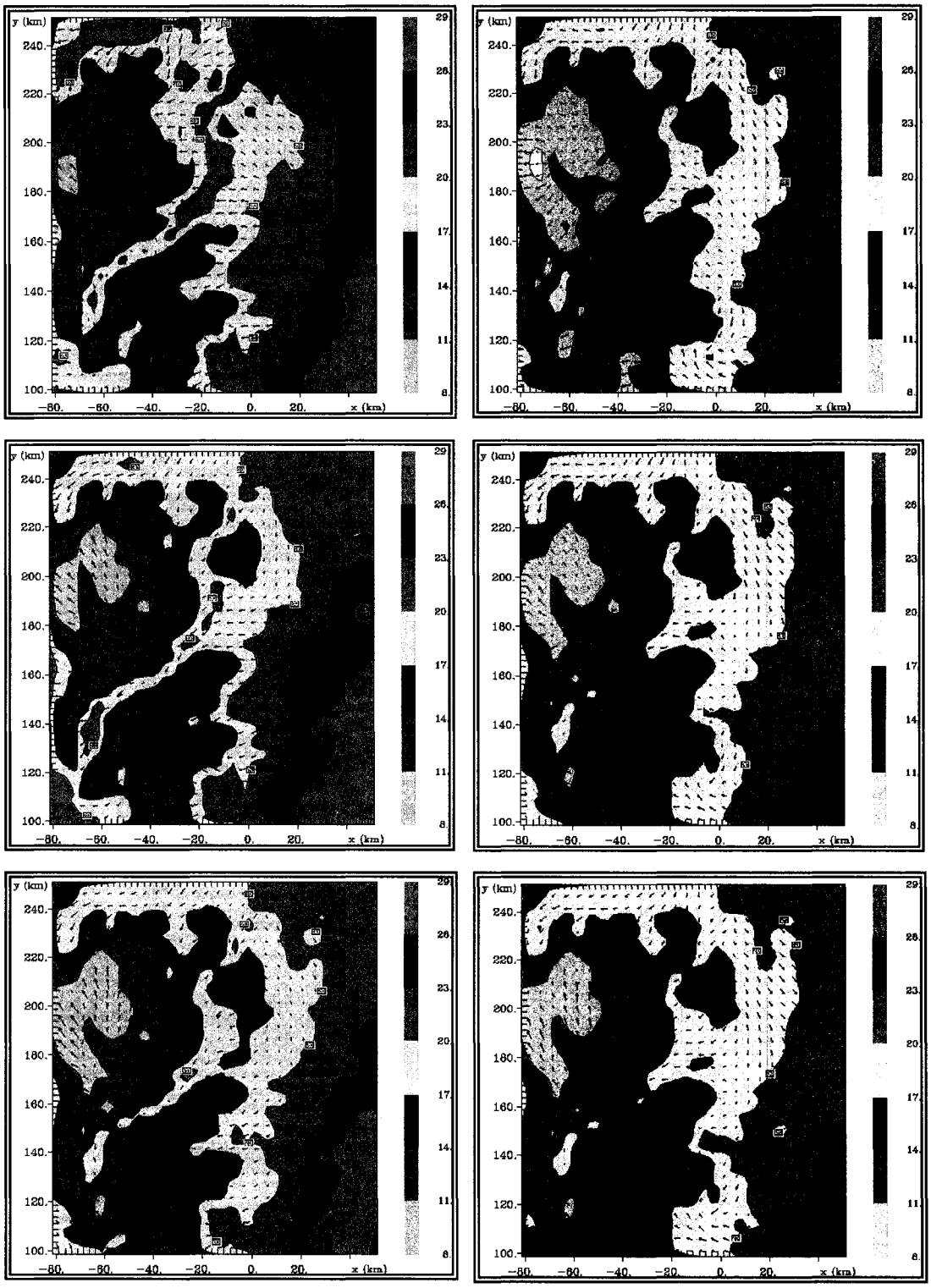

Figure 8-6: Pressure field results every twelve hours during the three days of simulation. Time from left to right and top to bottom is respectively: 09-25-98 at 6:00h, 09-25-98 at 18:00h, 09-26-98 at 6:00h, 09-26-98 at 18:00h, 09-27-98 at 6:00h and 09-27-98 at 18:00h.

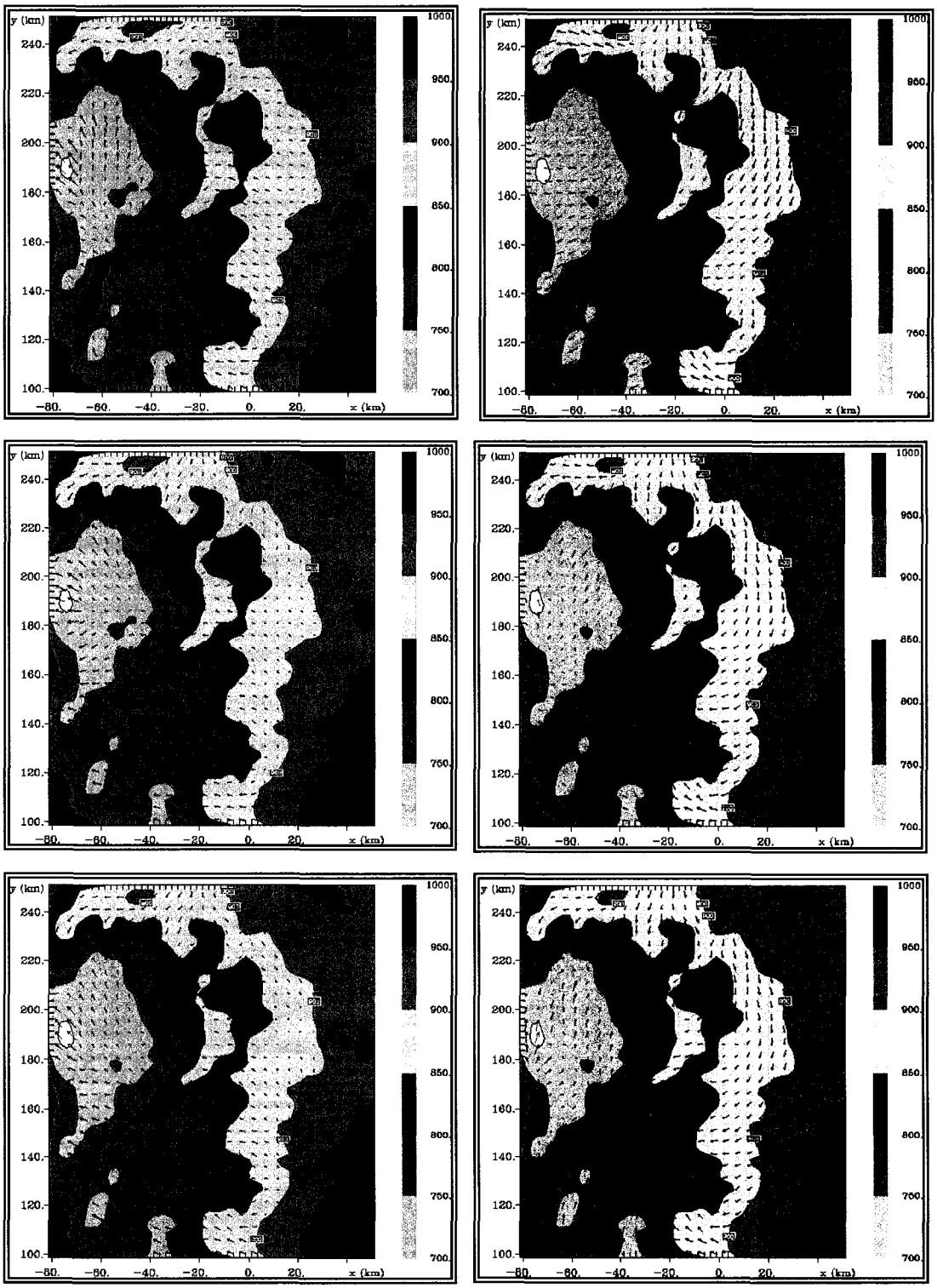

Figure 8-7: Precipitation for September 25 1998; volumes are plotted successively every three hours. Upper plots correspond to observed values and lower plots correspond to simulated values.

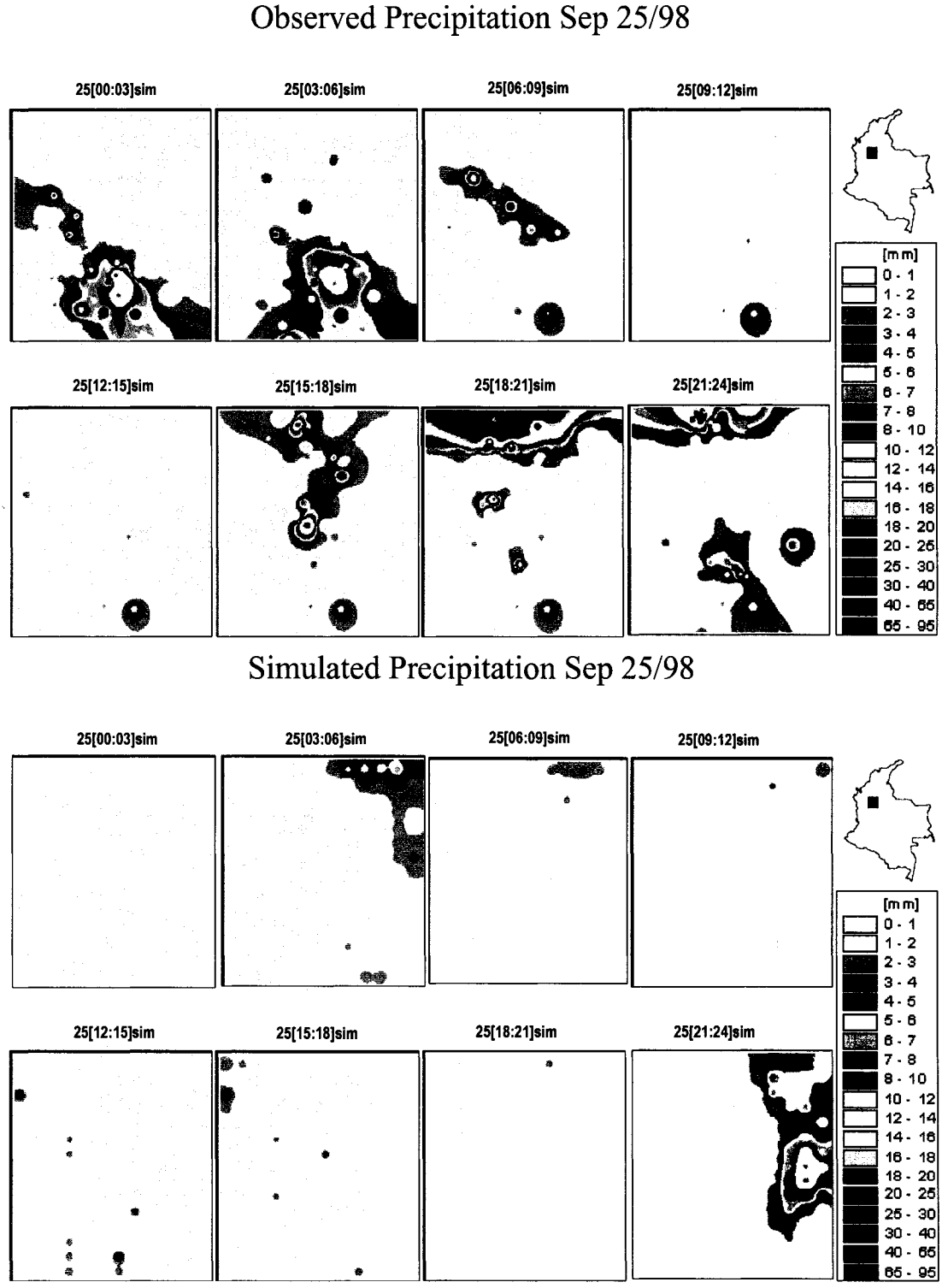

Figure 8-8: Precipitation for September 26 1998; volumes are plotted successively every three hours. Upper plots correspond to observed values and lower plots correspond to simulated values.

Observed Precipitation Sep 26/98

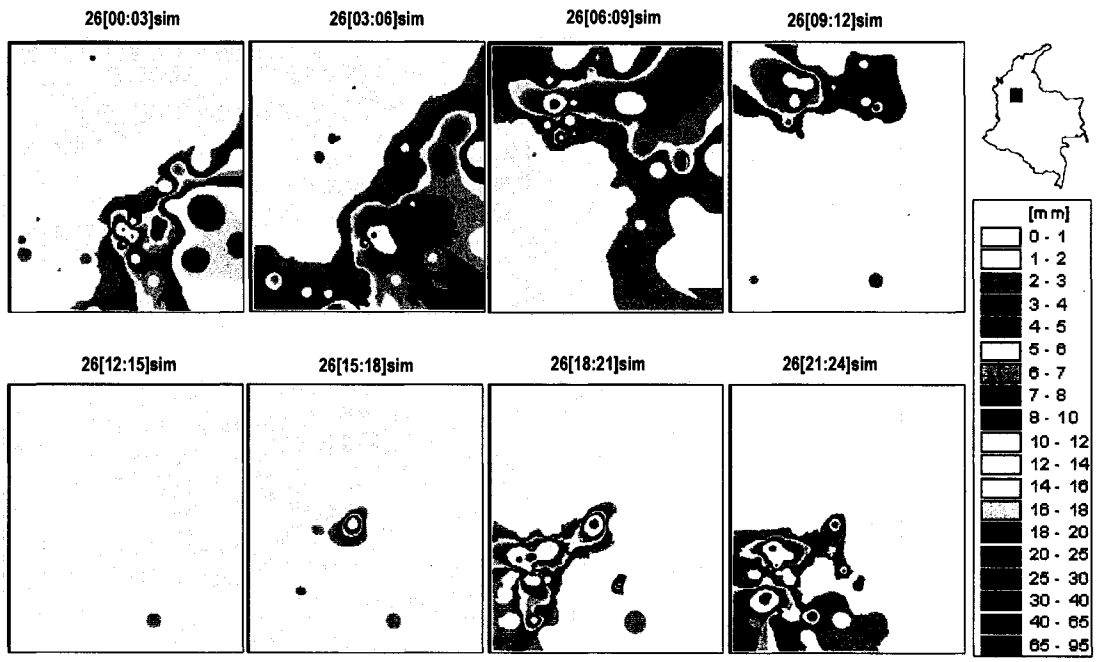

Simulated Precipitation Sep 26/98

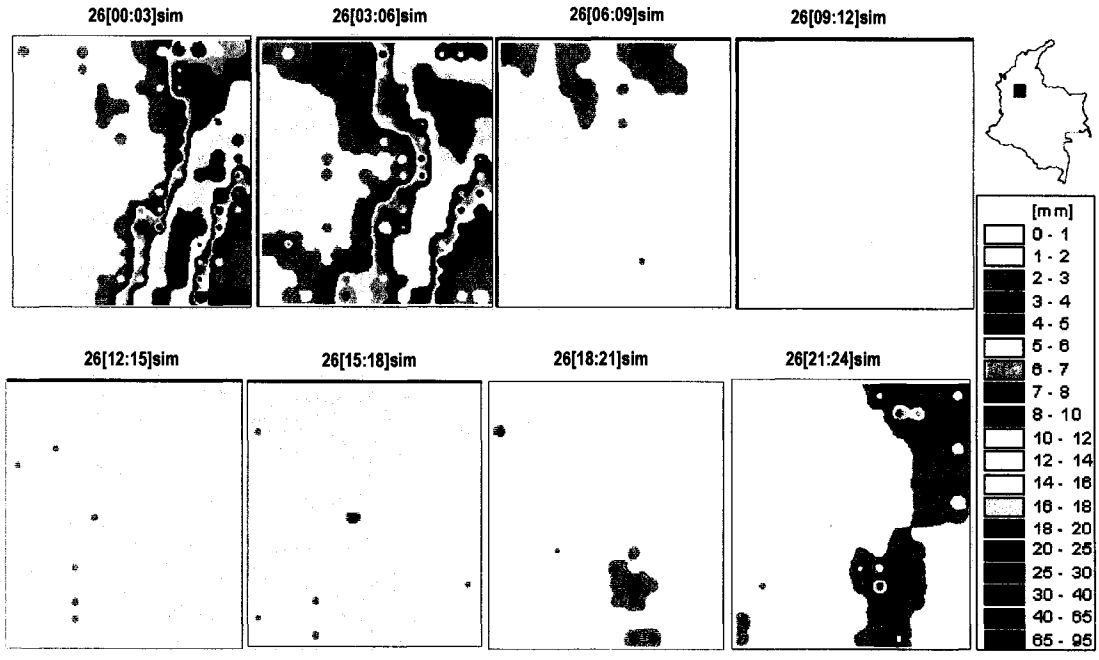

Figure 8-9: Precipitation for September 27 1998; volumes are plotted successively every three hours. Upper plots correspond to observed values and lower plots correspond to simulated values.

Observed Precipitation Sep 27/98

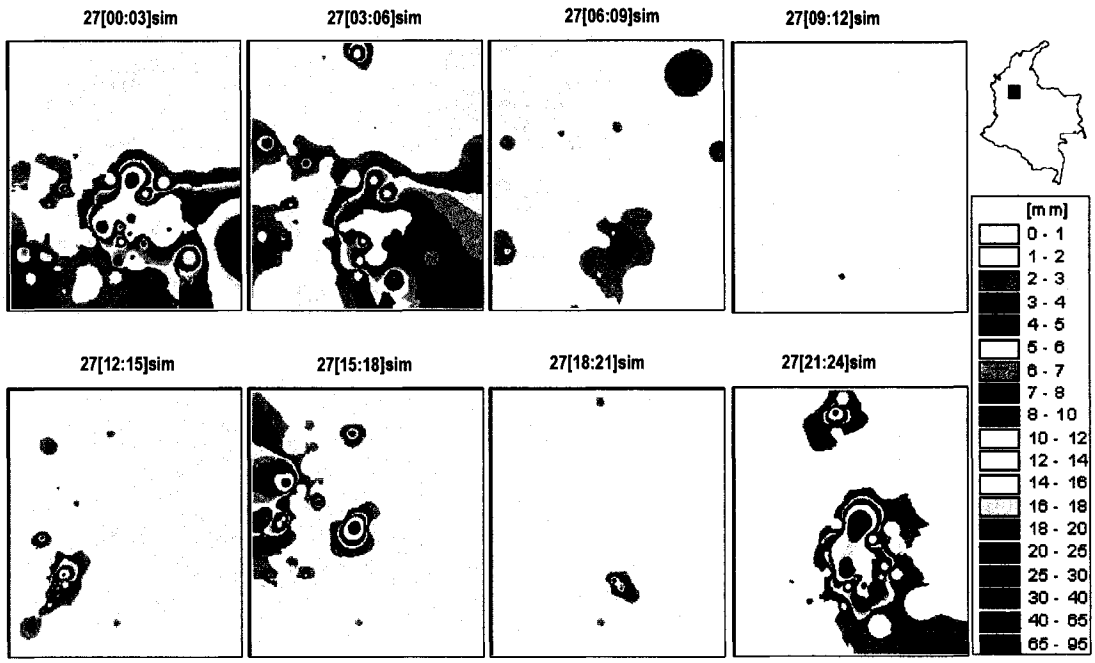

Simulated Precipitation Sep 27/98

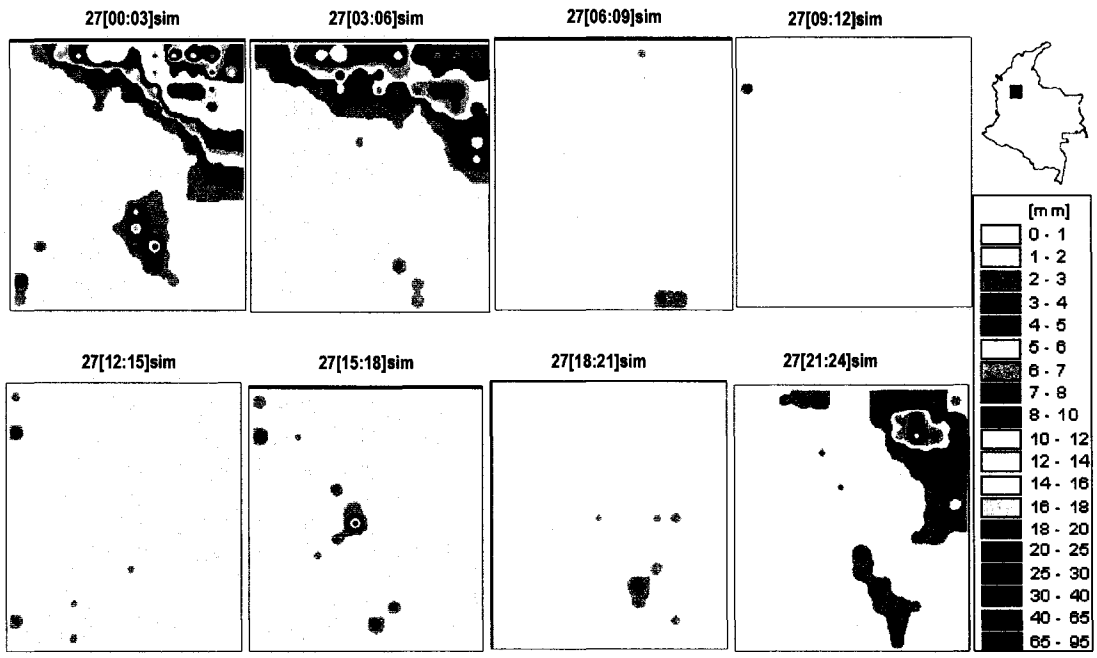

Figure 8-10: Precipitation for September 28 1998; volumes are plotted successively every three hours. Upper plots correspond to observed values and lower plots correspond to simulated values.

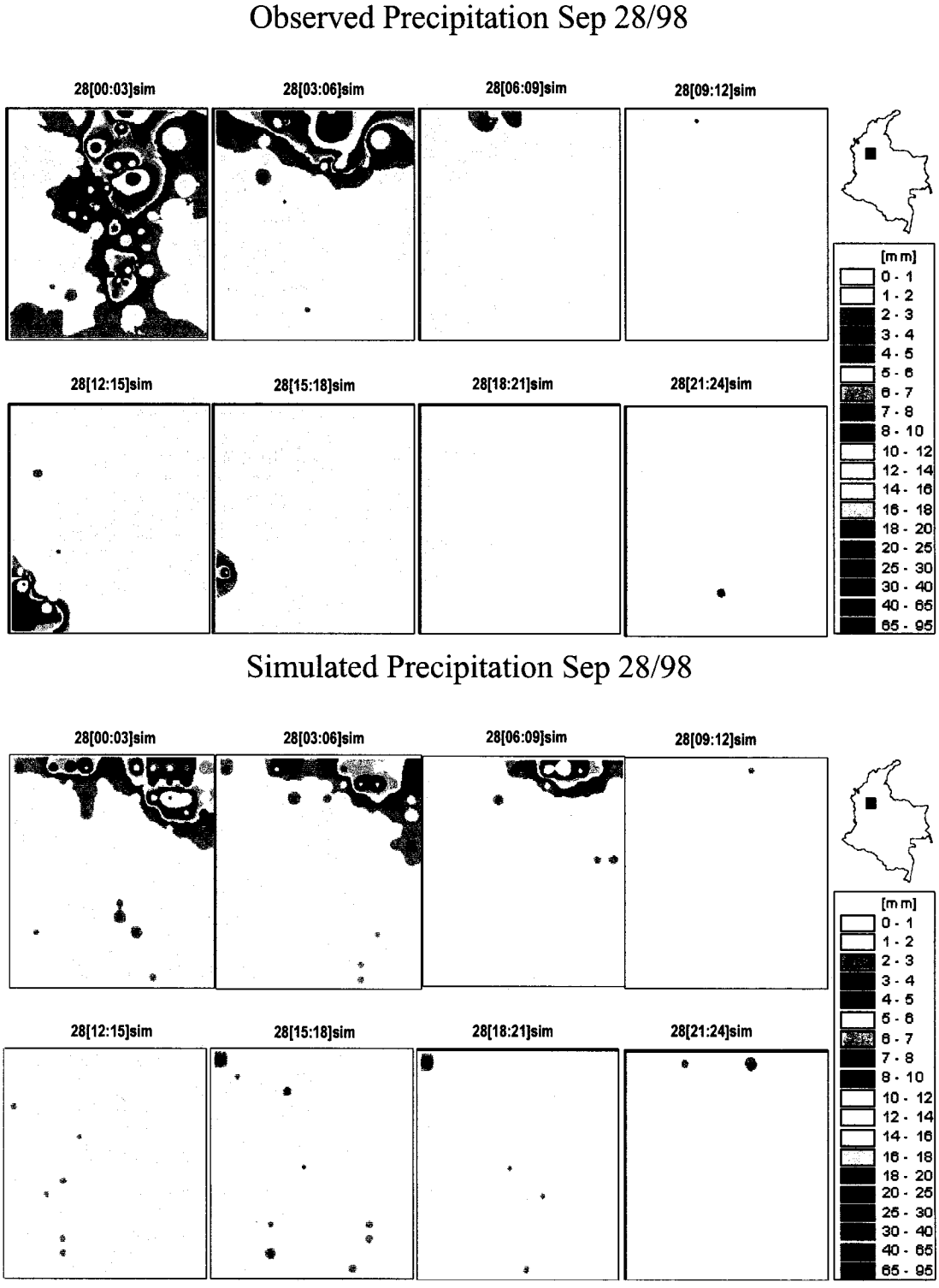

Figure 8-11: Precipitation for September 29, 1998; volumes are plotted successively every three hours. Upper plots correspond to observed values and lower plots correspond to simulated values.

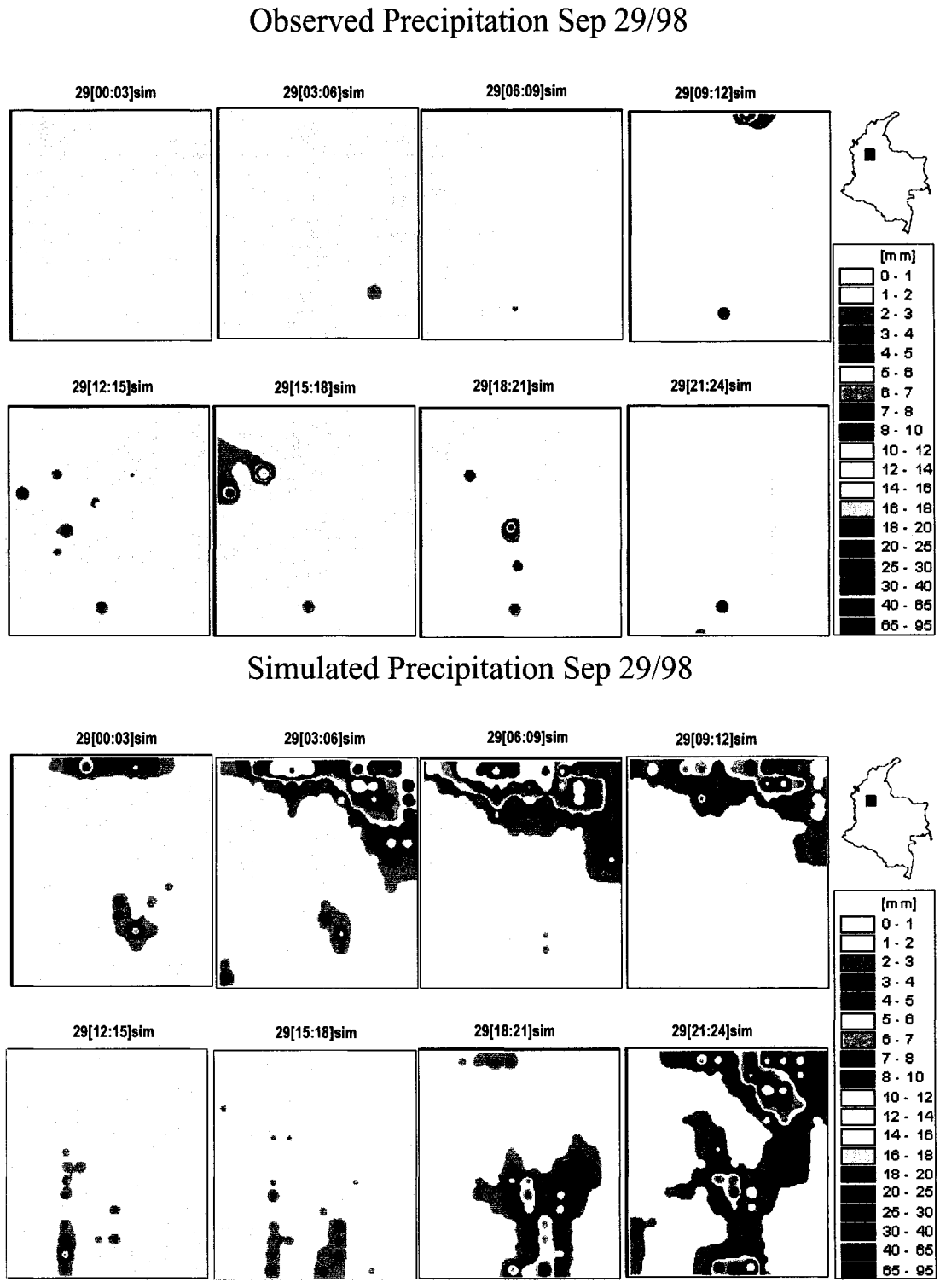

Figure 8-12: Precipitation September 25-29 1998; volumes are plotted successively every three hours, local time. Upper plots correspond to observed values and lower plots correspond to simulated values.

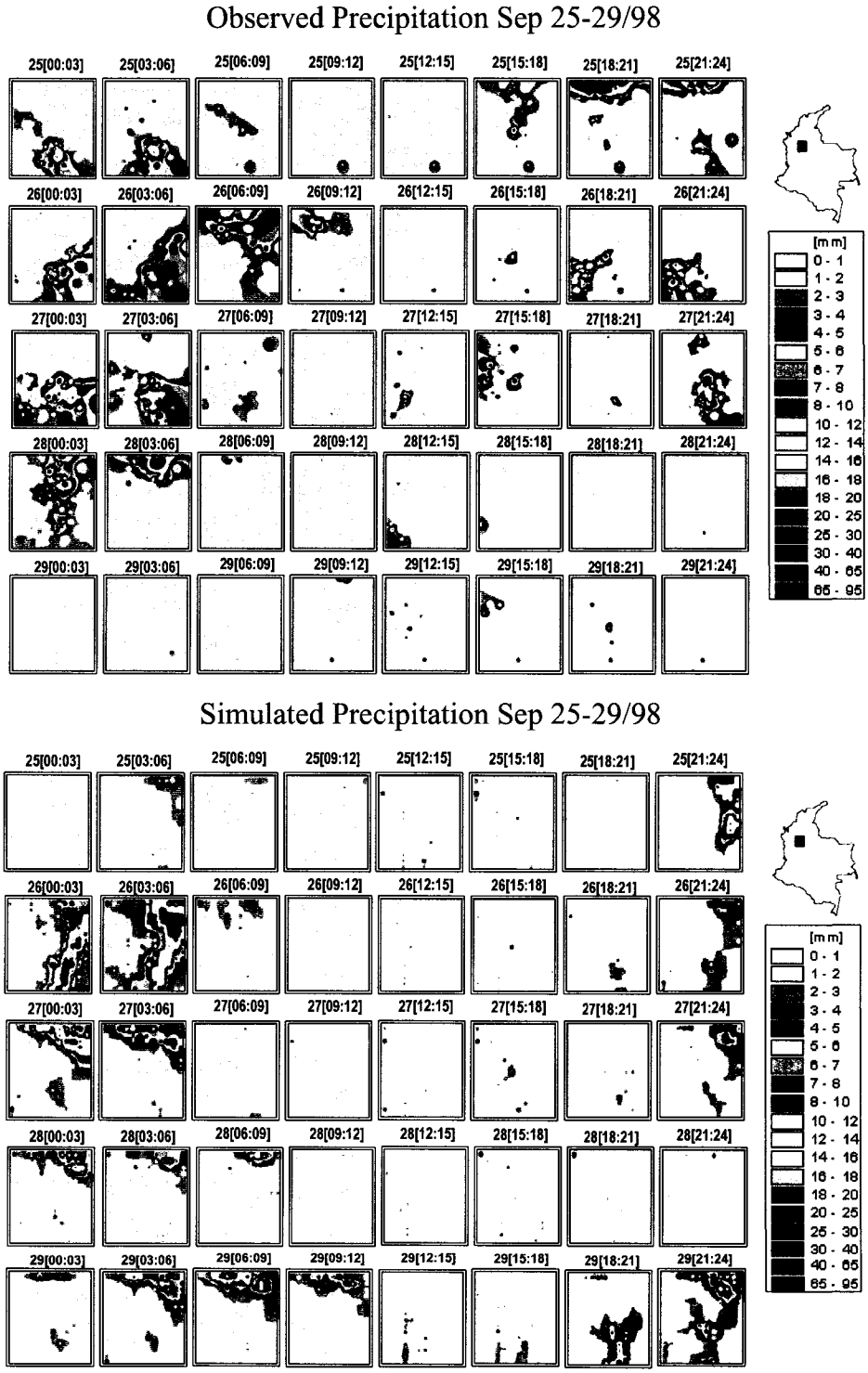

Figure 8-13: Diurnal Precipitation cycle from September 25-30 of 1998. Maximum intensity values in the area. Upper plot corresponds to observed values and lower plot corresponds to simulated values.

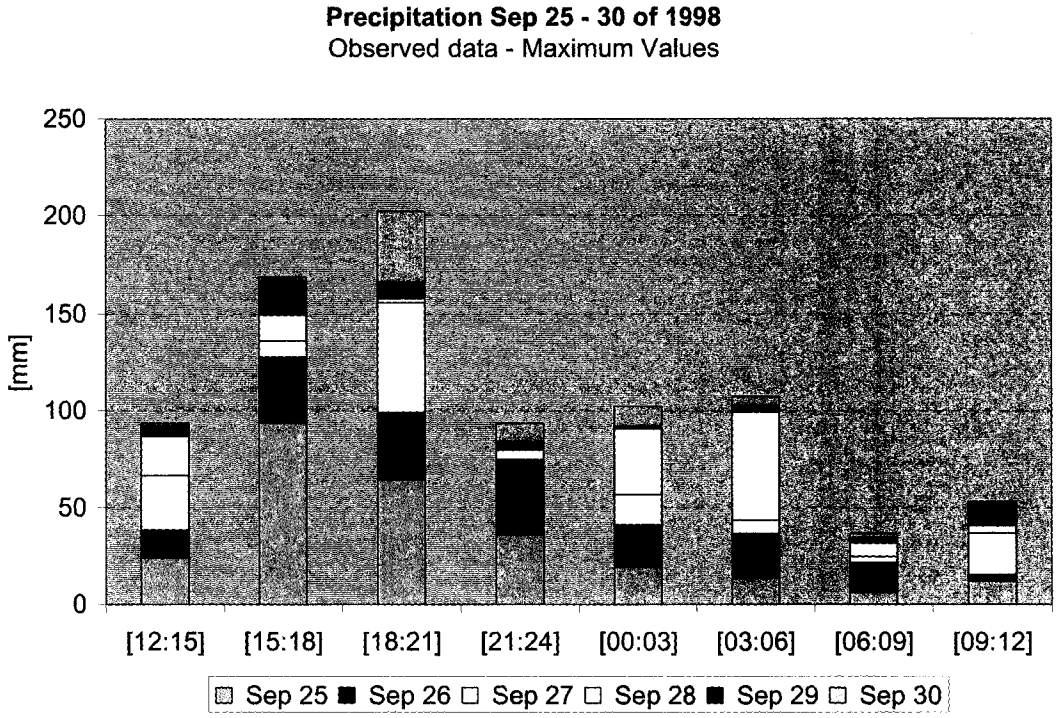

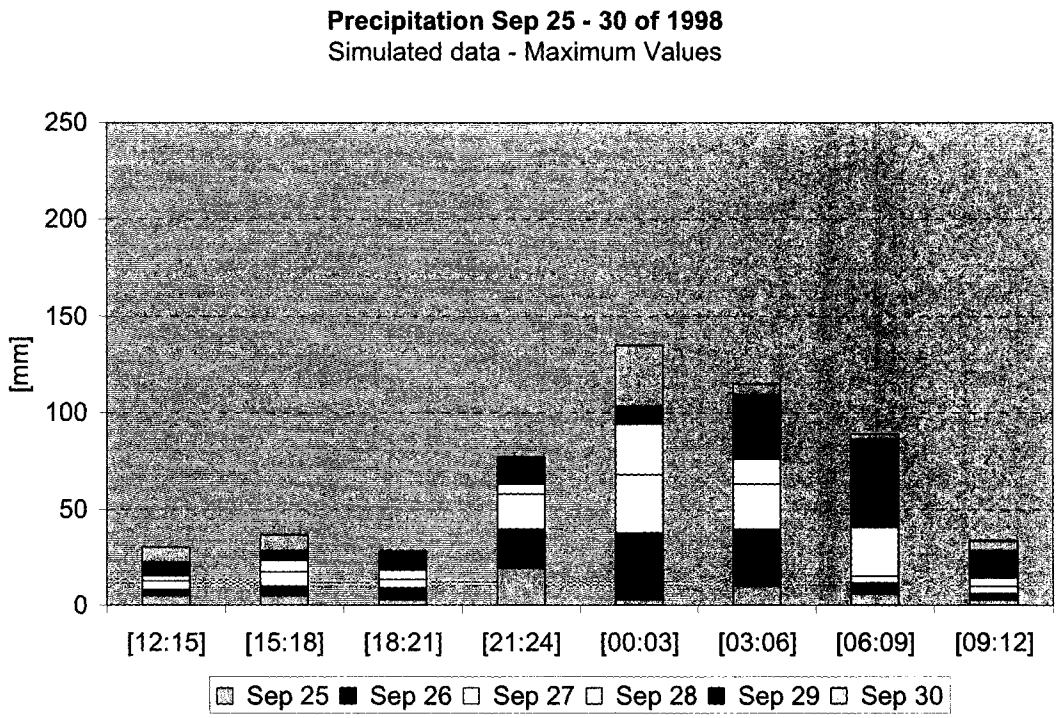

Figure 8-14: Diurnal Precipitation cycle from September 25-30 of 1998. Average intensity values in the area. Upper plot corresponds to observed values and lower plot corresponds to simulated values.

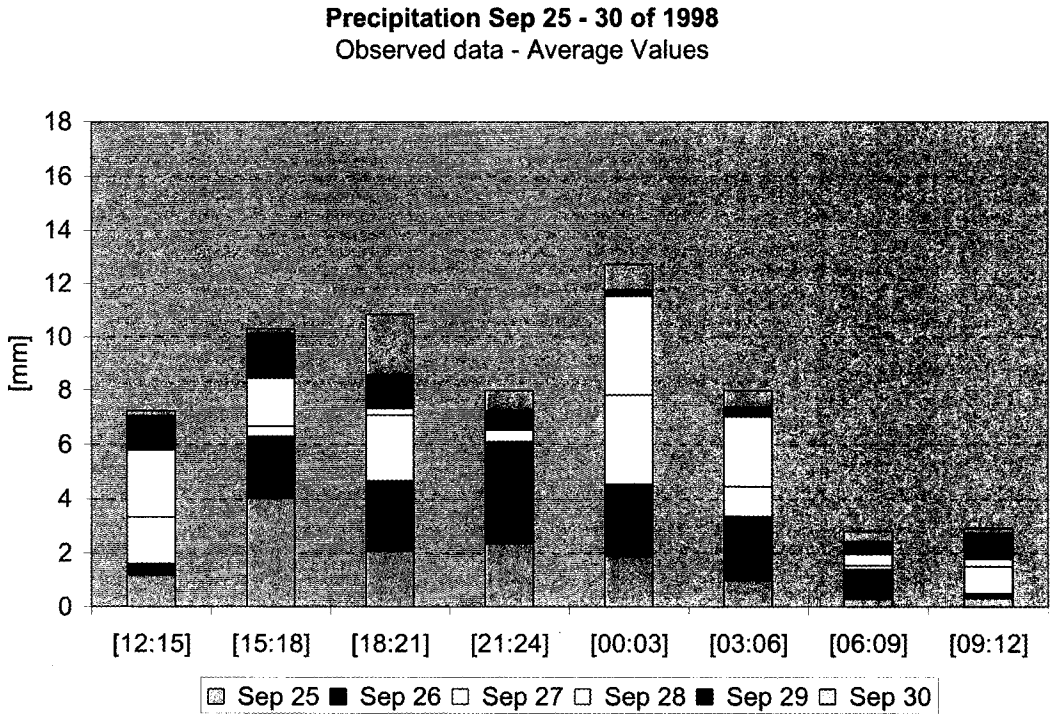

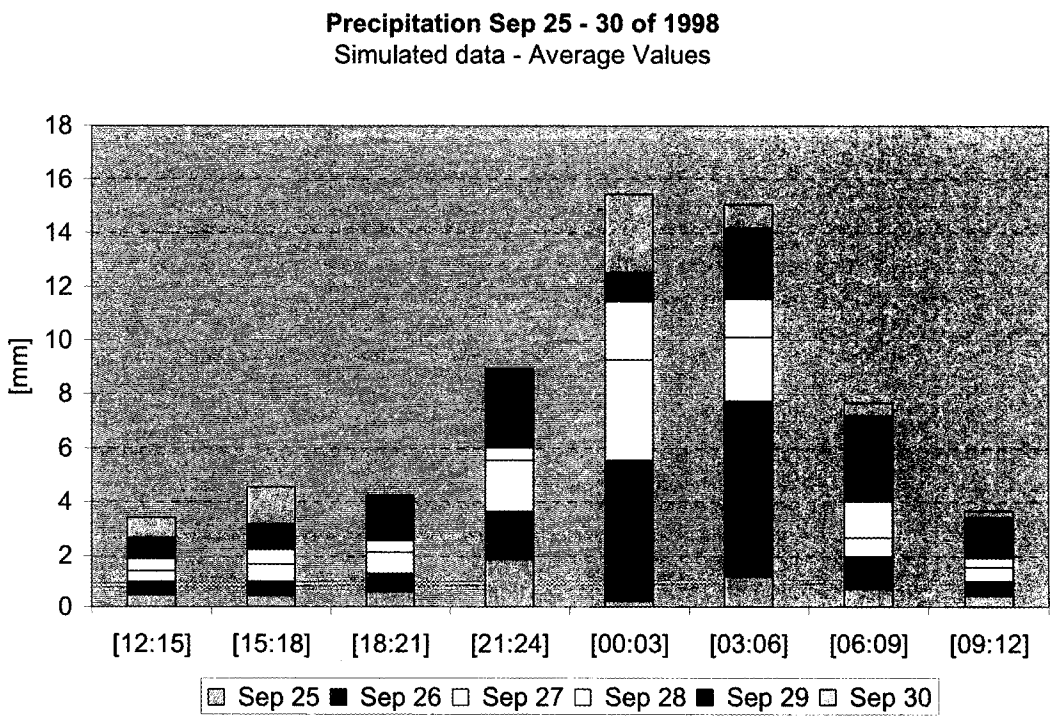

Figure 8-15: Diurnal Precipitation, September 25-30 of 1998. Upper plot corresponds to maximum values in the area of study and lower plot corresponds to average values on the area of study.

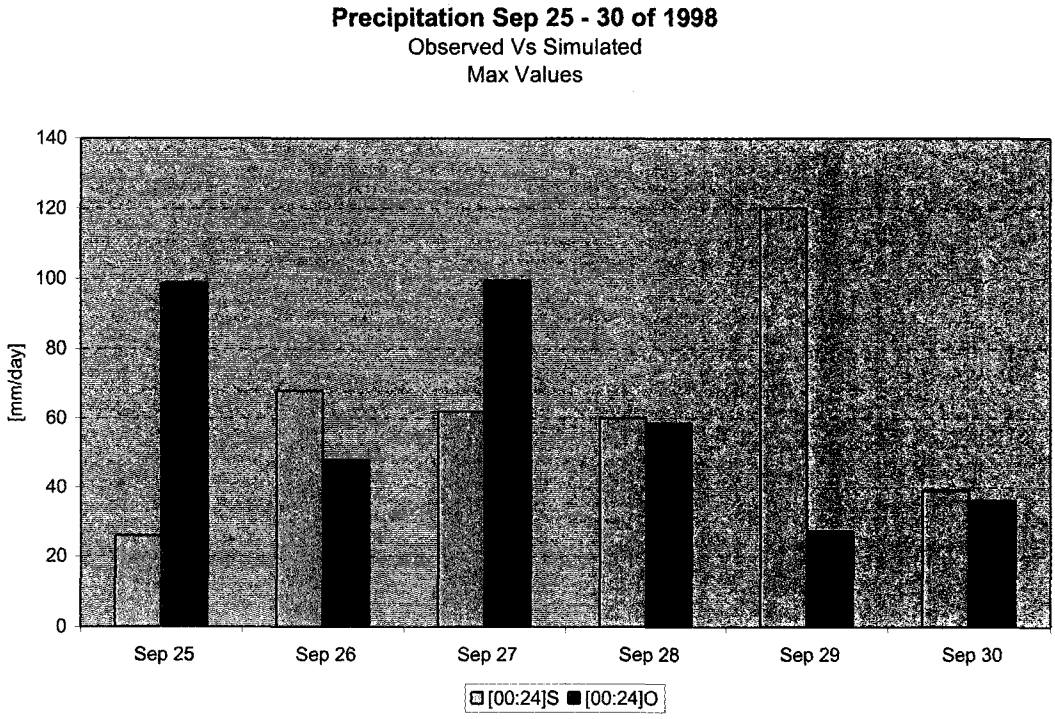

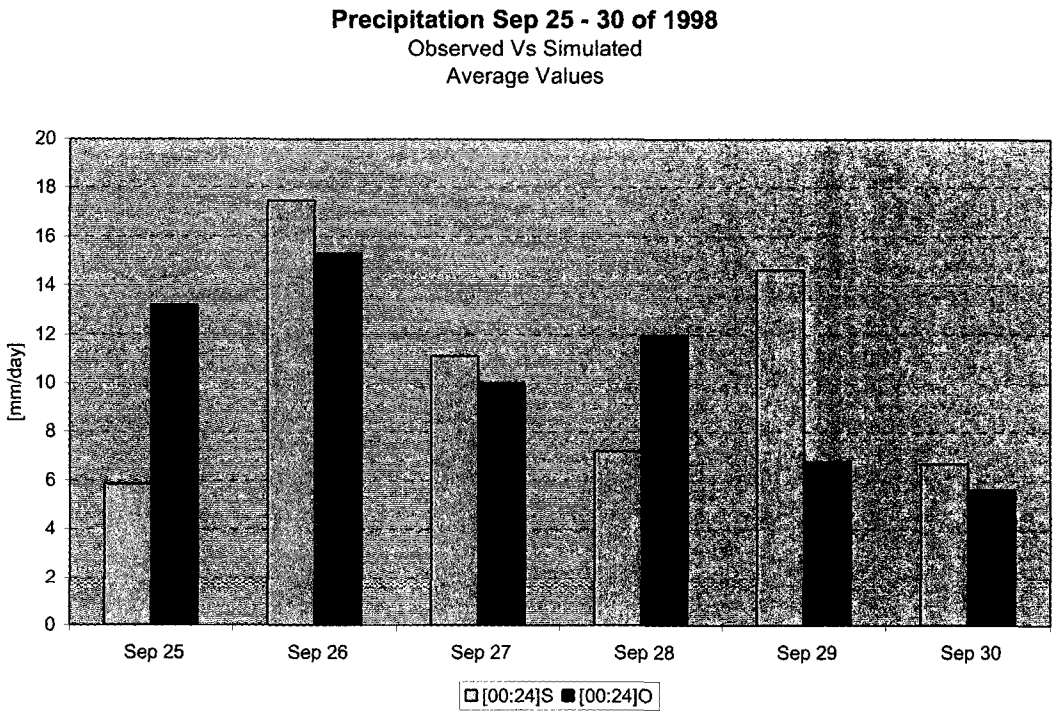

Figure 8-16: Precipitation for February 01-04 1999; volumes are plotted successively every three hours, local time. Upper plots correspond to observed values and lower plots correspond to simulated values.

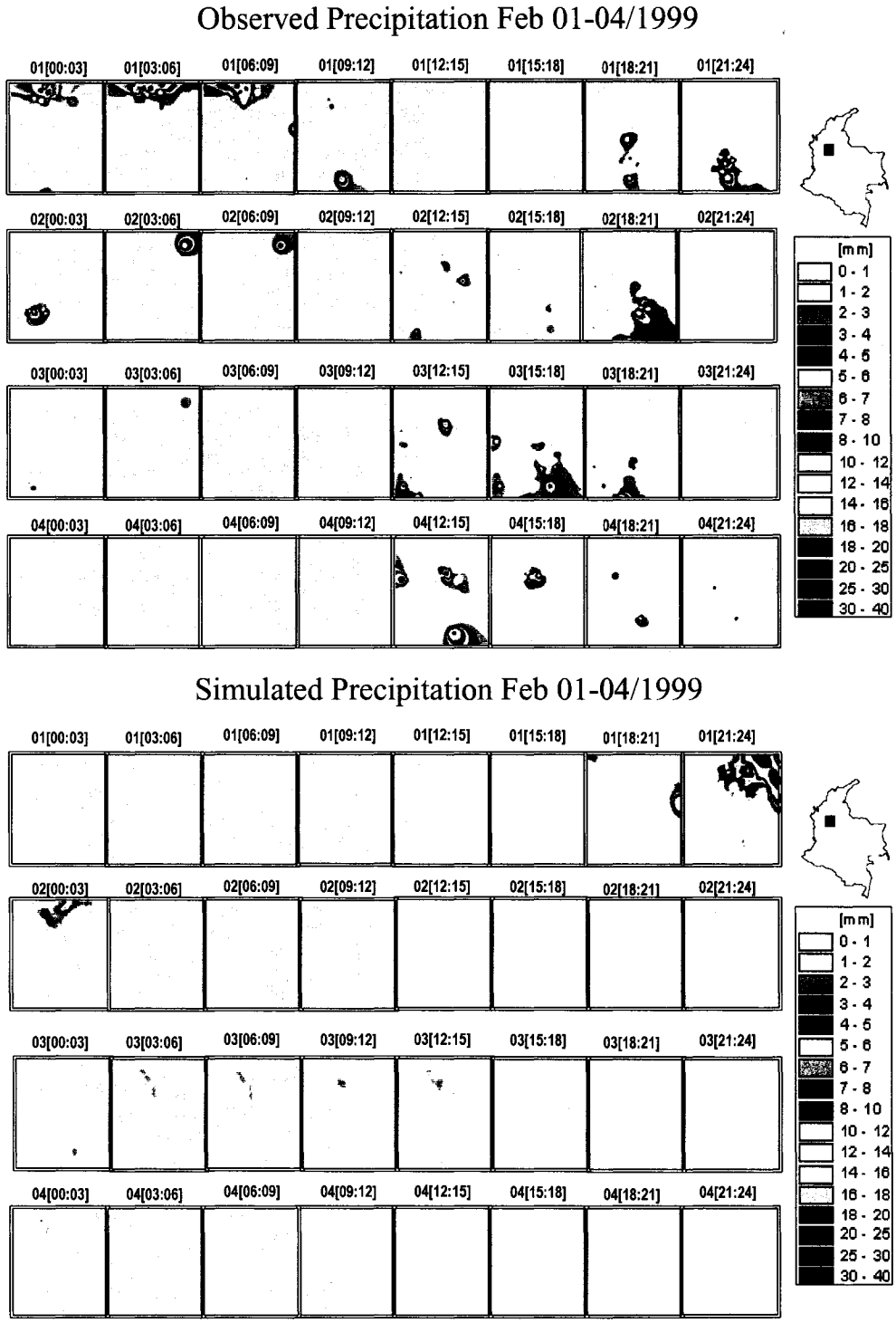

Figure 8-17: Precipitation for February 05-08 1999; volumes are plotted successively every three-hour period. Upper plots correspond to observed values and lower plots correspond to simulated values.

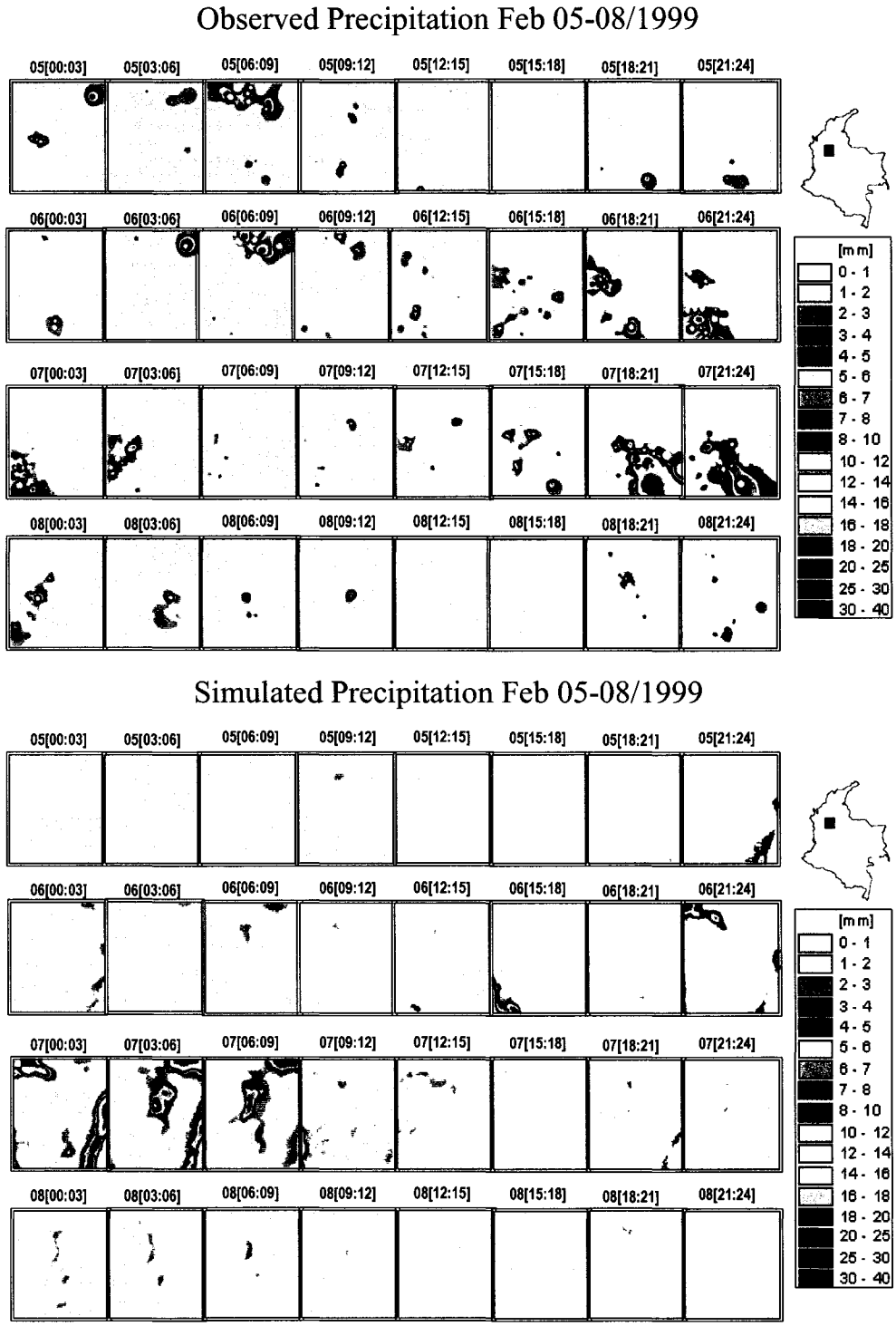

Figure 8-18: Diurnal Precipitation cycle from February 01-08 of 1999. Maximum intensity values in the area. Upper plot corresponds to observed values and lower plot corresponds to simulated values.

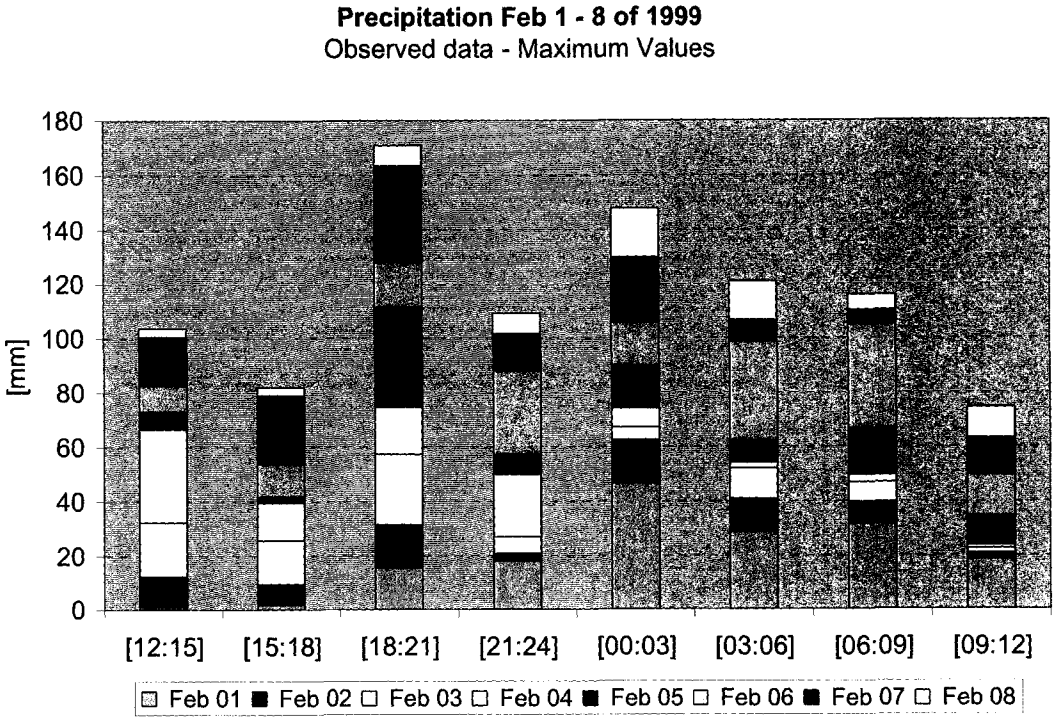

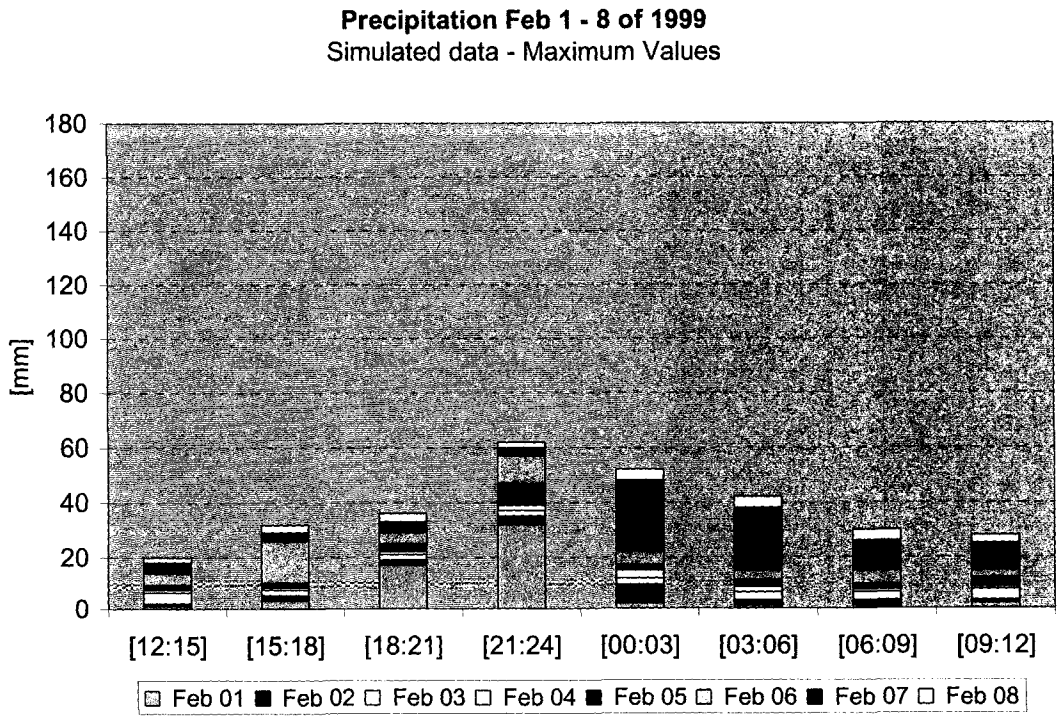

Figure 8-19: Diurnal Precipitation cycle from February 01-08 of 1999. Mean intensity values in the area with precipitation. Upper plot corresponds to observed values and lower plot corresponds to simulated values.

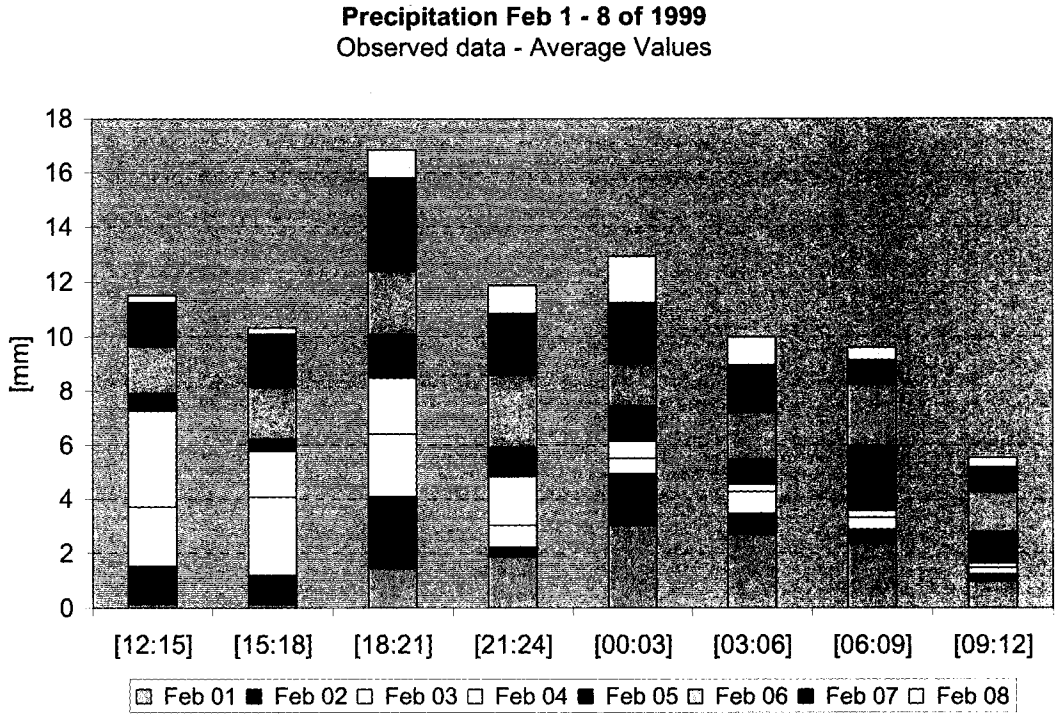

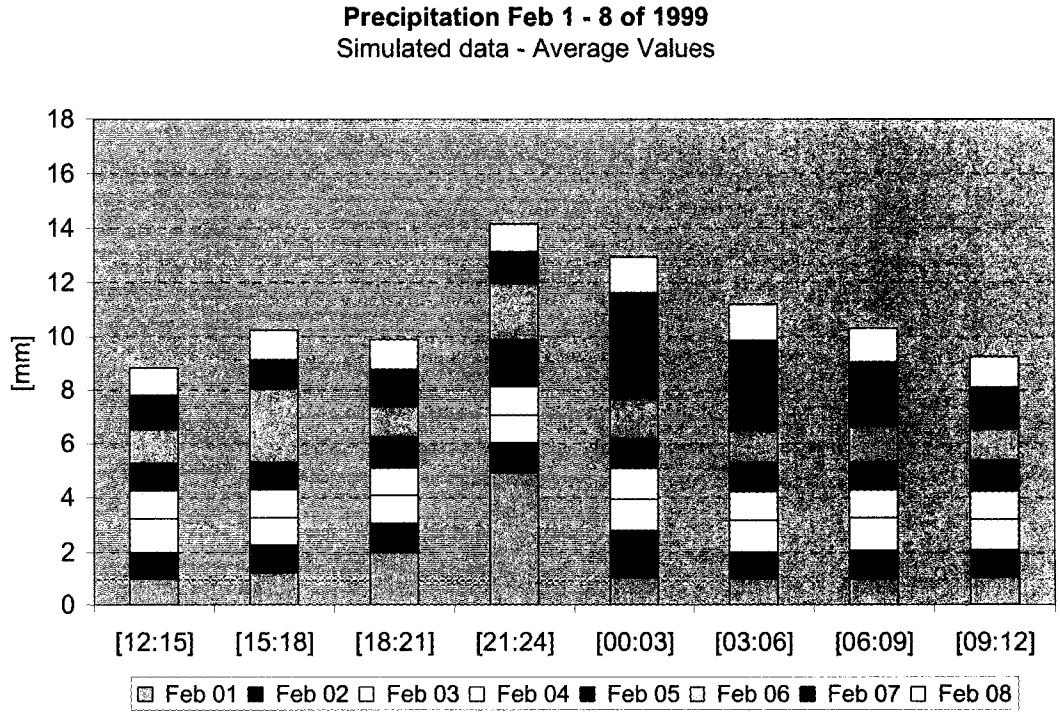

Figure 8-20: Diurnal Precipitation for elevations less than 1000-m. Upper plot corresponds to the observed average values in the area of study and lower plot corresponds to simulated average values in the area of study.

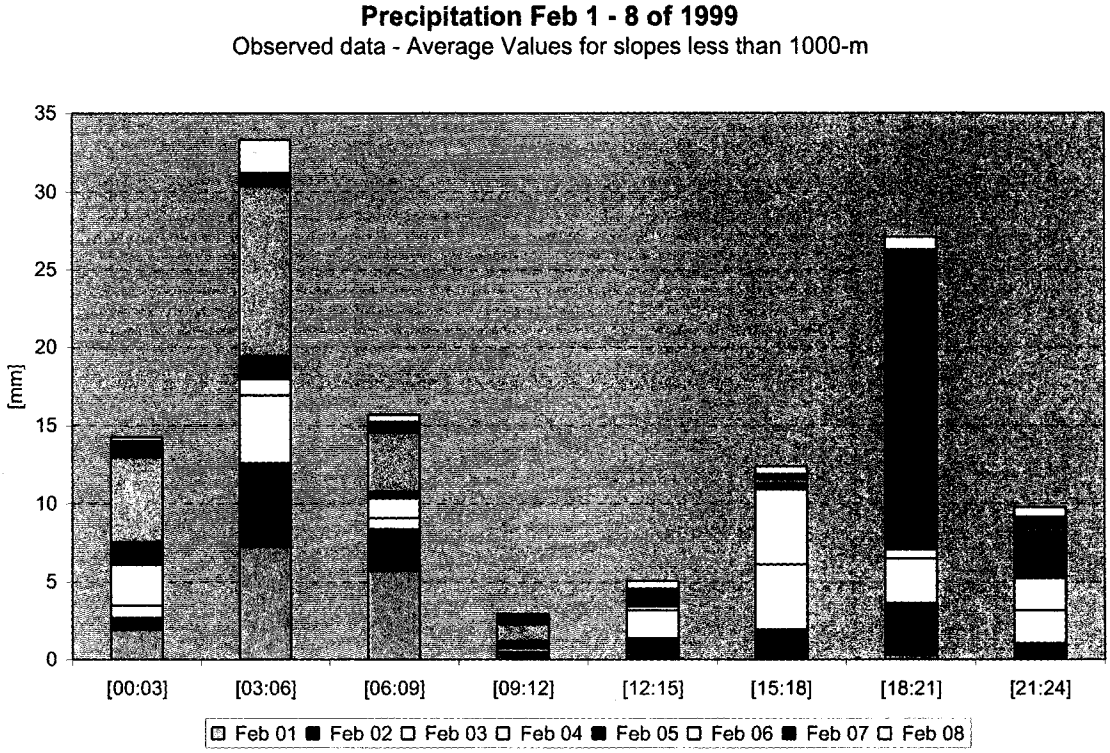

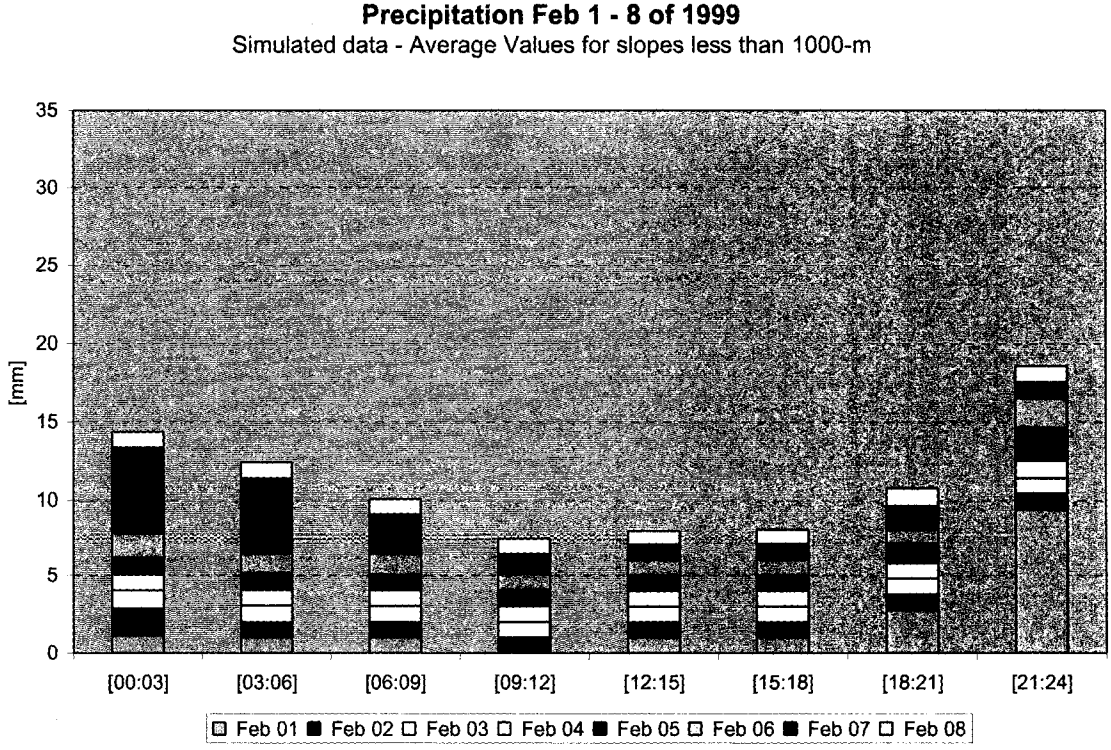

Figure 8-21: Diurnal Precipitation on the slopes between 1000 and 2000-m. Upper plot corresponds to the observed average values in the area of study and lower plot corresponds to simulated average values in the area of study.

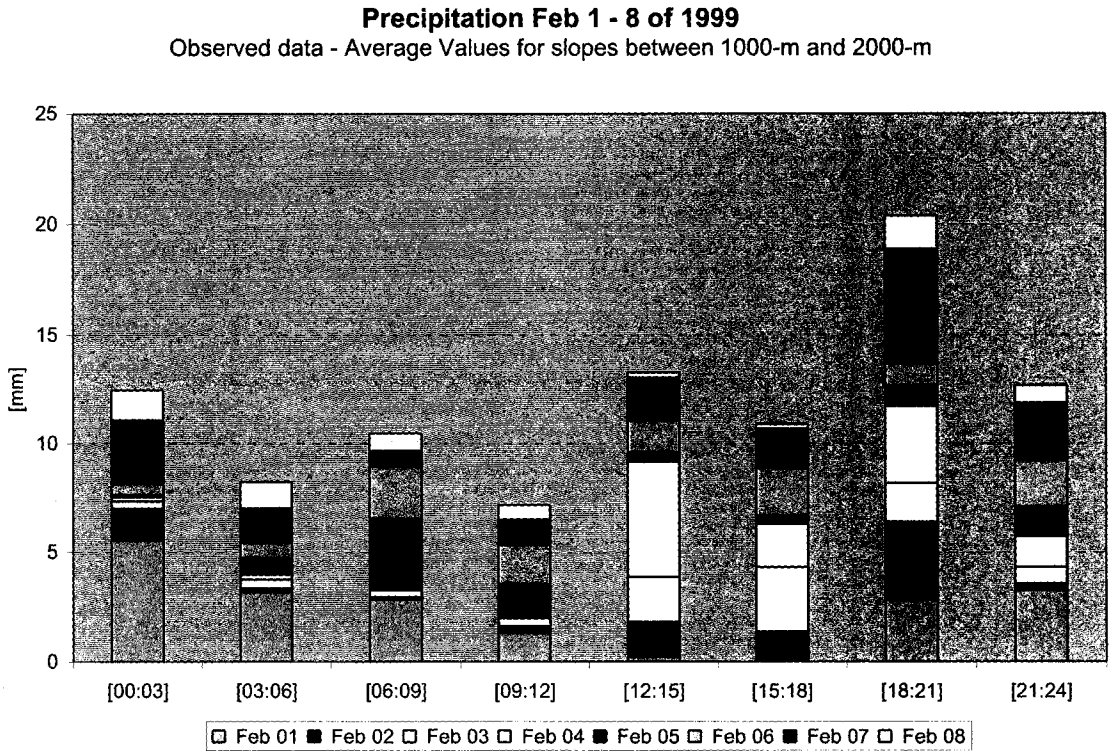

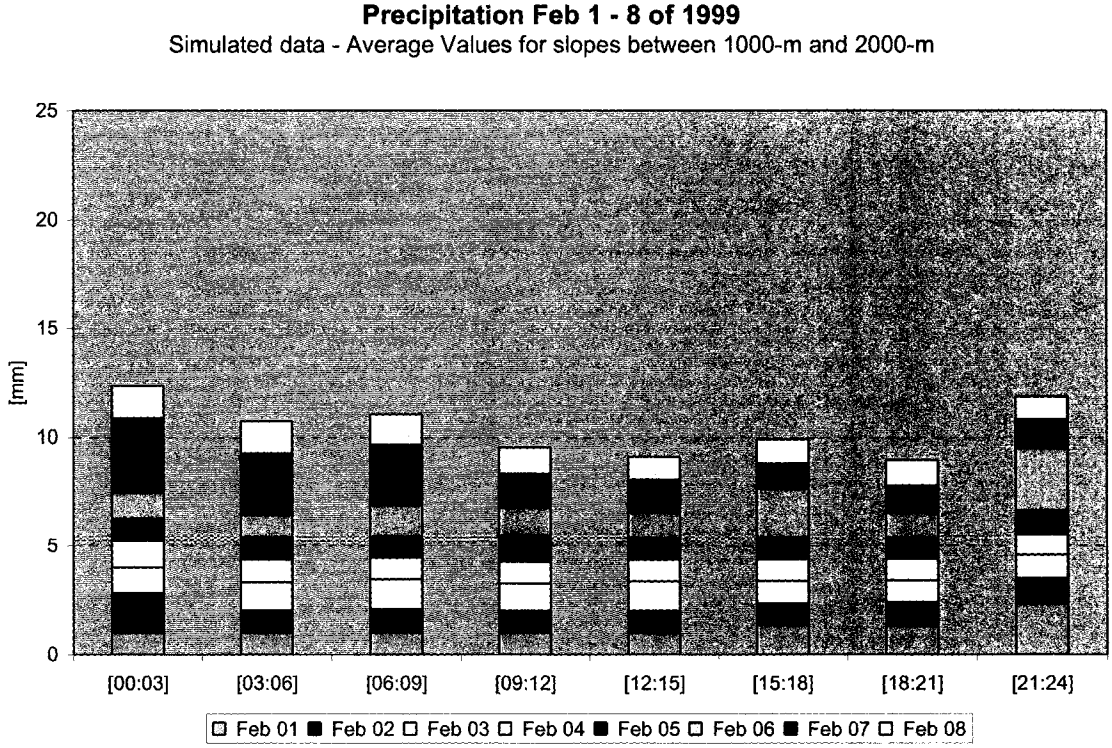

Figure 8-22: Diurnal Precipitation for elevations greater than 2000-m. Upper plot corresponds to the observed average values in the area of study and lower plot corresponds to simulated average values in the area of study.

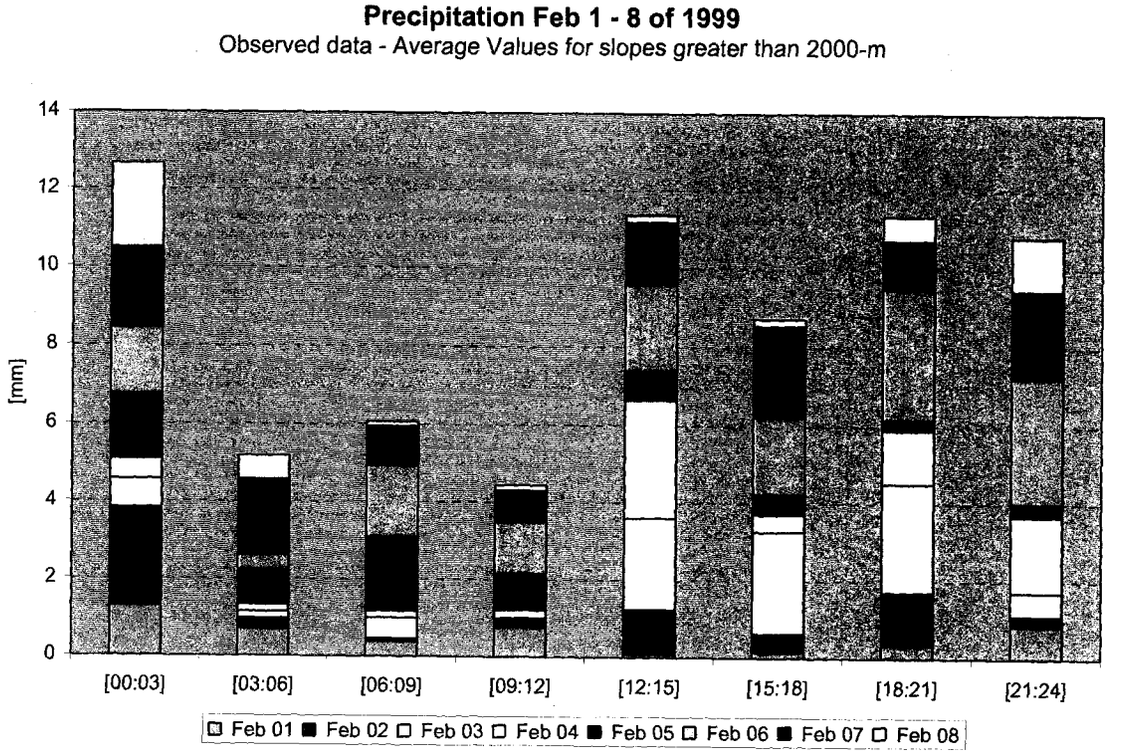

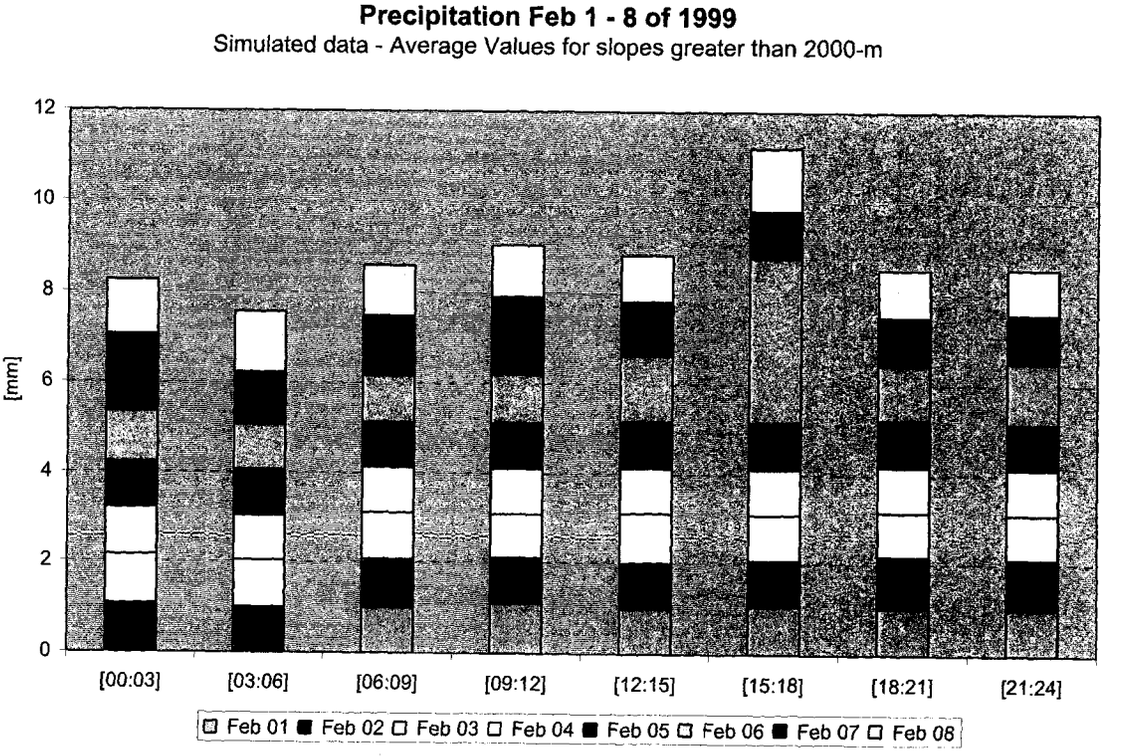

Figure 8-23: Precipitation for February 01-08 1999; volumes are plotted successively for every twenty-four hour period. Upper plots correspond to observed values and lower plots correspond to simulated values.

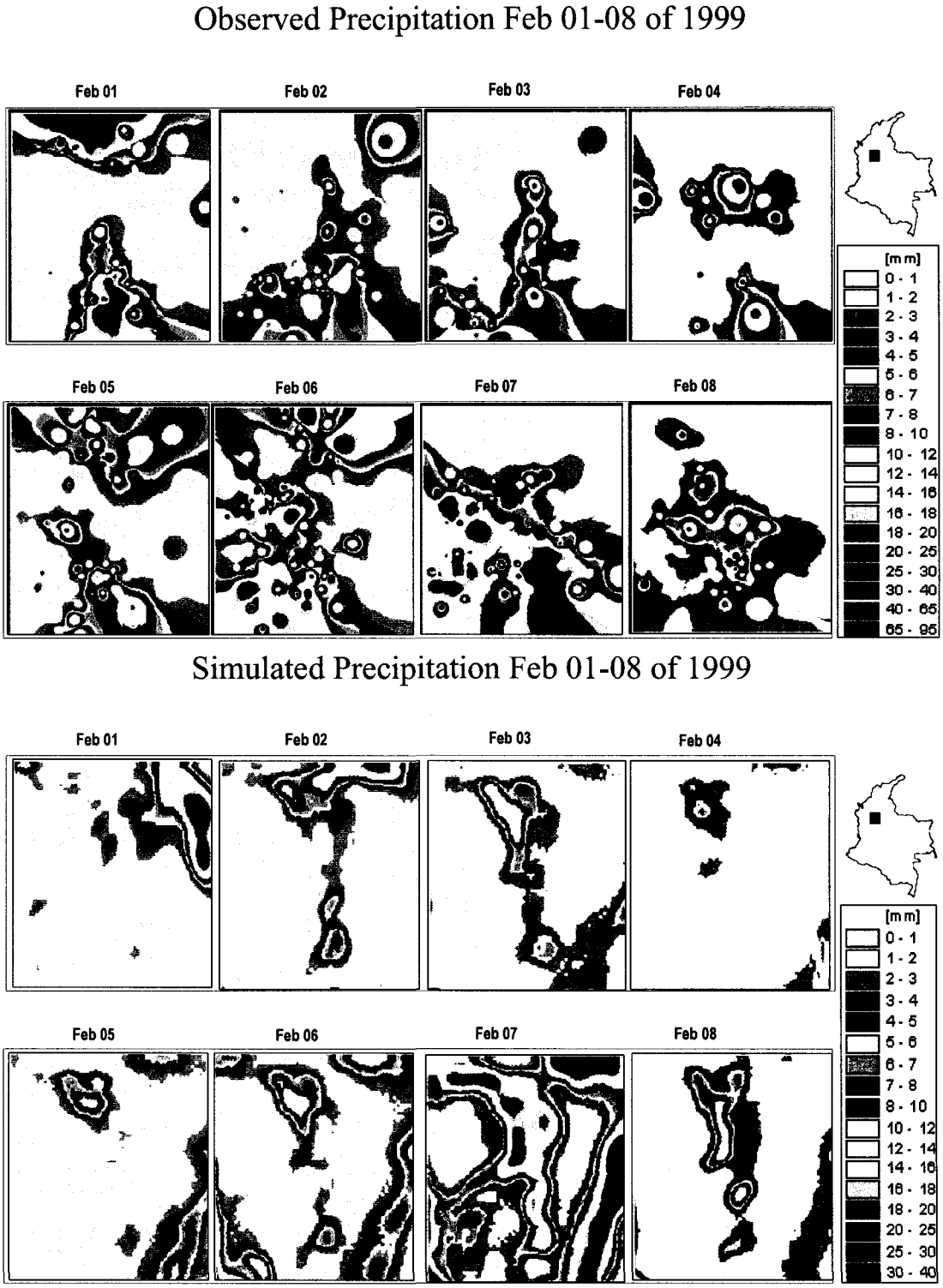

Figure 8-24: Diurnal Precipitation, February 01-08 of 1999. Upper plot corresponds to maximum values in the area of study and lower plot corresponds to average values in the area of study.

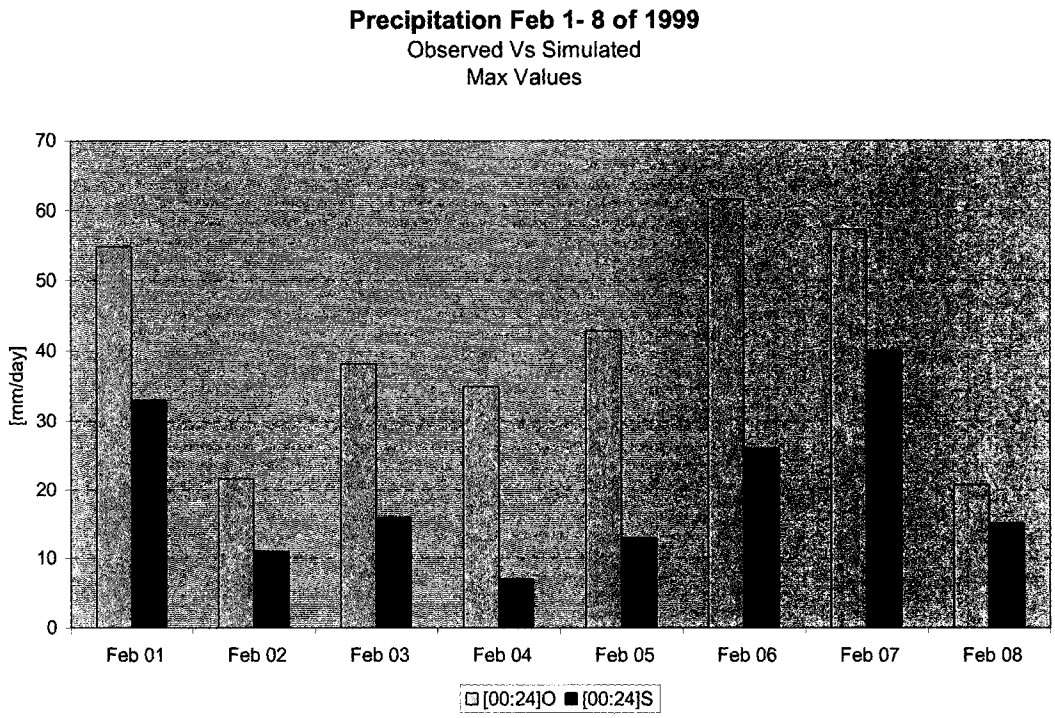

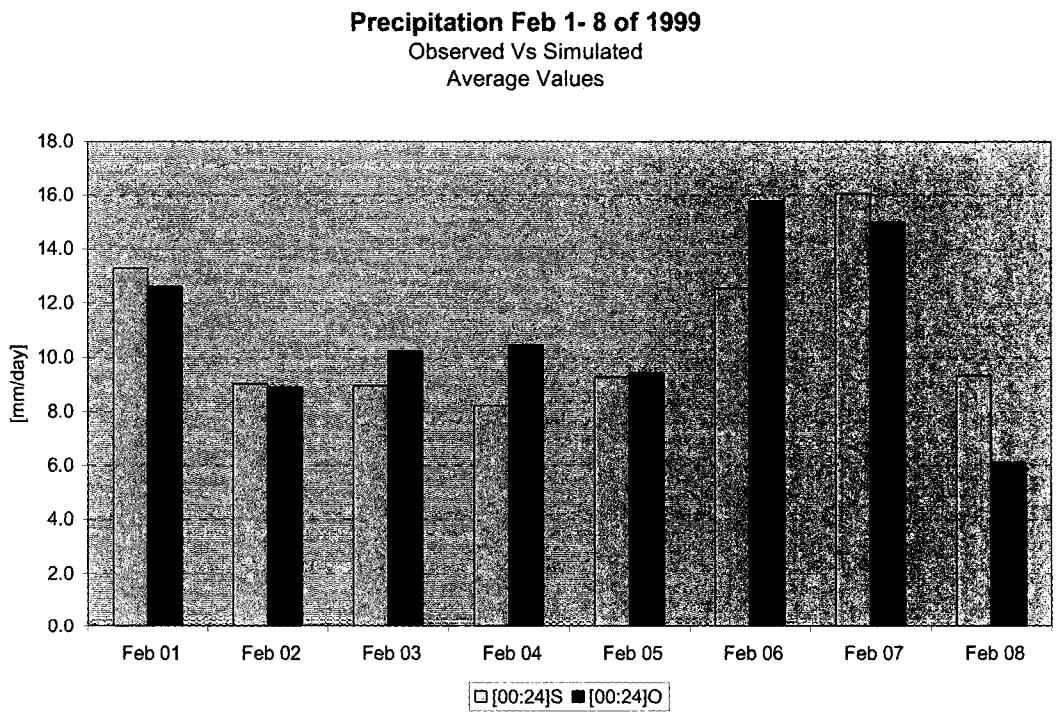

Figure 8-25: Guadalupe watershed - September 25-30 of 1998: Upper plot shows simulated and observed average values of precipitation. Lower plot shows the hydrologic response to these average values of precipitation and the streamflow measured in the basin.

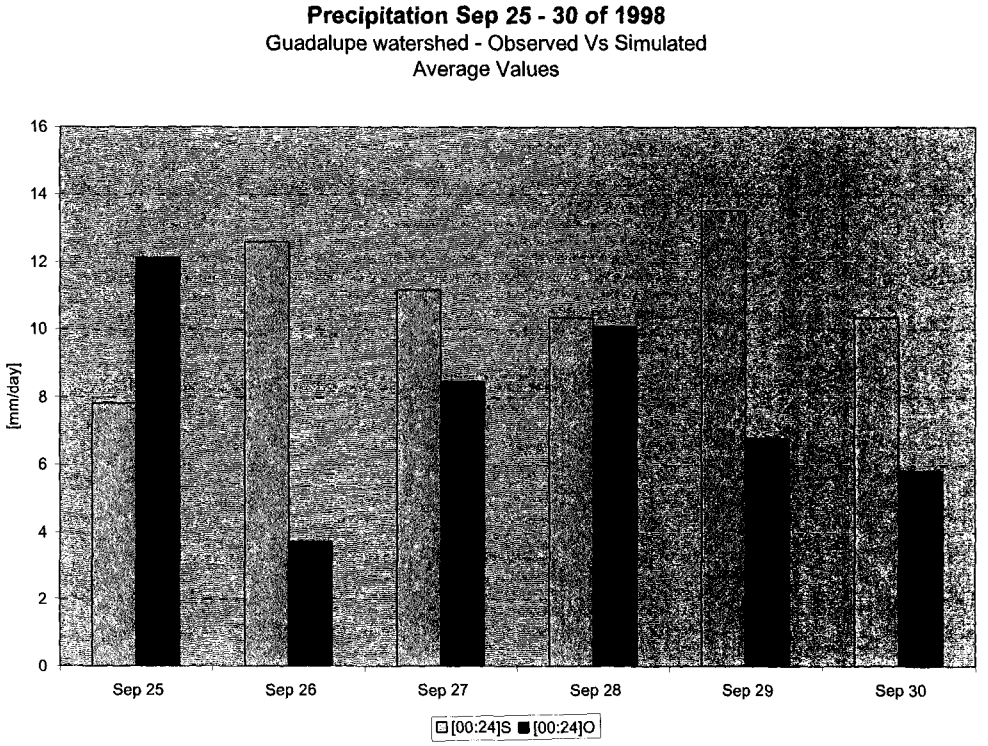

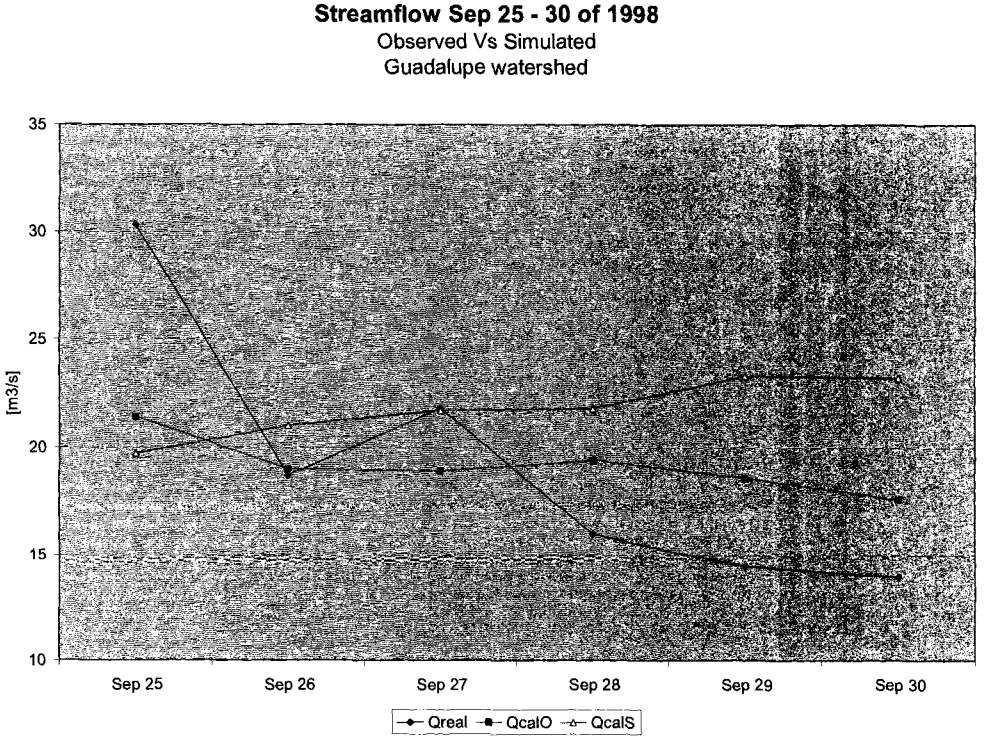

Figure 8-26: Guadalupe watershed - February 1-8 of 1999: Upper plot shows simulated and observed average values of precipitation. Lower plot shows the hydrologic response to these average values of precipitation and the streamflow measured in the basin.

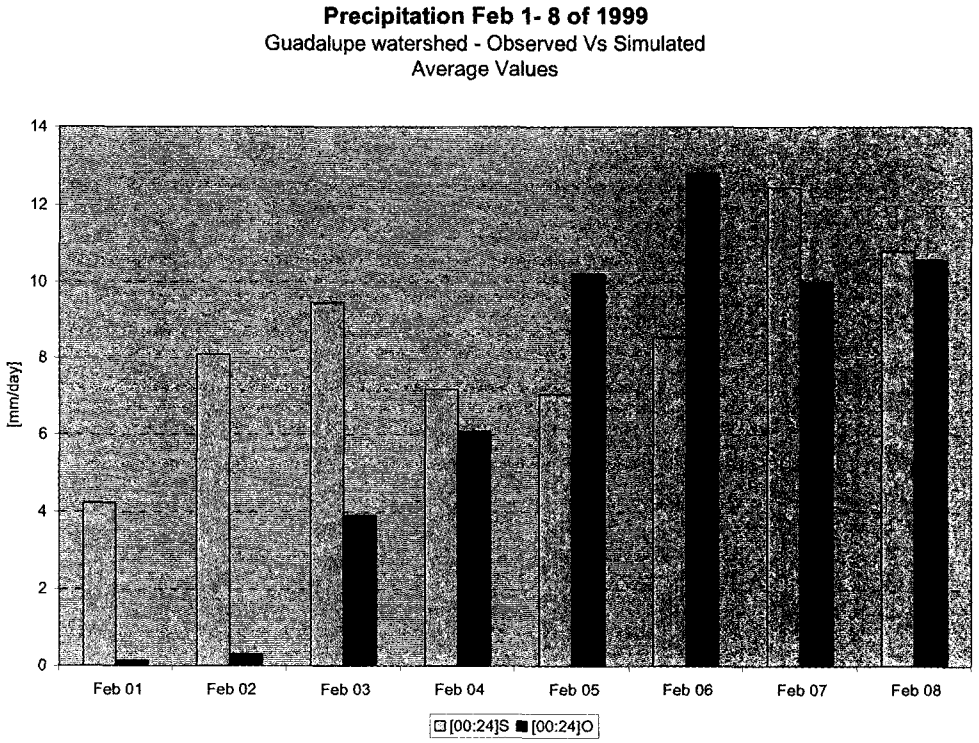

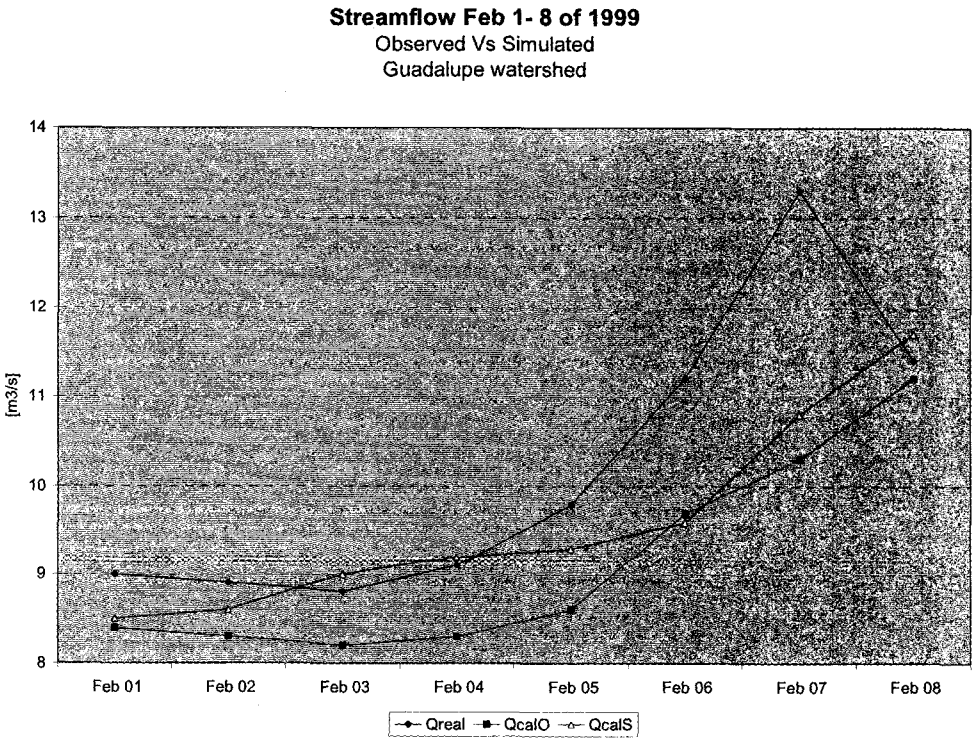

Figure 8-27: Guatape watershed - September 25-30 of 1998: Upper plot shows simulated and observed average values of precipitation. Lower plot shows the hydrologic response to these average values of precipitation and the streamflow measured in the basin.

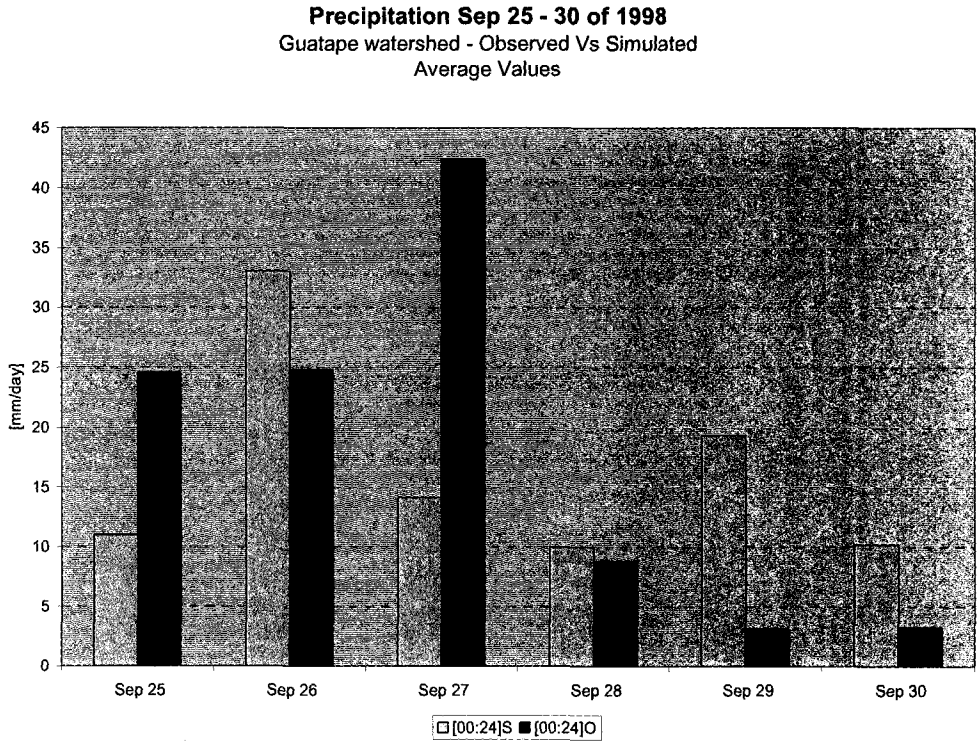

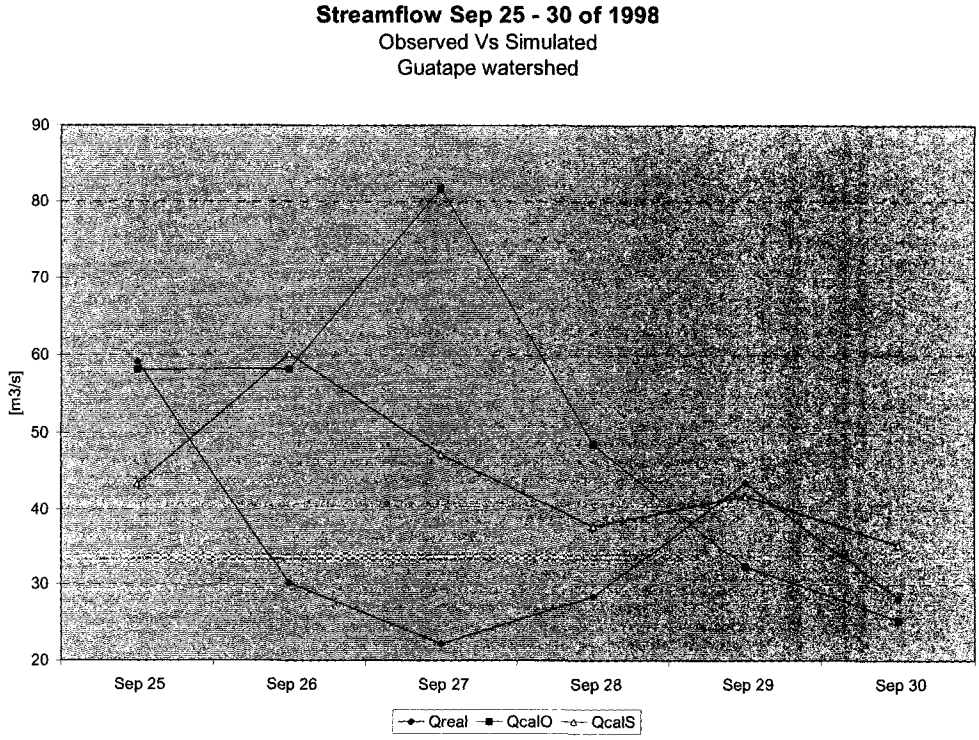

Figure 8-28: Guatape watershed - February 1-8 of 1999: Upper plot shows simulated and observed average values of precipitation. Lower plot shows the hydrologic response to these average values of precipitation and the streamflow measured in the basin.

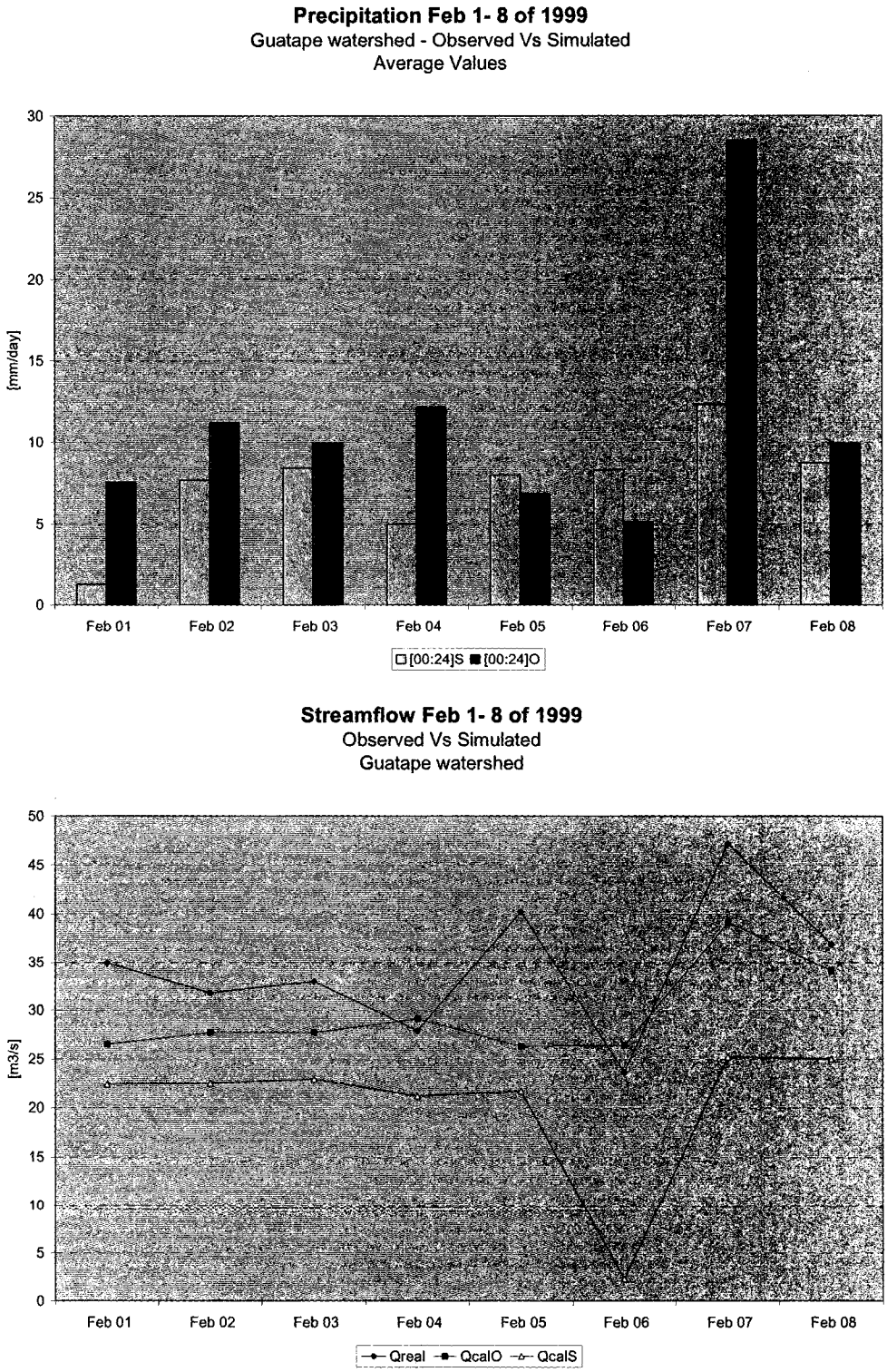

Figure 8-29: Nare watershed - September 25-30 of 1998: Upper plot shows simulated and observed average values of precipitation. Lower plot shows the hydrologic response to these average values of precipitation and the streamflow measured in the basin.

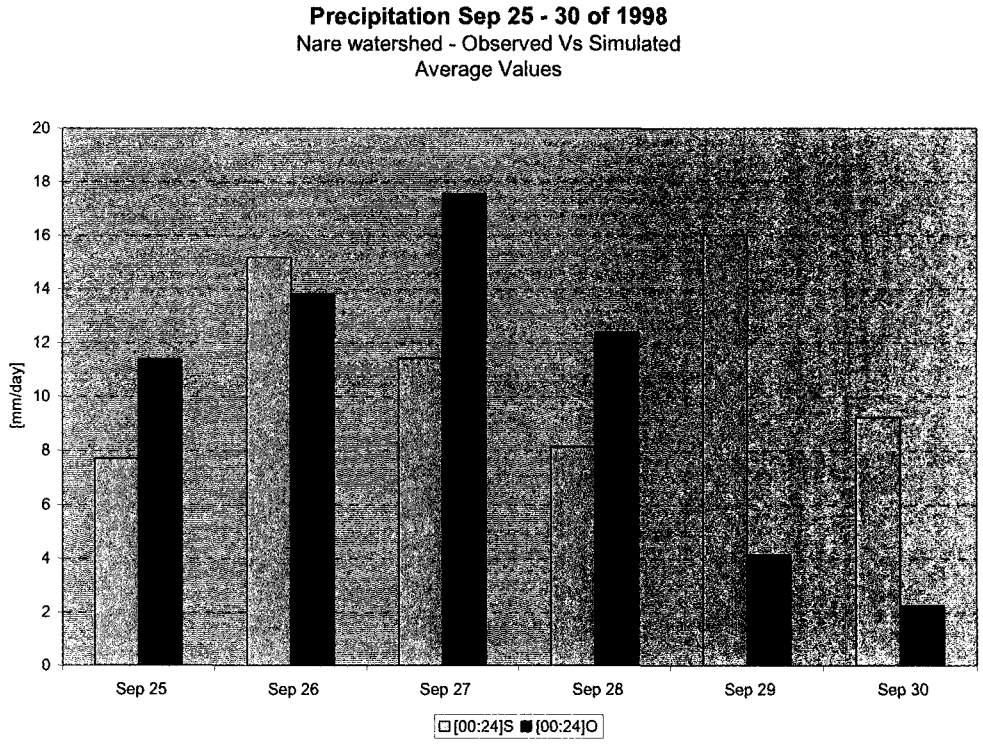

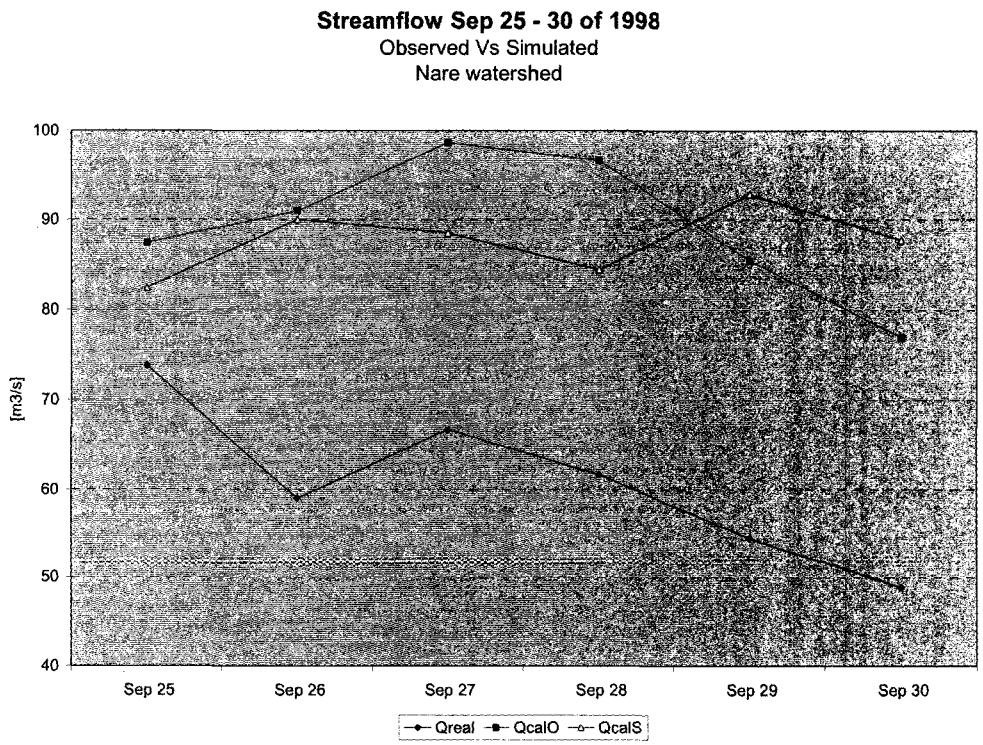

Figure 8-30: Nare watershed - February 1-8 of 1999: Upper plot shows simulated and observed average values of precipitation. Lower plot shows the hydrologic response to these average values of precipitation and the streamflow measured in the basin.

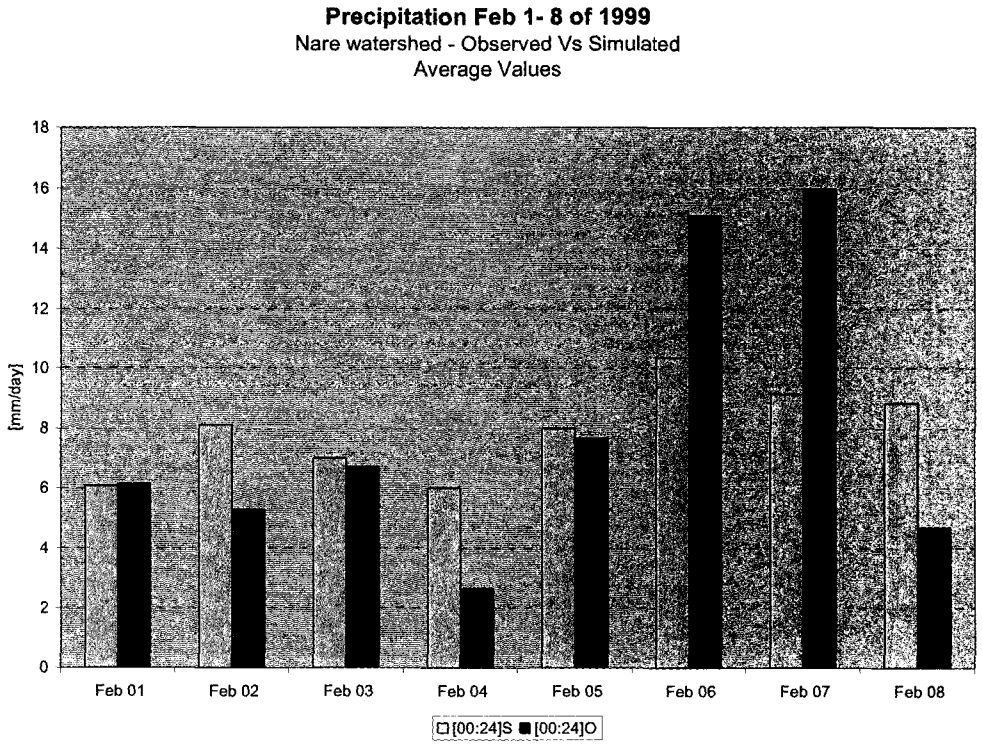

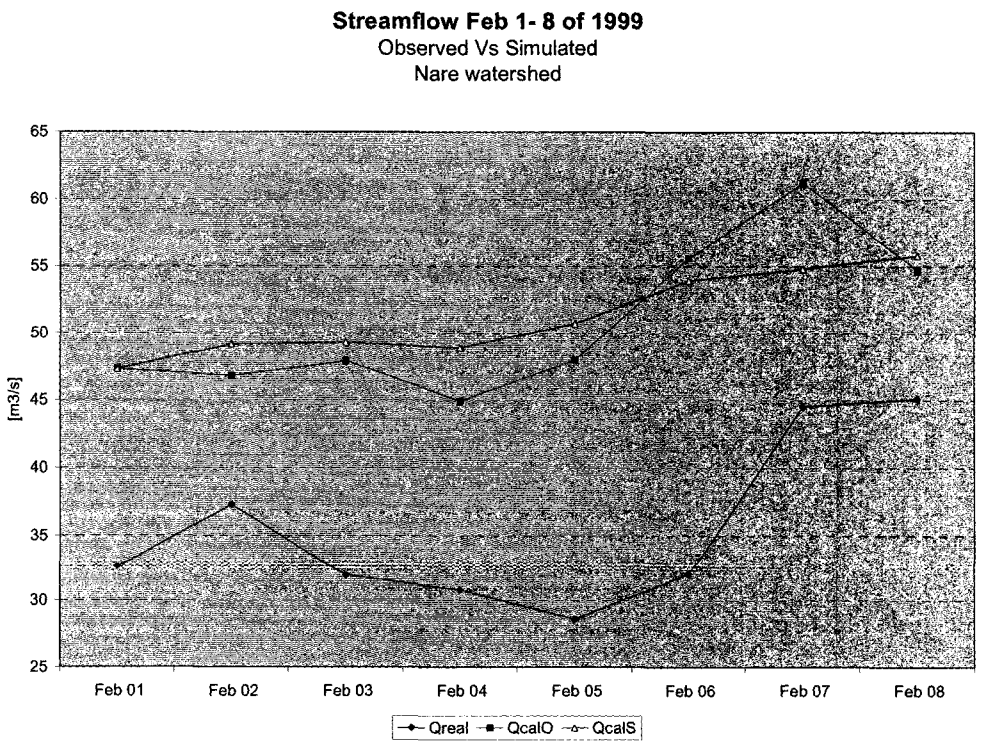

9 DISCUSSION AND COMMENTS

The contributions of this research focus on the implementation and application in Colombia of a set of models, a regional climate model and a hydrologic model. The main objective of this methodology of implementation is to describe and simulate the effects of macroclimatic phenomena and large scale atmospheric circulation on the regional and local hydro-climate system of Colombia, with special emphasis on precipitation and other important variables driving hydrologic response. This physically based technique is presented as suitable to translate knowledge of general macroclimate phenomena into information that can be used for optimal regional and local socio-economic planning and management of water resources.

9.1 Weather and Climate

In order to objectively assess the performance of a numerical model by comparing simulation results with observations in a specific region, it is first necessary to assess the quality of the data used to drive the model, e.g., the quality and density of surface and rawinsonde observations used as input data to the modeling system. In using a regional climatic model for mesoscale analysis, many of the surface and upper climate data available to use as initial and boundary conditions are not real observations, but *modeled observations* obtained through a process of temporal and spatial reanalysis. The resulting reanalysis data are a composite of modeled and observational information. When the real observations are scarce, as is the case for Colombia, reanalysis data are more a result of a global climate model than of the observed data. In Colombia, the limited observed available data could be sufficient for construction of an analysis of large-scale conditions as reanalysis data, but probably not for obtaining a good analysis of mesoscale and local features. Therefore, it is at these scales (mesoscale and local) where a mesoscale model such as CSU-RAMS may be expected to be useful. Therefore, this study does not focus on a comprehensive test of the RAMS model (the model has been thoroughly tested and

evaluated elsewhere), but on its great importance in order to model the mesoscale and local features of weather and climate.

In this study two different time scales were considered, the first one focusing on the annual cycle and the second focusing on the diurnal cycle. The seasonal time scale analysis attempts to describe and simulate observed hydroclimatological differences throughout a year as well as differences between dry and wet years. The diurnal time scale analysis attempts to describe and simulate the observed diurnal cycle and observed storms at a specific place and date.

One of the most important variables used in the optimal planning and management of water resources is precipitation because it constitutes a measure of the potentially available resource; therefore, comparison between RAMS simulation results and observed data focused mainly on this variable. However, as indicated in earlier chapters, precipitation processes are not explicitly resolved in RAMS but are parameterized, and the appropriate parameterization scheme depends on the grid size of the model implementation. Therefore, in addition to an assessment of the simulated precipitation, an assessment based on basic variables and properties of the atmosphere important in governing the precipitation process (e.g., temperature, specific humidity, convective available potential energy, etc.) was performed. Basic variables chosen for this comparison were temperature, wind velocity, pressure, water mixing ratio, and relative humidity field. If the basic variables, rather than precipitation itself, are simulated well, it is assumed that the discrepancy is the consequence of an inappropriate parameterization and that, therefore, either adjustments are required to the given parameterization or that a completely different parameterization should be used.

As indicated earlier, one of the most important characteristics of the temperature distribution in the tropics is that the diurnal temperature range, generally of around 10°C, is larger than the annual temperature range measured as the temperature difference between the warmest and coldest months, generally of around 5°C. Therefore, because of the particular temporal scales emphasized in this study (seasonal intra annual and diurnal scales), relevant measures of the veracity of the simulation of the heating cycle are the corresponding monthly and diurnal variations in temperature. It was shown that

simulation results compare well with observed data for both seasonal and diurnal scales. The model replicates reasonably well (see Chapter 6) monthly average temperature distributions as well as the amplitude between the coldest and the warmest month. Similarly, the model simulates reasonably well the observed diurnal temperature cycle (see Chapter 8) and, on most simulated days, the model replicates well the 8-10°C amplitude of the diurnal temperature oscillation. Therefore, our implementation of the CSU-RAMS model for Colombia succeeded in reproducing one of the main climatic characteristics of tropical regions, demonstrating the adequacy of the RAMS model to simulate weather and climate over a broad range of temporal and spatial scales, and a broad range of climatic regimes.

Simulated wind profiles compared reasonably well with reanalysis data. As expected from the climate simulations, confrontation between reanalysis and simulated maps show better agreement on oceanic areas. Similarity is expected near the model boundaries because of the nudging imposed in the analysis. Differences in the interior of the simulation domain are determined by the physics and dynamics of the model. An additional factor contributing to the more localized differences observed in the interior of the domain, especially over land, may be the difference between grid sizes of the reanalysis and simulated data, whereas reanalysis data come from a data set with a grid size of around 300 km, simulated data are obtained from a grid size of 160 km. Therefore, reanalysis data do not capture the dynamics of orographically driven circulations that, because of its higher resolution, the CSU-RAMS model implementation is able to describe and simulate more adequately. Therefore, these differences inland may be taken as a good indicator, especially when, as is the case here, they are well correlated with orography or other known local forcing. Unfortunately, the available observations were insufficient in order to check the diurnal cycle. However, it seems that topography influences air motions, actively producing local circulations driven by the trade winds (see Chapter 8). In conclusion, as for the case of temperature distributions, our implementation of the CSU-RAMS model for Colombia succeeded in capturing the main patterns of observed wind circulations. Being able to accurately simulate local wind patterns is a prerequisite to being able to simulate atmospheric moisture fluxes in the area of interest, a high priority in order to simulate precipitation. Finally, it is important to

highlight that, on a regional scale, surface wind patterns are highly spatially homogeneous and that they tend to be generally calm during the simulated period. This behavior also is a characteristic of wind fields in the tropics.

As is the case for temperature, simulated surface pressure compares well with reanalysis data. CSU-RAMS simulated surface pressure fields that match well the observations. As expected, the spatial distribution of observed surface pressure depends highly on Colombian orography and no major discrepancies between simulated pressure fields and those from reanalysis data appear. The Andes ranges mainly modulate the spatial distribution of this variable, whereas the temporal distribution at a monthly scale is almost negligible. This is corroborated by observed data, which show that the spatial distribution of the pressure field is almost constant throughout the year in Colombia.

Clearly, precipitation, the ultimate variable of interest in this study, and atmospheric moisture availability are intricately related. Therefore, the spatial distribution of observed precipitation and the spatial distribution of simulated atmospheric moisture should be in agreement. CSU-RAMS simulation results of surface relative humidity and water mixing ratio show good correspondence between each other. Maps of observed and simulated distributions of atmospheric moisture (see Chapter 6) show high values of atmospheric moisture in western Colombia and on the east slope of the Eastern range, which generally correspond well with the regions of high precipitation. Better simulation of these fields is shown for western Colombia and around the Andes Mountains. However, the model never reaches the super saturation shown in the reanalysis data. Major discrepancies occur in the Amazon and Llanos areas where the model seems to be drier than reanalysis. This fact is then reflected on the simulated precipitation, giving an unrealistic deficit of precipitation in those areas.

Finally, comparisons of rainfall patterns were performed with respect to both seasonal and diurnal temporal scales. Two aspects were examined for the seasonal scale: the annual cycle for a specific year was examined first, and seasonal differences between dry and wet years were examined last. These comparisons were performed at the mesoscale using 40 km grid cell size for the finest grid. With respect to the diurnal scale,

comparisons emphasized the diurnal cycle at the local scale using a finest grid cell size of 2.5 km.

Observations of monthly precipitation in Colombia indicate that enhanced rainfall occurs in western Colombia, over the Pacific region extending into the foothills of the western slope of the Andes western range. Similarly, the eastern slope of the Eastern range of the Andes and some regions located north of the Central range of the Andes also show relatively higher precipitation. These features of the distribution of monthly rainfall are replicated well in the model simulation results that are driven by initial and boundary fields containing wind and thermodynamic state variables. However, the model appears to produce excessive rainfall in some areas of the Pacific and mountain regions and to under-estimate rainfall over the Llanos and Amazon regions. Given the generally good simulation results for other atmospheric variables presented above, this disagreement in precipitation could be associated with deficiencies in the parameterization scheme used, pointing to a need to adjust the existing parameterization or develop new parameterizations to better match specific equatorial dynamics. However, despite the above discrepancy, mesoscale comparisons were very favorable to the model, showing not only the ability of the model to simulate the observed intra-annual variability of precipitation but also to be able to respond adequately to large scale climate signals to differentiate between wet or dry years. On the intra-seasonal timescale, the model simulates well not only the increase in precipitation observed in 1989 and the precipitation decrease observed in 1992, but also the magnitudes of the changes. Summarizing, at the largest scales, the observed and simulated patterns of rainfall are similar. Maximum rainfall in and around the mountains compares very well between simulated and observed data, but there is a large region in eastern Colombia with no observed data available where simulations seem to produce an unrealistic deficit. It appears that the interaction between large scale forcing and local relief is well simulated by the model, triggering the appropriate mechanisms to produce precipitation in mountain regions. However, the parameterization schemes implemented seem to have difficulty in initiating precipitation in large land low areas, as the Llanos and the Amazon.

An especially important characteristic of weather and for the purposes of this study is the mean diurnal cycle of rainfall. Therefore, an important test of our modeling

approach is its ability to simulate the diurnal cycle of precipitation for the region of interest. Using observations of hourly precipitation, it was shown that simulated rainfall at 3-h intervals compared qualitatively and quantitatively well with observed data during two short periods of 6 and 8 days. In the area of study, in the Central range of the Andes, rainfall tends to occur predominantly in the late afternoon and night hours, showing two maxima during this period of the day, and then diminishing through the late morning. Simulated data compare well, but the model tends to produce only one maximum of precipitation around midnight, and the period of enhanced precipitation starting late in the afternoon and ending in the early morning hours. Even though quantitative comparisons are difficult on small scales, the model does a good job, and we may summarize major differences as follows: 1) discrepancies in the maximum rainfall amounts reach values of up to 50%; 2) the maximum rainfall also tends to occur later in simulations; 3) the nocturnal rainfall over the studied area is lighter and dissipates earlier in the simulation; 4) the spatial distribution of simulated precipitation is partially out of phase; and 5) the duration of simulated storms is shorter, but the cycle among a cascade of storms is preserved.

In conclusion, comparison of simulated and observed data shows that the accuracy of modeled results may be influenced by several factors including: 1) the model representation of topography, 2) the initial and boundary conditions and, 3) the parameterization schemes used. Comparisons of temperature fields, pressure fields, water mixing ratio fields and relative humidity fields show that the CSU-RAMS model is capable of accurately simulating and reproducing the observations. On the other hand, comparisons of precipitation fields clearly show that there needs to be a better parameterization of precipitation-producing processes for tropical settings.

Importantly, a sensitivity analysis not included in the text of this dissertation, which was part of the model implementation procedure, showed that there were notable differences in the amount of precipitation in simulation results between various simulations in which either the radiation parameterization scheme was changed, or the precipitation parameterization scheme was changed, or parameter values of the bulk microphysics scheme were changed, but that the pattern of the spatial distribution was conserved. That is, model output is extremely sensitive to these changes, in particular

precipitation. It is challenging and difficult to determine exactly why a certain combination of parameters and/or parameterization schemes produces results more in agreement with observations because the convective parameterization, the bulk microphysics parameterization and the radiation schemes interact via numerous non-linear processes. However, understanding why one model arrangement is better than another is essential in order to determine the physical parameterizations that are optimal for predictability studies with CSU-RAMS in Colombia. On the other hand, the analysis presented in this study may help identify what processes must be accurately represented and which ones are important in tropical regions.

Finally, the CSU-RAMS model, as well as required, datasets have been improved since this research started. Therefore, the modeling tools and data required in order to apply the proposed methodology not only are available but, most important, are constantly improving, ensuring the methodological adjustments required to improve results. That is, the modeling approach implemented should be dynamic rather than static, requiring modifications and enhancements to those models as more is learned about the important governing processes. In conclusion, regardless of the complexity of tropical weather and climate processes and the dearth of theories and conceptual models to analyze and describe them relative to mid-latitude circulations, the results of this dissertation show that current models (e.g., CSU-RAMS) and currently available data allow for an adequate modeling leading to potential increases in understanding of the non-linear interactions between large scale atmospheric phenomena and local weather and climate, as demonstrated for the case of Colombia.

9.2 Hydrologic System Response

As indicated in the previous section, besides the appropriateness of the model itself, the most important element determining how well the hydrologic model describes the hydrologic system response is the quality of the data used to drive the model, including initial conditions, boundary conditions, and forcing. Consequently, given the modeling approach used here, namely a one-way coupling of a regional atmospheric model and a hydrologic model in which the hydrologic model is forced by the output

from the atmospheric model, the success of the hydrologic model will be directly dependent on the success of the atmospheric model.

In order to minimize uncertainties in the atmospheric model field results, observed field data should be incorporated during the modeling process to improve the hydrologic model results. In such a way, the atmospheric model output does not replace the observed data, but simply provides additional information of those fields difficult to measure. Accordingly, the coupled modeling approach should incorporate assimilation of available observed data during the simulation process.

Although fully distributed hydrologic models (and atmospheric models as well) allow for a more detailed description of the hydrologic system, the associated processes, and their response, their implementation and use is sometimes hampered by the lack of data to characterize the system and its forcing. This is especially true in Colombia. Measurements and observations of precipitation, soil moisture, surface pressure, relative humidity, and other important hydrometeorological variables are very sparse in space and in time, or do not exist. Generally, these sparse observations are used to obtain large scale averages that are appropriate only as indicators of possible ranges but not sufficient to be used as inputs for a modeling process. Consequently, an atmospheric model is an excellent tool for making inferences of information required for a distributed hydrologic modeling system.

In this study this step is taken in order to show the feasibility of linking the output of the atmospheric model with a hydrologic model, even if the last one is not a fully distributed model. The linked process has a great potential for developing operational short-term forecasts fundamental for an optimal water resources project operation. Despite the fact that the HBV-HMS is not a fully distributed model, that the model was driven by daily average precipitation values from simulations results, and that no calibration was performed, the results clearly showed that this approach is valid and useful. Results show that for both periods and for the three watersheds analyzed the simulated stream flow compares well with observed values.

9.3 Future Research

The work presented here constitutes the first attempt at developing a physically based modeling approach to improve the characterization and prediction of weather and climate in Colombia so that it can be used in the optimal planning and management of water resources in Colombia. The methodology implemented consists of coupling a mesoscale atmospheric model to a hydrologic model in order to make short-term streamflow forecasts. The results obtained have clearly validated this modeling approach as well as shown the great potential that such approach has to be further improved. The author expects that the work presented here will motivate additional studies by researchers and those in charge of managing water resources in Colombia. In particular, the following aspects are of importance:

- Adjustment of parameterization schemes and development of new schemes more appropriate for tropical regions.
- Incorporation of better initial and boundary conditions, and better relief representation.
- Testing a link with a full distributed hydrologic model.
- Using the set of models, a regional climate model and a hydrologic model, to analyze scenarios of climate change in Colombia, global warming, land use change, etc.
- Doing specific research on some particularities of the climate of Colombia, including: (1) The Pacific Jet Stream; (2) Precipitation particularities on the Sierra Nevada de Santa Marta; (3) The Atrato watershed, characterized by the largest amounts of precipitation in the world; (4) The Guajira Peninsula as the driest region of Colombia; (5) Wind velocity studies as a source for the new eolian electric project, already developed.

10 REFERENCES

Aceituno, P., 1988: On the functioning of the Southern Oscillationin the South American sector. Part I: Surface climate. Mon. Wea.Rev., 116, 505–524.

Aceituno, 1989: On the functioning of the Southern Oscillation in theSouth American sector. Part II: Upper-air circulation. J. Climate,2, 341–355.

Avissar Roni, 1993: Approach to Bridge the Gap Between Microscale Land-Surface Processes and Synoptic-Scale Meteorological Conditions Using Atmospheric Models and GIS: Potential for Applications in Agriculture. Environmental modeling with GIS / [edited by] Michael F. Goodchild, Bradley O. Parks, Louis T. Steyaert. New York : Oxford University Press, pp 123-134.

Avissar, R., and Y. Mahrer 1988: Mapping frost-sensitive areas with a three-dimensional local-scale numerical model. Part I: Physical and numerical aspects. J. Appl. Meteor., 27, 400-413.

Barnes, S. L., 1973: Mesoscale objetive map analysis using weighted time-series observations. NOAA Tech. Memo. ERL NSSL-62 [NTIS COM-73-10781], March, National Severe Storms Laboratory, Norman, Oklahoma, 60pp.

Bergström, S., 1976: Development and application of a conceptual runoff model for Scandinavian catchments. Ph.D. Thesis. SMHI Reports RHO No. 7, Norrköping.

Bergström, S., 1992: The HBV model - its structure and applications. SMHI Reports RH, No. 4, Norrköping.

Bergström, S., 1995: The HBV model. Contribution to: Computer Models of Watershed Hydrology, Water Resources Publications.

Bergström, S., and A. Forsman, 1973: Development of a conceptual deterministic rainfall-runoff model. Nordic Hydrology, Vol. 4, No. 3.

Bleck, R., and P. L. Haagenson, 1968: Objective analysis on isentropic surfaces. NCAR Tech. Note, TN-39, December, National Center for Atmospheric Research, Boulder, Colorado, 27pp.

Bliss, N.B., and L.M. Olsen, 1996: Development of a 30-arc-second digital elevation model of South America. In: Pecora Thirteen, Human Interactions with the Environment - Perspectives from Space, Sioux Falls, South Dakota, August 20-22, 1996.

Carvajal, L. F., J. E. Salazar, O. J. Mesa, y G. Poveda, 1998: Predicción hidrológica en Colombia mediante análisis espectral singular y máxima entropía. Ingeniería Hidráulica en México, Vol. XIII, Num 1, 07-16.

Chen, S. and W.R. Cotton, 1983: A one-dimensional simulation of the stratocumulus-capped mixed layer. Boundary-Layer Meteorol., 25, 289-321

Chen, S. and W.R. Cotton, 1987: The physics of the marine stratocumulus-capped mixed layer. J. Atmos. Sci., 44, 2951-2977.

Chen, S. and W.R. Cotton, 1988: The Sensitivity of a Simulated Extratropical Mesoscale Convective System to Long Wave Radiation and Ice-Phase Microphysics. J. Atmos. Sci., 45, 3897-3910.

Clark, T.L., 1977: A small-scale dynamic model using a terrain-following coordinate transformation. J comp. Phys., 24, 186-215.

Cox, R., B. L. Bauer, and T. Smith, 1998: A Mesoscale Model Intercomparison. Bulletin of the American Meteorological Society. v79, 2, 265-283.

Cotton, W.R., M.-S. Lin, C.J. Tremback, and McAnelly, 1989: A composite model of mesoscale convective complexes. Mon. Wea. Rev., 117, 765-783.

Cotton, W.R., G.J. Tripoli, R.M. Rauber, and E.A. Mulvihill 1986: Numerical simulation of the effects of varying ice crystal nucleation rates and aggregation processes on orographic snowfall. J Clima. Appli. Meteor., 25, 1558-1680.

Cotton, W.R., M.A. Stephens, T. Nehrkorm, and G.J. Tripoli 1982: The Colorado State University three-dimensional cloud/Mesoscale model – 1982. part II: An ice phase parameterization. J de rech. Atmos., 16, 295-320.

Davies, H. C., 1976: A lateral boundary formulation for multi-level prediction models. Quart. J. Roy. Meteor. Soc., 102, 405–418.

Davies, H. C., 1983: Limitations of some common lateral boundary schemes used in regional NWP models. Mon. Wea. Rev., 111, 1002-1012.

Deardorff, J.W., 1980: Stratocumulus-capped mixed layers derived from a three-dimensional model. Boundary Layer Meteorol., 18, 495-527.

Epstein, D., and J. A. Ramírez, 1994: Spatial Disaggregation for Studies of Climatic Hydrologic Sensitivity. *ASCE Journal of the Hydraulics Division* 120(12): 1449-1467.

Fritsch, J.M., and C.F. Chappell, 1980a: Numerical prediction of convectively driven mesoscale pressure systems. Part I: Convective parameterization. J. Atmos. Sci, 37, 1722-1733.

Gal-Chen, T., and R.C.J. Somerville, 1975: On the of a coordinate transformation for the solution of the Navier-Stokes equations. J. Comppt. Phys., 17, 209-228.

Gershunov, A. and T. P. Barnett, 1998: Interdecadal Modulations of ENSO Teleconnections. Bulletin of the American Meteorological Society. v79, 12, 2715-2725.

Gessler, R. D., 1995: Precipitation variability over Ecuador associatedwith the El Niño/Southern Oscillation. M.S. thesis, Dept. of Geography, University of Florida, 85 pp. [Available from P. Waylen, Dept. of Geography, University of Florida, Gainesville, FL32611-7315.]

GOALS, 1994: Global Ocean-Atmosphere-Land System for Predicting Seasonal to interannual Climate. National Academic Press, Washington, D.C.

Graham, L.P., S. Bergström, and D. Jacob, 1998: A discussion of land parameterization in hydrologic and climate models - example from the Baltic Sea Basin. Cont. to the Second International Conference on Climate and Water. Espoo, Finland, 17-20 August.

Graham, L. P., 1999: Modelling runoff to the Baltic basin. Ambio (28):328-334.

Grasso, L.D., 1992: Tornado genesis. M.S. Thesis, Department of Atmospheric Science, Colorado State University, Fort Collins, Colorado, 102 pp.

Halpert, M. S., and C. F. Ropelewski, 1992: Surface temperaturepatterns associated with the Southern Oscillation. J. Climate, 5,577–593.

Hastenrath, S., 1976: Variations in low-latitude circulations and extreme climatic events in the tropical Americas. J. Atmos. Sci.,33, 202–215.

Hastenrath, 1990: Diagnostic and prediction of anomalous river dischargesin northern South America. J. Climate, 3, 1080–1096.

Hill, G.E., 1974: Factors controlling the size and spacing of cumulus clouds as revealed by numerical experiments. J. Atmos. Sci., 31, 646.

Holton, J.R., 1992: An Introduction to the Dynamic Meteorology. Academic press, New York, 507p.

Horel, J. D., and J. M. Wallace, 1981: Planetary scale atmospheric phenomena associated with the Southern Oscillation. Monthly Weather Review, 109, 813-829.

IGAC, 1990: Antioquia – Caracteristicas Geograficas. Instituto Geografico Agustin Codazzi, Subdireccion de Geografia. Seccion de Imprenta y Ediciones IGAC. Santafe de Bogota.

Kalnay, E., M. Kanamitsu, R. Kistler, W. Collins, D. Deaven, L. Gandin, M. Iredell, S. Saha, G. White, J. Woollen, Y. Zhu, M. Chelliah, W. Ebisuzaki, W. Higgins, J. Janowiak, K. C. Mo, C. Ropelewski, J. Wang, A. Leetmaa, R. Reynolds, Roy Jenne, and Dennis Joseph, 1996: The NMC/NCAR 40-Year Reanalysis Project". Bull. Amer. Meteor. Soc., 77, 437-471.

Kang, B. and J.A. Ramírez, 2002: Stochastic Space-Time Inversion Schemes for NEXRAD Precipiation, Proc. AGU Hydrology Days 2002, J.A. Ramírez (ed), Hydrology Days Publications, Fort Collins, CO., 164-174.

Kidson, J. W., and C. S. Thompson, 1998: A comparison of Statistical and Model-Based Techniques for Estimating Local Climate Variations, J. Climate, 11, 735–753.

Kiladis, G., and H. F. Diaz, 1989: Global climatic anomalies associated with extremes in the Southern Oscillation, J. Climate, 2,1069–1090.

Kistler, R., E. Kalnay, W. Collins, S. Saha, G. White, J. Woollen, M. Chelliah, W. Ebisuzaki, M. Kanamitsu, V. Kousky, H. Dool, R. Jenne, and M. Fiorino. The NCEP/NCAR 50-years Reanalysis. Last revision 12 June, 1999. Submitted to the Bulletin of the American Meteorological Society

Kite, G.W., 1997: Simualting Colombia River flows with data from regional-scale climate models. Water Resour. Res. 33, 1275-1285.

Klemp, J.B. and D.R. Durran, 1983: An upper boundary condition permitting internal gravity wave radiation in numerical mesoscale models. Mon. Wea. Rev., 111, 430-444

Klemp, J.B. and D.K. Lilly, 1978: Numerical simulation of hydrostatic mountain waves. J. Atmos. Sci., 35, 78-107.

Klemp, J.B. and R.B. Wilhelmson, 1978a: The simulation of three-dimensional convective storm dynamics. J. Atmos. Sci., 35, 1070-1096.

Klemp, J.B. and R.B. Wilhelmson, 1978b: Simulation of right- and left-moving storms produced through storm splitting. J. Atmos. Sci., 35, 1097-1110.

Kousky, V. E., and M. T. Kayano, 1994: Principal modes of outgoinglongwave radiation and 250-mb circulation for the South American sector. J. Climate, 7, 1131–1143.

Kuo, H.L., 1974: Further studies of the parameterization of the influence of cumulus convection on largescale flow. J. Atmos. Sci., 31, 1232, 1240.

Lilly, D.K., 1962: On the numerical simulation of buoyant convection. Tellus, XIV, 2, 148-172.

Lee, T. J., 1992: The impact of vegetation on the atmospheric boundary layer and convective storms. Ph.D. Dissertation, Department of Atmospheric Science, Colorado State University, Fort Collins, Colorado, 137pp.

Lindström, G., 1997: A simple automatic calibration routine for the HBV model. Nordic Hydrology, Vol. 28, No. 3, pp 153-168.

Lindström, G., Johansson, B., Persson, M., Gardelin, M. and Bergström, S., 1997: Development and test of the distributed HBV-96 hydrological model. Journal of Hydrology, Vol. 201, pp. 272-288.

Lopez, M.E. and W.E. Howell, 1967: Katabatic winds in the equatorial Andes. Jour. Atmos.Sci., 24, 29-35.

Louis, J.F., 1979: A parametric model of vertical eddy fluxes in the atmosphere. Boundary-Layer Meteorol., 17, 187-202.

Lynch-Stieglitz, M., 1995: The development and validation of a new land surface model for regional and global climate modeling. Ph.D. thesis, Columbia University, 89 pp.

Maddox, R.A., 1980: Mesoscale convective complexes, Bull. Amer. Meteor. Soc., 61, 1374-1387.

Maddox, R.A., 1981: The structure and life-cycle of midlatitude mesoscale convective complexes. Atmospheric Science Paper No 336, Dept. of Atmospheric Science, Colorado State University, Fort Collins, Colorado, 80523, 311 pp.

Mahrer, Y. and R.A. Pielke, 1977: A Numerical Study of the Air Flow over Irregular Terrain. Contrib. Atmos. Phys., 50, 98-113.

Mapes, B.E., T.T. Warner, and Mei Xu, 2002: Diurnal patterns of rainfall in northwestern South America. Part I: Observations and context. MWR, revised August 2002

Mapes, B.E., T.T. Warner, and Mei Xu, 2002: Diurnal patterns of rainfall in northwestern South America. Part III: Diurnal gravity waves and nocturnal convection offshore. MWR, revised August 2002

Marengo, J.,and S. Hastenrath, 1993: Case studies of extreme climaticevents in the Amazon basin. J. Climate, 6, 617–627.

Martinez, M.T., 1993: Principales sistemas sinopticos en Colombia y su influencia en el comportamiento del tiempo, Atmosfera, 16, 1-10.

McCumber M.C., and R.A. Pielke, 1981: Simulation of the effects of surface fluxes of heat and moisture in a mesoscale numerical model. Part I: Soil layer. J. Geophys. Res., 86, 9929-9938.

McNider, R.T., 1981: Investigation of the impact of topographic circulations on the transport and dispersion of air pollutants. Ph.D. dissertation, University of Virginia, Charlottesville, VA 22903.

McNider, R.T., and R.A. Pielke, 1981: Diurnal boundary-layer development over slopping terrain. Journal of the Atmospheric Sciences. 38; 2128-2212.

McNider, R.T., M.D. Moran, and R.A. Pielke, 1988: Influence of diurnal and inertial boundary layer oscillations on long-range dispersion. Atmos. Environ., 22, 2445-2462.

McQueen, J. T., R. R. Draxler, B. J. B. Stunder and G. D. Rolph, 1997: Applications of The Regional Atmospheric Modeling System (RAMS) at the MOAA Air Resources Laboratory. NOAA Technical Memorandum ERL ARL-220, 50pp.

Mesa, O. J., G. Poveda, L. F. Carvajal y J. E. Salazar, 1994a: Efecto del fenómeno de El Niño-Oscilación del Sur en la hidrología Colombiana, *Memorias del XVI Congreso Latinoamericano de Hidráulica e Hidrología*, Vol. 3, IAHR, Santiago de Chile, 373-384.

Mesa, O. J., L. F. Carvajal, J. E. Salazar, y G. Poveda, 1994b: Predicción hidrológica usando redes neuronales, *Memorias del XVI Congreso Latinoamericano de Hidráulica e Hidrología*, IAHR, Santiago de Chile, Vol. 3, 385-396.

Mesa O.J, G. Poveda, L.F. Carvajal, 1997: Introduccion Al Clima de Colombia. Universidad Nacional de Colombia. Imprenta Universidad Nacional, Medellin.

Mesinger F., and A. Arakawa, 1976: Numerical methods used in Atmospheric Models. GARP publications series, No 14, WMO/ICSU Joint Organizing Committee, 64pp.

Meyers, M.P., and W.R. Cotton, 1992: Evaluation of the potential for wintertime quantitative precipitation forecasting over mountainous terrain with an explicit cloud model. Part I: Two-dimensional sensitivity experiments. J. Appl. Meteor., 31, 26-50

Molinari, j., 1985: A general form of Kuo's cumulus parameterization. Mon. wea. Rev., 113, 1411-1416.

Moss, M. E., C. P. Pearson, and A. I. McKerchar, 1994: The SOI as a predictor of the probability of low stremflows in Mew Zeland. Water Resources Research, 30, 2717–27

Orlanski, I., 1976: A simple boundary condition for unbounded hyperbolic floes. J. Compt. Phys., 21, 251-269.

Over T.M., 1995: A Space-Time Theory of Mesoscale Rainfall Using Random Cascades, Ph.D. dissertation, University of Colorado, Boulder, CO.

Over T.M., and V.K. Gupta, 1994: Statistical Analysis of Mesoscale Rainfall: Dependence of a Random Cacade Generator on Large-Scale Forcing. J. Appl. Meteorol., 33, 1526-1542.

Perkey, D.J. and C.W. Kreitzberg, 1976: A time-dependent lateral boundary scheme for limited-area primitive equarion models. Mon. Wea. Rev., 104, 744-755.

Philip, G.M. and D.F Watson, 1982: A precise method for determining contoured surfaces. Australian Petroleum Exploration Association Journal 22, 205-212.

Pielke, R.A., W.R. Cotton, R.L. Walko, C.J. Tremback, W.A. Lyons, L.D. Grasso, M.E. Nicholls, M.D. Moran, D.A. Wesley, T.J. Lee, and J.H. Copeland, 1992: A comprehensive meteorological modeling system -- RAMS. Meteor. Atmos. Phys., 49, 69-91.

Piotr J.F., G.J. Tripoli, J. Verlinde and W.R. Cotton, 1989: The CSU-RAMS Cloud Microphysics Module: General Theory and Code Documentation. Department of Atmospheric Science, Colorado State University, Fort Collins, CO 80523, September 1 of 1989. Paper No 451.

Poveda, G., 1994: Cuantificacion del efecto de el Niño y la Niña sobre los Caudales en Colombia, *Memorias del XVI Congreso Latino-Americano de Hidráulica e Hidrología*, IAHR, Santiago de Chile, Vol. 4, 107-117.

Poveda, G., and O. J. Mesa, 1993: Metodologias de prediccion de la hidrologia Colombiana considerando el evento El Niño-Oscilacion del Sur (ENOS). Atmosfera, 17 Sociedad Colombiana de Meteorologia. Bogota, Colombia.

Poveda, G., and O. J. Mesa, 1995: The relationship between ENSO and the hydrology of tropical South America. The case of Colombia. Proceeding of XV Hydrology Days, A.G.U., 227236.

Poveda, G., and O. J. Mesa, 1996: Las fase extremas del fenómeno ENSO (El Niño y La Niña) y su influencia sobre la hidrología de Colombia. Ingeniería Hidráulica en Mexico. XI(1):21-37.

Poveda, G. and O. J. Mesa, 1997: Feedbacks between the hydrology of tropical South America and large scale oceanic-atmospheric phenomena. J. Climate. 10(10) 2690-2702

Poveda, G., and C. Penland, 1994: Predicción de caudales medios en Colombia usando Modelación Lineal Inversa, *Memorias del XVI Congreso Latino-Americano de Hidráulica e Hidrología*, IAHR, Santiago de Chile, Vol. 4, 119-129.

Poveda, G., C. D. Hoyos, J. F. Mejía, L. F. Carvajal, O. J. Mesa, A. Cuartas and J. Barco, 2001: Prediccion no lineal de la hidrometeorologia de Colombia. Caso de estudio: Caudales del rio Nare. Posgrado en Aprovechamiento de Recursos Hidraulicos, Universidad Nacional de Colombia, Medellin - Colombia. correo-e: gpoveda@perseus.unalmed.edu.co.

Pulwarty, R. S., 1994: Annual and intrannual variability of convection over tropical South America. Ph.D. dissertation, University of Colorado, 220 pp. [Available from Dept. of Geography, University of Colorado, Boulder, CO 80305.]

Pulwarty, R. S., R.G. Barry and H. Riehl, 1992: Annual and seasonal patterns of rainfall variability over Venezuela, Erdkunde, 46, 273-289.

RAMS Technical Manual: RAMS, The Regional Atmospheric Modeling System. Technical Description. DRAFT. Atmospheric, Meteorologial, and Environmental Technologies – ATMET electronic page. http://www.atmet.com/html/docs/documentation.shtml.

Rasmusson, E. M., and T. H. Carpenter, 1982: Variations in tropical sea surface temperature and surface wind fields associated with the Southern Oscillation. Monthly Weather Review, 110, 354-384.

Rasmusson, E.M., and J.M. Wallace, 1983: Meteorological aspects of the El Niño/Southern Oscillation. Science, 222, 1195-1202.

Reynolds, R. W., 1988: A real-time global sea surface temperature analysis. J. Climate, 1, 75-86.

Reynolds, R. W. and D. C. Marsico, 1993: An improved real-time global sea surface temperature analysis. J. Climate, 6, 114-119.

Reynolds, R. W. and T. M. Smith, 1994: Improved global sea surface temperature analyses using optimum interpolation. J. Climate, 7, 929-948.

Richey, J. E., C. Nobre, and C. Deser, 1989: Amazon river dischargeand climate variability: 1903 to 1985. Science, 246, 101–103.

Rogers, J. C., 1988: Precipitation variability over the Caribbean andtropical Americas associated with the Southern Oscillation. J.Climate, 1, 172–182.

Saelthun, N.R., P. Aittoniemi, S. Bergström, K. Einarsson, T. Jóhannesson, G. Lindström, P. E. Ohlsson, T. Thomsen, B. Vehviläinen, and K. O. Aamodt, 1998: Climate change impacts on runoff and hydropower in the Nordic countries. Final report from the project "Climate Change and Energy Production" Tema Nord 1988:552, Oslo.

Salazar, J. E., O. J. Mesa, G. Poveda and L. F. Carvajal, 1994b: Modelamiento del fenómeno ENOS en la hidrología Colombiana mediante procesos autoregresivos dependientes del régimen, *Memorias del XVI Congreso LatinoAmericano de Hidráulica e Hidrología*, IAHR, Santiago de Chile, Vol. 4, 181-191.

Shaw, E.M., 1988: Hydrology in practice, second edition. Chapman and Hall, London, U.K.

Smagorinsky, J., 1963: General circulation experiments with the primitive equations. Part I, The basic experiment, Mon Wea. Rev., 91, 99-164.

Snow, J.W., 1976: The climate of northern South America. In: Climates of Central and South America, (W. Schwerdtfeger, ed.), Elsevier, Amsterdam, 295-403.

Stieglitz, M., R. David, F. James, and R. Cynthia, 1997: An Efficient Approach to Modeling the Topographic Control of Surface Hydrology for Regional and Global Climate Modeling. Journal of Cliamte, 10, 118-137.

Tremback, C. J., 1990: A numerical simulation of Mesoscale Convective Complex: Model development and numerical results. Ph.D. Dissertation. Department of Atmospheric Science, Colorado State University. 247 pp.

Tremback, C. J., J. Powell, W.R. Cotton and R.A. Pielke, 1987: the forward in time upstream advection scheme. Extension to higher orders. Mon. Wea. Rev., 115, 540-555.

Tremback, C. J., G.J. Tripoli, W.R. Cotton, 1985: A regional scale atmospheric numerical model including explicit moist physics and a hydrostatic time-split scheme. Preprints, 7th AMS Conference on Numerical Weather Prediction, June 17-20, Montreal, Quebec, Canada, Amer. Meteor. Soc., Boston, 433-434.

Tremback, C.J. and R. Kessler, 1985: A surface temperature and moisture parameterization for use in mesoscale numerical models. Preprints, 7th Conference on Numerical Weather Prediction, 17-20 June 1985, Montreal, Canada, AMS.

Trenberth, K. E., 1992: Global analyses from ECMWF and Atlas of 1000 to 10 mb Circulation Statistics. Tech. Rep. NCAR/TN-373+STR, National Center for Atmospheric Research, Boulder, Colorado.

Tripoli, G. J., and W. R. Cotton, 1982: The Colorado State University three-dimensional cloud/mesoscale model. Part I: General theoretical framework and sensitivity experiments. J. Rech. Atmos., 16, 185–220.

Uliasz, Marek. 1993: The Atmospheric Mesoscale Dispersion Modeling System. Journal of Applied Meteorology: Vol. 32, No. 1, pp. 139–140.

Vehvilainen, B., and J. Lohvansuu, 1991: The effects of climate change on discharges and snow cover in Finland. - Hydrological Sciences Journal, 36, 2, 4.

Velasco, I., and M. Fritsch, 1987: Mesoscale convective complexesin the Americas. J. Geophys. Res., 92(D8), 9591–9613.

Velez, I., G. Poveda, O. Mesa, 2000: Balances Hidrologicos de Colombia. Universidad Nacional de Colombia, Sede Medellin. Todograficas Ltda.

Walko, R. L., C. J. Tremback, and R. F. A. Hertenstein, 1995: RAMS, The Regional Atmospheric Modeling System version 3b User's Guide. AsTER, Inc., P.O. Box 466, Ft Collins, CO, 117pp

Warner T.T., B.E. Mapes, and Mei Xu, 2002: Diurnal patterns of rainfall in northwestern South America. Part II: Model simulations. , MWR, revised August 2002

Watson, D.F., G.M. Philip, 1985: A refinement of inverse distance weighted interpolation. Geo-Processing, 2:315-327.

Waylen, P. R., C. N. Caviedes, and M. E. Quesada, 1996: Interannualvariability of monthly precipitation in Costa Rica. J. Climate,9, 2606–2613.

Waylen P., and G. Poveda, 2002: El Niño–Southern Oscillation and aspects of western South American hydro-climatology. Hydrological Processes. 16, 1247–1260.

Wesley, D. A., 1991: An investigation of the effects of topographic on Colorado Front Range winter storms. Ph.D. Dissertation. Department of Atmospheric Science, Colorado State University, Fort Collins, Colorado, 197 pp.

Wilby R.L., and T.M.L. Wigley, 1997: Dowscaling general circulation model output: A review of methods and limitations. Progress in Physical Geography., 21,4, pp 530-548.

Wood E.F., 1995: Scaling behavior of hydrologic fluxes and variables, Empirical studies using a hydrologic model and remote sensing data. Hydrology. Precess., 9, 331-346.

Woolhiser D.A., T.O. Keefer, and K.T. Redmond, 1993: Southern Oscillation Effects on Daily Precipitation in the Southwestern United States. Water Resources Research, 29, 1287-1295.

Yu Z., M.N. Lakhtakia, B. Yarnal, R.A. White, D.A. Miller, B. Frakes, E.J. Barron, C. Duffy, F.W. Schuartz, 1999: Simulating the river-basin response to atmospheric forcing by linking a mesoscale meteorological model and hydrologic model system. Journal of Hydrology 218, 72-91.

APPENDIX 1

REGIONAL ATMOSPHERIC MODELING SYSTEM

A.1 BASIC EQUATIONS

The basic equations of the Regional Atmospheric Modeling System, RAMS, are the standard hydrostatic or non-hydrostatic Reynolds average primitive equations. The following description is based on RAMS Technical Manual, Tremback (1990) and McQueen et al. (1997).

A.1.1 Momentum equations

$$\frac{\partial u}{\partial t} = -u\frac{\partial u}{\partial x} - v\frac{\partial u}{\partial y} - w\frac{\partial u}{\partial z} - \theta\frac{\partial \pi'}{\partial x} + fv + \frac{\partial}{\partial x}(K_m\frac{\partial u}{\partial x}) + \frac{\partial}{\partial y}(K_m\frac{\partial u}{\partial y}) + \frac{\partial}{\partial z}(K_m\frac{\partial u}{\partial z})$$

$$\frac{\partial v}{\partial t} = -u\frac{\partial v}{\partial x} - v\frac{\partial v}{\partial y} - w\frac{\partial v}{\partial z} - \theta\frac{\partial \pi'}{\partial y} - fu + \frac{\partial}{\partial x}(K_m\frac{\partial v}{\partial x}) + \frac{\partial}{\partial y}(K_m\frac{\partial v}{\partial y}) + \frac{\partial}{\partial z}(K_m\frac{\partial v}{\partial z})$$

$$\frac{\partial w}{\partial t} = -u\frac{\partial w}{\partial x} - v\frac{\partial w}{\partial y} - w\frac{\partial w}{\partial z} - \theta\frac{\partial \pi'}{\partial z} + \frac{g\theta_v'}{\theta_o} + \frac{\partial}{\partial x}(K_m\frac{\partial w}{\partial x}) + \frac{\partial}{\partial y}(K_m\frac{\partial w}{\partial y}) + \frac{\partial}{\partial z}(K_m\frac{\partial w}{\partial z})$$

A.1.2 Thermodynamic equation

$$\frac{\partial \theta_{il}}{\partial t} = -u\frac{\partial \theta_{il}}{\partial x} - v\frac{\partial \theta_{il}}{\partial y} - w\frac{\partial \theta_{il}}{\partial z} + \frac{\partial}{\partial x}\left(K_h\frac{\partial \theta_{il}}{\partial x}\right) + \frac{\partial}{\partial y}\left(K_h\frac{\partial \theta_{il}}{\partial y}\right) + \frac{\partial}{\partial z}\left(K_h\frac{\partial \theta_{il}}{\partial z}\right) + (\frac{\partial \theta_{il}}{\partial t})_{rad}$$

A.1.3 Water species mixing ratio continuity equation

$$\frac{\partial r_n}{\partial t} = -u\frac{\partial r_n}{\partial x} - v\frac{\partial r_n}{\partial y} - w\frac{\partial r_n}{\partial z} + \frac{\partial}{\partial x}\left(K_h\frac{\partial r_n}{\partial x}\right) + \frac{\partial}{\partial y}\left(K_h\frac{\partial r_n}{\partial y}\right) + \frac{\partial}{\partial z}\left(K_h\frac{\partial r_n}{\partial z}\right) + (\frac{\partial r_n}{\partial t})_{con}$$

A.1.4 The compressible non-hydrostatic mass continuity equation

$$\frac{\partial \pi'}{\partial t} = -\frac{R\pi_o}{C_v\rho_o\theta_o} + (\frac{\partial \rho_o\theta_o u}{\partial x} + \frac{\partial \rho_o\theta_o v}{\partial y} + \frac{\partial \rho_o\theta_o w}{\partial z})$$

If the hydrostatic option is used, the vertical momentum and the mass continuity equations will be respectively,

$$\frac{\partial \pi}{\partial z} = -\frac{g}{\theta_v} + g(r_T - r_v)$$

$$\frac{\partial \rho u}{\partial x} + \frac{\partial \rho v}{\partial y} + \frac{\partial \rho w}{\partial z} = 0$$

$$\pi = C_p \left(\frac{P}{P_o}\right)^k$$

where:

u East-west wind component
v North-south wind component
w Vertical wind component
f Coriolis parameter
K_m Eddy viscosity coefficient for momentum
K_h Eddy viscosity coefficient for heat and moisture
θ_{il} Ice-liquid water potential temperature
r_n Water mixing ratio species of total water, rain, pristine, crystals, aggregates, and snow
ρ Density
rad Subscript denoting tendency from radiation parameterization
con Subscript denoting tendency from convective parameterization
g Gravitational acceleration
r_T Total water mixing ratio
r_v Water vapor mixing ratio
π Total Exner Function
π' Perturbation Exner Function
θ_v Virtual potential temperature
θ_o Base-state potential temperature
R Dry gas constant
P Pressure
C_p Specific heat of dry air (1004 J K^{-1} Kg^{-1})
P_o Reference pressure (1000 mb)
k Constant = 0.286

The *primed* variables represent the deviation from the base state variable denoted as a_o. The relationship between θ and θ_{il} is given by (Tripoli and Cotton, 1981),

$$\theta = \theta_{il}(1 + \frac{L_v r_n}{C_p} T_v)$$

Where L_v is the latent heat of vaporization and T_v is the virtual temperature.

A.2 BASIC PARAMETERIZATIONS

A.2.1 Turbulent mixing parameterization

Field variables that can be explicitly resolved are directly dependent on the horizontal and vertical grid spacing configured in RAMS.

The contribution of the resolved variables due to turbulent transport is given by convergence of the fluxes, e.g.

$$\left(\frac{\partial u_j}{\partial t}\right)_{TURB} = \frac{\partial}{\partial x_i}\left(\overline{u_i' u_j'}\right)$$

$$\left(\frac{\partial \phi}{\partial t}\right)_{TURB} = \frac{\partial}{\partial x_i}\left(\overline{u_i' \phi}\right)$$

The unresolved transport is parameterized using K-theory, in which the covariance is evaluated as the product of an eddy mixing coefficient and the gradient of the transport quantity. As an example, for scalars, the equation is:

$$\overline{u_i' \phi'} = -K_{hi} \frac{\partial \phi}{\partial x_i}$$; Where K_{hi} :Eddy mixing coefficient

For velocity component and comparable vertical and horizontal grid spacing, the Reynolds stresses are:

$$\overline{u_i' u_j'} = \overline{u_j' u_i'} = -K_{mi}\left(\frac{\partial u_i}{\partial x_j} + \frac{\partial u_j}{\partial x_i}\right)$$; Where K_{mi} :Eddy mixing coefficient for momentum

For velocity component and horizontal grid spacing much larger than vertical grid spacing, an additional expression is used whenever i and/or j is 3

$$\overline{u_i' u_j'} = -K_{mi}\left(\frac{\partial u_i}{\partial x_j}\right)$$

For evaluating K_{mi} and K_{hi} there are four basic options. Two of them are known as the local schemes; one applies with small horizontal grid spacing and the other with large horizontal grid spacing. The other two are known as the Turbulent Kinetic Energy schemes (TKE); as for the first group, one applies in case of small horizontal grid spacing and the other in case of large horizontal grid spacing.

A.2.1.1 Local deformational scheme with small horizontal grid spacing

K_{mi} and K_{hi} are evaluated as:

$$K_{mi} = \rho(C_x\Delta x)(C_z\Delta z)\{S_3 + F_H[max(0,-F_B)]^{0.5}\}[max(0,1-R_{hm}R_i)]^{0.5}$$

$$K_{hi} = -R_{hm}K_{mi}$$

$$S_3 = \left[\left(\frac{\partial u_i}{\partial x_j} + \frac{\partial u_j}{\partial x_i}\right)^2\right]^{0.5}$$

$C_x; C_z$: Dimensionless coefficients used to obtain characteristic horizontal and vertical mixing length scales

F_H: Optional flag set to either 0 or 1

F_B: Brunt-Vaisala frequency

R_i: Richardson number

R_{hm}: A specified ratio of scalar to momentum mixing coefficients

S_3: Magnitude of the three dimensional rate-of-strain tensor

A.2.1.2 Local deformational scheme with large horizontal grid spacing

The horizontal eddy mixing coefficient is evaluated as:

$$K_i = \rho_0 max[K_{mh}, (C_x\Delta x)^2\{S_2^{0.5}\}]$$

$$K_{mh} = 0.075K_A(\Delta x^{4/3})$$

S_2: Horizontal strain rate

K_A: User-specified coefficient of order 1

The vertical eddy mixing coefficient is evaluated with the same expression, with C_z, Δ_z, S_1 replacing C_x, Δ_x, S_2, respectively

A.2.1.3 Turbulent Kinetic Energy schemes (TKE)

If the horizontal grid spacing is large, vertical mixing coefficients are calculated using Mellor and Yamada (1974) scheme and the horizontal mixing coefficients are evaluated by the local deformation scheme. If the horizontal grid spacing is small, the Deardorff (1980) scheme is used for both horizontal and vertical mixing coefficients.

The Mellor and Yamada (1974, 1982) technique is called the level 2.5 scheme with modifications for a case of growing turbulence (Helfand and Labraga, 1988). The wind fields (u and v), potential temperature (θ), and TKE (e) are provided by the prognostic fields in RAMS. The base of this scheme is the prognostic equation for TKE solved in the model:

$$TKE = e = 0.5(\overline{u'^2} + \overline{v'^2} + \overline{w'^2})$$

The prognostic equation for TKE is

$$\frac{\partial e}{\partial t} = -u\frac{\partial e}{\partial x} - v\frac{\partial e}{\partial y} - w\frac{\partial e}{\partial z} + \frac{\partial}{\partial x}K_e\frac{\partial e}{\partial x} + \frac{\partial}{\partial y}K_e\frac{\partial e}{\partial y} + \frac{\partial}{\partial z}K_e\frac{\partial e}{\partial z} + P_s + P_b + \varepsilon$$

$$P_s = K_m\left[\left(\frac{\partial u}{\partial x}\right)^2 + \left(\frac{\partial v}{\partial y}\right)^2\right]$$

$$P_b = -\frac{g}{\theta}K_h\frac{\partial \theta_v}{\partial z}$$

$$\varepsilon = a_e\frac{e^{3/2}}{l}$$

P_s: Shear production term

P_b: Buoyancy production term

ε: Dissipation term

The vertical eddy diffusivities for momentum, heat and TKE are evaluated as:

$$K_m = S_m l\sqrt{2e}$$

$$K_h = S_h l\sqrt{2e}$$

$$K_e = S_e l\sqrt{2e}$$

The wind and temperature enter these calculations in the form of dimensionless vertical gradients:

$$G_m = G_u^2 + G_v^2$$

$$G_u = \frac{l}{\sqrt{2e}} \frac{\partial u}{\partial z}$$

$$G_v = \frac{l}{\sqrt{2e}} \frac{\partial v}{\partial z}$$

$$G_h = -\frac{g}{\theta} \frac{l^2}{2e} \frac{\partial \theta}{\partial z}$$

The turbulent length scale, l, is evaluated as (Mellor and Yamada, 1972):

$$l = \frac{k(z + z_0)}{1 + k(z + z_0)/l_\infty}$$

$$l_\infty = 0.1 \frac{\int_0^H z\sqrt{e}\,\partial z}{\int_0^H \sqrt{e}\,\partial z}$$

Where k is the Von Karman constant and z_o is the roughness length.

An upper limit for l in stable conditions is given by (Andre et. al, 1978):

$$l \le 0.75 \left[\frac{2e}{\frac{g}{\theta} \frac{\partial \theta}{\partial z}} \right]^{0.5} \text{; hence } G_h \ge -0.75^2$$

In the level 2.5 scheme, the nondimensional eddy diffusivities, S_m and S_h depend on nondimensional gradients of wind and potential temperature:

$$S_m = \frac{A_1\{1 - 3C_1 - 3A_2[B_2(1 - 3C_1) - 12A_1C_1 - 3A_2]G_h\}}{1 - 3A_2(7A_1 + B_2)G_h + 27A_1A_2^2(4A_1 + B_2)G_h^2 + 6A_1[1 - 3A_2(B_2 - 3A_2)G_h]G_m}$$

$$S_k = A_2 \frac{1 - 6A_1S_mG_m}{1 - 3A_2(4A_1 + B_2)G_h}$$

Where values for the constants are (Mellor and Yamada, 1982)

$$\{A_1, A_2, B_1, B_2, C_1, S_e, a_e\} = \{0.92, 0.74, 16.6, 10.1, 0.08, 0.20, 2^{2/3}/16.6\}$$

A.2.2 Surface Layer Parameterization

To determine the fluxes from the land surface (water surface, bare soil and vegetated surfaces) into the atmosphere, RAMS uses the scheme of Louis (1979). The expressions for the surface layer fluxes are:

$$H = \rho C_p u_* \theta_*$$

$$LE = \rho L_v u_* q_*$$

$$\tau = \rho u_*^{\ 2}$$

Where H and LE are the sensible and the latent heat flux respectively, τ is the momentum flux, and u_*, q_* and θ_* are the surface layer scaling parameter.

Two non-linear functions, F_m and F_h, are used to evaluate the vertical eddy fluxes of momentum and sensible heat:

$$u_*^2 = a^2 u^2 F_m\left(\frac{z}{z_0}, Ri_B\right)$$

$$u_*\theta_* = \frac{a^2}{R} u \Delta\theta F_h\left(\frac{z}{z_0}, Ri_B\right)$$

$$u_* r_* = \frac{a^2}{R} u \Delta r F_h\left(\frac{z}{z_0}, Ri_B\right)$$

$$a^2 = \frac{k^2}{\left(\ln\frac{z}{z_0}\right)^2}$$

Where k=0.40, is Von Karman's Constant; R, a dimensionless constant, is the ratio of transfer coefficients of momentum and heat in the neutral limit; z_o the roughness length; and the bulk Richardson number is:

$$Ri_B = \frac{gz\Delta\theta}{\bar{\theta}u^2}$$

$$F = 1 - \frac{bRi_B}{1 + c\,|\,Ri_B\,|^{1/2}} \quad \text{if the case is unstable}$$

$$F = \frac{1}{(1 + b' Ri_B)^2} \quad \text{if the case is stable}$$

$$c = C^* a^2 b\left(\frac{z}{z_0}\right)^{1/2}$$, with C*=7.4 for F_m and C*=5.3 for F_h

Where b and b' are empirical constants and common values are b=9.4 and b'=4.7.

A.2.3 Soil and Vegetation Parameterization

Three different classes of land cover are considered: water surface, bare soil and vegetated surface. Temperature and moisture values are required for these three classes. For water surfaces, the moisture value used is the saturation mixing ratio defined at the surface pressure and water vapor. For the other two classes, prognostic temperature and moisture models can be used. For bare soil RAMS uses the multi-layer soil model described by Tremback and Kessler (1985).

The moisture diffusivity, hydraulic conductivity, and moisture potential are given by (Clapp and Hornberger, 1978),

$$D_\eta = \frac{-bK_f\Psi_f}{\eta}\left[\frac{\eta}{\eta_f}\right]^{b+3} \qquad \text{Moisture diffusivity}$$

$$K_\eta = K_f\left[\frac{\eta}{\eta_f}\right]^{2b+3} \qquad \text{Hydraulic conductivity}$$

$$\Psi = \Psi_f\left[\frac{\eta_f}{\eta}\right]^{b} \qquad \text{Moisture potential}$$

Where η is the soil moisture content expressed in terms of volume of water per volume of soil, the subscript "*f*" means saturation conditions, and *b* is a constant related on soil texture class. RAMS supports 12 different soil types from sand to peat and the constant values are given in the following table.

Soil class	$n_f(m^3m^{-3})$	$\psi_f(m)$	$K_f(ms^{-1})$	b	$C_d(Jm^{-3}K^{-1})$
Sand	0.395	-0.121	0.0001760	4.05	1465000
Loamy sand	0.410	-0.090	0.0001563	4.38	1407000
Sandy loam	0.435	-0.218	0.0000347	4.90	1344000
Silt Loam	0.485	-0.786	0.0000072	5.30	1273000
Loam	0.451	-0.478	0.0000070	5.39	1214000
Sandy clay loam	0.420	-0.299	0.0000063	7.12	1177000
Silty clay loam	0.477	-0.356	0.0000017	7.75	1319000
Clay loam	0.476	-0.630	0.0000025	8.52	1227000
Sandy clay	0.426	-0.153	0.0000022	10.40	1177000
Silty clay	0.492	-0.490	0.0000010	10.40	1151000
Clay	0.482	-0.405	0.0000013	11.40	1088000
Peat	0.863	-0.356	0.0000080	7.75	874000

The volumetric specific heat C_s and the thermal diffusivity λ [m2/s] of the soil are given by:

$$C_s = (1-\eta)C_d + \eta C_w$$

$$\lambda = \frac{e^{-(\log_{10}|\Psi|+2.7)}}{C_s}(4.187)(10^7), \log_{10}|\Psi| \leq 5.1$$

$$\lambda = \frac{0.00041}{C_s}(4.187)(10^7), \log_{10}|\Psi| \geq 5.1$$

C_d and C_w are the specific heat of the dry soil and water respectively.

Heat is diffused into the soil by

$$\frac{\partial \theta_s}{\partial t} = \frac{\partial}{\partial z}\left[\lambda \frac{\partial \theta_s}{\partial z}\right]$$

Where θ_s is the potential temperature of the soil, and it is considered constant at the deepest soil level, and the potential temperature at the ground surface is evaluated using the following prognostic equation.

$$C_s \Delta Z_g \frac{\partial \theta_g}{\partial t} = \alpha_g R_s\downarrow + R_L\downarrow - \sigma T^4 + \rho_a C_p u_* \theta_* + \rho_a L_v u_* q_* - |C_s \lambda \frac{\partial \theta_s}{\partial z}|_g$$

Where:

$R_s\downarrow, R_L\downarrow$: Short wave and long wave radiation

$R_s\downarrow + R_L\downarrow$: Net radiation

$\rho_a C_p u_* \theta_*$: Sensible heat flux to the atmosphere

$\rho_a L_v u_* q_*$: Latent heat flux and

$|C_s \lambda \frac{\partial \theta}{\partial z}|_g$: Soil flux.

θ_g: Ground potential temperature

α_g: Albedo of the soil surface

C_s: Volumetric specific heat of the soil

λ: Thermal conductivity

L_v: Latent heat of vaporization

ρ_a: Air density near the ground

σ: Stefan-Boltzmann constant

u_*, θ_* and q_*: Surface layer scaling parameters for momentum, heat and specific humidity, respectively

ΔZ_g: Vertical spacing in the soil.

Using the prognostic soil model developed by McCumber and Pielke (1981) and modified for RAMS by Tremback and Kessler (1985), values of soil moisture and soil temperature are found. For the top soil layer the soil moisture is

$$\frac{\partial n_s}{\partial t} = \frac{\frac{\rho_a u_* q_*}{\rho_w} - D_\eta \frac{\partial n}{\partial z} - K_\eta}{\Delta Z_g}$$

The moisture diffusion in all other soil levels is governed by,

$$\frac{\partial \eta_s}{\partial t} = \frac{\partial}{\partial z}\left[D_\eta \frac{\partial \eta}{\partial z} + K_\eta \right]$$

Where ρ_w is the water density, n is the soil moisture, D_n is the moisture diffusivity and K_n is the hydraulic conductivity. Both, D_n, K_n are a function of n and soil type.

The effective mixing ratio is defined as:

$$r_v = \beta r_g + (1-\beta) r_a$$

Where:

r_a: Mixing ratio of the air

r_g: Mixing of the air within the top layer of the soil (mixing ratio at the ground surface) computed by (Philip, 1957) as

$$r_g = e^{\left[\frac{g\psi_g}{R_v T_g}\right]} r_s\left(T_g P_g\right)$$

g: Gravitational acceleration

R_v: Gas constant for water vapor

r_s: Saturation mixing ratio at temperature T_g and pressure P_g

β: A weighting factor evaluated as:

$$\beta = 0.25\left(1 - \cos(\min[1, \frac{\eta_g}{\eta_{fc}}\pi])\right)^2$$

η_{fc}: Soil moisture at field capacity.

The "big leaf" approach is used for the vegetated surface. It is considered that there is a layer of vegetation overlying a shaded soil. For the shaded soil, an approach similar to that for bare soil is used, taking into account the following differences in the surface energy budget equation:

$$C_s \Delta Z_g \frac{\partial \theta_g}{\partial t} = \tau_{veg} \alpha_g R_s \downarrow + \sigma T_{veg}^4 - \sigma T_g^4 + \rho_a C_p u_* \theta_* + \rho_a L_v u_* q_* - | C_s \lambda \frac{\partial \theta_s}{\partial z} |_g$$

τ_{veg} : Short-wave transmissivity through the vegetation layer

T_{veg} : Temperature of the vegetation layer.

A prognostic temperature equation is used for vegetation layer,

$$C_{veg} \Delta Z_{veg} \frac{\partial \theta_{veg}}{\partial t} = (1 - \tau_{veg}) \alpha_{veg} R_s \downarrow + R_l \downarrow + \sigma T_g^4 - 2\sigma T_{veg}^4 + 2\rho_a C_p u_* \theta_* + \rho_a C_p u_* q_*$$

Where the ***veg*** subscript makes a reference for the vegetation values. The factor of two in the long-wave emissions and the sensible heat terms denotes the transfer of energy from both sides of the leaf surface. The latent heat term does not contain this factor since stomata usually occur on one side of the leaf.

The effective mixing ratio for vegetation is

$$r_{veg} = r_{veg} \gamma + (1 - \gamma) r_a$$

Where r_{vegs} is the saturation mixing ratio as function of the vegetation temperature and atmospheric pressure and γ is the stomatal resistance function.

RAMS defines a vertical "root" profile to determine the moisture that is transpired from the vegetation. The vertical "root" profile is taken from the Biosphere-Atmosphere Transfer Scheme, BATS (Dickinson et. al., 1986). Additionally, RAMS uses other parameters also defined in BATS, such as, eighteen vegetation classifications, vegetation albedo, emissivity, roughness height, displacement, fractional coverage and leaf area index.

The grid area average velocity fluxes are

$$\overline{u'w'} = -\cos\left(\frac{u}{\sqrt{u^2 + v^2}}\right)\left(f_w \left(u_*^2\right)_w + f_g \left(u_*^2\right)_g + f_{veg} \left(u_*^2\right)_{veg} + f_s \left(u_*^2\right)_s\right)$$

$$\overline{v'w'} = -sin\left(\frac{v}{\sqrt{u^2+v^2}}\right)\left(f_w\left(u_*^2\right)_w + f_g\left(u_*^2\right)_g + f_{veg}\left(u_*^2\right)_{veg} + f_s\left(u_*^2\right)_s\right)$$

The average potential temperature and the water vapor fluxes are

$$\overline{w'\theta'} = -\left(f_w\left(u_*\theta_*\right)_w + f_g\left(u_*\theta_*\right)_g + f_{veg}\left(u_*\theta_*\right)_{veg} + f_s\left(u_*\theta_*\right)_s\right)$$

$$\overline{w'r_v'} = -\left(f_w\left(u_*r_*\right)_w + f_g\left(u_*r_*\right)_g + f_{veg}\left(u_*r_*\right)_{veg} + f_s\left(u_*r_*\right)_s\right)$$

Where the subscripts w, g, veg, and s refer to water, bare ground, vegetation, and shaded ground respectively. f is the grid fraction of each component and LAI is the leaf area index.

A.2.4 Radiation parameterization

The current version of RAMS has implemented two options of radiation parameterizations for both Long and Shortwave Radiation. The first set, taken from Mahrer and Pielke (1977), is simple and efficient but it does not account for clouds. The second set, developed by Chen and Cotton (1983), takes into account the amount of condensate present in the simulated atmosphere but it is computer-time consuming.

A.2.4.1 Shortwave radiation scheme without cloud effects

$$R_s = S(1-A)(G-a_w)$$

$$S = S_0\cos(Z)$$

$$\cos(Z) = \sin(\phi)\sin(\delta) + \cos(\phi)\cos(\delta)\cos(\psi)$$

$$G = 0.485 + 0.515\left[1.041 - 0.16\left(\frac{0.000949p + 0.051}{\cos(Z)}\right)^{0.5}\right]$$

$$a_w = 0.077\left[\frac{\tau(z)}{\cos(Z)}\right]^{0.3}$$

$$\tau(z) = \int_z^{top} \rho r_v \partial z$$

R_s: Net shortwave radiation flux at the surface
Z: Zenith angle
S: Solar flux on a horizontal surface
S_0: Solar constant

ϕ: Latitude

δ: Solar declination

ψ: Hour angle

G: Empirical function to take into account oxygen, ozone and carbon dioxide (Kondrat`yev, 1969; and Atwater and Brown, 1974)

p: Pressure in millibars

a_w: Empirical function to take into account absorption of shortwave radiation by water vapor (McDonald, 1960)

z: Vertical level

τ: Optical path of water vapor above a vertical level z

A: Albedo

The change in the atmospheric temperature due to absorption by water vapor is:

$$\left(\frac{\partial T}{\partial t}\right)_s = 0.0231\frac{S}{\rho c_p}\left[\frac{\tau(z)}{\cos(Z)}\right]^{-0.7}\frac{\partial \tau}{\partial z}$$

To account for topography the expression for the solar radiation on a slanted surface is:

$$S_{sl} = S_0\cos(i)$$

$$\cos(i) = \cos(\alpha)\cos(Z) + \sin(\alpha)\sin(Z)\cos(\beta - n)$$

$$\alpha = \tan^{-1}\left[\left(\left(\frac{\partial z_g}{\partial x}\right)^2 + \left(\frac{\partial z_g}{\partial y}\right)^2\right)^{0.5}\right]$$

$$\beta = \sin^{-1}\left(\frac{\cos(\delta)\sin(\phi)}{\sin(Z)}\right)$$

$$n = \frac{\pi}{2} - \tan^{-1}\left[\left(\frac{\partial z_g}{\partial x}\right)\Big/\left(\frac{\partial z_g}{\partial y}\right)\right]$$

S_{sl}: Solar flux on a slanted surface

i: Angle of incidence of the solar rays on the sloped surface

α: Angle of the slope

β: Solar azimuth

n: Slope azimuth

In consequence, the downward solar flux at the ground is:

$$R_{s/sl} = R_s\frac{\cos(i)}{\cos(Z)}$$

A.2.4.2 Longwave radiation scheme without cloud effects

The downward radiative flux to the surface of the earth is given by:

$$R_L = \left(\sigma T_{top}^4 - \sigma T_N^4\right)\left(\varepsilon(N+1,top) - \varepsilon(N,top)\right);\ \text{N: given level}$$

Where the atmospheric temperature tendency due to the longwave radiative flux divergence at level N is given by:

$$\left(\frac{\partial T}{\partial t}\right)_L = -\frac{1}{\rho C_p \Delta z}\left[\left(\sigma T_N^4 - \sigma T_g^4\right)\left(\varepsilon(N+1,0) - \varepsilon(N,0)\right) + \left(\sigma T_{top}^4 - \sigma T_N^4\right)\left(\varepsilon(N+1,top) - \varepsilon(N,top)\right)\right]$$

$$\varepsilon(i,j) = \varepsilon_v(i,j) + \varepsilon_c(i,j)$$

$$\varepsilon_c(i,j) = 0.185\left[1 - \exp\left(0.03919\tau_c^{0.4}\right)\right]$$

$$\varepsilon_v(i,j) = \begin{cases} 0.11288\log_{10}\left(1+12.63\overline{\tau_v}\right) & \log_{10}\overline{\tau_v} \le -4 \\ 0.104\log\overline{\tau_v} + 0.440 & -4 < \log_{10}\overline{\tau_v} \le -3 \\ 0.121\log\overline{\tau_v} + 0.491 & -3 < \log_{10}\overline{\tau_v} \le -1.5 \\ 0.146\log\overline{\tau_v} + 0.527 & -1.5 < \log_{10}\overline{\tau_v} \le -1 \\ 0.161\log\overline{\tau_v} + 0.542 & -1 < \log_{10}\overline{\tau_v} \le -0 \\ 0.136\log\overline{\tau_v} + 0.542 & \log_{10}\overline{\tau_v} > -0 \end{cases}$$

$$\tau_v = \sum_j^i \Delta\tau_v\ ;\ \tau_c = \sum_j^i \Delta\tau_c$$

$$\Delta\tau_v = r_v \rho \Delta z$$

$$\Delta\tau_c = 0.0004148239 g \rho \Delta z$$

τ_v: Total optical path for water vapor between level i and j

τ_c: Total optical path for CO_2 between level i and j

$\varepsilon_v(i,j)$: Water vapor emissivities of a layer between level i and j. Kuhn (1963) and Jacobs et al. (1974)

$\varepsilon_c(i,j)$: CO_2 emissivities of a layer between level i and j. Kondrat`yev (1969)

σ: Stefan-Boltzmann costant

r_v: Water vapor mixing ratio

A.2.4.3 Long and Short wave radiation scheme with cloud effects

The longwave radiation is a full solution of the radiative transfer equations using an emissivity approach taking into account the condensate effects. The shortwave

radiation is a 3-band scheme that takes into account the condensate effects. The full description of these two schemes is in Chen and Cotton (1983).

A.2.5 Convective Parameterization

Modified versions of the two most used convective parameterization schemes are available in RAMS. These are the Kuo (1974) scheme and the Fritsch and Cappell (1980a) scheme.

A.2.5.1 A simplified Kuo convective parameterization

This convective parameterization is a modification of the generalized form of the Kuo (1974) scheme. This is an equilibrium scheme; convection acts to consume the convective instability that is supplied by the larger scales. Thermodynamic and moisture equations due to the moist convection are:

$$\left(\frac{\partial \theta}{\partial t}\right)_{con} = L(1-b)\pi^{-1} I \frac{Q_1}{\int_{z_g}^{z_{ct}} Q_1 \partial z}$$

$$\left(\frac{\partial r_T}{\partial t}\right)_{con} = bI \frac{Q_2}{\int_{z_g}^{z_{ct}} Q_2 \partial z}$$

θ: Potential temperature
r_T: Total water mixing ratio
I: Rate at which the resolvable scale is supplying moisture to a particular grid column.
b: Moisture partitioning parameter, which determines what fraction of I is used to increase the moisture of the column.
$1-b$: Precipitation efficiency
Q_1 and Q_2: Vertical profiles of the convective heating and moistening

A.2.5.2 Kain-Fritsch convective parameterization scheme

The Kain-Fritsch (KF) scheme is a modified version of the earlier Fritsch-Chappell scheme. The postulate of the scheme is to rearrange mass in a vertical column to eliminate Convective Available Potential Energy (CAPE), which is a measure of the potential instability of the atmosphere. This is accomplished via moist updraft and downdraft processes, as well as dry ascent and descent that compensates for the moist processes.

A.2.6 Bulk microphysics parameterization

This parameterization is a bulk water type model, where it is assumed that the various water categories may be represented by continuous specified size distributions and then bulk parameterizations are developed for the various physical processes based on the assumed size distributions, transferring mass between the categories of water classes. The scheme used in RAMS model unifies the treatment of different distributions making possible to define the distribution-weighted properties in a simple and concise way. The descriptions of all microphysical processes are simplified by an introduction of an interaction scheme. The scheme includes cloud water, rain, pristine crystals, snow, graupel and aggregates. A full description of this scheme, the general theory and code documentation, is in Paper No. 451 of the Department of Atmospheric Science of Colorado State University, Piotr et. al (1989).

APPENDIX 2

A summary of the stations with historical hydrometeorological data of Colombia collected for and used in this work is given in this appendix. The gauge locations and altitudes above sea level are included. To get a good idea about the state of measurements of observed climate variables in Colombia, it is recommended to take a look at Mesa et al. (1997) and Velez et al. (2000), and to review the IDEAM electronic page http://www.ideam.gov.co

The information described here was gotten from the following government institutions in Colombia: Interconexión Eléctrica S. A. (ISA), Empresas Públicas de Medellín (EPM) and Universidad Nacional de Colombia, sede Medellín (UN). However, all these information can be acquired at the Hydrology, Meteorology and Environmental Studies Institute, IDEAM (Instituto de Hidrologia, Meteorologia y Estudios Ambientales), agency responsible for collecting and archiving all hydro-meteorological information in Colombia. It wants to be pointed that Velez et al. (2000) was one of main source of information for the present research. In their job they make a good recollection and homogenization of data, and spatial distribution maps that were very useful for RAMS comparison results.

Among the different climate variables required for comparison with RAMS results, precipitation and stream flows are the ones that have a better-collected data. However the precipitation gauge stations in Colombia do not cover in a homogeneous way the whole territory. Most of the measurements are from those regions where the hydroelectric or the agriculture projects are, from zones with a high flood risk, or from the most populated and industrialized zones are. Other variables as temperature, dew point temperature, vapor pressure, atmospheric pressure, relative humidity, soil humidity and evaporation have a poor record of measurements no only in time but also in space and in frequency, then for these variables were able to get just annual and in some cases monthly averages observed data.

Tables A2-1 and A2-2 summarize the gauging stations used in this study.

Table A2-1: Gauge stations for basic observed data used in the diurnal cycle analysis – Weather analysis

CODE	NAME	TYPE	LATITUDE (+: N) (-: S)	LONGITUDE (+: E) (-: W)	ELEVATION (m.a.s.l)
1107007	Cruces	PVG	6.4710	-76.3187	950
1107008	Mande	PVG	6.4454	-76.4771	495
1107009	Santa Barbara	PVG	6.4072	-76.0819	2595
1107010	El Sireno	PVG	6.3925	-76.2543	1210
1107012	Pabon	PVG	6.1580	-76.1620	1920
1107015	La Palmera	PVG	6.1472	-76.0465	2506
1107017	San Jose De Urrao	PVG	6.2378	-76.1352	1870
2308021	La Fe	PVG	6.0988	-75.4945	2150
2308022	La Severa	PVG	6.2622	-75.4570	2170
2308023	Las Palmas	PVG	6.1550	-75.5394	2495
2308024	Vasconia	PVG	6.2068	-75.4822	2510
2308025	El Retiro	PVG	6.0511	-75.5205	2190
2308026	La Mosca	PVG	6.3090	-75.4635	2155
2308027	Rionegro La Macarena	PVG	6.1603	-75.3616	2070
2308030	El Carmen	PVM	6.0709	-75.3283	2180
2308034	Rioabajo	PVG	6.2427	-75.3139	2070
2308035	Santuario	PVM	6.1291	-75.2439	2175
2308037	Guatape	PVM	6.2413	-75.1582	1900
2308038	San Vicente	PVM	6.2807	-75.3325	2155
2308044	Corrientes	PVG	6.3092	-75.2650	1980
2308046	La Pradera	PVG	6.2857	-74.9867	1100
2308050	San Roque	PVM	6.4827	-75.0346	1440
2308052	Cocorna	PVM	6.0639	-75.1882	1350
2308053	Caracoli	PVG	6.4156	-74.7612	600
2308054	Granada	PVM	6.1356	-75.1810	2050
2308055	San Luis	PVM	6.0486	-75.0019	1080
2308057	El Pital	PVG	6.3021	-74.9135	1110
2308061	El Bizcocho	PVG	6.3167	-75.0833	1070
2308070	Calderas	PVG	6.1593	-75.1005	2070
2308071	Bellalina	PVG	6.5511	-75.1040	1460
2308077	Guacharacas	PVG	6.5357	-74.9389	830
2308083	La Rapida	PVG	6.2312	-75.0435	1380
2308084	Tocaima	PVG	6.3537	-75.1110	1570
2308085	La Cascada	PVG	6.2415	-75.0761	1700
2308086	Samaria	PVG	6.2764	-75.1161	1350
2308087	Palmas – San Roque	PVG	6.4404	-74.9123	1100
2308096	La Playa Pantan.	PVG	5.9838	-75.4620	2320
2308496	Cañafisto	PVG	6.1576	-74.8081	-
2308505	Santa Rita	CLM	6.3129	-75.1624	1900
2308517	El Peñol	CLM	6.2333	-75.2167	1880

Table A2-1: Continued

CODE	NAME	TYPE	LATITUDE (+: N) (-: S)	LONGITUDE (+: E) (-: W)	ELEVATION (m.a.s.l)
2308523	Playas	CLM	6.3373	-74.9656	1210
2308709	Rioabajo Rn-4a	LMG	6.2651	-75.3007	1980
2308790	Rn-9b El Silencio	LMG	6.2999	-75.0167	979
2308799	Embalse De Playas	LMM	6.2926	-74.9403	-
2308951	Jaguas	TLP	6.3522	-74.9906	-
2309502	La Sierra Nare	CLM	6.2327	-74.5607	138
2310009	Ceiba La Floresta	PVG	6.6290	-74.8776	1260
2310010	La Teresa	PVG	6.8191	-74.6848	730
2310011	Versalles	PVG	6.7339	-74.9567	1220
2310504	La Guaira	CLM	6.6635	-74.7641	927
2310505	La Honda	CLM	6.7012	-74.5747	540
2618008	Mesopotamia	PVG	5.8890	-75.3222	2410
2618010	La Union	PVM	5.9705	-75.3543	2500
2623023	Espiritu Santo	PVG	6.9696	-75.5332	2240
2625007	Villanueva	PVG	7.0885	-75.4400	2000
2701034	Mazo	PVG	6.2628	-75.5091	2455
2701035	Chorrillos	PVG	6.2991	-75.5061	2370
2701036	Caldas	PVG	6.0480	-75.6292	1930
2701037	Fabricato	PVG	6.3644	-75.6037	2422
2701038	San Antonio De Prado	PVG	6.1877	-75.6649	2000
2701042	Riogrande Bocacero	PVG	6.5218	-75.4042	2120
2701045	Villa Hermosa - Planta	PVG	6.2608	-75.5506	1690
2701046	San Cristobal	PVG	6.2837	-75.6390	1890
2701047	Miguel De Aguina	PVG	6.2650	-75.5719	1549
2701051	El Boton	PVG	6.6662	-75.5702	2500
2701053	Alto San Andres	PVG	6.4365	-75.4445	2240
2701054	Santa Rosa	PVM	6.6387	-75.4581	2550
2701055	Aragon	PVG	6.7849	-75.5634	2630
2701056	Girardota	PVG	6.3855	-75.4575	1350
2701057	Barbosa	PVM	6.4333	-75.3333	1290
2701058	Rionegrito	PVG	6.6374	-75.3567	2435
2701059	El Chaquiro	PVG	6.7578	-75.4938	2750
2701060	Gomez Plata	PVM	6.6923	-75.2324	1800
2701066	Gabino	PVG	6.5543	-75.2097	1080
2701070	Haiton	PVG	6.6146	-75.2781	2120
2701072	El Gomez	PVG	6.7420	-75.6551	2675
2701073	Medina	PVG	6.4257	-75.5354	2620
2701074	Belmira	PVM	6.6049	-75.6674	2520
2701075	Entrerrios	PVM	6.5656	-75.5209	2285
2701076	Niquia	PVG	6.3764	-75.5363	2150

Table A2-1: Continued

CODE	NAME	TYPE	LATITUDE (+: N) (-: S)	LONGITUDE (+: E) (-: W)	ELEVATION (m.a.s.l)
2701090	-	-	6.6833	-75.2167	-
2701093	Ayura	PVG	6.1689	-75.5681	1750
2701094	San Bernardo	PVG	6.8565	-75.5772	2740
2701095	Desv. Riogrande Ii	PVG	6.5089	-75.4520	2280
2701099	Boqueron Amalfi	PVG	6.8603	-74.9977	1600
2701100	Cajamarca	PVG	6.8255	-75.0988	1780
2701101	Alto De La Sierra	PVG	6.5676	-75.6005	2750
2701102	El Silencio	PVG	6.9402	-74.9971	1600
2701103	Mina La Viborita	PVM	6.9333	-75.0833	1460
2701105	Santa Maria	PVG	7.0920	-74.7548	390
2701106	Planta Manantiales	PVG	6.3209	-75.5436	1790
2701107	Guanacas	PVG	6.7144	-75.3262	2350
2701108	La Sirena	PVG	6.7382	-75.3028	1925
2701109	Dos Bocas (Ermitaño)	PVG	7.4529	-74.9101	75
2701113	Bocatoma Ana Diaz	PVG	6.2535	-75.6468	1910
2701114	Cucaracho	PVG	6.2869	-75.6119	1830
2701115	Astillero	PVG	6.2596	-75.6788	2420
2701116	El Tururo	PVG	6.5971	-75.5781	2450
2701118	Los Atajos	PVG	6.6994	-75.5220	2575
2701122	El Convento	PVG	6.3378	-75.5163	1580
2701501	El Roble	CLM	6.9621	-75.1315	1175
2701514	El Mango	CLM	6.7989	-75.1449	960
2701518	Troneras	CLM	6.7833	-75.2500	1800
2701522	San Pedro	CLM	6.4987	-75.5742	2392
2701523	Cucurucho	CLM	6.6585	-75.5196	2580
2701525	Amalfi	CLM	6.9673	-75.0419	1500
2701707	Puente Belmira Rg-6	LMG	6.6500	-75.5333	2440
2701713	Palmichal G-8	LMG	6.7000	-75.2667	1780
2701764	Emb.Troneras G-2d	LMG	6.7833	-75.2500	1776
2701767	La Ye - Rg-10	LMG	6.4833	-75.5500	2340
2701793	Captacion Rio Grande	TLP	6.4833	-75.4667	2302
2702008	El Cedro	PVG	7.1898	-75.3599	1100
2702009	El Tabor	PVG	6.7939	-75.3814	2430
2702012	Angostura	PVG	6.8833	-75.3333	1675
2702013	La Teresita	PVG	6.8625	-75.4528	2590
2702024	Madreseca	PVG	7.2585	-75.0452	650
2702025	Media Luna	PVG	7.2053	-75.3212	700
2702029	Montañitas	PVG	6.6782	-75.3951	2640
2702030	Subestacion Yarumal	PVM	6.9670	-75.4180	2230
2702035	Soledad	PVG	7.0419	-75.2185	1100

Table A2-1: Continued

CODE	NAME	TYPE	LATITUDE (+: N) (-: S)	LONGITUDE (+: E) (-: W)	ELEVATION (m.a.s.l)
2702037	Las Cruces	PVG	7.1639	-75.0604	910
2702039	San Jose - Anori	PVG	7.1687	-75.2627	1310
2702040	Espiritu Santo	PVG	7.2039	-75.1921	1130
2702041	La Plancha	PVG	7.1399	-75.2257	1225
2702495	Nuevo Campamento	PVG	6.9738	-75.3161	1750
2702499	Cedeo	TPG	7.0667	-75.3500	-
2702599	Climatologica Nechi	TCL	7.2340	-75.3132	680
2702703	La India - Tc-4	LMG	6.8104	-75.3135	1845
2702980	Descarga Miraflores	TLP	6.7840	-75.3204	2015

Table A2-2: Gauge stations for basic observed data used in the seasonal analysis – Climate analysis

CODE	DEPARTMENT	TYPE	LATITUDE (+: N) (-: S)	LONGITUDE (+: E) (-: W)	ELEVATION (m.a.s.l)
4801501	Amazonas	SP	-3.8500	-69.9500	84
1111001	Antioquia	PM	6.7667	-76.1500	1370
1202501	Antioquia	CO	8.1167	-76.7333	1
2308021	Antioquia	PG	6.1000	-75.5000	2150
2308022	Antioquia	PG	6.2667	-75.4500	2170
2308023	Antioquia	PG	6.1500	-75.5333	2495
2308024	Antioquia	PG	6.2000	-75.4833	2510
2308025	Antioquia	PG	6.0500	-75.5167	2190
2308026	Antioquia	PG	6.3167	-75.4667	2250
2308027	Antioquia	PG	6.1500	-75.3667	2070
2308028	Antioquia	PG	6.1500	-75.3667	2290
2308029	Antioquia	PM	6.1333	-75.4333	2098
2308042	Antioquia	PG	6.3833	-74.9833	1320
2308049	Antioquia	PG	6.2000	-74.9833	1000
2308504	Antioquia	AM	6.1333	-75.3833	2090
2308519	Antioquia	CO	6.2167	-74.8500	790
2317502	Antioquia	SS	7.0167	-74.7167	630
2502139	Antioquia	PM	8.0000	-75.2000	70
2502514	Antioquia	CO	8.1000	-74.7667	200
2618009	Antioquia	PG	5.9167	-75.4500	2110
2618018	Antioquia	PG	5.7000	-75.2833	2530
2619501	Antioquia	CO	5.5333	-75.8500	1570
2623009	Antioquia	PG	6.4167	-75.6167	2525
2701032	Antioquia	PM	6.7833	-75.2333	1650
2701034	Antioquia	PG	6.2667	-75.5167	2455
2701035	Antioquia	PG	6.3000	-75.5000	2353
2701036	Antioquia	PG	6.0667	-75.6333	1875
2701037	Antioquia	PG	6.3667	-75.6000	2422
2701038	Antioquia	PG	6.1833	-75.6667	2000
2701040	Antioquia	PM	6.5500	-75.4000	2070
2701042	Antioquia	PG	6.5167	-75.4000	2120
2701043	Antioquia	PM	6.5167	-75.4167	2150
2701044	Antioquia	PM	6.5500	-75.3667	1784
2701045	Antioquia	PG	6.2667	-75.5500	1690
2701046	Antioquia	PG	6.2833	-75.6333	1890
2701047	Antioquia	PG	6.2500	-75.5667	1549
2701050	Antioquia	PM	6.7333	-75.2833	1800
2701062	Antioquia	PM	6.3333	-75.6667	3150
2701507	Antioquia	SP	6.2167	-75.6000	1490
2701509	Antioquia	CP	6.3167	-75.5333	1438

Table A2-2: Continued

CODE	DEPARTMENT	TYPE	LATITUDE (+: N) (-: S)	LONGITUDE (+: E) (-: W)	ELEVATION (m.a.s.l)
2701518	Antioquia	CO	6.7833	-75.2500	1800
2702009	Antioquia	PG	6.8000	-75.3833	2430
2702020	Antioquia	PG	7.0667	-75.4333	2400
3705501	Arauca	SS	7.0667	-70.7333	128
2903507	Atlantico	CP	10.5000	-75.1333	10
2904008	Atlantico	PM	10.7833	-74.8500	80
2904502	Atlantico	SP	10.8833	-74.7833	14
1401501	Bolivar	CP	10.7833	-75.2667	20
1401502	Bolivar	SP	10.4500	-75.5167	2
1401503	Bolivar	CP	10.3833	-75.5333	1
2502004	Bolivar	PM	9.1833	-74.3500	25
2502510	Bolivar	CP	9.2667	-74.8167	18
2901502	Bolivar	AM	9.7167	-75.1167	152
2903004	Bolivar	PG	10.2500	-75.3500	60
2903503	Bolivar	CO	9.8500	-75.3167	60
2401011	Boyaca	PM	6.0833	-73.4667	1242
2401502	Boyaca	CO	5.8833	-73.6000	1700
2403026	Boyaca	PM	6.4000	-72.4500	2749
2403047	Boyaca	PG	5.5667	-72.9833	2870
2403512	Boyaca	AM	5.8167	-73.0667	2485
2403513	Boyaca	CP	5.5667	-73.3667	2690
3507001	Boyaca	PG	5.4000	-73.3333	2360
3507005	Boyaca	PM	5.2333	-73.4500	2300
3507007	Boyaca	PM	5.1500	-73.3667	1900
3507010	Boyaca	PM	4.9833	-73.4500	1600
3507019	Boyaca	PG	4.8833	-73.3667	1850
3507026	Boyaca	PG	4.9500	-73.4000	2120
3519005	Boyaca	PM	5.2833	-72.7000	842
2302013	Caldas	PM	5.1000	-75.3500	3580
2302501	Caldas	CO	5.2000	-75.1333	1420
2304008	Caldas	PM	5.3500	-74.9167	970
2613505	Caldas	CP	4.9667	-75.7000	1400
2615502	Caldas	CP	4.9833	-75.5833	1310
2615505	Caldas	CO	5.0500	-75.4833	2150
2615511	Caldas	SP	5.0333	-75.4667	2080
2615512	Caldas	CP	5.0833	-75.6833	933
2616003	Caldas	PM	5.4167	-75.5333	1500
2618005	Caldas	PM	5.6333	-75.4667	1600
2618504	Caldas	CO	5.3833	-75.3833	2821
4403502	Caqueta	SS	1.6000	-75.5333	244

Table A2-2: Continued

CODE	DEPARTMENT	TYPE	LATITUDE (+: N) (-: S)	LONGITUDE (+: E) (-: W)	ELEVATION (m.a.s.l)
4404503	Caqueta	CO	1.3333	-75.8000	300
4601501	Caqueta	CP	2.1500	-74.8000	300
3521002	Casanare	PM	5.3500	-72.4000	320
3523003	Casanare	PG	5.7333	-72.1000	350
2601002	Cauca	PM	2.2500	-76.4500	2800
2602002	Cauca	PM	2.6167	-76.3667	2650
2602003	Cauca	PM	2.6833	-76.5333	1840
2602004	Cauca	PM	3.0167	-76.4833	1112
2603002	Cauca	PM	2.4500	-76.6167	1730
2603005	Cauca	PM	2.5000	-76.8167	1720
2603011	Cauca	PM	2.4667	-76.9333	2500
2603503	Cauca	SP	2.4333	-76.5833	1730
2603505	Cauca	CO	2.4500	-76.5833	1850
2603506	Cauca	CP	2.4000	-76.8000	1700
2605006	Cauca	PM	2.9833	-76.6833	1060
2605506	Cauca	CO	3.1000	-76.6000	970
5201004	Cauca	PM	2.2667	-76.7500	1750
5201007	Cauca	PG	2.2500	-76.7333	1500
5201502	Cauca	CO	2.1500	-77.0500	580
5202503	Cauca	CO	1.7667	-77.1667	1174
5304501	Cauca - Guapi	CP	2.6167	-77.8167	10
5307003	Cauca - Pto Lopez	PG	2.9500	-77.2000	80
2321001	Cesar	PM	8.2000	-73.7500	90
2803503	Cesar	SP	10.4333	-73.2500	138
2804020	Cesar	PM	10.0667	-73.7667	120
2804501	Cesar	CO	10.3667	-73.6333	1000
1101001	Choco	PM	5.4500	-76.5333	100
1102001	Choco	PM	5.9000	-76.2000	1850
1104501	Choco	SP	5.7167	-76.6167	53
5402001	Choco	PM	5.1000	-76.7000	35
5402005	Choco	PM	4.9167	-76.2333	2034
5601501	Choco	CO	6.2333	-77.4000	4
1303001	Cordoba	PM	8.1833	-76.0667	100
1307502	Cordoba	CO	8.9167	-75.5833	40
1308503	Cordoba	CO	9.3667	-75.9667	22
1308504	Cordoba	SS	8.8167	-75.8500	20
2501010	Cordoba	PM	8.0167	-75.7667	160
2502014	Cordoba	PM	8.9500	-75.4500	60
2502515	Cordoba	CO	8.3167	-75.1333	22
2119009	Cundinamarca	PM	3.9833	-74.4833	1900

Table A2-2: Continued

CODE	DEPARTMENT	TYPE	LATITUDE (+: N) (-: S)	LONGITUDE (+: E) (-: W)	ELEVATION (m.a.s.l)
2119503	Cundinamarca	CO	4.3500	-74.4167	1550
2120008	Cundinamarca	PM	4.5833	-74.0333	3047
2120011	Cundinamarca	PM	4.7000	-73.9833	2750
2120013	Cundinamarca	PM	4.5500	-74.0500	3000
2120023	Cundinamarca	PM	4.6167	-74.0667	2700
2120024	Cundinamarca	PM	4.5833	-74.0167	3250
2120026	Cundinamarca	PG	5.0667	-74.0500	3062
2120027	Cundinamarca	PG	5.1000	-73.7000	2670
2120031	Cundinamarca	PM	4.7500	-74.0667	2691
2120032	Cundinamarca	PM	4.6167	-74.0500	3125
2120034	Cundinamarca	PM	4.4000	-74.1500	3056
2120040	Cundinamarca	PG	4.6333	-74.0333	3000
2120043	Cundinamarca	PG	5.2000	-73.6000	2700
2120044	Cundinamarca	PM	5.0000	-74.1333	2703
2120050	Cundinamarca	PM	4.7667	-73.9500	2600
2120080	Cundinamarca	PG	4.9833	-73.9000	2700
2120088	Cundinamarca	PG	5.1833	-74.0000	3140
2120106	Cundinamarca	PG	5.0333	-74.0333	3160
2120509	Cundinamarca	CO	4.4000	-74.1500	3050
2120516	Cundinamarca	CO	4.7167	-74.1833	2545
2120523	Cundinamarca	CP	4.6333	-74.1000	2556
2120524	Cundinamarca	CO	4.5667	-74.0667	2800
2120530	Cundinamarca	CO	4.5167	-74.0500	3256
2120536	Cundinamarca	CO	4.3500	-74.1333	3455
2120540	Cundinamarca	CP	5.1167	-73.8667	2580
2120541	Cundinamarca	CP	5.1500	-73.9833	3100
2120542	Cundinamarca	AM	4.7000	-74.2000	2543
2120545	Cundinamarca	CO	4.9833	-73.9667	2698
2120548	Cundinamarca	CP	5.0333	-73.7167	2760
2120561	Cundinamarca	CP	4.5500	-74.2500	2565
2303502	Cundinamarca	SP	5.4833	-74.6500	172
2306025	Cundinamarca	PM	5.0667	-74.6000	1060
2306028	Cundinamarca	PG	5.0000	-74.4833	880
2401512	Cundinamarca	CP	5.4667	-73.7333	2580
3502001	Cundinamarca	PM	4.3167	-73.9667	1300
3503504	Cundinamarca	CO	4.4833	-73.9000	2999
3503505	Cundinamarca	CO	4.5000	-73.8833	1897
3506009	Cundinamarca	PM	4.7000	-73.5167	1760
3506018	Cundinamarca	PM	4.7500	-73.5333	1920
3506028	Cundinamarca	PM	4.8333	-73.6333	1800

Table A2-2: Continued

CODE	DEPARTMENT	TYPE	LATITUDE (+: N) (-: S)	LONGITUDE (+: E) (-: W)	ELEVATION (m.a.s.l)
3109502	La Guajira	CO	4.0167	-67.6667	90
1504501	La Guajira	CO	11.2500	-73.0500	20
1508001	La Guajira	PM	12.3333	-71.3000	5
1508503	La Guajira	CO	11.2167	-72.3667	118
2801029	La Guajira	PM	10.7667	-73.0167	300
2103006	Huila	PM	1.6333	-76.0333	1345
2105502	Huila	CP	2.4167	-75.9167	1070
2106503	Huila	CO	2.3667	-75.5500	1500
2108003	Huila	PM	2.6667	-75.5167	600
2111034	Huila	PM	3.0667	-75.1333	1500
2111502	Huila	SS	2.9667	-75.3000	439
1507503	La Guajira	CP	11.7667	-72.4500	1
1501505	Magdalena	SP	11.1333	-74.2333	4
1501506	Magdalena	CP	11.1167	-74.0500	2200
2502125	Magdalena	PM	9.9167	-74.1167	120
2502509	Magdalena	SP	9.0667	-73.9833	34
2906004	Magdalena	PM	10.5167	-74.2000	40
3207503	Meta	CO	3.0333	-73.7333	325
3503001	Meta	SP	4.3667	-73.6833	1800
3503502	Meta	SP	4.1667	-73.6167	423
3512001	Meta	PM	4.3333	-72.1000	150
5102001	Narino	PG	1.3333	-78.1500	950
5204502	Narino	SP	1.4167	-77.2667	1796
5103501	Nariño	SS	1.8167	-78.7500	3
5204501	Nariño	AM	1.2000	-77.3000	2710
5205501	Nariño	SP	0.8167	-77.6333	2961
5205507	Nariño	CO	1.2667	-77.4667	1700
1605017	Norte	PM	8.4167	-73.4333	1545
1601005	Norte Santander	PM	8.1667	-72.4833	165
1601501	Norte Santander	SP	7.9333	-72.5167	250
1601506	Norte Santander	CO	7.5833	-72.6000	1235
1602008	Norte Santander	PM	7.5500	-72.7833	1280
1602502	Norte Santander	CO	8.1500	-72.5667	90
1602506	Norte Santander	CO	7.7667	-72.8000	1000
1603501	Norte Santander	CP	8.6500	-72.7000	50
3701001	Norte Santander	PM	7.3000	-72.5000	1560
4401501	Putumayo	AM	1.0000	-76.6000	440
4701002	Putumayo	PG	1.1167	-76.9667	2070
4701003	Putumayo	PM	0.5000	-76.5167	260
4701503	Putumayo	CO	1.1833	-76.9167	2100

Table A2-2: Continued

CODE	DEPARTMENT	TYPE	LATITUDE (+: N) (-: S)	LONGITUDE (+: E) (-: W)	ELEVATION (m.a.s.l)
2612006	Quindio	PM	4.6167	-75.7667	1400
2612010	Quindio	PG	4.6667	-75.6167	2040
2612506	Quindio	SP	4.4500	-75.7667	1204
2612507	Quindio	CO	4.5167	-75.6667	1450
2613504	Risaralda	SP	4.8167	-75.7333	1342
2613507	Risaralda	CO	4.7833	-75.5333	2120
2314001	Santander	PM	6.6667	-73.6500	1520
2315503	Santander	SP	7.0167	-73.8000	126
2315504	Santander	CO	6.8667	-73.7667	162
2319504	Santander	CP	7.1333	-73.1000	1018
2401068	Santander	PG	5.8000	-73.7000	2145
2402001	Santander	PM	6.5667	-73.1333	1470
2402004	Santander	PM	6.1333	-73.1167	1814
2402502	Santander	CP	6.5167	-73.2167	975
2403029	Santander	PM	6.5000	-72.6000	1856
2403037	Santander	PG	6.2500	-72.8333	3080
2404001	Santander	PM	6.6333	-73.2333	1300
2502504	Sucre	CP	8.7000	-75.1833	30
2502508	Sucre	SS	9.3333	-75.2833	166
2113503	Tolima	CP	3.5833	-75.1167	415
2116003	Tolima	PM	4.0500	-74.6833	450
2116005	Tolima	PM	3.6667	-74.8333	800
2117002	Tolima	PM	3.9833	-74.8667	306
2118503	Tolima	CP	4.0500	-74.9667	360
2118504	Tolima	SS	4.2833	-74.8000	286
2121507	Tolima	CO	4.4500	-75.2667	1300
2121510	Tolima	CO	4.4333	-75.4333	1920
2124504	Tolima	SS	4.4333	-75.1500	928
2125007	Tolima	PG	4.8000	-74.9333	477
2125047	Tolima	PM	5.1333	-74.9500	1500
2205004	Tolima	PG	3.5833	-75.3833	486
2605009	Valle	PM	3.4333	-76.6167	1730
2606002	Valle	PM	3.3167	-76.3500	1000
2607004	Valle	PM	3.5833	-76.3000	1065
2607076	Valle	PM	3.3500	-76.2500	1038
2607501	Valle	AM	3.5167	-76.3167	975
2607505	Valle	CO	3.5667	-76.2833	1020
2608007	Valle	PM	3.7000	-76.4333	987
2608010	Valle	PM	3.4500	-76.6500	1869
2608502	Valle	CO	3.4500	-76.5500	1070

Table A2-2: Continued

CODE	DEPARTMENT	TYPE	LATITUDE (+: N) (-: S)	LONGITUDE (+: E) (-: W)	ELEVATION (m.a.s.l)
2609009	Valle	PM	3.5667	-76.2667	1145
2610509	Valle	CO	4.2667	-75.9167	1540
2610516	Valle	SP	4.1000	-76.2167	955
2611015	Valle	PM	4.8000	-76.0000	960
2611504	Valle	CP	4.5333	-76.0500	920
5311501	Valle	SP	3.8500	-76.9667	14
5311502	Valle	CP	3.8833	-77.0667	10
5311503	Valle	CO	3.8167	-76.5167	1360
5407502	Valle	CO	4.0000	-76.9500	50
4206501	Vaupes	SS	1.2667	-70.2333	207
3401501	Vichada	SP	4.5500	-70.9167	171
3801504	Vichada	CO	6.2000	-67.4500	53